Heat Pump Integrated Energy Systems for Future Zero-Emission Vehicles

Thesis by

Nan Zhang

Submitted in fulfilment of the requirements for

the Degree of Doctor of Philosophy

James Watt School of Engineering

College of Science and Engineering

University of Glasgow

Date of Submission

June 2023

Abstract

Climate action is essential to limit the global warming temperature to 1.5 ºC by 2050, ensuring the phasing out of fossil fuels in the transport sector successfully. It is expected that batteries or hydrogen fuel cells will most likely be the main driver of future zero-emission vehicles to achieve the zero-emission target for transport. One of the key research challenges in fully electric vehicles is the thermal management in electric vehicles including cabin, battery, motor, and other electronics. The literature review summarised the recent development and research on battery thermal management, cabin thermal management, and integrated approaches. Based on the research gap in current integrated energy management system for zero emission vehicles, the thesis started from the integrated energy system for heating. An advanced fuel cell battery electrical vehicle energy system integrating with heat pump technology was proposed to extend the driving range, increase the overall energy efficiency. A maximum COP of 6.07 could be observed when the evaporator coolant inlet temperature was 32℃. Compared to conventional air source heat pumps and Positive Temperature Coefficient (PTC) heaters, the proposed system has the lowest cost which was £10.40/time. In order to further evaluate the performance of the proposed system from a vehicle perspective, the proposed system was applied to the electric vehicle and analyzed from a vehicle perspective with the help of the vehicle motion model. An Energy, Exergy, Environment, and Economic (4E) analysis method was conducted to investigate the integrated system comprehensively. It is shown that the highest COP_{sys} of the proposed system was 5.8 and could improve the driving range (DR) by 65% to 110% compared to the reference systems. The environmental impact decreased by 13kg/year per car compared to current EVs, and the reduction was primarily sourced from indirect emissions. The operating cost which included driving and heating was 28.9% higher than cited for an ASHP and PTC system and 41% higher than the PTC baseline system. Besides the heating integrated energy system, in order to provide a comprehensive vehicle management system, an integrated cooling energy system was provided. An integrated cooling system was developed for future electric vehicles by integrating the fuel cell, battery, metal-hydride, heat pump, and liquid desiccant dehumidification and regeneration system with the objective to reduce power consumption and extend the driving range in summer. Two operating modes were investigated. Under the heat pump supplemental mode, the proposed system can operate at 36 ºC with a COP greater than 4, which is 56% higher than the cited published results. And the insufficient cooling during transitions could be reduced compared to non-compressive mode.

Contents

Abstract i
List of Tables v
List of Figures vi
List of Publications ix
Acknowledgements x
Declaration xi
Nomenclature xii
1. Introduction 1
1.1 Background 1
1.2 Integrated Vehicle Thermal Management System 2
1.3 Research Aim and Objectives 2
1.4 Thesis Outline 3
2. Literature Review 5
2.1 Introduction 5
2.2 HPAC in Battery Thermal Management System 6
2.2.1 Optimal design on normal demands battery thermal management 7
2.2.2 BTMS focus on extreme operating conditions 13
2.2.3 Summary 20
2.3 Heat Pump in EV and Cabin Comfort 23
2.3.1 EV heat pump performance enhancement 26
2.3.2 HPAC with cabin 35
2.3.3 Summary 40
2.4 Performance and Advanced Control for HPAC Based Integrated VTMS 42
2.4.1 Integrated system design 42
2.4.2 Integrated system control strategy and intelligent algorithm 53
2.4.3 Summary 54
2.5 Chapter Summary 58
3. Heat Pump and Fuel Cell Integrated Energy System 61
3.1 Introduction 61
3.2 System Description 64
3.3 Model Development 66
3.3.1 PEMFC heat generation model 66
3.3.3 Heat transfer model of heat exchanger 71
3.3.4 Compressor model and electronic expansion valve (EEV) 75
3.3.5 Simulation procedure 76

3.3.6 Performance indicators 79
3.4 Reults and Discussion 79
3.4.1 Effect of fuel cell output current 80
3.4.2 The impact of battery discharging rate and subcooling degree 82
3.4.3 Effect of ambient temperature and coolant inlet temperature 87
3.4.4 Equivalent effective battery capacity and payback duration 89
3.5 Chapter Summary and outlook 93
4. 4E Analysis of the Heat Pump and Fuel Cell Integrated System Applying to Electric Vehicles 95
4.1 Introduction 95
4.2 System Description 98
4.3 Model Development 100
4.3.1 PEM fuel cell energy model 100
4.3.2 Battery energy model 103
4.3.3. Heat exchanger model 105
4.3.4 Compressor and expansion valve model 108
4.3.5 Vehicle motion model 110
4.3.6 Energy performance indicators 113
4.3.7 Exergy analysis and indicators 114
4.3.8 Environmental impacts indicators 116
4.3.9 Economic analysis and indicators 118
4.3.10 Simulation procedure 120
4.4. Results and Discussion 121
4.4.1 Energy analysis 121
4.4.2 Exergy analysis 129
4.4.3 Environmental analysis 134
4.4.4 Economic analysis 137
4.5 Chapter Summary and Outlook 139
5. Hybrid Integrated Cooling System for Fuel Cell Extender Electric Vehicle 142
5.1 Introduction 142
5.2 System Description 147
5.3 Model Development 149
5.3.1 PEMFC and battery model 149
5.3.2 Open metal hydride thermal model 150
5.3.3 Hollow fibre liquid desiccant dehumidifier heat and mass transfer model 154
5.3.4 Heat pump model 156
5.3.5 Performance indicator 158

5.3.6 Simulation procedure.....160
5.4 Results and Discussion.....163
5.4.1 Performance of the non-compressive cooling and dehumidification cycle.....163
5.4.2 Performance of the metal hydride assisted cooling and dehumidification cycle with supplement of heat pump.....172
5.5 Chapter Summary.....178
6. Conclusions and Future Plan.....180
6.1 Conclusions.....180
6.2 Future plan.....182
References.....183
Appendix 1.....195

List of Tables

Table 2.1 Different battery thermal management methods in the extreme operating situation and abnormal situations 22
Table 2.2 Comparison of refrigerant based BMTS 23
Table 2.3 Latest works regarding frosting and defrosting on OHX 42
Table 2.4 Comparison of latest integrated thermal management approaches 56
Table 2.5 Comparison of the performance and operating mode of different integrated systems 57
Table 3.1 Value of empirical parametric coefficient of activation losses [159] 67
Table 3.2 Parameters for fuel cell model and battery [167] 69
Table 3.3 The specification of heat pump components 71
Table 3.4 Constant of C and m in Eq.(3.36) for cross flow 75
Table 3.5 Operating conditions in the simulation 77
Table 3.6 Components cost for the proposed system 92
Table 4.1 Parameters for fuel cell model [164] 102
Table 4.2. Specifications for battery model 104
Table 4.3 Vehicle and components specifications 112
Table 4.4. CO_2 emission factor for H_2 production under different methods [207] 117
Table 4.5 Components comparison and capital costs 118
Table 4.6 Operating conditions in the simulation 120
Table 2. Specifications of the metal hydride 152
Table 5.1 Specifications of the components 158
Table 5.2 Operating conditions and physical properties in the simulation 162

List of Figures

Figure 2.1. Parallel air-cooling battery thermal management with spoilers [19] 7
Figure 2.2. Construction of battery block [23] 8
Figure 2.3. (a) New designed coolant based BTMS (b) Typical BTMs [25] 9
Figure 2.4. Direct contact HFE-7000-based BTMS [28] 10
Figure 2.5. Structure of hybrid cooling plate [35] 12
Figure 2.6. Heat generation rate under different discharging rates for 18650 [38] 13
Figure 2.7. Heat generation under different charging rates (square [39], triangle [40], circle [41]) 14
Figure 2.8. Heat rate of the battery while thermal runaway [42] 15
Figure 2.9. Working principle of atomized refrigerant based BTMS [46] 16
Figure 2.10. Proposed aluminium plate – water and PCM-based BTMS [48] 18
Figure 2.11. Structure of three-layer and two-layer PCM and micro-channel-based BTMS [52] ... 19
Figure 2.12. Schematic diagram of water mist system [53] 19
Figure 2.13. Average cooling load under different speeds (Ambient temperature: 35^{o}C, cabin set temperature: 27^{o}C) [57] 24
Figure 2.14. Average heating load under different speeds (Ambient temperature: -20^{o}C, cabin set temperature: 20^{o}C) [57] 24
Figure 2.15. Principle of the heat pump cycle 25
Figure 2.16. (a) baseline heat pump (b) IHX VI heat pump [74] 28
Figure 2.17. (a) upstream (b) downstream vapour injection heat pump [75] 29
Figure 2.18. Schematic of kangaroo cycle [79] 30
Figure 2.19. Reversible heat pump working principle [81] 31
Figure 2.20. Intermediate cooling compressor [84] 32
Figure 2.21. Schematic of secondary loop heat pump system [90] 33
Figure 2.22. Test bench of newly designed air source heat pump [91] 34
Figure 2.23. Schematic diagram of the flexible heat pump based on modified Evans-Perkins cycle [92] 35
Figure 2.24. Recirculation air strategy and energy-consuming calculation flow chart [93] 36
Figure 2.25. Improved AC system [94] 37
Figure 2.26. Dehumidification heat pump schematic diagram [95] 38
Figure 2.27. Schematic diagram of a heat pump with a desiccant dehumidification system [96] ... 38
Figure 2.28. Cooling capacity variation of SMPC, rule-based, DP controller [100] 40
Figure 2.29. Windshield defogging method. 41
Figure 2.30. Scheme diagram of a coupled heat pump and coolant BTM system [108] 43
Figure 2.31. Scheme diagram of dual evaporator heat pump-based VTMS [115] 45
Figure 2.32. Ejector-based VTMS scheme diagram [116] 46
Figure 2.33. EV thermal system [118] 47
Figure 2.34. Schematic of test rig [120] 48
Figure 2.35. Refrigerant-based vehicle thermal management operating diagram 49
Figure 2.36. Principle of PEMFC [124] 50
Figure 2.37. A heat pump-based fuel cell electric vehicle thermal management system [126] 51
Figure 2.38. Schematic diagram of the fuzzy control strategy 53
Figure 3.1. Schematic diagram of the heat pump assisted thermal management system for fuel cell backup battery-powered electrical vehicles 65
Figure 3.2. Schematic diagram of fuel cell backup battery-powered electrical vehicles 66
Figure 3.3. Validation of fuel cell heat generation model 69
Figure 3.4. Validation results of the battery thermal model under discharging (a) and charging (b) scenarios 70
Figure 3.5. Validation results of the heat exchanger heat transfer coefficient model 75

Figure 3.6. Validation results of the simplified compressor model [109].....76
Figure 3.7. Flow chart of proposed system simulation 78
Figure 3.8. (a) Variation of air temperature and COP (b) variation of vapour quality and heating capacity (c) variation of coolant, air, and refrigerant mass flow rate with respect to fuel cell output current (T_{amb}=0℃, $T_{cl\_eva\_inlet}$=30℃, C_{dch}=0.237, T_{sub}=0℃).....82
Figure 3.9. The impact of battery discharging rate on (a) air outlet temperature and vapor quality and (b) heating capacity and COP (T_{amb}=0℃, $T_{cl\_eva\_inlet}$=30℃, I_{FC}=220A, T_{sub}=0℃).....84
Figure 3.10. Pressure to enthalpy cycle diagram under different battery discharging rate (T_{amb}=0℃, $T_{cl\_eva\_inlet}$=30℃, I_{FC}=220A, T_{sub}=0℃) 85
Figure 3.11. The impacts of the subcooling degree on outlet air temperature and COP (a) and operating range (b) (T_{amb}=0℃, $T_{cl\_eva\_inlet}$=32℃, I_{FC}=220A for (a), C_{dch}=0.237).....87
Figure 3.12. Impact of ambient air temperature on COP and outlet air temperature and comparison with previous publications 88
Figure 3.13. Influence of condenser coolant inlet temperature on outlet air temperature and COP 89
Figure 3.14. Variation of battery capacity of the proposed system over operating time 91
Figure 3.15. Comparison of the amount of electricity that can be used for driving and increasing rate for proposed system, EVASHP system, and PTC system 91
Figure 3.16. Economic analysis for each system and payback cycle for the proposed system under 4 hours of operating period.....93
Figure 4.1. Schematic diagram of the heat pump assisted energy management system for FCBEV 100
Figure 4.2. Fuel cell heat generation model validation by comparison with experimental data in Ref. [164].....102
Figure 4.3. Battery energy model validation by comparison with the experimental data in Ref. [166].....105
Figure 4.4. Heat exchanger model validation (a) evaporator by comparison with experimental data in Ref. [170] and (b) condenser by comparison with experimental data in Ref. [171].....108
Figure 4.5. Compressor model validation by comparison with experimental data in Ref. [196] ..110
Figure 4.6. Vehicle motion model validation by comparing with experimental data in Ref. [194] 113
Figure 4.7. The impacts of fuel cell current output on (a) COPsys, COP and PWHR (b) DR and DRER compared with EVASHP [69] and PTC (T_{amb}=-20 ºC, $T_{cl,eva,inlet}$=30 ºC , C_{dch}=0.26) 123
Figure 4.8. The impacts of battery discharging C rate on (a) COPsys, COP, and PWHR (b) DR and DRER compared with EVASHP [69] and PTC (T_{amb}=-20 ºC, $T_{cl,eva,inlet}$=30 ºC, I_{FC}=220A).....125
Figure 4.9. The impact of battery discharging C rate on (a) COPsys, COP, and PWHR (b) DR and DRER compared with EVASHP [176] and PTC (C_{dch}=0.26, $T_{cl,eva,inlet}$=30 ºC, I_{FC}=220A).....127
Figure 4.10. The impacts of evaporator coolant inlet temperature on (a) COPsys, COP and PWHR (b) DR and DRER compared with EVASHP [69] and PTC (C_{dch}=0.26, T_{amb}=-20 ºC, I_{FC}=220A) .129
Figure 4.11. The exergy of the proposed system 133
Figure 4.12. Environmental (TWEI and $TEWI_{DR}$) analysis and comparison. (a) different systems (b) different refrigerants (GWPs) (c) different CO_2 factor 137
Figure 4.13. Analysis of system economic performance. (a) $EOC_{driving}$ and EOC_{heat}, (b) PP (C_{dch}=0.26, $T_{cl\_eva\_inlet}$=30℃, I_{FC}=220A, T_{amb}=0℃).....139
Figure 5.1. Marco schematic diagram of system 148
Figure 5.2. Schematic diagram of the open metal-hydride subsystem.....149
Figure 5.3. Open metal hydride thermal model validation compared to Ref. [133] 153
Figure 5.4. Metal hydride's pressure variation along with its hydrogen capacity 153
Figure 5.5. Characteristic curve of the pressure of the metal hydride.....154
Figure 5.6. Condenser validation model by comparison with the experimental data in Ref. [247] 157

Figure 5.7. Proposed system numerical model simulation flow chart 161
Figure 5.8. The impacts of the ambient temperature and air mass flow rate on air outlet temperature (a), specific humidity (b), cooling capacity (c) (RH_{air}=80%, X_{sol}=62%, B_{ch}=0.1, $T_{sol,MH,out}$=23 ºC) 165
Figure 5.9. The impacts of the battery charging C rate and air mass flow rate on air outlet temperature (a), specific humidity (b), cooling capacity (c) (RH_{air}=80%, X_{sol}=62%, T_{amb}=30 ºC, $T_{sol,MH,out}$=23 ºC) 166
Figure 5.10. The impacts of the solution temperature and air mass flow rate on air outlet temperature (a), specific humidity (b), cooling capacity (c) (RH_{air}=80%, X_{sol}=62%, T_{amb}=30ºC, B_{ch}=0.1) 169
Figure 5.11. Real-time performance of the non-compressive cooling cycle (T_{abs}=35 ºC, T_{des}=30 ºC, RH_{air}=80%, X_{sol}=62%, T_{amb}=30 ºC, m_{air}=0.03kg/s) 170
Figure 5.12. The impacts of the ambient temperature on performance and comparison with published results (RH_{air}=80%, X_{sol}=62%, B_{ch}=0.1C, m_{air}=0.07kg/s B_{dch}=0.57C, $Q_{eva+chi}$=3kW) 172
Figure 5.13. Impact of the battery discharging C rate on performance (RH_{air}=80%, X_{sol}=62%, B_{ch}=0.1, m_{air}=0.07kg/s, Tamb=30 ºC, $Q_{eva+chi}$=3kW, B_{ch}=0.1) 175
Figure 5.14. Impacts of the battery charging C rate on performance (RH_{air}=80%, X_{sol}=62%, B_{ch}=0.1, m_{air}=0.07kg/s, Tamb=30 ºC, Q_{eva} =1.7kW, B_{dch}=0.57, Q_{chi}=1.3kW) 176
Figure 5.15. Real-time performance of the non-compressive cooling cycle (T_{abs}=35 ºC, T_{des}=30 ºC, RH_{air}=80%, X_{sol}=62%, T_{amb}=30 ºC, m_{air}=0.07kg/s) 177

List of Publications

Journal articles

1. **Nan Zhang**, Yiji Lu, Sambhaji Kadam, Zhibin Yu, Investigation of the integrated fuel cell, battery, and heat pump energy systems, Energy Conversion and Management, Volume 276, 2023, 116503
2. **Nan Zhang**, Yiji Lu, Zahra Hajabdollahi Ouderji, Zhibin Yu, Review of heat pump integrated energy systems for future zero-emission vehicles, Energy, Volume 273, 2023, 127101
3. **Nan Zhang**, Yiji Lu, Sambhaji Kadam, Zhibin Yu, A fuel cell range extender integrating with heat pump for cabin heat and power generation. Applied Energy, Volume 348, 121600
4. **Nan Zhang**, Yiji Lu, Zhibin Yu, A cleaner and efficient energy system achieving a sustainable future for road transport. Journal of Cleaner Production, Volume 418, 2023,137982

Conference proceedings

1. **Nan Zhang**, Yiji Lu, Zahra Hajabdollahi Ouderji, Zhibin Yu, Heat pump integrated thermal management system in future zero-emission vehicles, IGEC2023, 4-8 July, online.
2. **Nan Zhang**, Yiji Lu, Sambhaji Kadam, Zhibin Yu, Numerical analysis of the heat pump assisted integrated thermal management for fuel cell back up battery electric vehicles, ICAE 2022, 8-11 Aug, Bochum
3. **Nan Zhang**, Yiji Lu, Sambhaji Kadam, Zhibin Yu, The performance of a heat pump assisted integrated cooling and dehumidification system for zero emission vehicles, IGEC 2023, 10-13 July, Glasgow

Acknowledgements

There will always be someone to help you along the way to success, especially during the PhD process. I would like to thank my tutors, colleagues and family members who have been tirelessly encouraging me, giving me help and support, so that I can successfully complete my studies.

First and foremost, I would like to show my heartfelt appreciation to my primary supervisor Dr. Yiji Lu. Whether it is study or life, you are always on call and help me from morning till night. You are so kind and working with you makes everything easier. Furthermore, you can always make effective and reasonable suggestions based on your experience at critical time points. I can't imagine how difficult my Ph.D. study would be without your help. Your expertise, insights, and constructive feedback have been instrumental in shaping my research, and I am extremely grateful for your mentorship.

I would like also to express my sincere gratitude to my secondary supervisor, Prof. Zhibin Yu, for his unwavering support, guidance, and encouragement throughout my Ph.D. journey. It was you who provided me with the opportunity to study for a Ph.D. and respected my ideas. Your spirit of hard work always inspires me. Your expertise and knowledge have been invaluable, and I feel incredibly fortunate to have had the opportunity to work with you.

I am also deeply grateful to my colleagues and fellow researchers in the research group. Kadam, thanks for your support, you have the patience to entertain my endless questions. You are like my third supervisor although it is not officially shown in the system. Michael, you were the first colleague I met when I arrived in Glasgow, and I will never forget the day you showed me around the school. Saif and Miryam, it was really nice to work with you, we always sit together from JWS to Rankine, you can always provide me with the information that I really need and add fun to my boring study life. Andy, Ebraheem, Zahra, Meng, and other colleagues in the research group, it was really great to work with you all.

Finally, I owe a special debt of gratitude to my family, who have been a constant source of love, encouragement, and motivation throughout my Ph.D. journey. Their support and understanding have been a great source of strength for me, and I am forever grateful for their love.

Declaration

I am aware of and understand the policy of the University of Glasgow regarding plagiarism and I certify that the work in this thesis is my own, except where indicated by referencing, and is in accordance with University and School guidance on good academic conduct.

……..

Nan Zhang

June, 2023

Nomenclature

Symbols

A	area [cm^2] for fuel cell [m^2] for heat exchanger
Ac	circulation area [m^2]
a	acceleration [m/s^2]
BC	battery capacity [kWh]
Bo	boiling number
C_{O2}	oxygen concentration at the catalyst interface
C_O	convective number
Cp	specific heat capacity [J/ (kg K)]
Cv	EEV flow coefficient
Cd	drag coefficient
D	mass diffusivity [m/s]
D_h	hydraulic diameter [m]
e	chemical exergy [kJ/kg]
E	exergy [J]
E_{nerst}	open-circuit reversible voltage [V]
f	fanning friction factor
F	Faraday's constant 96485 [coulombs/mol] or force
Fr	Froude number
g	gravitational acceleration 9.8 [m/s^2]
G	mass flux [kg/m^2s]
Ga	Galileo number
h	heat transfer coefficient
H	enthalpy [J/kg]
i	current density [A/cm^2]
i_{fg}	enthalpy of vaporization [J/kg]
I	current[A]
Ja	Jakob number
k	conductivity
l	thickness [cm]
$\dot{m}$	Mass flow rate [kg/s]
M	molecular weight [kg/mol]
Me	Metal
M_{veh}	vehicle weight [kg]
N(n)	Number of cells
Nu	Nusselt number
P	partial pressure [atm]
Pr	Prandtl number
Q	heat [W]
q''	Heat flux [W/m^2]
$\dot{q}$	Specific energy [MJ/kg]
R	universal gas constant 8.31447 [kPa·m3/(kmol·K)]
Re	Reynolds number
R_{wall}	wall heat transfer resistance
R_{ions}	ionic resistance
$R_{electrons}$	electronic resistivity
R_m	membrane specific resistivity
S	entropy [J/(kg·K)]

t	time [s]
T	temperature [K]
T_0	reference temperature [K]
U	total heat transfer coefficient [W/m^2/K]
U_h	Overall heat transfer coefficient [W/m2/K]
v	velocity [m/s]
V	voltage [V]
V_a	activation voltage [V]
V_c	concentration voltage [V]
W	energy consumption [W]
x	mole fraction
X	vapor quality
X_{tt}	turbulent-turbulent Lockhart Martinelli parameter

Greek symbols

λ	conductivity [W/(m·K)]
δ_{wall}	thickness of the plate [m]
ρ	density [kg/m^3]
μ	dynamic viscosity [Pa·s]
η_0	overall surface efficiency
η_{isen}	isentropic effectiveness
φ	void fraction
γ	compressing ratio
ε	efficiency
θ_{leak}	leakage rate
ϕ	packing fraction
σ	membrane thickness [m]
ω	specific humidity [kg/kg]
β	inclination angle
ϵ	porosity

Subscripts

act	activation loss
ach	airflow channel
annular	annular flow
amb	ambient
bat	battery
c	cold
cab	cabin
cell	single fuel cell
cg	charging
chr	battery charging
chi	chiller
cl	coolant
comp	compressor
con	concentration loss
cond	condenser
cs	cross-section
dis	compressor discharging
dch	battery discharging
de	dehumidification
des	destruction
dr	drag resistance

econd	external condenser
eff	effective
eq	equivalent
eva	evaporator
ele	electrons
exv	expansion valve
f	fin area
fc	fuel cell
f_{rr}	rolling coefficient
forced	forced flow
FC	fuel cell stack
gr	gradient resistance
h	hot
hp	heat pump
H_2	Hydrogen
H_2O	Water
w	water
i	inlet
inn	inner
irr	irreversible
icond	internal condenser
IHX	internal heat exchanger
l	liquid
lab	labour
lo	liquid only
m	mean
mod	module
nernst	nernst open circuit
ohm	ohmic losses
o	outlet
out	outer
op	operating
O_2	oxygen
OC	open circuit
OHX	external heat exchanger
ref	refrigerant
rev	reversible
rr	rolling resistance
s	solid
ser	series
sol	solution
sub	subcooling
suc	compressor suction
sys	system
SP	separate plate
tf	traction force
tot	total
v	vapor
veh	vehicle
wall	wall of heat exchanger
wavy	wavy flow
wo	water only

Abbreviations:

AC	Air Conditioning
ACC	additional capital cost
ASHP	Air source heat pump
BC	initial battery pack capacity
BEV	battery electrical vehicle
BTMS	Battery Thermal Management System
CC	capital cost
COP	Coefficient of Performance
COD	Cathode Oxygen Depletion
CPFC	cost per fully charging cycle
CWHRS	Conventional Heat Pump Waste Heat Recovery System
DC	direct current
DI	Downstream Injection
DP	Dynamic Programming
DRE	driving range extension
DRER	driving range extension rate
DWHRS	Direct Heat Pump Waste Heat Recovery System
EV	Electric Vehicle
EEV	Electric Expansion Valve
EER	Energy Efficiency Rating
EEBC	equivalent effective battery capacity
EOC	effective operating cost
ERV	Energy Recovery Ventilator
EVASHP	electrical vehicle air source heat pump
FC	Fuel Cell
FCBEV	fuel cell battery electrical vehicle
FCBEEV	fuel cell battery range-extended electrical vehicle
GHG	greenhouse gas
GWP	Global Warming Potential
HEV	Hybrid Electric Vehicle
HFE	Hydrofluoroether
HVAC	Heating, Ventilation and Air Conditioning
HPAC	Heat Pump Air Conditioning
HX	Heat Exchanger
ICE	Internal Combustion Engine
IHX	Internal Heat Exchanger
LMTD	logarithmic mean temperature difference
MPC	Model Predictive Control
MWHRS	Multi-stage Heat Pump Waste Heat Recovery System
NEDC	New European Driving Cycle
NSGA	Non-dominated Sorting Genetic Algorithm
OHX	Outdoor Heat Exchanger
OSA	Outside Air
PID	Proportional Integral Derivative
PEMFC	Proton Exchange Membrane Fuel Cell
PTC	Positive Temperature Coefficient
PCM	Phase Change Material
PP	payback duration
PWHR	percentage of waste heat recovery
RH	Relative Humidity [%]
RIHP	Refrigerant Injection Heat Pump
SOC	State of Charge
SOH	State of Health
SDP	Stochastic Dynamic Programming
S-CPCM	Serpentine Composite Phase Change Material

TEWI	Total Equivalent Warming Impact
UI	Upstream Injection
VI	Vapor Injection
VTMS	Vehicle Thermal management system
WLTD	worldwide harmonized light vehicles test cycle
WLTP	Worldwide Light Vehicle Test

1. Introduction

1.1 Background

Climate change is causing warming across the world and bringing more and more frequent heat waves. The hottest temperature in Europe was 47ºC in Portugal and 38.7ºC in the UK. The UK Met Office predicted that Summer will be between 1 and 6ºC warmer and up to 60% drier in 50 years' time. Global warming will lead to rising sea levels which will cause floods that will harm coastal cities and cause droughts in inland cities. The main reason for global warming is greenhouse gas (GHG) emissions and CO_2 are one of the main sources. As a result, the commitment to achieve carbon neutrality by 2050 (to limit the global temperature rise to 1.5ºC compared to the pre-industrial levels) was reaffirmed at COP26 in Glasgow in 2021. In 2021, CO_2 accounted for 85% of total GHG emissions in the UK, and the total GHG emissions were 424.5 $MtCO_{2e}$ [1]. 26% of the total GHG emissions in the UK come from the transport sector and road traffic contributed 87% of that. Therefore, several governments have committed to ending the sales of new fossil fuel vehicles by 2030 and achieving complete net zero road traffic by 2050. In order to help meet these ambitious targets, vehicle electrification is an important step. However, the biggest factor hindering the promotion of electric vehicles is the driving range. Driving range decreases dramatically when air conditioning for heating and cooling is on as well as when the battery and other electronic devices require further cooling in summer. Different from traditional Internal Combustion Engine (ICE) vehicles, in winter, current zero emission vehicles lack concentrated high-temperature waste heat and distributed low-temperature waste heat is not easy to be utilized. In summer, temperature-sensitive batteries and increasing thermal comfort requirements increase the energy consumption of air conditioning. Providing heating and cooling load with high efficiency and eliminating driving range anxiety play an important role in decarbonization. Based on that, several technologies have been investigated separately the thermal management system of electric vehicles. One of these promising potential solutions in vehicle thermal management systems is heat pump technologies which have received significant research interest over the decades. However, instead of considering each component separately, integrating the whole system has received significant interest recently and shows great potential to solve the problems comprehensively.

1.2 Integrated Vehicle Thermal Management System

Integrated Vehicle thermal management (IVTM) entails regulating heat and cooling flow inside the vehicle to ensure all the components and space can be operated in their respective optimal temperature range. For the ICE vehicles, its vehicle thermal management system mainly includes engine and cabin thermal management. A water/coolant system exists in the ICE vehicle in order to release the engine waste heat or recycle the waste for cabin heating in winter. Meanwhile, a traditional air conditioning system is adopted for cabin cooling in summer. However, Integrated Vehicle Thermal Management Systems (IVTMS) in electric vehicles are more complex compared to traditional ICE vehicles. This can be explained from two perspectives. For summer, the components in electric vehicles are much more sensitive to those in traditional ICE vehicles, like the battery operating temperature needs to keep within 25 ^{o}C to 40 ^{o}C. For winter, as there is no high temperature waste heat from ICE in electric vehicles, heating cabins and electronics for autopilots need different vehicle management strategies as well. With the help of IVTMS in winter, although the thermal management performance could be improved [2], the source of the waste heat is unstable. For summer, the IVTMS can control the battery and cabin temperature well, but it also increases the load of air conditioning. These shortages highlight the need for significant further improvements in IVTMS for both heating and cooling.

1.3 Research Aim and Objectives

The broad reaching aim of this thesis is to design potential solutions for the VTMS (Vehicle Thermal Management System) of future zero-emission vehicles in order to increase the efficiency of VTMS and reduce the driving range deduction caused by VTMS in both summer and winter.

The objectives of this work can be summarized as:

- To identify and discuss the latest research and solutions for EVs' thermal management system and figure out the challenges of thermal management system for EVs.
- To design a highly integrated energy management system for future zero-emission vehicles, build up a numerical model, and evaluate the performance of the proposed system.
- According to the design and initial performance analysis of the proposed system in objective 2, the performance investigation of the proposed system applying to an

electric vehicle is needed. It is necessary to provide a quantitative analysis about how much driving range deduction, how much operating cost and how much CO_2 emission could be reduced with the help of the designed system in objective 2. As a result, a 4E method (Energy, Exergy, Environment, and Economics) was adopted to further evaluate the performance and improvements of the system from a vehicle perspective comprehensively.

- Besides the heating system in objectives 2 and 3, the cooling system is also very important in the VTMS. It is also important to build a highly integrated energy system for summer to reduce the driving range deduction and increase the cooling efficiency. Therefore, objective 4 is to design and set up a model for an innovative integrated cooling system for future zero-emissions vehicles and evaluate its performance.

1.4 Thesis Outline

The thesis presented has been structured as an alternative format thesis. Chapters 2 to 5 were constructed based on published or submitted papers.

In Chapter 2, A broad review was carried out according to the latest published works regarding battery thermal management, cabin thermal management, and current integrated VTMS. The advantages and disadvantages of each thermal management method were concluded, and research gaps were identified.

In Chapter 3, based on the research gaps concluded in the literature review, a heat pump assisted, fuel cell backup battery electric vehicle energy management system for winter was designed. A numerical was developed and the performance was evaluated from a system level.

As the feasibility of the proposed system has been demonstrated in Chapter 3, in Chapter 4, in order to further investigate the performance of the vehicle installed the proposed integrated energy system, the vehicle motion model was introduced, and the proposed system was further investigated via a 4E analysis from a vehicle perspective.

In order to provide a comprehensive vehicle thermal management system including heating and cooling, in Chapter 5, an integrated cooling system was developed by integrating the fuel cell, battery, metal-hydride, heat pump, and liquid desiccant dehumidification and

regeneration system with the objective to reduce power consumption, extend the driving range and improve the cabin thermal comfort in summer. Numerical models were developed and evaluated.

In Chapter 6, the conclusion of the findings of the study was offered and any future work following any recommendations in the study is described.

2. Literature Review

2.1 Introduction

During the last 30 years, although the explosion of the Internal Combustion Engine (ICE) vehicle brought great convenience to the world, ICE technology contributed to over 14% of worldwide greenhouse gas emissions [3]. In order to create a zero-carbon future and tackle climate change, an increasing number of countries are starting to make plans to achieve a 100% reduction of carbon dioxide (CO_2), including the UK which plans to achieve this aim by 2050 [4]. Therefore, electric vehicles have become the most discussed topic in the world.

The thermal management systems of the Electric vehicle (EV) are very different compared to the conventional ICE vehicle. The EV thermal management is very sensitive as the optimal operating range for a battery in EV is between 15 ^{o}C and 35 ^{o}C, and outside of this range will cause efficiency reduction and capacity losses [5]. Hydrogen fuel cell electric vehicles also face similar challenges. A proper operating temperature range is important for performance, otherwise, it will cause irreversible performance loss [6]. Meanwhile, the principle of cabin thermal management in low temperatures is significantly different from ICE vehicles as there is no longer engine waste heat Currently, most EVs are using Positive Temperature Coefficient (PTC) posistor but it will reduce up to 50% driving range [7]. Hence, it is vital to adopt an advanced heating and cooling system for both cabin and battery of electric vehicles. Wu *et al.* [8], Zhao *et al*.[9] and Qin *et al.* [10] completed detailed reviews on liquid-based, hybrid medium based, and forced air-based battery thermal management systems (BTMS) in 2019, 2020, and 2021 respectively. Only Kim *et al.* [11] comprehensively reviewed recent BTMS in 2019 and briefly mentioned a direct refrigerant-based cooling system for batteries. Tomaszewska *et al.* [12] briefly mentioned battery thermal management for fast charging, including liquid immersion cooling, two-phase liquid cooling, and phase change material (PCM) cooling which was proved sufficient with external cooling technologies under a 2C charging rate. However, for battery preheating before fast charging, only internal preheating was discussed and the performance of systems using a refrigerant to cool down the battery while fast discharging was not explored. Hence, it is necessary to further discuss refrigerant-based battery thermal management systems to ensure thermal safety under fast charging and increase efficiency under normal operation. In addition to battery thermal management, HPAC (heat pump air conditioning) based EV cabin thermal management is another important part of the EV thermal management system and

was also critically reviewed by Peng, Qi and Zhang *et al.* [7, 13-15] between 2014 and 2018. The latest literature concluded and demonstrated that these systems have a promising future in extending the driving range and enhancing cabin thermal comfort. However, only Zhang *et al.* [14] reviewed integrated thermal management systems proposed before 2016 and put more focus on battery cooling without considering cabin thermal comfort. Furthermore, Lajunen *et al.* [16] also presented a review, including cabin thermal models, and analysed the methods for enhancing thermal efficiency. Therefore, in order to manage thermal dissipation more effectively and achieve a longer driving range, heat pump-based integrated vehicles should be analysed thoroughly.

This chapter presents a comprehensive review of the latest thermal management for electric vehicles including battery thermal management, cabin thermal management, and cabin and battery integrated thermal management systems. Of particular interest is the utilization of the HPAC system in EVs, not only from the cabin aspect but also from the whole vehicle level. In order to achieve the aim of this study, the specific objectives are:

- Battery thermal management discussion: Provide the latest BTMS in terms of normal or extreme working conditions and comprehensively conclude the performance of different managing approaches under extreme or abnormal operating situations and indicated the potential method that can best fulfil the whole condition task and introduce how HPAC system could participate in the BTM system.

- Heat pump-based cabin comfort management overview: An in-depth summary of heat pump performance improvement technologies for EV cabin thermal management and methods for addressing the fogging issue on the windshield was conducted. Limitations of the current research were identified.

- System-level design: The performance of heat pump-assisted secondary coolant loop-based or pure refrigerant-based BTMS and fuel cell electric vehicle integrated system was summarized, and the intelligent control algorithm was introduced. Potential methods to improve the system performance was determined.

2.2 HPAC in Battery Thermal Management System

Battery thermal management system (BTMS) is one of the most important topics in EV research, due to its relevance to both battery efficiency and passenger safety. Recently,

battery thermal management, in general, has six which are air cooling, coolant cooling, heat pipe cooling, phase change material methods, refrigerant, and hybrid management methods. Scholars now are optimizing existing thermal management methods while exploring new BTMS.

2.2.1 Optimal design on normal demands battery thermal management

2.2.1.1 Air-based battery thermal management system

Air-based battery thermal management system is one of the most popular systems in commercial EVs. Normally, an ambient air-based battery thermal management system results in a simple structure and low weight. Chen *et al.* [17, 18] recently conducted a series of detailed studies on the flow pattern of air cooling battery thermal management systems. It can be shown that optimization of the outlet region has better effects on thermal management. Comparing typical Z-type flow pattern and seven other optimization cases, the seventh case called BTM-VII-opt re-allocated the outlet in the middle position of the top of the battery, can maximize the temperature and temperature difference by 4.5 ºC and 7.7 ºC respectively when heat generation was approximately 11.8W per block. Zhang *et al.* [19] designed an air-based BTMS with spoilers, in which several boards were installed on the bottom of the cooling channel to increase the airflow rate of the front-end cooling channel. The structure proposed by Zhang *et al.* is shown in **Figure 2.1** and they analysed the impacts of the number and position of those spoilers on BTMS performance. The results pointed out that the highest cooling performance occurred when five spoilers were located in the fourth to eighth distribution sections. Furthermore, higher inclination and height of the spoiler can lead to an improved cooling performance. With optimal spoilers, the air-cooling method can keep the battery temperature within an acceptable range when the heat generation for each battery is 11.8W.

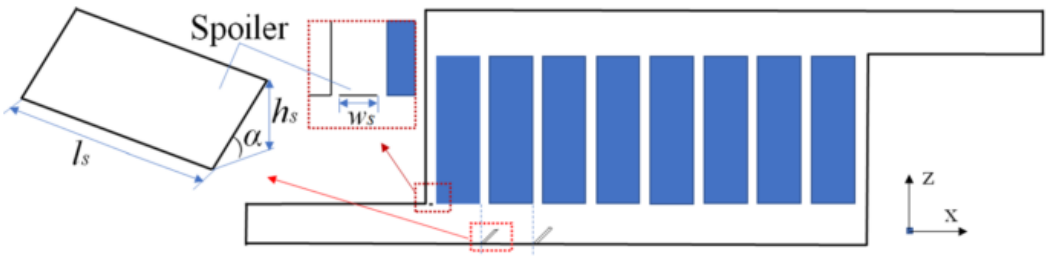

Figure 2.1. Parallel air-cooling battery thermal management with spoilers [19]

Additionally, a multi-objective optimization algorithm was introduced into the air cooling battery system by Chen *et al.* [20] in order to achieve optimal energy, maximum battery temperature and battery temperature difference with regard to structural parameters. The results indicated that NSGA-III_DE can provide a better performance which can lead to a 16.7% energy consumption reduction and 60.7% battery temperature difference reduction.

2.2.1.2 Coolant-based BTMS

Yang *et al.* [21] discussed the performance of coolant-based BTMS under different flow paths and claimed that, compared to basic type Z flow path (coolant inlet at bottom of the front boundary while outlet at top of the end boundary), type D (a parallel flow with coolant inlet and outlet on the middle of the front and back boundary) can decrease the temperature difference and maximum temperature by 1.7% and 20%. Furthermore, increasing the number of coolant inlets and outlets can improve the cooling efficiency of the thermal management system. A similar topic also was discussed by Wang *et al.* [22]. They designed a modular liquid cooling battery thermal management module and investigated its performance under four flow patterns. The conclusions show that parallel flow can largely improve the temperature uniformity of the battery module. Moreover, three parallel flow layouts were simulated in which layout III (staggered flow) provided the lowest maximum temperature and temperature difference when the discharging rate was 3C, while the ambient temperature was 30ºC. Tan *et al.* [23] designed an HFE-6120-based direct coolant cooling BTMS (shown in **Figure 2.2**) and analysed its performance under a 3C charging rate in terms of maximum temperature, temperature difference, and power consumption with the variation of the channel layer, coolant flow rate etc. The temperature difference can be reduced by 18.1% by adding a channel layer, however, the power consumption will increase by 17% as a trade-off.

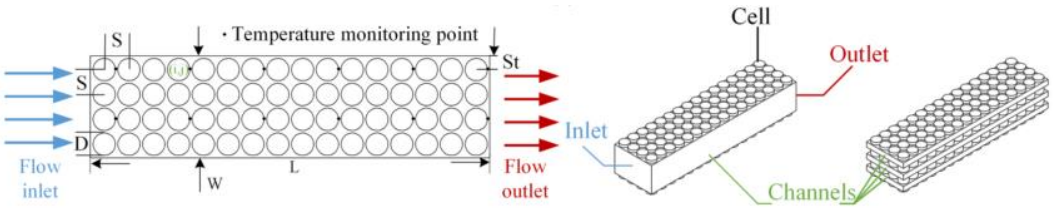

Figure 2.2. Construction of battery block [23]

Chang *et al.* [24] also investigated the performance of a reciprocating liquid flow BTMS which allowed the direction of coolant flow to be changed periodically. The results indicated

that the coolant flow rate can be reduced by up to 89.5%, compared to normal coolant battery thermal management when battery temperature uniformity remains the same. Meanwhile, when the coolant flow rates are the same, the proposed reciprocating system can reduce the maximum temperature and temperature difference by 1.67 ºC and 3.77 ºC respectively. Additionally, an optimization of the structure of a coolant-based battery management system for large-scale packs was introduced by Chung and Kim [25]. They suggested that the newly designed structure, as shown in **Figure 2.3** (a), can improve the ratio of the equivalent heat conductance to the system volume by 64% while the maximum temperature difference was reduced to 5.4 ºC under a 2C charging rate, compared with the typical structure, as shown in **Figure 2.3** (b)

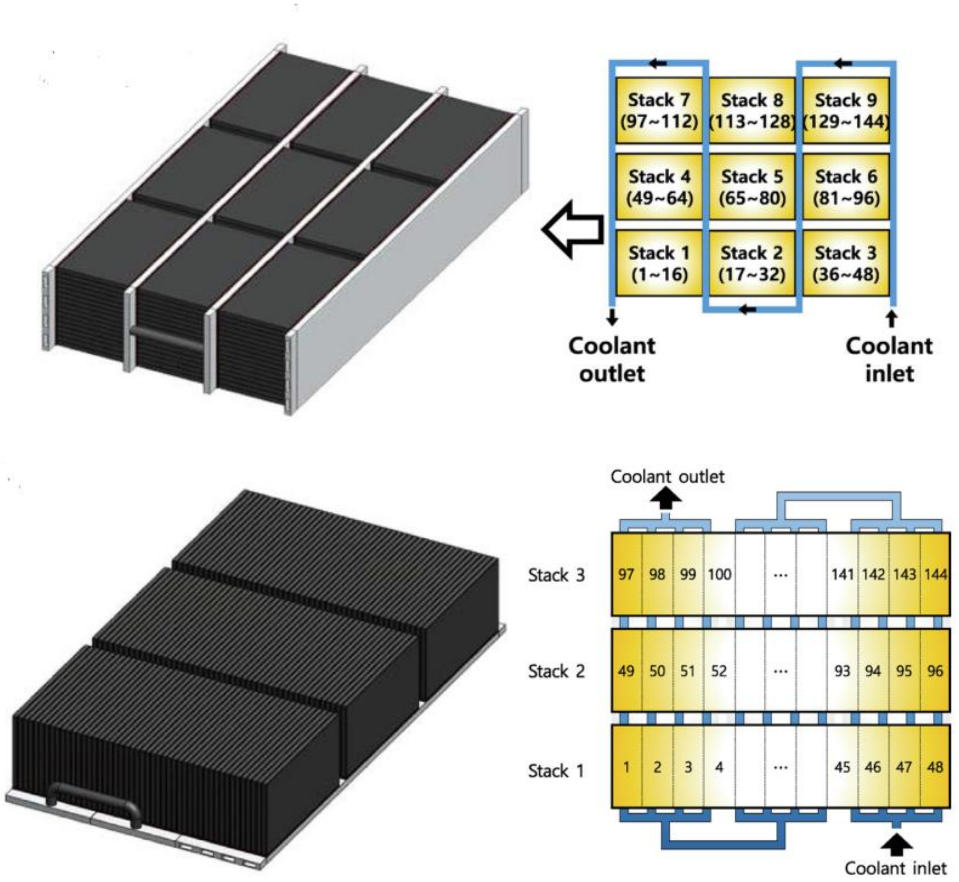

Figure 2.3. (a) New designed coolant based BTMS (b) Typical BTMs [25]

Furthermore, in order to reveal the battery temperature response after a sudden change to optimize control conditions, Huang *et al.* [26] analyzed the upper limit and cooling time delay of a liquid-based cooling plate battery thermal management system. The results showed cooling capacity would no longer improve when the liquid mass flow rate was over a specific value. For the proposed system, that cap was 475 Reynolds number. A hysteresis

phenomenon can always be observed, especially under a low discharge rate. For example, the time delay was approximately 66.37s when the discharge rate was only 1C.

2.2.1.3 Refrigerant based BTMS

Zhu *et al.* [27] experimentally studied the performance of R1233zd-based BTMS for EVs. They showed that the increase of refrigerant mass flow can gradually enhance the performance of the proposed BTMS under lower heat flux. However, under higher heat flux, little effect on the heat transfer coefficient can be observed when increasing refrigerant mass flow, as the cooling effect is mainly based on boiler heat transfer. In addition, Wang and Wu [28] also investigated the performance of an HFE-7000 based direct contact BTMS, as shown in **Figure 2.4**, by experiment and numerical simulation when the discharge rate varied from 1C(3A) to 5C. They suggested that nucleate boiling heat transfer dominates the temperature uniformity between the individual battery while forced convection plays a key role in maximum temperature.

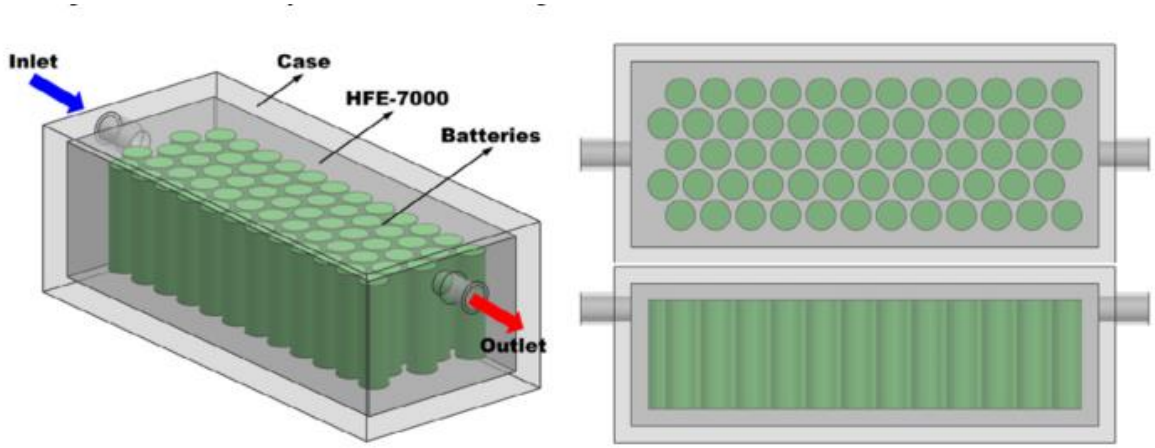

Figure 2.4. Direct contact HFE-7000-based BTMS [28]

Park *et al.* [29] analyzed and simulated the performance of a refrigerant (R-134a) based BTMS and compared it with a PCM-based BTMS. It can be demonstrated that at ambient 25 ºC, with an increase of refrigerant temperature (20 ºC -25 ºC), the battery temperature difference also decreases at a given discharge rate to a certain point and begins a reverse trend. Moreover, compared to refrigerant-based battery cooling systems, PCM's performance is not impressive in cyclic operations because the latent heat capacity cannot be recovered quickly under a 2C discharging rate in three cycles with 30-minute breaks between each cycle. Meanwhile, the performance of a two-phase refrigerant cooling was experimentally assessed under various operation ranges, including outlet refrigerant state

and battery charging rate by Hong *et al.* [30]. The weight of the proposed system is 56% lighter than a liquid cooling system. Additionally, they also undertook a comparison with the coolant cooling module. The results showed that outflow refrigerant superheat can cause the divergence of the temperature even when the vapour ratio is 0.95 and the temperature difference was also out of range. Meanwhile, the proposed R134a-based BTMS can provide 16.1% more battery capacity and 15% lower internal resistance under harsh environmental conditions. However, the optimal vapor pressure is still not clear. Shen *et al.* [31] designed a new structure for refrigerant(R134a) BTMS and explored its performance. They suggested that under mild conditions, the higher the discharge rate the greater the maximum temperature can be observed, from a module perspective. The maximum difference from the module perspective was 16 ^{o}C under a 2C charging rate. However, from the cell aspect, the maximum temperature difference along the refrigerant direction was 5K between starting point to the exiting point. Similarly, Wang *et al.* [32], also from a structural perspective, designed a new refrigerant plate for BTMS to improve the cooling and uniformity performance. A proposed structure with a specific type (first, second and third flow pass has 1, 2 and 3 tubes, respectively) can achieve the highest heat transfer rate of 810.8W(m^2/K) and the most suitable pressure drop of 1.67kPa.

2.2.1.4 Hybrid BTMS

The hybrid cooling method usually includes a heat pipe or a PCM supplemented by a matching cooling medium to cool it down. Those components can apply latent heat within atmospheric pressure but cannot recover quickly without a second cooling medium. Yue *et al.* [33] developed a BTMS with a heat pipe, air cooling and water spraying system. They demonstrated that under an experimental 3C discharging rate, the proposed hybrid BTMS can maintain the maximum temperature at 35.1 ^{o}C while it can reach 41.9 ^{o}C under a pure air cooling system and can save around 62% energy consumption compared with the air cooling method. Chen *et al.* [34] discussed the impact of PCM with passive air convection-based BTMS on battery cycle life and compared it with active air cooling BTMS. The results showed the active air cooling method keeps the battery temperature under a safe range when the ambient temperature is over 50 ^{o}C. However passive PCM cooled by natural convection cannot fulfil this situation. Meanwhile, active air cooling can improve the battery cycle life range by 20% which is 16% higher than PCM with passive air convection-based BTMS, but the latter method can offer higher battery temperature uniformity. Akbarzadeh *et al.* [35] designed and simulated a hybrid liquid cooling plate that contains PCM and coolant inside,

as shown in **Figure 2.5**. One of the advantages of the suggested hybrid liquid cooling plate was that it was 36% lighter than a normal aluminium cooling plate with an equivalent volume. During the first dynamic cycle, the designed cooling plate needed more time to cool down the contacting surface to the setpoint as the PCM inside released more heat. However, from the multi-cycle perspective, a hybrid cooling plate can save 21% of total time consumption.

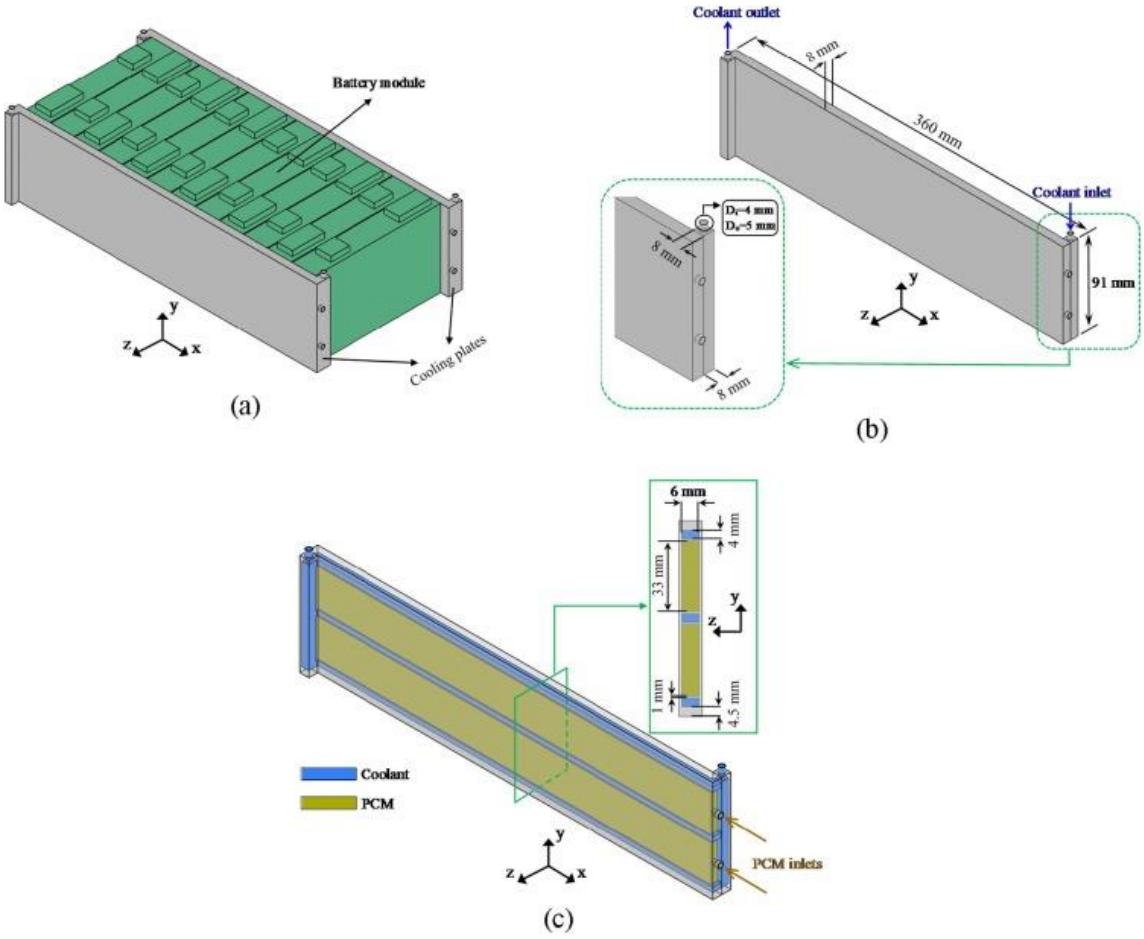

Figure 2.5. Structure of hybrid cooling plate [35]

Similarly, Lv *et al.* [36] also undertook research on a PCM coupled with active air convection BTMS. They designed a novel S-CPCM (serpentine composite phase change material) which can not only save the weight of PCM in order to increase battery energy density by 13.8Wh/kg but can also achieve a lower maximum battery temperature than a normal PCM structure under the same active air convection. Yao *et al.* [37] discussed the performance of a heat pipe and refrigerant-based BTMS. They suggested that the proposed system showed an ability to control the battery within an acceptable temperature range even when the ambient temperature was 38 ºC and the battery heat generation rate was 40 W/cell. Meanwhile, this system can also maintain the temperature difference below 3 ºC, which is mainly caused by the superheat at the outlet of the refrigerant pipe.

2.2.2 BTMS focus on extreme operating conditions

Different from normal operations, extreme fast charging and discharging and thermal runaway will generate huge heat. Jindal *et.al.* [38] investigated the heat generation rate while discharging a 1100mAh 18650 battery and the results are depicted in **Figure 2.6**.

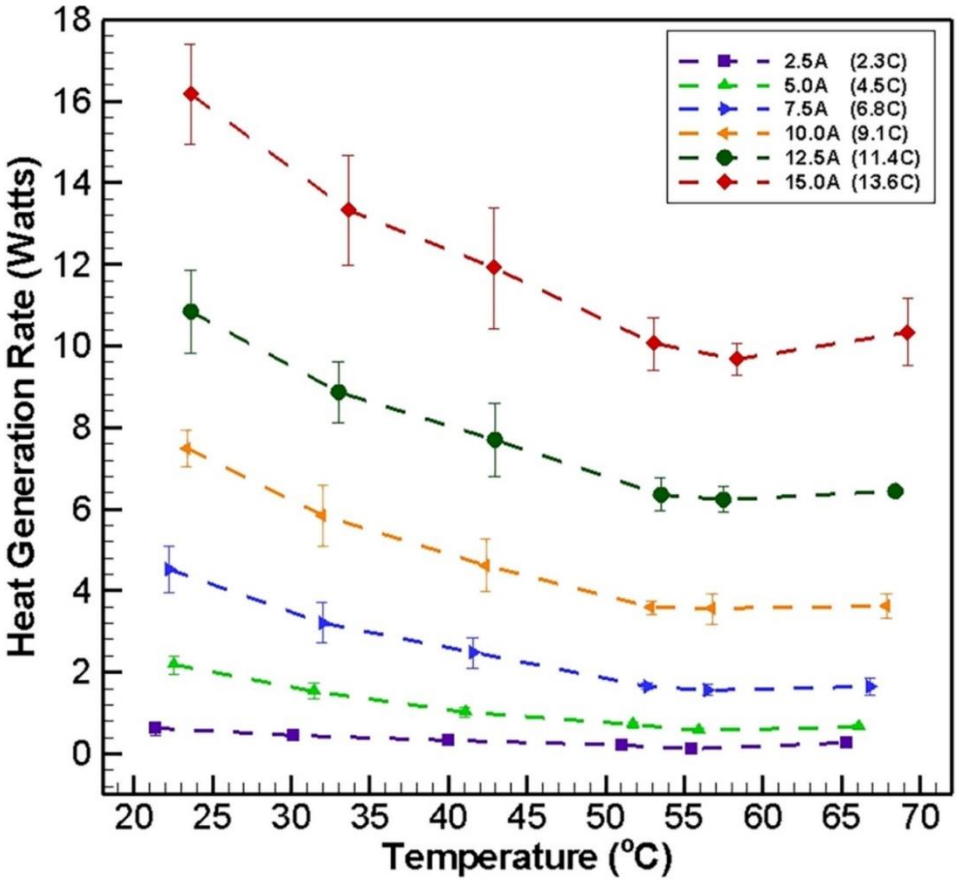

Figure 2.6. Heat generation rate under different discharging rates for 18650 [38]

When the charging rate for a 2300mAh battery increases from 1.6C to 3.2C, the heat generation will also vary from 5W to 16W [39] and the heat generation rate can reach 29.7W and 81W when the charging current rate is 6C and 10C [40]. As for the 1100mAh battery, its heat generation is 10.45W, 25.48W and 54.44W when the charging rate become 3C, 5C and 8C respectively [41], details are shown in **Figure 2.7**.

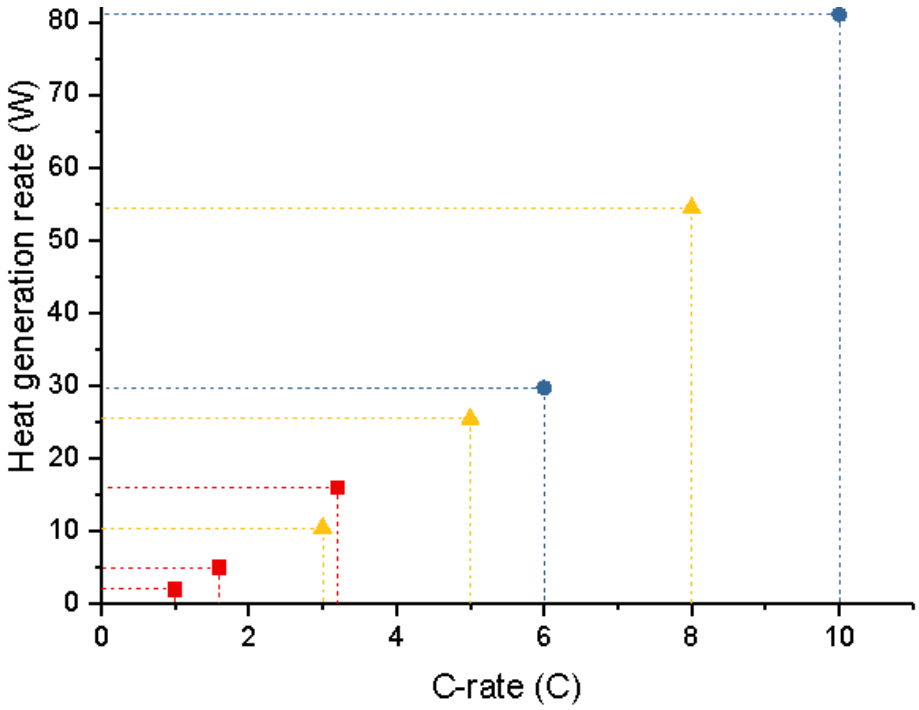

Figure 2.7. Heat generation under different charging rates (square [39], triangle [40], circle [41])

The long charging time, due to the low C rate charging current, has been one of the major issues that restrict the popularization of EVs. Fast charging technology can shorten the charging period dramatically but is accompanied by a higher heat generation rate. Therefore, it is necessary to explore BTMS for fast charging. Thermal runaway is another extreme operating condition for BTMS which is much more severe than extreme fast battery charging and discharging. It may happen due to the short-circuit inside the battery caused by various forms of mechanical, electrical, or thermal abuse. When short-circuit happens, the battery will generate a huge amount of heat and release flammable gases, the heat flow shown in **Figure 2.8**. The battery shows exothermic behaviour, and the peak heat flow reaches 90.34 W/g. If the heat cannot be released quickly, it will cause a fire in the battery pack. Hence, it is also necessary to find a proper BTMS that can inhibit thermal diffusion before the battery heat flow reaches the peak.

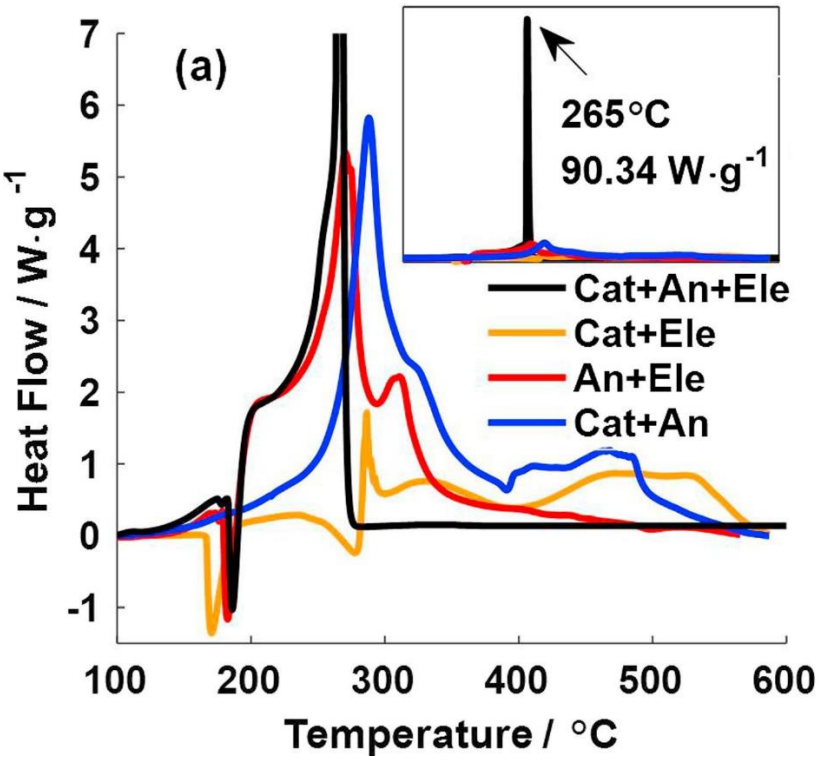

Figure 2.8. Heat rate of the battery while thermal runaway [42]

2.2.2.1 BTMS for extremely fast charging

Bao *et al.* [43] studied the performance of a forced-air cooling-based BTMS for fast charging. It was determined that the pure air cooling method cannot fulfil the task of battery thermal management during fast charging, because under a 5C charging rate, the maximum temperature and maximum temperature difference will increase by 13.1 ºC and 7.9 ºC compared to the results at a 1C charging rate situation, although the air velocity has increased from 0.6m/s to 4m/s. However, the energy required for each degree of decrease will decrease with the increase of the charging C-rate. Ye *et al.* [41] numerically analyzed the heat pipe with copper plate and forced air convection-based battery thermal management for fast charging. The conclusions showed heat pipes with fins can control the average temperature of the battery to around 40 ºC while charging at 8C. However, such achievement of such performance may not be available when considered from a pack-level perspective. Additionally, a liquid and PCM-based BTMS was introduced by Zheng *et al.* [44]. They undertook a stable simulation under an 8C charging rate and the outcomes showed that only when the coolant velocity was above 0.4m/s, the battery pack could be cooled down to below 40 ºC. It should be mentioned that the thermal conductivity of filling PCM is the key factor for extremely fast charging thermal management. Wang and Zhang [45] also investigated refrigerant-based battery thermal management systems. They spotted that setting

temperature as the only threshold to trigger the cooling procedure would be less effective when the C-rate was increasing, while adding SOC (State Of Charge), as another parameter to indicate that the cooling procedure, will achieve better cooling responsiveness. AI-Zareer *et al.* [46] designed a novel atomized refrigerant-based BTMS for extreme charging and discharging scenarios as shown in **Figure 2.9**. The results showed that the proposed design can successfully maintain battery temperature under 40ºC when the charging rate is 8C.

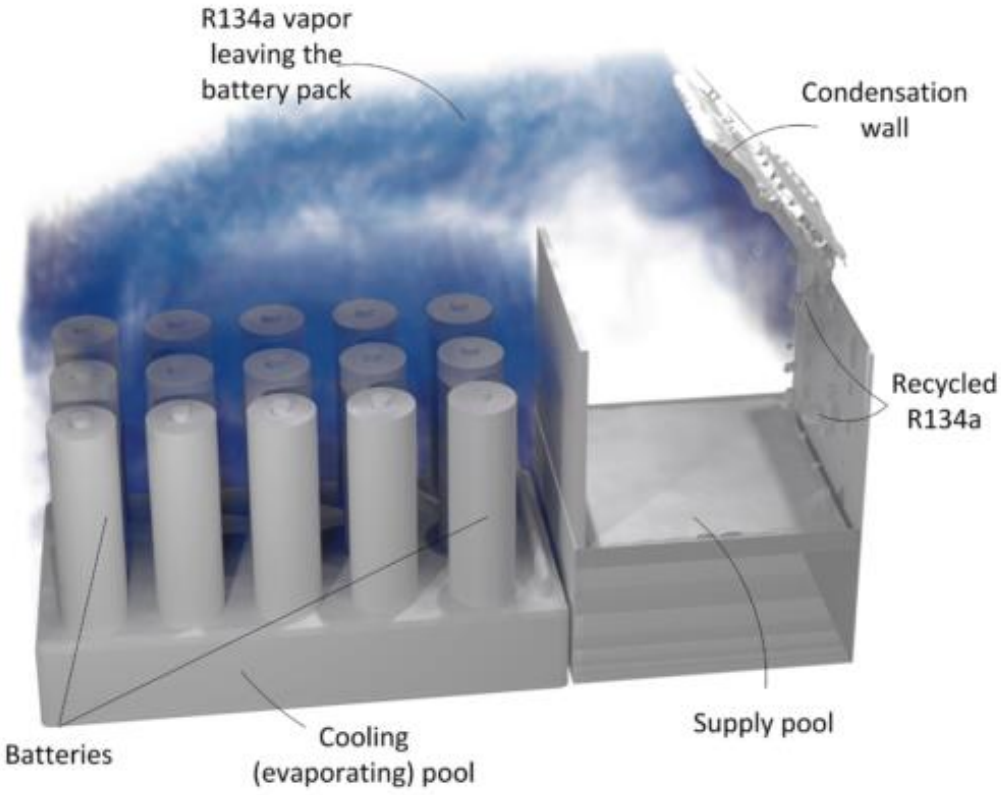

Figure 2.9. Working principle of atomized refrigerant based BTMS [46]

2.2.2.2 BTMS for extreme fast discharging

As well as extreme fast charging, Qian [47] also discussed the performance of a normal parallel cooling plate in the liquid cooling-based BTMS on the fast discharging process. The results indicated that the proposed liquid system can successfully control the battery temperature under 40 ºC when the discharging rate is 5C. Meanwhile, the author also explored the impacts of the shape of the mini-channel, channel width, and flow pattern on cooling performance by simulation. But only a mini-channel with suitable width can provide better performance. Zhang *et al.* [48] also experimented on a 5C discharging rate but used PCM to cool down the battery. They claimed that during the start-up stage, the temperature of the battery needs to be 51 ºC to reach the critical temperature of PCM and the performance

deterioration occurs in the 2nd cycle without a water cooling system. In addition, an air and water cooling integrated battery thermal management system was introduced by Yang *et al.* [49]. Through the simulation results, it can be shown that the increase of water flow rate can apparently reduce maximum battery temperature by 11.4K at a 4C discharging rate and 80% degree of discharge. However, air velocity showed less impact on cooling performance than water flow rate as the maximum temperature can only be reduced by 2.22 ºC when the air flow rate varies from 0m/s to 4m/s.

2.2.2.3 BTMS for thermal runaway

In 2017, Xu *et al.* [50] designed a new mini-channel with multiple aluminium multi-port extrusions and investigated the possibility of using novel mini-channel-based BTMS to prevent thermal abuse while thermal runaways occur. However, the results suggest the proposed system cannot avoid thermal runaways even when the water flow rate reaches 10L/min. The proposed system is only able to prevent propagation to a certain extent if the coolant flow in each cell is controlled independently. Nevertheless, Mohammed et al. [51] designed a new cooling plate with pins installed on it for a coolant-based single battery thermal management system and conducted a thermal runaway simulation. This novel cooling plate could minimize the coolant pressure drop and improve temperature uniformity. It was determined that the proposed system, with a 30L/min coolant flow rate and 53kPa pressure drop, could cool down the temperature of single 20Ah battery to 75 ºC during thermal runaway. Zhang *et al*. [48] proposed an aluminium plate–water and PCM-based battery thermal management system as shown in **Figure 2.10** to prevent thermal runaway. The results suggested that this system could successfully delay the heat transfer among firing batteries and adjacent batteries, and control the temperature of adjacent batteries below 100 ºC. However, although Zheng *et al.* [44] believed that increasing the thermal conductivity could improve thermal management performance under normal situations, higher PCM conductivity would cause faster thermal runaway propagation. Simultaneously increasing water volume was the only way to avoid thermal runaway propagation.

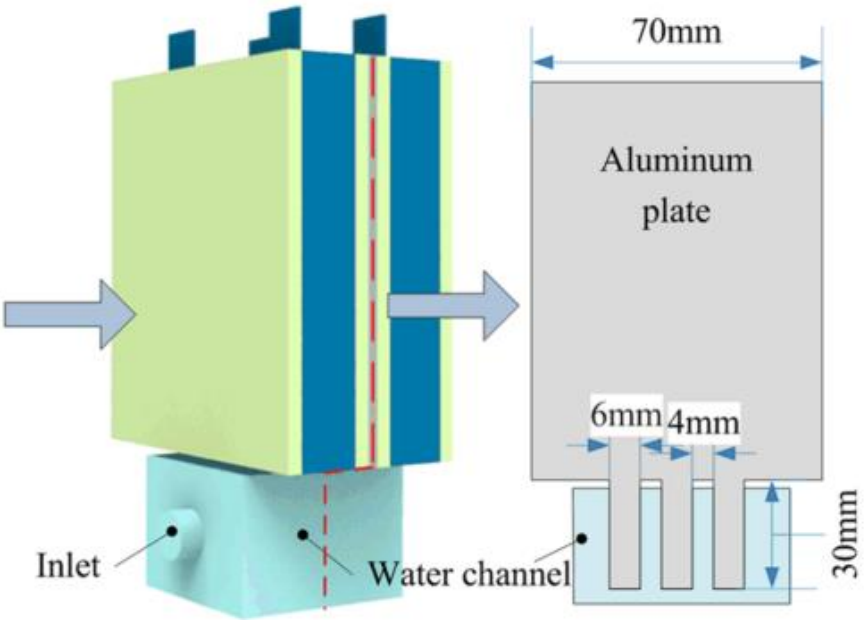

Figure 2.10. Proposed aluminium plate – water and PCM-based BTMS [48]

Similarly, Kshetrimayum *et al.* [52] also studied preventing battery thermal runaway using PCM and micro-channel-based battery thermal management systems. The results demonstrate that pure PCM-based BTMS can only reduce the speed of thermal abuse. Integrating a micro-channel to PCM-only BTMS can sufficiently avoid thermal runaway according to its coolant flow rate. For example, a coolant flow rate lower than 0.01m/s cannot fulfil the task while that over 0.5m/s can even handle thermal runaway from three batteries. It also should be noted that an extra micro-channel cannot enhance the performance compared with a two-layer micro-channel as shown in **Figure 2.11**. Liu *et al*. [53, 54] first studied a water mist system to control thermal propagation. A schematic diagram of the water mist system can be seen in **Figure 2.12**. The results indicated that the water mist method can provide a cooling rate of over 100K/s during thermal runaway and prevent thermal abuse a few seconds after the first battery thermal runaway occurs. However, there are some risks that the water mist system cannot suppress propagation if it is triggered after battery #3 catches fire. Afterwards, they tried to introduce a water mist system to a series of parallel-connected batteries. It can be found that the water mist operating situation became more challenging as the critical temperature reduced to 77 ^{o}C in parallel connected batteries, which means phase change cannot occur during the cooling procedure.

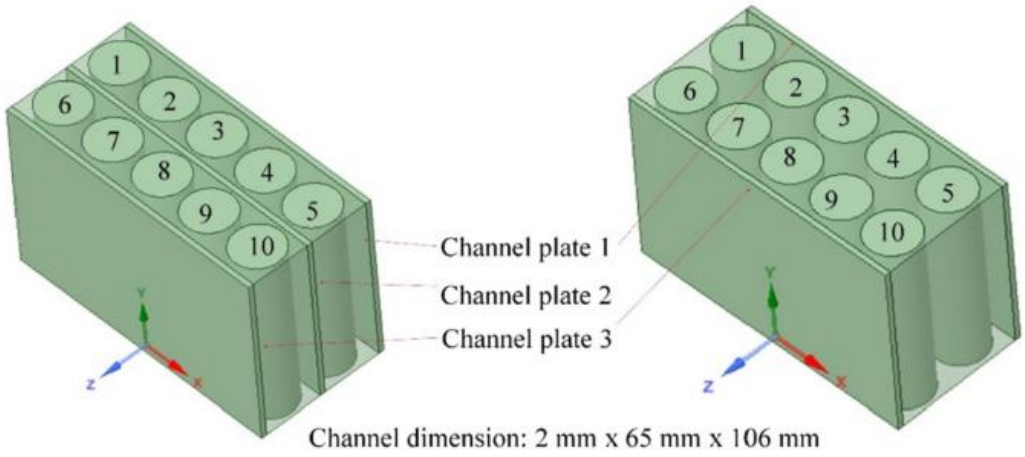

Figure 2.11. Structure of three-layer and two-layer PCM and micro-channel-based BTMS [52]

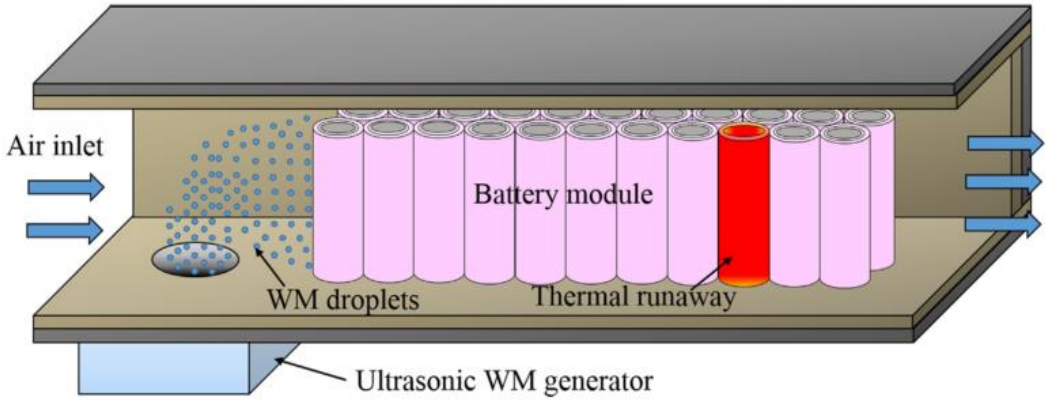

Figure 2.12. Schematic diagram of water mist system [53]

Similarly, Huang *et al.* [55] also investigated the performance of a water spray system in suppressing battery runaway by experiment. They suggested that the spray trigger temperature should be very close to the temperature at which battery voltage starts dropping in order to shorten the spraying time which can significantly reduce energy consumption. Shen and Gao [31] numerically discussed the cooling performance of the designed refrigerant and cooling plate based on the thermal runaway situation. The results indicate cold plate refrigerant-based BTMS cannot suppress a single battery's thermal runaway, but can sufficiently avoid the thermal runaway spreading to adjacent batteries and control the batteries along the X-axis under 123.85 ºC and those along the Y-axis under 83.15 ºC. In addition, Liu *et al.* [56] proposed a refrigerant spray system for both overall and local overheating situations. They believed that the proposed system can effectively prevent thermal proportion while enhancing battery temperature uniformity changes. The

temperature reduction of measurement points can be up to 70 ºC and can also reduce oxygen concentration down to 0.5% and maintain it under 5% for 488s to inhibit thermal release.

2.2.3 Summary

In this section, the latest advanced battery thermal management systems were introduced. Generally, current battery thermal management systems can successfully control the battery temperature within a suitable working temperature under normal operating conditions. How to achieve higher performance and the temperature uniformity of every single battery, without losing thermal capacity and efficiency, are important topics. Additionally, performance under extreme conditions, such as extreme charging and discharging or thermal runaway, attracts increasing attention. It can be seen that most of the recent studies related to the coolant and air-based BTMS are more focused on the flow pattern and structural design. However, the system rarely works well when cooling or heating demands are too high. Meanwhile, scholars also investigated the impact of different hybrid cooling combinations on cooling performance and structure optimization. Although PCM-based hybrid BTMS can work under extreme thermal management conditions to some certain extent, such system primarily depends on the cooling medium of the PCM. Although using air and coolant can achieve better performance than pure air and coolant cooling method, but the continuous working ability of PCM has yet to be verified. Meanwhile, the contradiction between the performance of the thermal management and thermal runaway propagation may exist due to the heat conductivity. Few scholars tried to use refrigerant from HPAC system as the cooling medium, although it shows good cooling performance and temperature uniformity, but a further comparison to the performacne of pure refrigerant-based BTMS is needed. In addition, it has been demonstrated, in a small number of papers, that a refrigerant-based BTMS can fulfil not only normal tasks, but also extreme thermal management conditions, including extreme fast charging/discharging and even thermal runaway. The comparison of different thermal management approaches under extreme and abnormal situations is described in Table 2.1. Table 2.2 summarised the research focused on refrigerant-based BTMS. Hence, as only a small number of papers focus on refrigerant-based BTMS and its application in extreme conditions, further investigations should be done in order to propose a full-range battery thermal management system. Moreover, as concluded, refrigerant based BTMS and Hybrid methods show great potential for all operating ranges. However, refrigerant is the most important part in those BTMS which is supplied by HPAC

system. Integrating and adjusting HPAC for battery cooling and heating is also one of the vital topics in the future.

Table 2.1 Different battery thermal management methods in the extreme operating situation and abnormal situations

Battery thermal management	Type	Advantages		Disadvantages		Performance
Operating situation		Normal situation	Extreme situation	Normal situation	Extreme situation	Thermal runaway
Air		Simple structure Lightweight Energy saving	-	Low heat transfer coefficient Hard to achieve temperature uniformity	Failed	-
Coolant		Higher heating/cooling capacity Good uniformity	Easy to control Operating condition is limiting	Additional heat exchanger, pump and coolant circulation Higher weight	High Coolant mass flow rate Large coolant storage Larger contacting surface	Water in the cooling plate needs 10L/min-30Lmin to prevent thermal runaway Water or non-flammable spraying is sufficient but needs very precisive trigger point control
Refrigerant	Cold Plate or Chiller	Rapid heating or cooling High cooling/heating capacity Omitting a heat exchanger	Can cover most extreme situations even under 8C discharging rate with acceptable uniformity Low mass flow rate Maintains high battery density	Complex controller to achieve uniformity Complex principle, Leakage, Additional EEV (Electric Expansion Valve) and other components	High pressure Greater power consumption Vibration	The refrigerant in the cooling plate can avoid heat spread and refrigerant spraying can quickly control abnormal battery within acceptable temperature
	Heat pipe+air/coolant	High thermal conductivity Effective temperature uniformity Lower energy consumption	Low weight Low cost	Weight increases Complicated structure Reduce battery density	Performance highly dependent on its cooling medium Need more fins and cooper plates	Depends on the cooling medium mass flow rate
Hybrid method	PCM+air/coolant		Can maintain a good uniformity within a certain duration		Cannot continuously operating Material selection is important	Higher thermal conductivity will lead to poor performance in preventing thermal runaway which is contrary to normal situation

Table 2.2 Comparison of refrigerant based BMTS

Author	year	battery	Refrigerant	Charing/discharging rate/heat generation	Research focus	method
Zhu[27]	2020	Dummy	R1233zd	3.2kW	Performance of R1233zd	Experiment
Wang and Wu[28]	2020	NCM811 lithium-ion	HFE-700	1C-5C discharging rate	Performance of HFE-700	Verified Simulation
Park *et al*.[29]	2019	40Ah LiFePO4	R134a	1C-2C discharging rate	Performance of R134a based BTMS and comparison with PCM based BTMS	Verified Simulation
Hong *et al*.[30]	2020	86.5Ah	R1234yf	0.5C-2.0C charging rate	Performance of an R1234yf based BTMS with mini-channel and cold plate	Experiment
Shen *et al*.[31]	2020	94Ah lithium-ion battery	R134a	1C-2C discharging rate	A new cold plate with fins and different connection ways	Verified Simulation
Wang *et al*.[32]	2020	2.2Ah 18 650 battery	R134a	2C discharging rate	Structural design of a novel cold plate	Simulation
Wang and Zhang[45]	2021	Samsung SDI 94 Ah battery	N/A	1C-2.5C charging rate	Performance of SOC threshold and temperature threshold on refrigerant based BTMS	Verified Simulation
Al-Zareer *et al*. [46]	2020	Sony 18650 cylindrical battery	R134a	6C-8C charging and discharging rate	Performance of a new directly contacted R134a based BTMS	Simulation
Liu *et al*.[56]	2021	dummy	R410a	Thermal runaway	Impact of an R410a based spraying BTMS on preventing thermal runaway	Experiment

2.3 Heat Pump in EV and Cabin Comfort

EVs always face substantial cooling and heating loads [57, 58] as shown in **Figure 2.13** and **Figure 2.14**. Different from ICEs, the heat source for EVs is not sufficient and due to the energy sensitivity of EVs, the present commercial PTC solution and AC system offer significant modification and optimisation potential. In order to extend the EV driving range and improve EV cabin comfort, many scholars have investigated the novel heat pump technologies and applied them to cabin thermal comfort and some problems can be met in EV cabins.

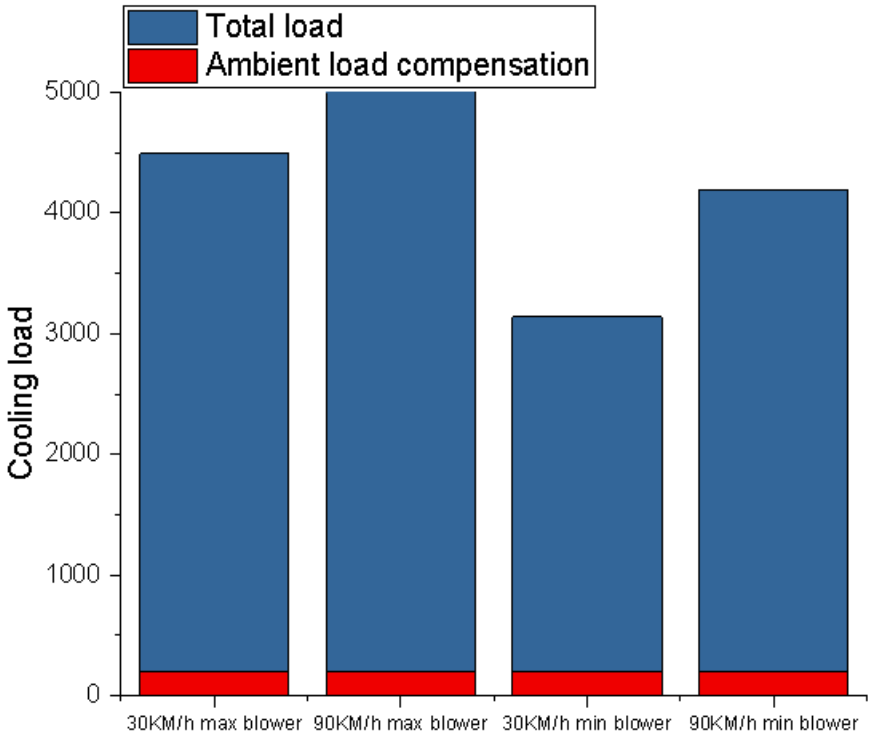

Figure 2.13. Average cooling load under different speeds (Ambient temperature: 35°C, cabin set temperature: 27°C) [57]

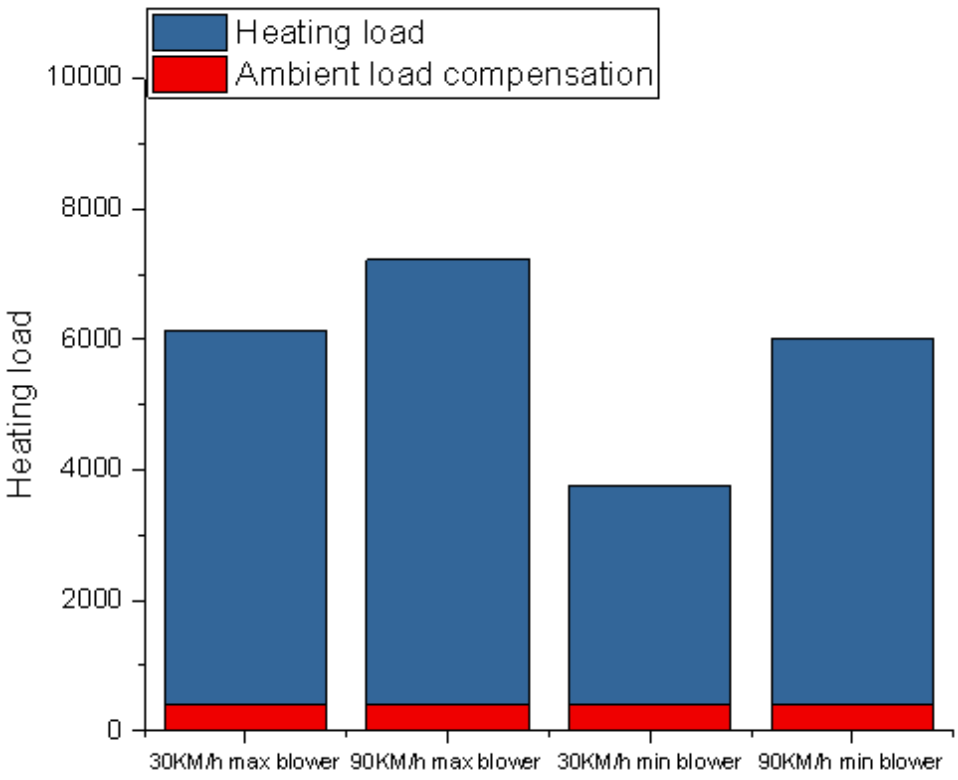

Figure 2.14. Average heating load under different speeds (Ambient temperature: -20°C, cabin set temperature: 20°C) [57]

The basic heat pump cycle is made up of the same components as the conventional refrigeration cycle. It includes four processes namely an evaporation process an expansion process a condensation process and a compression process. The four key components are shown in **Figure 2.15**.

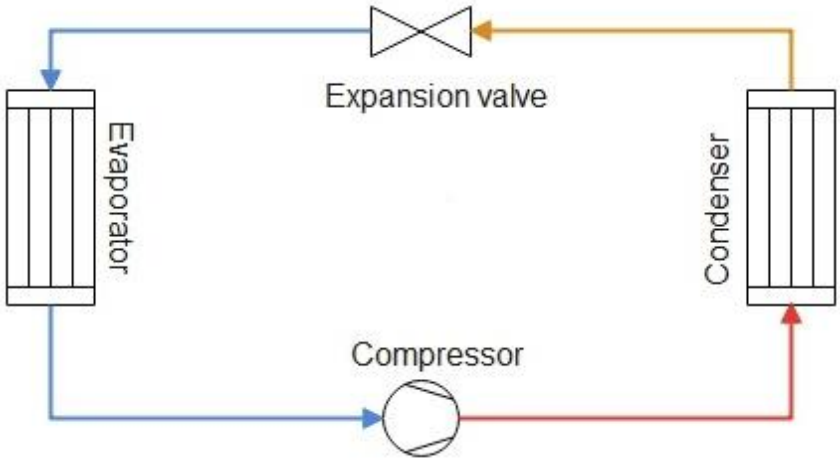

Figure 2.15. Principle of the heat pump cycle

Starting from the outlet of the evaporator, the low-pressure and low-temperature vapor refrigerant is intake by the compressor. The refrigerant is compressed by the compressor and becomes high temperature and high pressure at the outlet of the compressor. After the compression process, the refrigerant flows through the condenser to release the heat to the end-user side. The vapor refrigerant becomes middle-temperature liquid refrigerant when exits from the condenser and is throttled by the expansion valve. At the outlet of the expansion valve, the low-temperature, low-pressure liquid-vapor mixed refrigerant flow through the evaporator to extract heat from low-temperature source and finish one cycle. Several works have demonstrated that applying heat pump to electric vehicles can improve the driving range deduction during cabin heating at mild low temperature compared to using Positive Temperature Coefficient (PTC) heater [59, 60] because of the high operating COP. However, the heat pump itself cannot provide sufficient stable heat without the supplement from PTC heater due to the on-board space limitation. More and stricter refrigerant GWP regulations further reduced the COP of heat pumps [61]. Therefore, integrated vehicle thermal management system is necessary.

2.3.1 EV heat pump performance enhancement

2.3.1.1 Selection & Optimisation of different working fluids (refrigerants)

Although the most popular refrigerant in the world at the current time is R134a, due to serious environmental problems caused by refrigerants and their high GWP (Global Warming Potential) characteristics, increasingly restricting limitations are being implemented. For example, the EU intends to prohibit refrigerants with a GWP greater than 150 and, similarly, the US will ban R134a in 2026 [62]. Hence, an increasing number of scholars have attempted to identify an alternative to R134a.

Wu *et al*. [63] made a comprehensive assessment of seven different refrigerants for applications in EVs. With TEWI (Total Equivalent Warming Impact) analysis, R744 (CO_2) has the highest heating capacity and the smallest compressor dimension but the lowest COP (Coefficient of Performance), due to its working pressure. Yu et al. [64] also established a heating load model without considering frost formation, which was verified by a test based on the WLTP (Worldwide Light Vehicle Test) driving cycle to evaluate the energy consumption of the heat pump system for BEV. Nine different types of refrigerants were compared to analyse the performance of the heat pump system. According to the results, R152a achieves an increase in the driving range peak, the greatest energy reduction, and the greatest expansion of the driving range, approximately 30% at -20 ºC can be achieved. R1234yf has a very low GWP but its heating capacity may not be sufficient in extreme winter weather. Meanwhile, R32 has a promising future as it has a lower GWP than R1234yf and a higher COP than R744, whilst the TEWI emission is 11% lower than R134a. Song *et al*. [65] designed a CO_2 heat pump system for an electric bus which can gain 15.3kW heating capacity with a COP of 1.78 at -20 ºC ambient temperature when the cabin set temperature is 20ºC. A novel refrigerant made up of CO_2 and R41 was investigated experimentally by Yu *et al*. [66] The results indicate that in heating mode, pure CO_2 has a higher heating capacity than a CO_2/R41 mixture but with lower COP than the mixture. The more R41, the less the charging amount which is sensitive to the heating capacity. R41 can reduce refrigerant density, which accounted for the reduction of the mass flow rate. In the cooling mode, as the ratio of R41 increases, the compressor works less. An R744 heat pump system was also investigated by Dong *et al*. [67]. Their results show that the proposed system can provide a greater heating capacity than the R134a heat pump under the same conditions, specifically a result which is 1.8 times higher than R134a at -10 ºC and can provide 7500W at ambient -

20 ºC. Therefore, it can fulfil the heating task without PTC. Liu *et al*. [68] discussed a propane (R290) heat pump system, considering the variation of ambient temperature, indoor air velocity, and outdoor air velocity. According to the results, R290 has a more promising future than CO_2. When the ambient temperature is over -10ºC it can achieve a 42.8% greater heating capacity and 15.3% higher COP than the CO_2 heat pump system [69]. However, when the ambient temperature is lower than -20 ºC, the proposed system can only provide 86% heat compared to a CO_2 heat pump. Direk and Yuksel [70] concluded that R1234yf has a lower heating capacity, compared to R134a at all compressor speeds when the mass equivalence method is applied in the experiment. However, Feng and Hrnjak *et al.* [71] achieved different outcomes from their own test rig which showed that R1234yf can provide 28% more heating capacity than R134a at -20 ºC but with lower HPF (heating capacity divided by compressor work). This is because R1234yf can achieve a higher compressor speed before reaching atmospheric pressure.

2.3.1.2 Vapor injection technology

As the operating range of a heat pump for EV varies from -20 ºC now to -40 ºC in the future, basic heat pump systems cannot cover the whole range and, as a result, many scholars have tried to study vapour injection heat pumps technology, particularly increasing their heating capacity and COP. Choi *et al*. [72] numerically and experimentally analysed a vapour injection (VI) EV heat pump system, particularly for cold start-up conditions. Results show that the COP of a VI heat pump system when the ambient temperature is -15 ºC is always higher than a base heat pump system under all intermediate pressure ratios and the rate of increase varies from 5% to 10% when the intermediate pressure ratio increases from 0.1 to 0.2. Zhai and Chen [73] reported that an R410a vapour injection EV heat pump can provide more than 30% heating capacity and 20% greater COP compared with a regular heat pump at -25 ºC and it can save approximately 31% power compared with PTC water heater system. It should be mentioned that the lower the ambient temperature is, the higher COP increase can be observed. An internal heat exchanger-type vapour injection heat pump was evaluated by Kwon *et al*. [74] as shown in **Figure 2.16**.

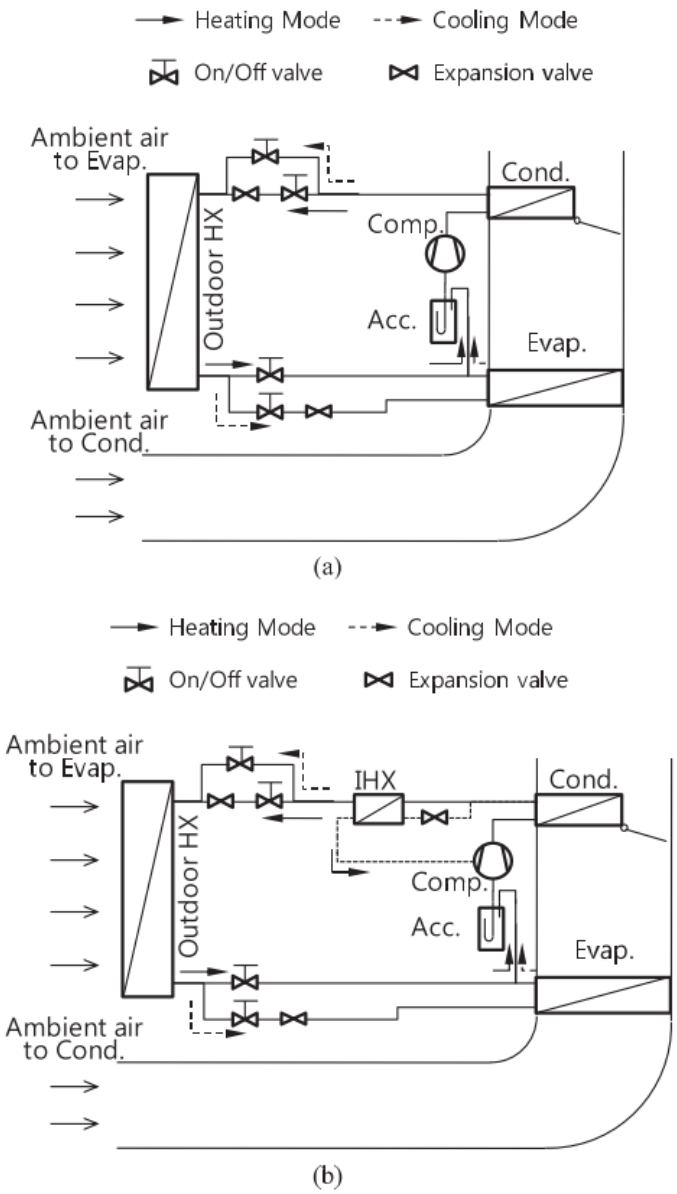

Figure 2.16. (a) baseline heat pump (b) IHX VI heat pump [74]

With an increase in inlet indoor air temperature, the vapour injection heat pump can increase its refrigerant mass flow whereas the baseline heat pump refrigerant mass flow decreases. As a result, with the increase in inlet indoor air temperature, the baseline heat pump's heating capacity decreases while the vapour injection system's capacity increases. Li *et al*. [75] evaluated upstream and downstream economized vapour injection heat pumps including the compressor speed, injection pressure and other parameters. The schemes of upstream and downstream vapour injection heat pumps are shown in **Figure 2.17**. It can be concluded that a DI (downstream injection) system has a better heating capacity than UI (upstream injection) system at all compressor speeds and injection pressures. Similarly, the DI system always has a better COP at lower compressor speeds and only reaches the same level as the UI system at 8500 RPM. Jung *et al.* [76, 77] experimentally investigated the impacts of injection angle

and IHX length on a vapour injection heat pump. With a fixed injection angle of 44℗, there's an optimal IHX length which is 300mm in an ambient temperature greater than 0 ºC. With fixed IHX length, the refrigerant mass flow rate will increase with the increase of angle injection. The highest value of COP appears at an angle of 40℗ due to the increased inter-cooling effect and optimized total mass flow rate.

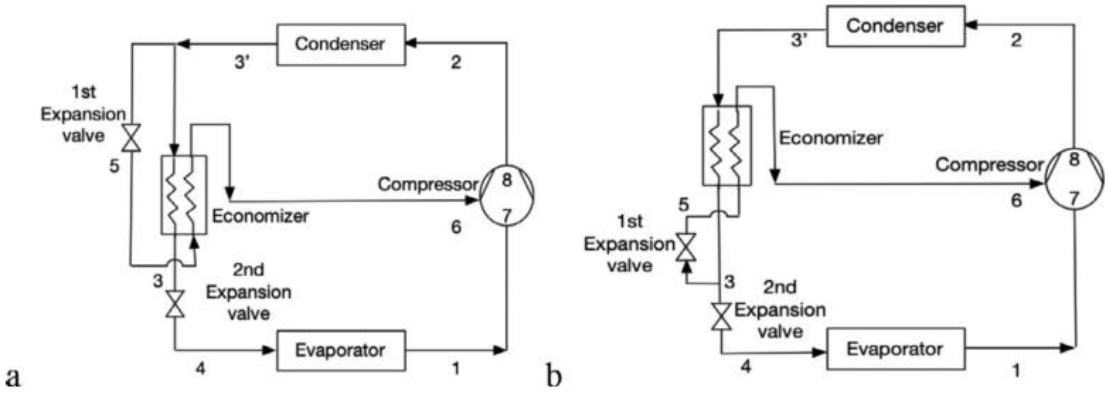

Figure 2.17. (a) upstream (b) downstream vapour injection heat pump [75]

An experimental device was set up by Fei *et al.* [78] to explore the performance of a RIHP (Refrigerant Injection Heat Pump). The system not only includes vapour injection but also contains a two-phase refrigerant injection. It can be concluded that vapour injection has a better heating performance than two-phase refrigerant injection and both can achieve a greater heating capacity than a non-injection system. However, in the case of RIHP, the increasing speed of heating capacity is lower than the growth of electricity consumption when the compressor speed is increasing. Based on the traditional vapor injection cycle, Mei *et al*. [79] evaluated a kangaroo heat pump that contains a sub-cycle and a vapor injection cycle. It shows advantages in extremely cold weather. The schematic of the kangaroo cycle is shown in **Figure 2.18**. They demonstrated that with the help of the kangaroo cycle, the heating capacity could increase by 25.7% compared to the traditional VI cycle under the same conditions. However, the side effect is similar to the traditional VI system. Additional energy consumption is needed to produce more heating capacity which leads to a decrease in COP if PTC is not highly required.

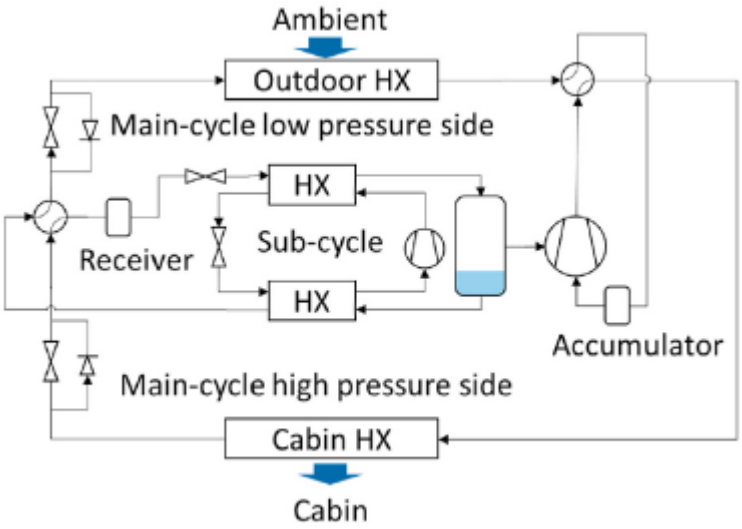

Figure 2.18. Schematic of kangaroo cycle [79]

In addition to these studies, Wang *et al.* [80] tried to use a machine learning method to predict the performance of EVI systems and find optimal injection pressure. The simulation results are highly consistent with the experimental results, within an error margin of 8.3%, and using the proposed machine learning method an optimal injection pressure can be achieved.

2.3.1.3 Novel system design

A reversible heat pump system was tested by Cuevas et al. in terms of isentropic, volumetric effectiveness, and COP [81]. The working principle of the proposed reversible heat pump is shown in **Figure 2.19**. It was concluded that both isentropic effectiveness and volumetric effectiveness will decline with compressor pressure and the proposed test device can provide a COP of 2.1 while considering the frosting phenomenon on OHX. Furthermore, this study also shows that the conventional external louvred fin and flat tube heat exchanger for ICE is not suitable to be an evaporator as the pressure drop is too high, reaching 1 bar.

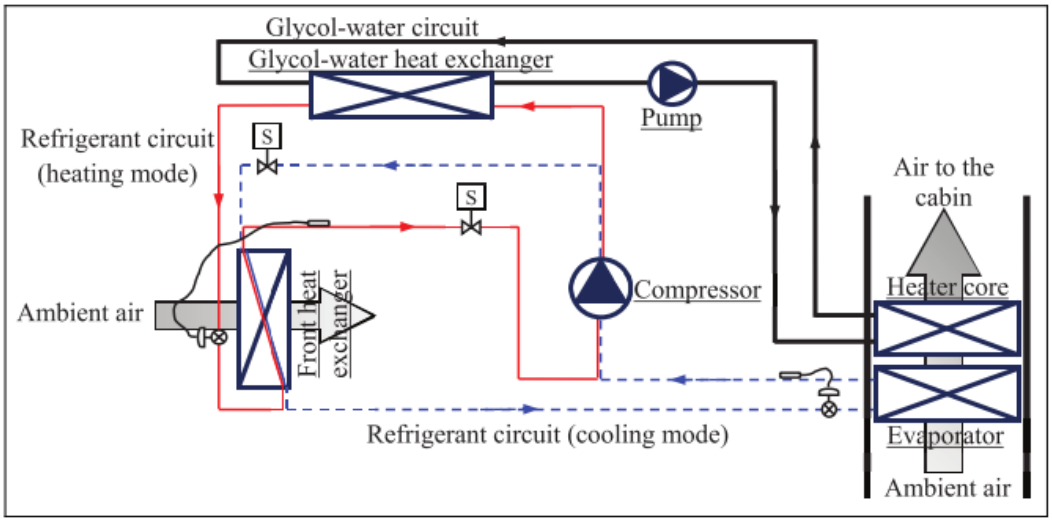

Figure 2.19. Reversible heat pump working principle [81]

Wang *et al.* [69, 82] proposed a series gas cooler CO_2 EV heat pump system with a newly designed compressor specifically for EV CO_2 heat pump systems. The results show that at -20 °C, the proposed system can achieve a heating capacity of 5.6 kW and a COP of 1.8. This is higher than the R134a gas injection system with the same operating conditions. Next, this group of researchers also provided a numerical model for the proposed SGC heat pump which indicates that such a system increases the heating capacity and COP by 33.7% and 35%, respectively. Similarly, Li *et al.* [83] did an experimental study on the performance of a gas-mixing heat pump and a comparison was made with an ordinary heat pump. The study indicates that in an ordinary heat pump, the discharge temperature decreases with the increase of ambient temperature and is not feasible under 10 °C because the discharge temperatures are beyond the compressor's limitations. However, the trend of discharge temperature variation with an increase in ambient temperature is inversed in gas-mixing heat pumps and can still work at -20 °C degrees with the EER (Energy Efficiency Rating) equals to approximately 1.5. Chen *et al.* [84] performed an experiment on a CO_2 heat pump with an intermediate cooling compressor (ICC) as shown in **Figure 2.20**. Compared with the traditional CO_2 heat pump system, the ICC can largely decrease the discharge temperature and improve both the heating capacity, by up to 132%, and the COP by 62% in an ambient temperature of approximately -20 °C. Wang *et al*. [85] investigated the performance during the frosting and defrosting of a CO_2 heat pump with a two-stage gas cooler under constant heating capacity operation. Different from the traditional operation method (constant compressor speed), the proposed system can provide stable heat without the help of the PTC. However, the frosting speed of the proposed system is higher than a traditional system which leads to a COP reduction after running a certain period of time. As the dynamic

characteristics are fundamentally different from the conventional system, the authors developed an effective defrosting criterion by adding suction temperature and time parameters on top of traditional judgment criteria in order to avoid false defrost and lowest the impact on cabin comfort. Although the average COP of the proposed system in mild weather (around 0°C) is higher than the traditional operating method, the decreasing trend in COP with the decrease in ambient temperature may make the COP of the proposed system lower than the traditional system. The results of this study can still provide good implications for applying CO_2 heat pumps in EVs, for example, using the constant compressor speed method for extreme cold weather while using the constant heating capacity method for mildly cold weather.

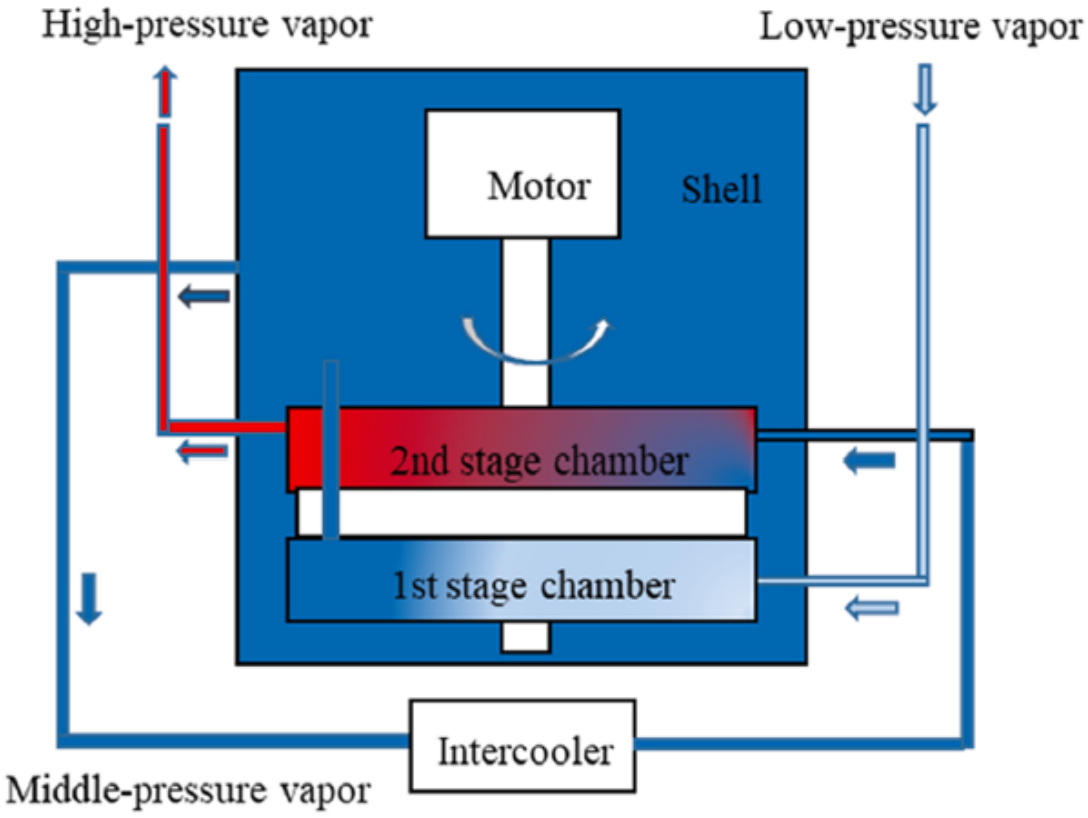

Figure 2.20. Intermediate cooling compressor [84]

Furthermore, Li *et al.* [86, 87] undertook a series of theoretical investigations on the impact of refrigerant charging amount on a heating performance of a secondary loop ACHP system. The conclusion is that the refrigerant charging amount has more influence on suction temperature compared to discharge temperature and sub-cooling is increased with the increase of refrigerant mass flow rate prior to the critical point while superheat shows an opposite trend. Simultaneously, the same group of researchers explored the relationship

between oil charge amount and heat pump system performance [88]. The results show that there's an optimal ORC for the system, under different air velocities, to achieve the highest COP and this can also improve lubrication and efficiency of the compressor. However, refrigerant gas from the evaporator would contain non-negligible liquid droplets if the oil charge mass exceeds a certain degree. Tang *et al.* [89] discussed an exergy analysis of their proposed heat pump-based EV heating system. When compressor speed drops from 5500 rpm to 3000rpm, the exergy destruction decreases by 18.2% while the efficiency increases by 10.9%. When the ambient temperature is higher, the exergy destruction of the system is mainly caused by the compressor, accounting for 55%. Additionally, a three heat exchangers-based mobile heat pump was investigated by Feng and Hrnjak [71] and they demonstrated that refrigerant maldistribution caused by ice on OHX leads to the waste of heat transfer surface in a high superheat area and at -20 °C, the compressor speed needs to be slowed down to avoid vacuum suction. Aiming to solve the frost on OHX when the ambient temperature is lower, Li *et al.* [90] introduced a secondary loop heat pump system as shown in **Figure 2.21** to prevent the frosting phenomenon on OHX. The conclusions indicate that the proposed system doesn't attenuate up until 5 hours from the start while the OHX can be totally blocked after 50 minutes in a traditional direct heat pump at -20 °C.

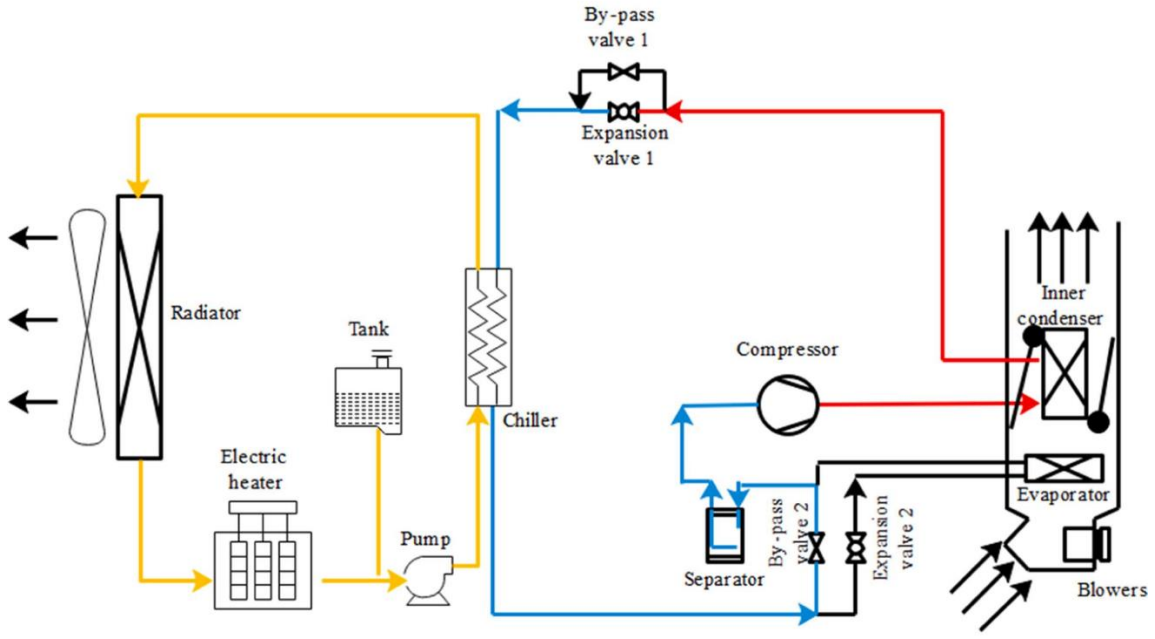

(b) Secondary loop system

Figure 2.21. Schematic of secondary loop heat pump system [90]

In 2021, Li *et al.* [91] designed a new air source heat pump system for EV as shown in **Figure 2.22**. It has two-bypass valves that can significantly reduce the components and cost.

The introduced system can provide a 13% higher maximum peak heating capacity when air volume is 300 m^3/h, compared to a normal heat pump system with 400m^3/h at -10 ºC.

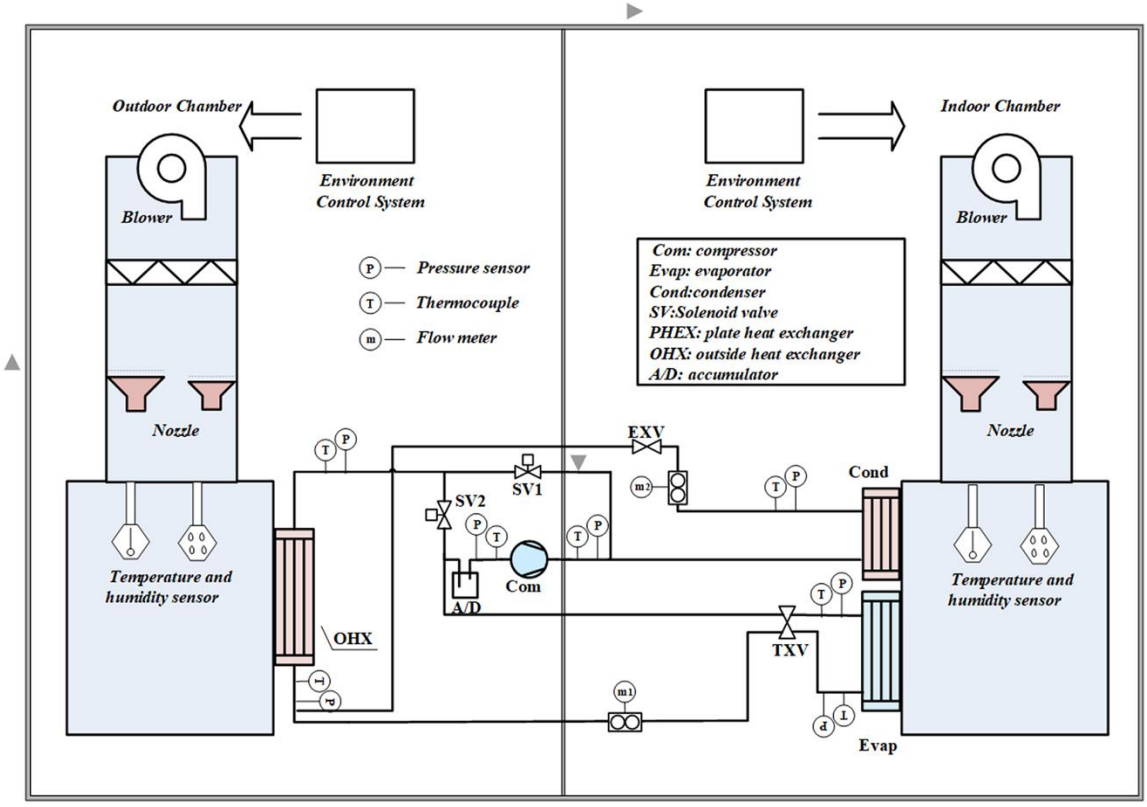

Figure 2.22. Test bench of newly designed air source heat pump [91]

In 2022, Yu *et al*. [92] proposed a flexible heat pump designed based on the modified Evans-Perkins cycle. The principle is demonstrated in **Figure 2.23**. The system integrated a heat storage cycle in order to recover the sub-cooling heat carried by hot liquid refrigerant at the outlet of the condenser. The waste heat can be charged into either PCM heat storage or liquid heat storage tank and can be discharged for higher heat output or for stable heat output while defrosting. The theoretical improvement in COP is 25% when using R290 as the refrigerant. However, only a 3.7% improvement was demonstrated as a water tank was used for heat storage. The newly designed system has the potential future for application in EVs as it can provide stable and sufficient heat to the cabin while defrosting without using PTC if the defrost strategy is proper. Therefore, further investigation could focus on finding a proper PCM for this flexible heat pump, completing the experiment under different ambient temperatures, and setting optimal charging and discharging strategies for defrosting.

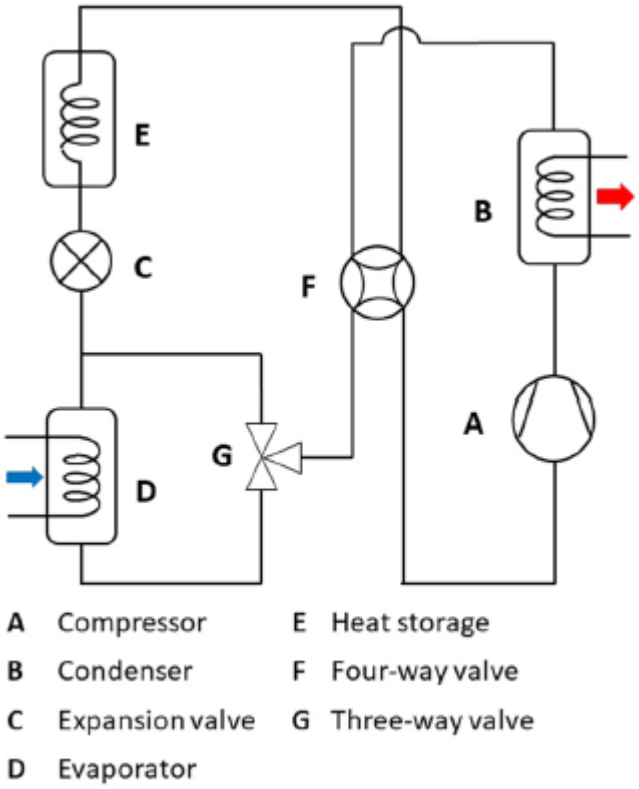

Figure 2.23. Schematic diagram of the flexible heat pump based on modified Evans-Perkins cycle [92]

2.3.2 HPAC with cabin

The main function of a heat pump is to solve the cabin comfort problem while the EV is on the road. In recent years, many researchers have paid close attention to the heating and cooling performance of the heat pump in combination with cabin parameters and characteristics. To achieve a higher COP under stricter emission limitations, some researchers have tried to switch refrigerants while others have tried to use recirculation air.

2.3.2.1 Indoor glass dehumidification

Wang *et al.* [69] analysed the impact of recirculation air from the cabin on heating demands. The results show that air recirculation can substantially reduce the heating demands from 5.6kW to 4.3kW with the return air ratio varying from 0-40% and with little influence on COP. However, the recirculation air rate is decided by several factors related to the cabin. Pan *et al.* [93] undertook numerical research on the impact of the air recirculation rate determined by cabin CO_2 concentration limits and the anti-fog requirement on energy consumption. They pointed out that the energy-saving effect of the proposed strategy with recirculation air, as shown in **Figure 2.24**, can save more energy when using a heat pump

compared to PTC under OSA (Outside Air) mode. Between 33%-57% of energy in heating mode and 48%-60% of energy in cooling mode can be saved. Furthermore, in heating mode, with the windshield thermal conductivity higher than 0.3, the energy-saving effect caused by a CO_2 limit will not be obvious.

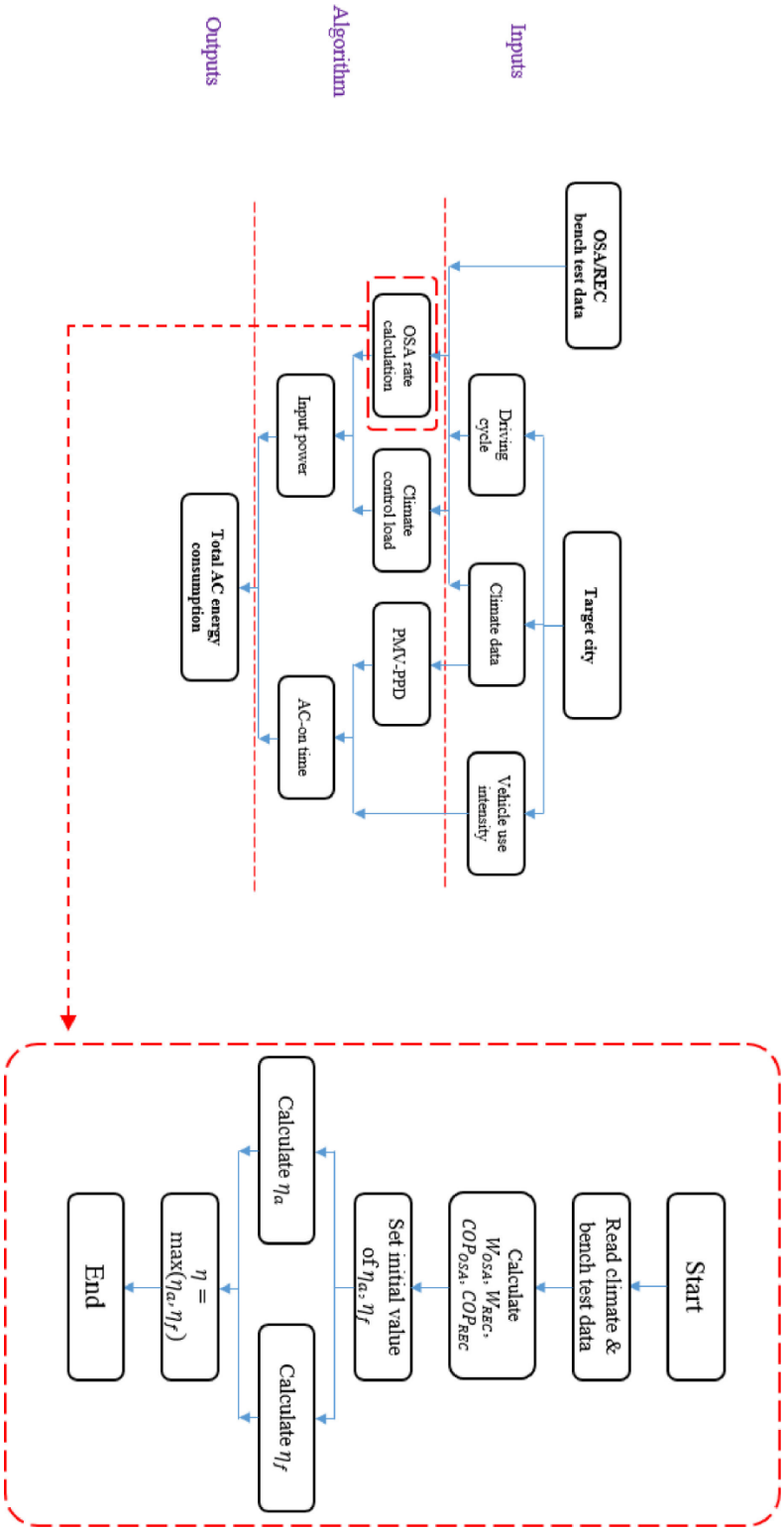

Figure 2.24. Recirculation air strategy and energy-consuming calculation flow chart [93]

To reduce the effect of the fogging phenomenon on the windshield, Zhang *et al.* [94] applied a continuous air curtain to the front windshield to achieve a maximum air recirculation rate. Compared to a no-air recirculation HP system, the improved system, shown in **Figure 2.25**, can reduce heating demands by up to 62% when ambient temperature varies from -5 ºC to -20 ºC, although the air curtain will increase heat dissipation by around 12%. However, system COP will decrease with an increase in recirculation air rate, but the equivalent COP is 12.1% higher than the non-return system.

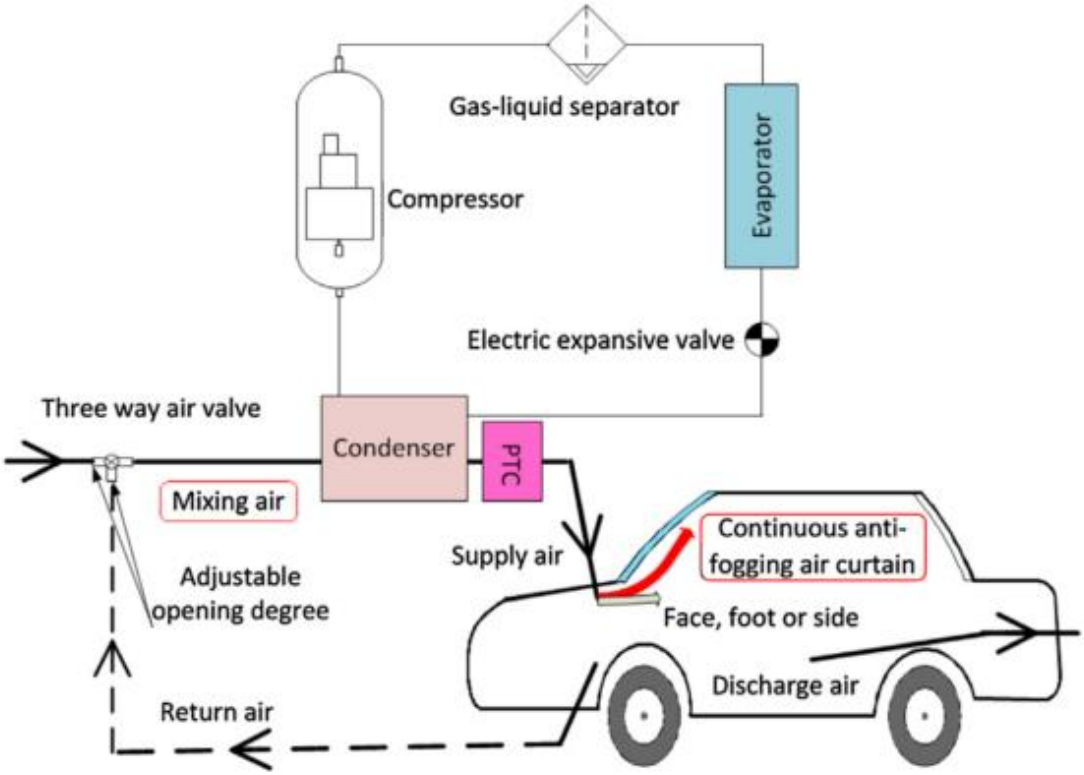

Figure 2.25. Improved AC system [94]

Apart from using post-processing methods to handle fogging problems in a cabin based on a heat pump system, some scholars also undertook research on pre-processing methods. Chang et al. [95] tried to assemble a dehumidification module to pre-process outdoor air as shown in **Figure 2.26**. Inlet indoor air will be dehumidified by HX2 and finally become hot and dry air via HX1. The outcomes show that the proposed system can achieve the dehumidifying ability of around 1.47L/(kW-h).

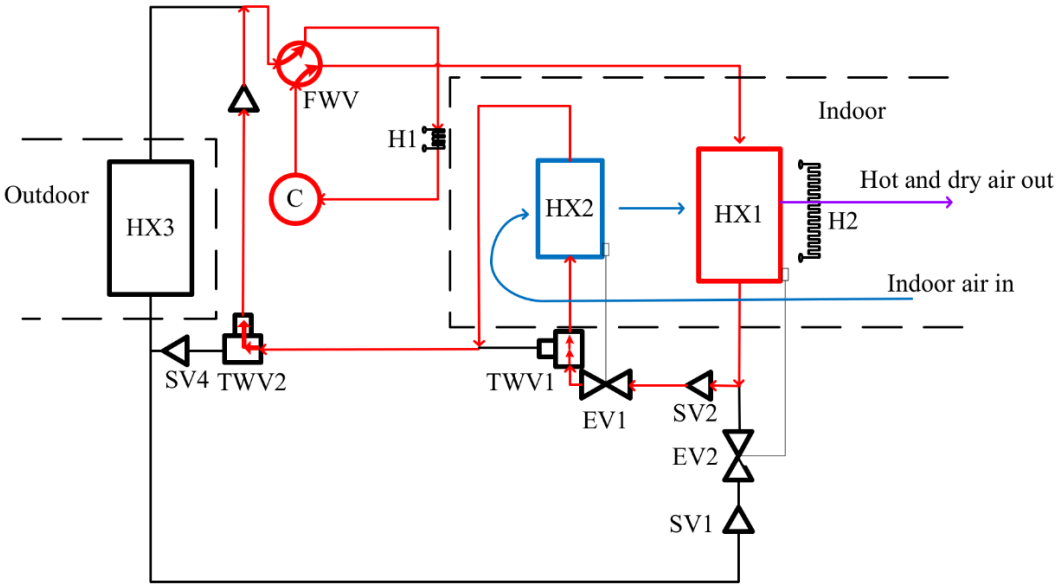

Figure 2.26. Dehumidification heat pump schematic diagram [95]

Similarly, Zhang *et al.* [96] also focused on a pre-processing method to integrate a desiccant dehumidification system for solving cabin problems, including increasing recirculation air and de-fogging windows. The schematic diagram is shown in **Figure 2.27**. The results confirm that cabin heating load and power consumption reduce by 42% and 38% at -20 ºC, meanwhile, the driving range at -20 ºC increases to 172km.

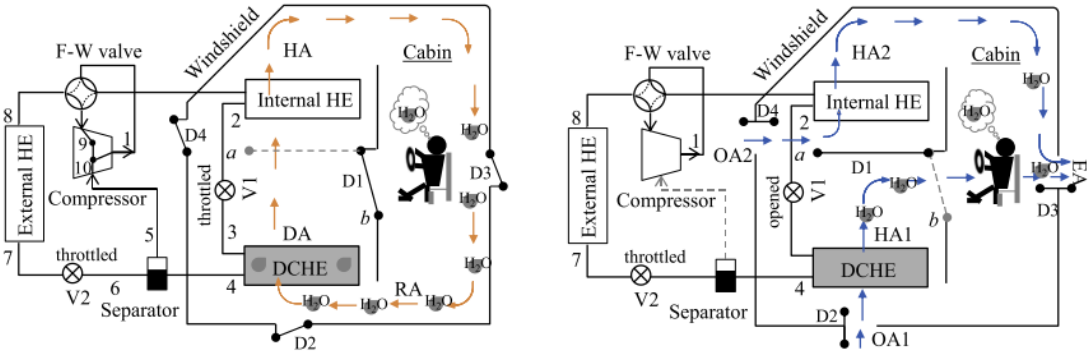

(a) Interior-Air Mode (b) Fresh-Air Mode

Figure 2.27. Schematic diagram of a heat pump with a desiccant dehumidification system [96]

Bellocchi *et al.* [97] designed and analysed a heat pump system combined with a recirculation air and energy recovery ventilator which is a membrane-based air-to-air heat exchanger for heat and moisture transfer. The driving range and energy consumption ratio were discussed and compared with a non-recirculation system using the Worldwide

harmonized Light Vehicle Test Cycle (WLTC). With air recirculation and ERV system, the HVAC energy consumption ratio can be saved by up to 14% and realise an increase of 2-6% in driving range and can achieve up to 53% energy reduction compared to a PTC heater in heating mode. However, the energy recovery ventilator, as well as desiccant dehumidification mentioned by Zhang *et al.* [96], may occupy the space of the compressor, and the system layout should be further considered.

2.3.2.2 Advanced controller and intelligent algorithms

A demand-based control system was proposed by Dvorak, Basciotti and Gellai [98] to reduce the total energy consumption in terms of current heating demands. The results demonstrate that with the suggested control strategy, energy consumption is reduced by 34%. He et al. [99] evaluated an AC system for the EV cabin with a Stochastic Dynamic Programming (SDP) using summer conditions in terms of electricity consumption while considering solar radiation. Compared to rule-based control logic, DP and SDP can save electricity by over 14% and 10.35% respectively. Following this, the same group conducted further research on Stochastic Model Predictive Control (SMPC) applied to an EV AC system in order to improve energy efficiency [100]. The results indicate that SMPC control logic has a similar impact on AC energy-saving, with the proposed SMPC control logic able to reduce energy consumption by 11.5%-14.16%. The cooling capacity variations of those three controllers under a low-speed driving cycle are represented in **Figure 2.28**.

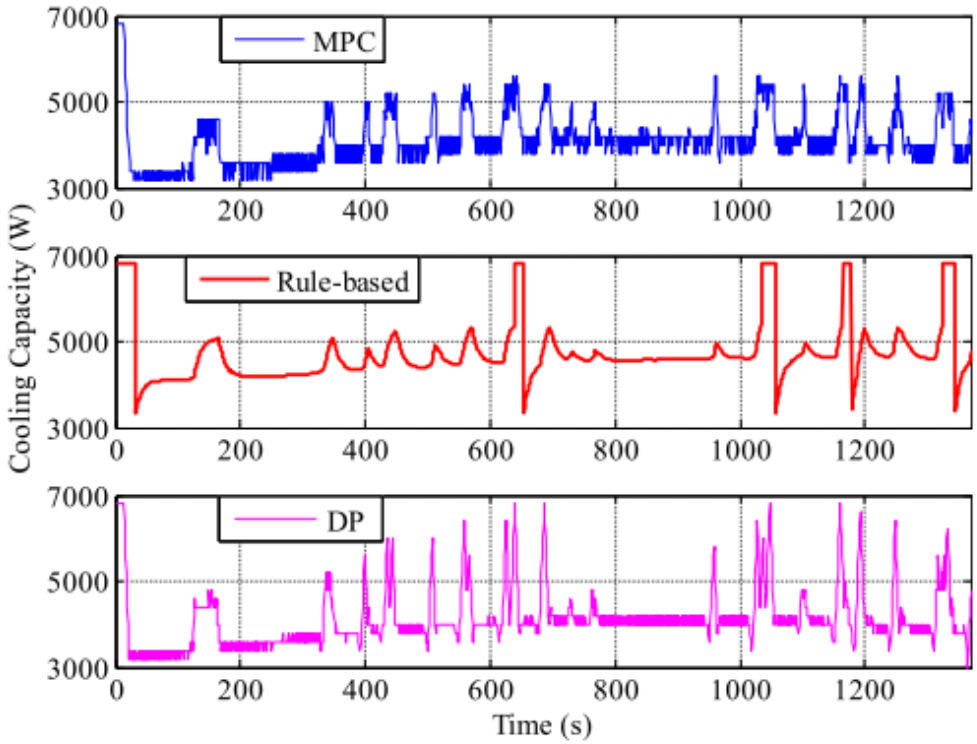

Figure 2.28. Cooling capacity variation of SMPC, rule-based, DP controller [100]

Covk *et al.* [101] first introduced a two-level hierarchical structure control strategy which was designed for the micro-AC system-based EV HVAC system, including low-level feedback controllers for accuracy and a high-level controller for controlling cabin air temperature and providing reference for low-level controllers. The cooling capacity can be transformed into a control allocation map which can be used as an input for a lower controller and reduce energy consumption by 25%. Then a genetic algorithm-based optimal control input allocation map was proposed for EV's heating up scenario in Ref. [102]. The allocation map is based on the two levels of hierarchical control strategies mentioned above, however, such an optimal allocation map is only based on HVAC efficiency, and more criteria should be included. Zhu and Elbel [103] implemented reinforcement learning on HP defrost control for EVs. With introduced reinforcement learning, optimal deforestation strategies can always be created, and the predictions were verified by experimental results.

2.3.3 Summary

In this chapter, recent EV heat pump performance-enhancing technologies as well as their performance combined with physical problems and advanced controllers were discussed. Many scholars introduced CO_2 into EV heat pumps as it can achieve the highest heating capacity without any supplementary technologies. However, it has been proven that the COP

of a normal CO_2 heat pump is always lower than other common refrigerants such as R134a, R32, R410 etc. Hence, those who investigated the CO_2 heat pump tried to use a gas cooler or intermediate cooling compressor to enhance COP while scholars who selected the other refrigerants prefer using vapour injection technologies to increase heating capacity. However, when adopting vapor injection technology, the trade-off between heating capacity and COP of the system should be considered as the PTC heater always works as a backup when the heat pump cannot provide enough heat.

Some researchers also connected heat pumps with cabins as they are closely related. As well as COP and heating capacity, windshield defogging, air recirculation and CO_2 concentration problems caused by air recirculation are also discussed, and a tree structure of the windshield defogging method is shown in **Figure 2.29**. Furthermore, as a combination system, advanced controllers can also significantly reduce energy consumption, including Stochastic Dynamic Programming (SDP) and two layers model predictive control (MPC), which can save more energy than demands-based and rule-based controllers.

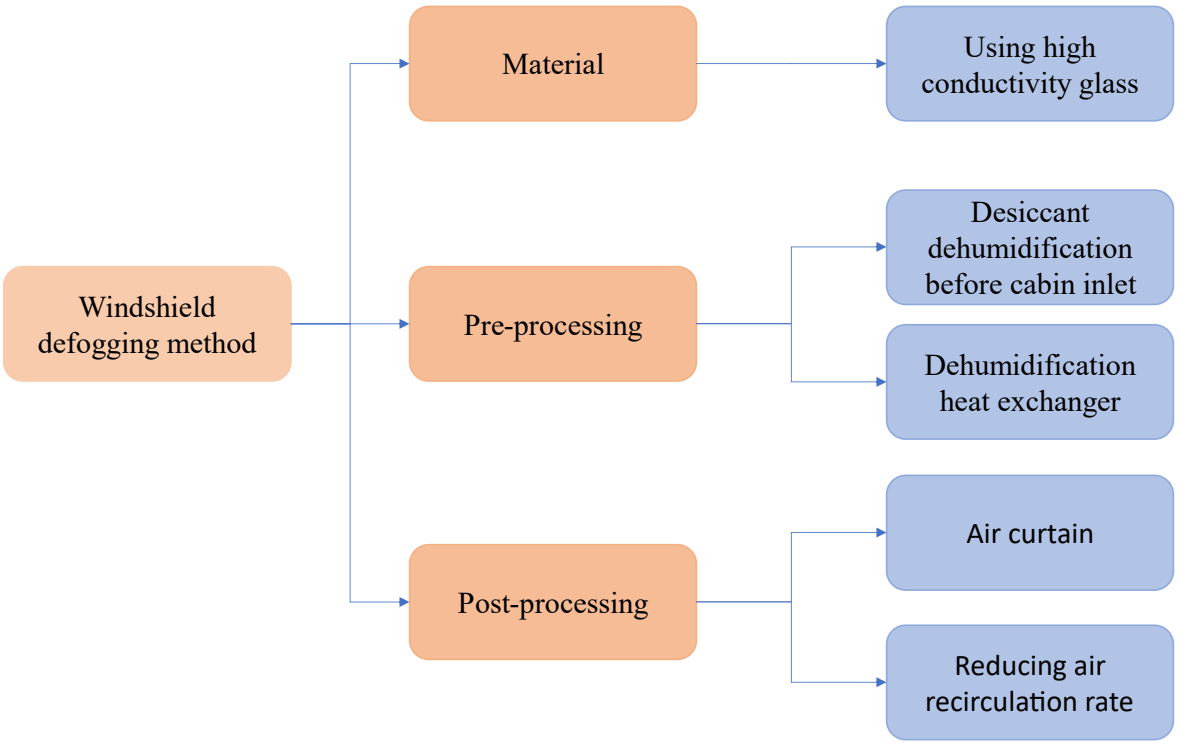

Figure 2.29. Windshield defogging method.

It should also be mentioned that ice on the outdoor heat exchanger is also a serious problem. Thick ice on OHX can largely decrease the heat transfer coefficient and lead to a lower COP. Hence, how to prevent the frosting phenomenon and how to defrost while EVs are driving on the road without affecting cabin comfort and the energy consumption is important. A

conclusion of the latest works on frosting and defrosting on OHX is shown in **Table 2.3**. Ice on OHX is harmful to heat pump performance, however, current defrosting methods require cabin heating to be halted whilst defrosting takes place and only a limited number of studies focus on preventing frosting. Therefore, further work is needed on advanced methods for predicting, preventing, and eliminating ice on the OHX. Furthermore, combined with cabin thermal management, investigating the impact of defrosting and cabin thermal management on driving range deduction is also important.

Table 2.3 Latest works regarding frosting and defrosting on OHX

Author	Year	Ambient	Refrigerant	Preventing method	Defrosting method	Effect
Cuevas et al. [81]	2019	-15 °C	R134a	N/A	Reversing cycle/ turning off the compressor	Achieves a COP of 2.1
Feng and Hrnjak [71]	2018	-20 °C	R1234yf	N/A	N/A	Reduces heating capacity by 38%
Li et al. [90]	2021	2 °C	R134a	Secondary loop	N/A	Attenuation starts at 5h of operation, 3h longer compared to an indirect system
Li et al. [104]	2020	-3 °C, 0 °C, 3 °C	R134a	N/A	N/A	Minimum COP is only 1.6
Zhu and Elbel[103]	2018	65%RH 75%RH 85%RH	N/A	N/A	Reinforcement learning control	Saves energy consumption by 12%
Zhou et al.[105]	2017	-20 °C 80%RH	N/A	N/A	Reversing cycle	Finishes defrosting within 100s

2.4 Performance and Advanced Control for HPAC Based Integrated VTMS

In the traditional vehicle, due to the different structures of EVs, the HPAC system is always seen as a separate system. In present EVs, the AC system should be always connected to the cabin and battery and in some cases to the motor due to the higher thermal sensitivity of EVs. Many scholars are beginning to pay attention to this problem from two aspects which are performance and control optimization.

2.4.1 Integrated system design

2.4.1.1 HPAC system with coolant/water cooling BTM

Ahn *et al.* [106] first designed a dehumidifying heat pump for electric vehicles utilizing waste heat sources in EVs and conducted a series of experiments on it. The results show that

a dual-source dehumidifying heat pump can provide 15.8% higher heat capacity and 5.2% higher COP than an air-source only dehumidifying heat pump. However, a newly introduced single heat source operation mode which runs air-source only mode and waste heat only mode separately shows a higher COP compared to the dual-source mode when the outdoor air temperature is -10 ºC and waste heat is 1.5kW. Lee *et al.* [107] launched a heat pump for an electric bus with a coolant source which uses the wasted heat of the electric devices and combined with an air source heat pump. The proposed integrated system that can provide 23.0 kW of heat under all tested compressor frequencies and outdoor temperatures which is sufficient for an electric bus. Following this, Zou *et al*. [108] analysed the performance of a VTMS (Vehicle Thermal management system) integrated system with a coolant battery cooling method as shown in **Figure 2.30**. The conclusions show the energy-saving rate of the proposed coupling system at -20 ºC varies from 3% to 7% with an increase in battery discharging rate. Meanwhile, the energy-saving rate can also be improved with the rising of ambient temperature to the cabin setpoint temperature.

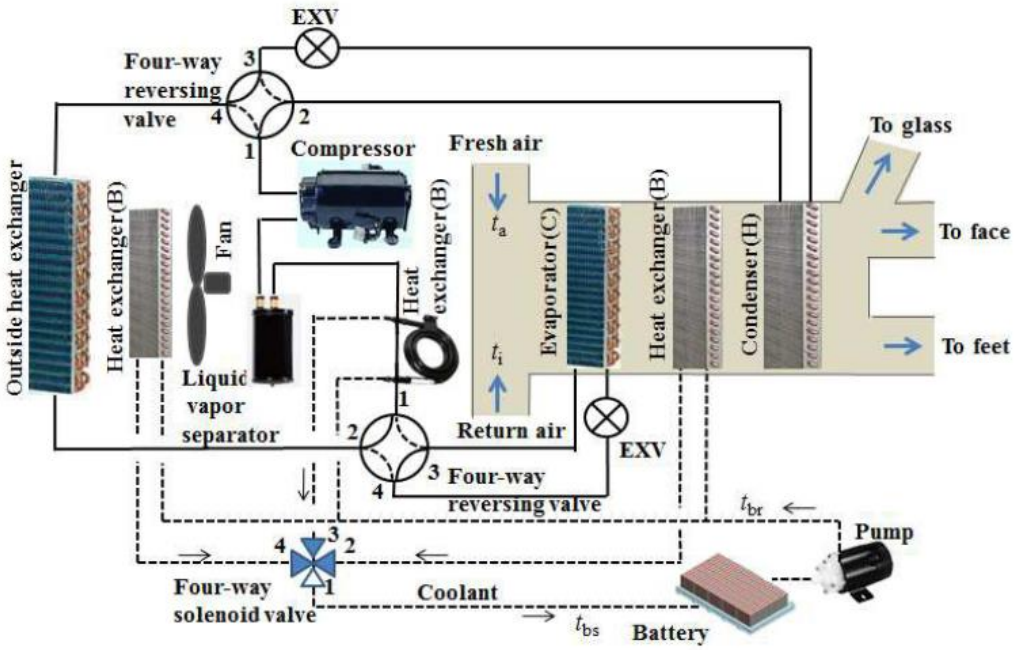

Figure 2.30. Scheme diagram of a coupled heat pump and coolant BTM system [108]

Moreover, Tian *et al.* [109], in 2018, proposed an heat pump based integrated thermal management system for electric vehicles and an experiment on cabin comfort was set in an environmental chamber. In order to investigate the effects on driving range and electricity consumption, a hybrid simulation method based on EVTMS was built in ADVISOR to combine with battery cooling and the motor cooling cycle. The results show that under HP and Motor Cooling Cycle (MCC) working mode, the driving range can be extended by up

to 37% and electricity consumption can be reduced by approximately 14kWh per 100Km. Over the next two years, the same group of researchers investigated a heat pump integrated system with a water and coolant cooling system [110, 111]. The results show that the system COP varies from 2.05 to 4.07 when waste heat from the battery increases to 2KW. With such a secondary loop heat pump EVTM system, the annual operation cost saving of the EVTMS ranges from 162.31€ to 249.44 € and the payback period is in the range of 4.47–6.77 years. The lowest ambient temperature in this study is only -7 ºC, but the supply air temperature is below 30 ºC when the waste heat from the motor is lower than 1kW. This brings a concern that if the ambient temperature is even lower, the supply air temperature may not be sufficient for heating. Moreover, the authors didn't consider the battery waste heat which could enhance the heating performance. Varma *et al.* [112] studied a HPAC system integrating battery cooling and pointed out that cabin cooling airflow over an evaporator has the highest sensitivity to average cabin temperature while the battery cooling refrigerant circuit chiller outlet pipe diameter has the most sensitivity to battery temperature. Furthermore, Ding *et al.* [113] introduced a distributed multiple-heat source system (battery waste heat, motor ,waste heat and heat pump heating system) for an electric bus with four different control stages in terms of ambient temperature which indicates that when compared with traditional air conditioning heating. At -22 ºC, during the first 0.2h, the heating performance of traditional air conditioning heating and that of proposed multiple-heat source system are almost identical. However, when the battery self-heated to 20 ºC, the proposed distributed system can save up to 60% energy in the following 2h. Additionally, Rana *et al.* [114] also investigated a universal VTMS and compared it with a benchmark thermal management system. With the designed cabin and battery integrated model, the predicted COP can reach 5.6 which is close to the result of 5.1 achieved by the test rig, while the conventional benchmark test rig can only achieve a COP of 2.7. Zhang *et al.* [115] studied a dual evaporator heat pump-based cabin and battery thermal management system mainly focused on an EEV opening shown in **Figure 2.31**. The opening of the battery branch's EEV can affect the superheat of the cabin evaporator which will affect cabin cooling performance and it was suggested this should be on a relatively large angle at the initial stage to achieve rapid cool down of the battery unit and then turned down to collectively adjust cabin and battery temperature based on the set point. Moreover, an integrated system can provide an additional 1.04kW cooling capacity than the cabinet-only mode.

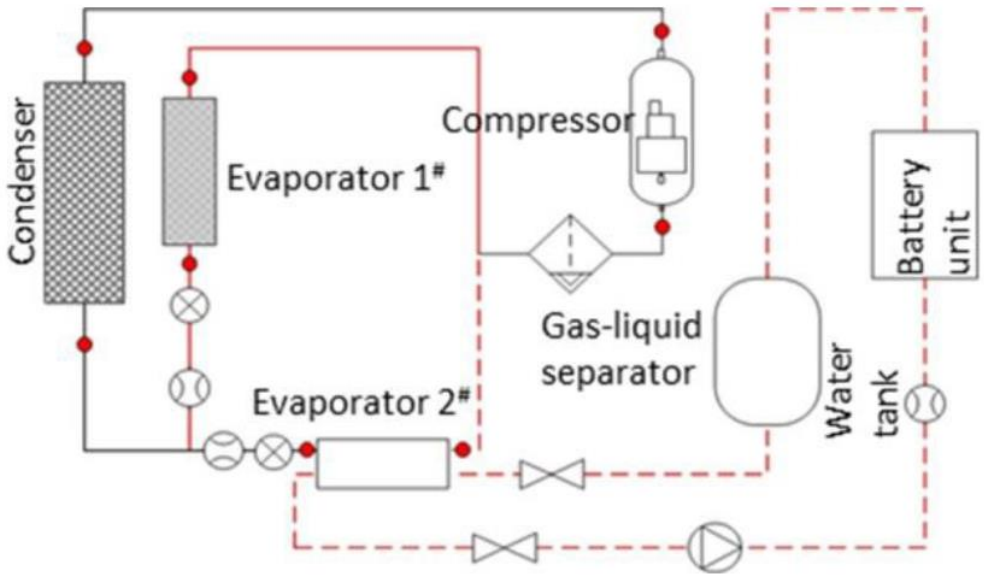

Figure 2.31. Scheme diagram of dual evaporator heat pump-based VTMS [115]

Similarly, Alkhulaif *et al.* [116] explored the performance of a coolant battery cooling VTMS with an ejector based HPAC system, as shown in **Figure 2.32**. In the base system without an ejector, the chiller and evaporator temperature and pressure in the model must be the same. However, in the modified ejector-based VTMS, the compressor in different branches can vary which can significantly improve COP, under all operating temperature values, in the approximate range of 7.17%-77.9% and can reduce refrigerant mass flow rate by approximately 12%. Zhang *et al.* [117] completed an exergy analysis on a cabin and battery mixed thermal management system based on the HPAC system. The conclusions indicate that the pressure change components like the compressor and expansion valves are the main factors of exergy loss in both cooling and heating modes and it should be noted that the internal condenser shows a great impact on exergy loss in heating mode when ambient temperature and compressor speed is low.

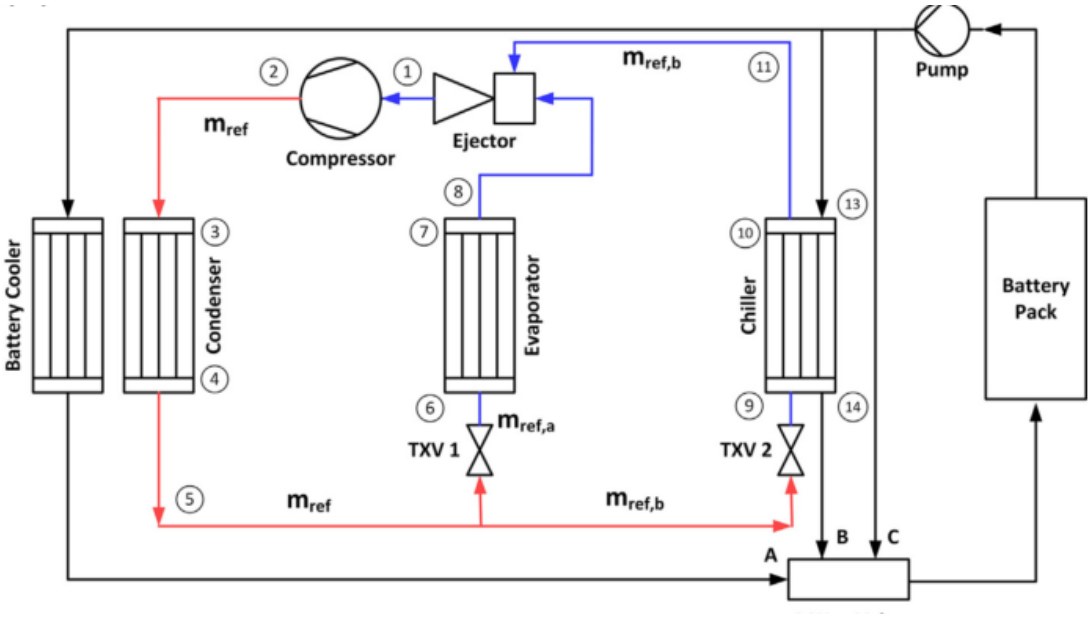

Figure 2.32. Ejector-based VTMS scheme diagram [116]

Jeffs *et al.* [118] conducted research on the whole EV thermal system including motor, transmission, thermal battery, cabin exhaust, and battery waste heat, as shown in **Figure 2.33**. With those multi-heat sources integrating with heat pump system, lots of operating modes can be generated. The outcomes indicate that dynamically selecting operating modes can significantly reduce electric energy consumption. The results show that 14.8% of average energy saving can be achieved. However, it should be noted that, in the Warmup cycle, none of the combinations can meet the requirement when the ambient temperature is under -20 ºC. In the case of the NEDC (New European Driving Cycle) test cycle, those combinations are useless once the temperature is below 0 ºC

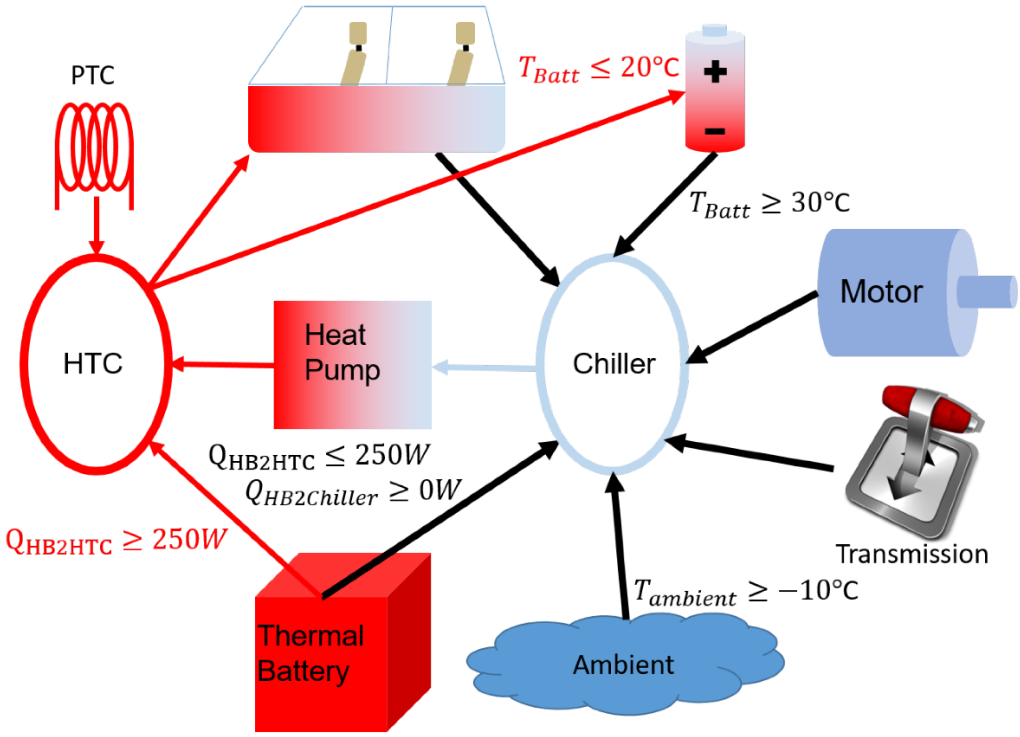

Figure 2.33. EV thermal system [118]

Lee *et al.* [119] introduced and compared three heat pump integrated thermal management systems with coolant heat recovery systems. Three systems are conventional heat pump waste heat recovery system (CWHRS), multi-stage heat pump waste heat recovery system (MWHRS), and direct waste heat recovery system (DWHRS). CWHRS extracts the waste from the coolant of power electronics and electric motors with the same operating temperature as the OHX side; In the MWHRS, the waste recovery cycle has a higher operating temperature compared to that in the CWHRS and the refrigerant in the waste heat recovery cycle is injected into the vapor injection compressor, while DWHRS introduced the high-temperature coolant to the cabin IHX directly. The results show that those three strategies have different advantages under different operating conditions. CWHRS is the best choice of those three for the start-up stage as MWHRS and DWHRS both have significant time delays. Once crossing the time delays, both MWHRS and DWHRS will provide a higher heat transfer rate to the cabin. However, when the system requires the supplement of the PTC, MWHRS has the greatest advantages. It should be noted that the cross-point of power consumption of MWHRS and CWHRS is far behind that of heat transfer rate to the cabin of MWHRS and CWHRS, therefore, there is a trade-off between those cross-points. Furthermore, the authors didn't consider the frosting effect when considering the impacts of the ambient temperature on performance which may have a big influence on it. It would be better to have an experiment in practical conditions under different ambient temperatures to compare those three thermal management strategies.

2.4.1.2 HPAC system with refrigerant cooling BTMS

Cen *et al.* [120, 121] experimentally investigated an integrated VTMS by integrating HPAC system and BTM. They adopted refrigerant based BTMS instead of coolant based BTMS. It was investigated in terms of the battery temperature difference and the test rig diagram is shown in **Figure 2.34**. The results show that a change in the refrigerant quality and pressure drop along the path will affect refrigerant temperature and lead to an uneven battery temperature. At the same time, the refrigerant circulation configurations have a significant impact on battery temperature difference, of approximately 4°C when the battery cold plate's inlet and outlet for refrigerant flow are on the same side while 10 °C can be achieved when the inlet and outlet are on different sides. Shen *et al*. [122] simulated a new BTMS of refrigerant-based EV combined with an HPAC system designed for high temperature operating conditions with simple control logic.

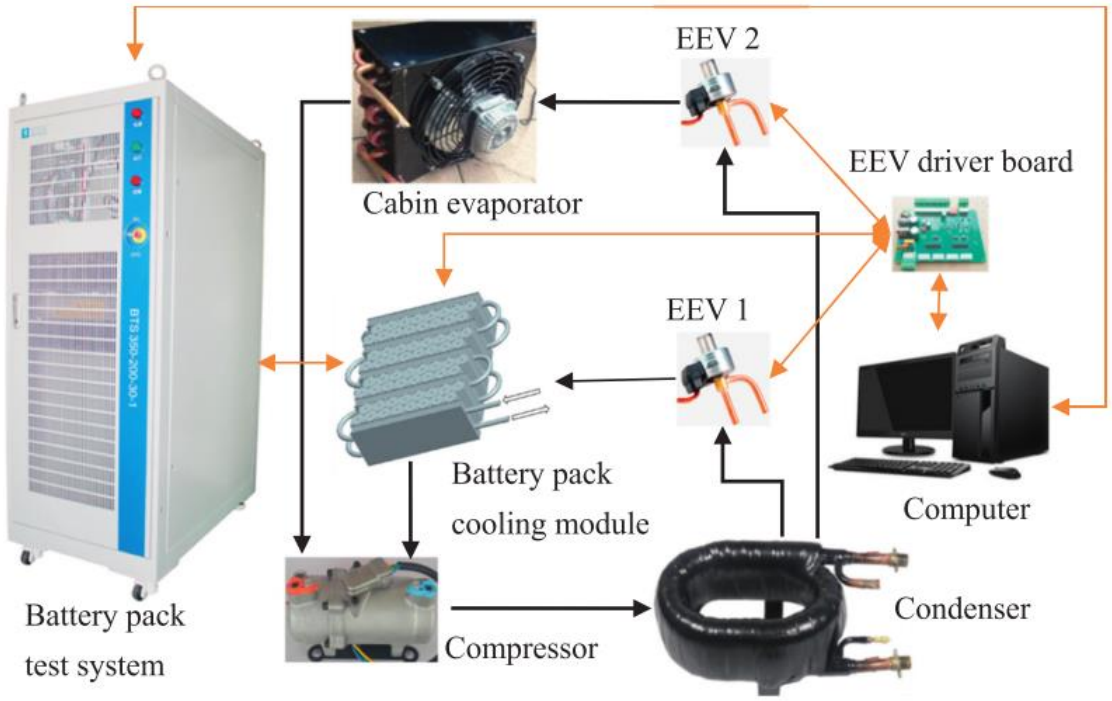

Figure 2.34. Schematic of test rig [120]

They analysed the energy COP and exergy COP of a refrigerant-based battery and cabin thermal management system which shows that, with the rise of ambient temperature energy, COP is reduced from 3.9 to 2.9 while exergy COP increased from 22% to 28%. Additionally, in 2021, Guo and Jiang [123] proposed a novel Heat pump based VTMS for both battery and cabin mixed cooling and heating and analysed the performance of that procedure within 3 NEDC test cycles. The system operating diagram can be seen in **Figure 2.35**. In cooling

mode, when the ambient temperature is 35 ºC, the energy consumption of TMS in the 1st NEDC cycle accounts for the largest ratio, which is approximately 20%, compared to the next two cycles in which the ratio can reduce to 9.3%. Meanwhile, in heating mode, both cabin and battery can be heated to 20 ºC within 15 mins when the ambient temperature is 0 ºC. Additionally, it should be noted that cabin temperature is more sensitive than the battery in the early stage of start-up.

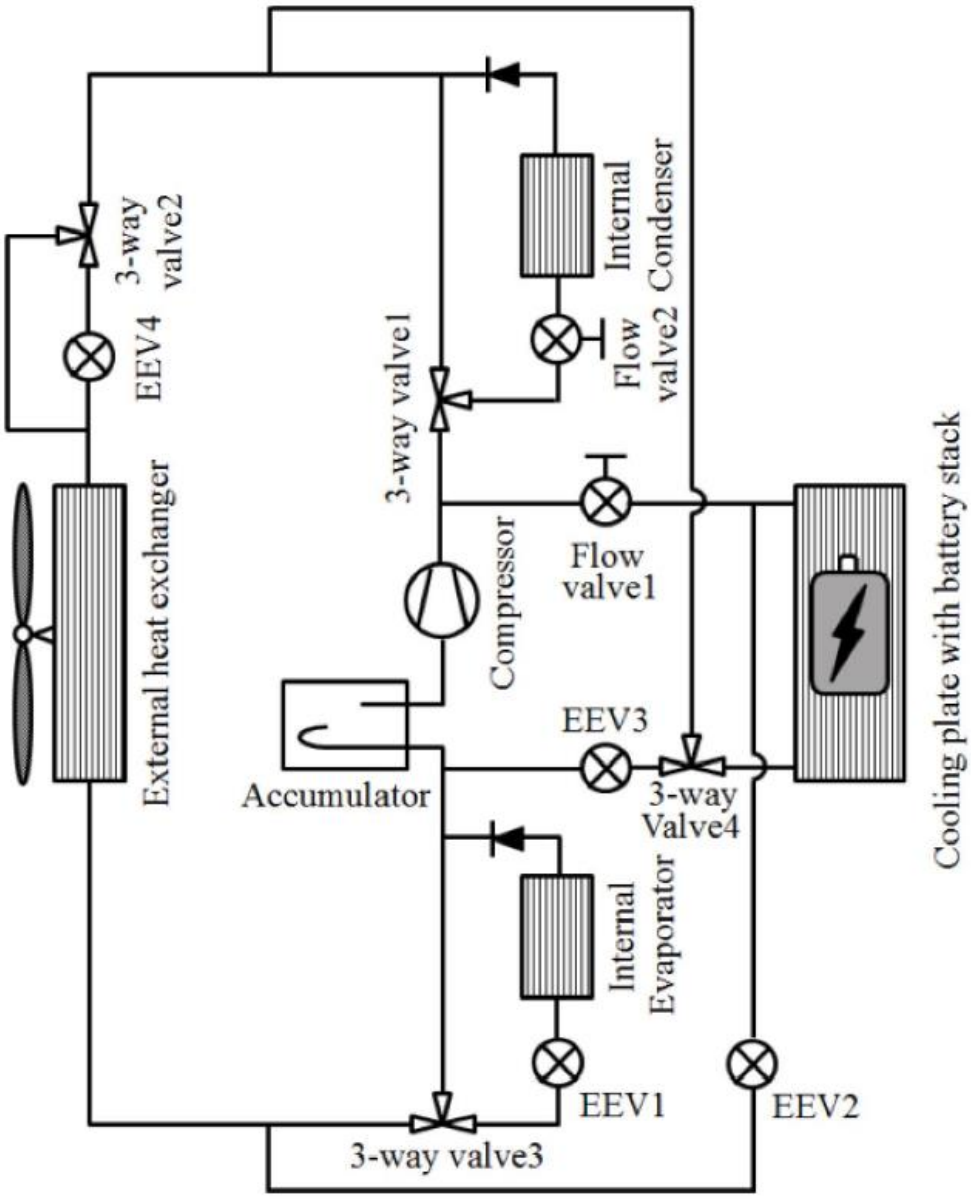

Figure 2.35. Refrigerant-based vehicle thermal management operating diagram

2.4.1.3 Fuel cell hybrid electric vehicle thermal management system

Fuel cell is device that can generate heat and electricity at the same time. Based on the materials of construction and operating temperature, fuel cells are categorised mainly into five groups: Polymer Electrolyte Membrane Fuel Cell (PEMFC), Alkaline Fuel Cell (AFC), Phosphoric Acid Fuel Cell (PAFC), Solid Oxide Fuel Cell (SOFC), and Molten Carbonate Fuel Cell (MCFC). Among them, PEMFC is considered the best option to applied to automobiles since it has low operating temperature (60 ºC to 80 ºC) which allows it starts up quickly. PEMFC compromises anodic and cathodic regions and a polymer membrane electrolyte. The principle of the PEMFC is shown in **Figure 2.36**. The H_2 enters the PEMFC from the anode side. The H_2 inside the PEMFC undergoes a chemical reaction and separate the hydrogen molecules into H^+ and e^- and releases heat at the same time. The electrons flow from the anode to cathode and generate electrical current. H^+ flows across the polymer membrane which can also be called electrolyte to the cathode side. The O_2 on the cathode side combines with the electrons and H^+ becomes water. The chemical reaction is expressed as below:

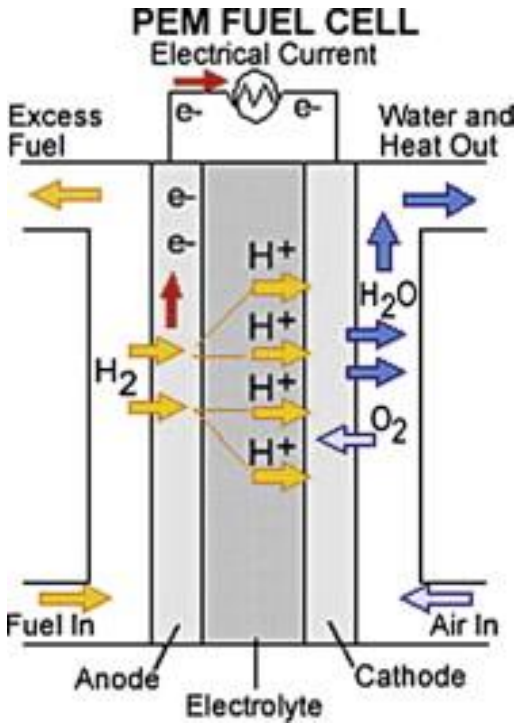

Figure 2.36. Principle of PEMFC [124]

$$2H_2 \rightarrow 4H^+ + 4e^- \quad (2.1)$$

$$O_2 + 4e^- + 4H^+ \rightarrow 2H_2O \quad (2.2)$$

PEMFCs can provide high power density leading to compact size and light weight compared to Li-Battery and response load changes more rapidly. Therefore, according to its electricity and heat cogeneration and zero-emission characteristic, PEMFC would be a promising component for the integrated energy management for EVs. Xu *et al.* [125] designed a fuel cell VTMS with 4 coolant loops for cooling motor, charging air, proton exchange membrane fuel cell (PEMFC), and Li-ion battery. PEMFC was cooled by ambient air while battery was cooled by HPAC system while cabin heating air was preheated by the waste heat from PEMFC and heated to the set point by HPAC system. However, the investigation only focused on PEMFC and motor loop. With the work of the designed PID controller, the system can maintain the charge air to the FC below 75 ºC and coolant exit from the FC at approximately 75 ºC, which is the optimum operating temperature for PEMFC. Kim *et al.* [126] studied a cold-start performance of a secondary loop heat pump-based fuel cell EV thermal management system. During the start-up stage, the cabin branch is closed in order to meet the fuel cell stack setpoint quicker. The system layout is shown in **Figure 2.37** which is similar to the secondary coolant loop EVTMS. The results show that compared to the baseline, a Hyundai system using cathode oxygen depletion (COD) heater heating coolant, the proposed system can save 27.3% of time consumption and 9.3% energy to arrive at a suitable operating temperature of 25 ºC at -20 ºC.

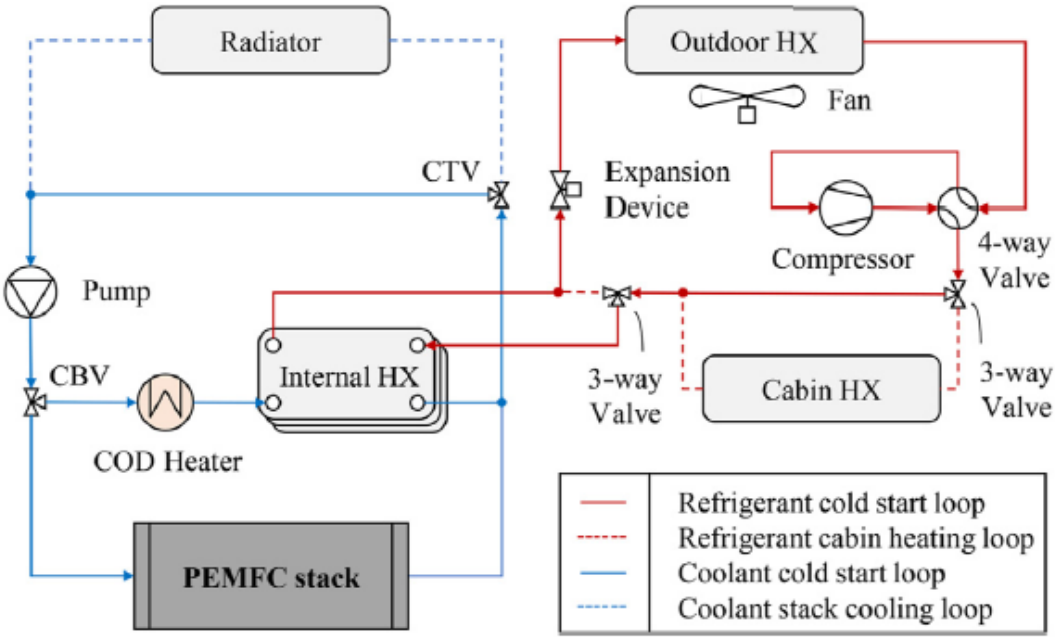

Figure 2.37. A heat pump-based fuel cell electric vehicle thermal management system [126]

Applying a different strategy, Sefkat and Ozel tried to use the waste heat from onboard hydrogen vessels to heat or cool batteries via coolant [127]. They developed a fuzzy logic controller to control the fuel supply system and vessel temperature. The results show that by using hydrogen waste heat, the proposed TMS can save up to 79.31% energy compared to a system without a fuzzy logic controller. Lu *et al*. [128] utilized a heat pump system in an EV with a fuel cell range extender inside. The heat pump recovered the waste heat from the small fuel cell stack and battery pack and supplied it to the cabin. The proposed system can always provide sufficient and enough heat (over 6kW) to the cabin in any cold weather with a COP of over 4. At the same time, the equivalent effective battery capacity has an obvious increase due to the power supply from the small fuel cell and the lower power consumption of the heating system. The proposed fuel cell range extender EV is a potential format of future zero-emission vehicles as both hydrogen and electricity are key elements for decarbonization. This system not only can provide a higher energy efficiency but also provide a new idea for extending the driving range and providing high cabin comfort simultaneously. Further investigation could focus on the experiment performance of such system and analyze the cost of the system in detail. Metal hydrides are a class of materials containing metal or metalloid bonded to hydrogen. When hydrogen atoms react with metal to form a bond, they can either receive one extra electron or share it with the metal. By this, the metal hydride can exist in solid, liquid or gas phase. For the solid metal hydride, it can be a metal, insulator, semimetal or semiconductor [129]. The principle during the absorption and desorption of the metal hydrides are expressed as below [130]:

$$MH_x + \frac{y}{2}H_2 \leftrightarrow MH_{x+y} + \Delta_R H \tag{2.3}$$

The absorption of hydrogen into the metal hydride (lift to right) is an exothermal reaction which releases thermal energy to the outside while the desorption process (right to left) is endothermal reaction. Both reactions follow a strong temperature-pressure dependence, it will bring heating and cooling effects at specific temperature levels if the metal hydride system works in the middle of high-pressure source and a hydrogen sink. Such working situation can be easily found Therefore, metal hydrides have good potential to be used in the cooling system of electric vehicles with on-board fuel cell stack [131]. Bürger *et al*. [132] developed an open-metal-hydride system with an integrated a fuel cell in order to utilise the energy waste during the pressure drop between the H_2 supply procedure from hydrogen vessel to the fuel cell stack. The experimental results revealed that the system can provide 276 $kW/MH_{(kg)}$ while providing 7kW electric power. However, the performance of the

proposed system was affected by the temperature difference between absorption and desorption temperature. Thermal loss occurs when the two metal hydrides work alternately, resulting in a 17% loss of cooling capacity within one cycle, even showing negative effects in the first 20 seconds of the cycle [133].

2.4.2 Integrated system control strategy and intelligent algorithm

PID controllers have been widely used in industries. Cen *et al.* [121] designed an optimized PID controller with a sigmoid function which can control the battery pack temperature difference to 2 ºC when the discharging rate is between 0.5C and 1C. Shen *et al.* [122] also applied a battery temperature and HPAC PID controller to the integrated system and developed an optimal control logic which ensures the cabin has higher priority while in routine control, both cabin and battery have the same priority. The results show that optimal control logic can result in lower cabin temperature fluctuations under the same battery temperature control performance. In order to better extend the driving range, Min *et al.* [134] used a fuzzy controller (shown in **Figure 2.38**) in their EVTMS to enhance battery life and the results were compared with the traditional PID control utilised in the experiment. The comparison identifies that the fuzzy control strategy can extend battery lifetime by approximately 3.11% - 3.76% but shows a higher cabin fluctuation. However, the entire results are based on PTC heating rather than heat pump heating. Similarly, Pan *et al.* [135] also investigated a fuzzy control logic for BTMS and HPAC integrated EV energy management strategy based on Markov theory prediction. The proposed control strategy can reduce battery energy consumption by 8.14% while considering air conditioning loads and leads to an increase in driving range compared with the rule-based logic threshold strategy.

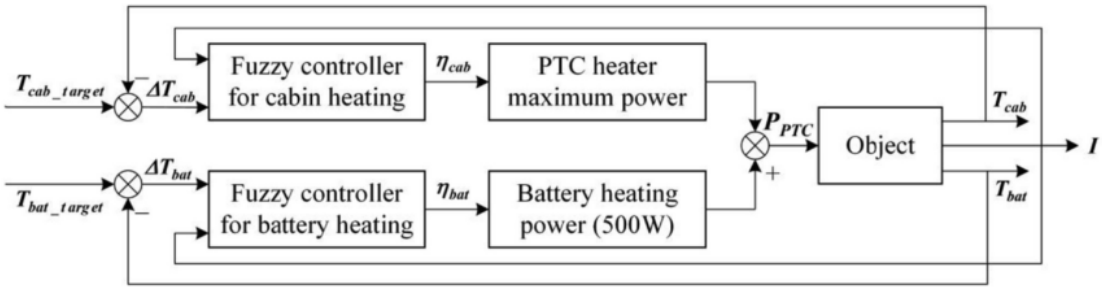

Figure 2.38. Schematic diagram of the fuzzy control strategy.

Compared with basic fuzzy logic, a battery-aware cabin climate control strategy was proposed by Vatanparvar and Faruque *et al.* [136] which can optimize the power

consumption the HVAC system and reduce the battery stress The conclusions demonstrate that the proposed control strategy can reduce battery lifetime degradation by 13.2% and decrease energy consumption by approximately 14.4%. Furthermore, thermal comfort cost by basic fuzzy logic is nearly zero for lower temperature fluctuations but the proposed control strategy can contribute to improved battery life. However, in this study, the authors only considered the SOC and SOH (State of Health) of a battery without battery temperature. In addition, one emerging trend in optimizing vehicle thermal management is leveraging vehicle connectivity in terms of weather and traffic forecasts by which vehicles can anticipate upcoming events and precisely control energy consumption behaviours to save energy [137]. Mohammad *et al.* [138] developed a two layers MPC-based cabin and BTM strategy for the HEV (Hybrid Electric Vehicle) energy management system via vehicle speed and traffic predictions over different prediction horizons. Compared to traditional single-layer MPC, up to 6.1% of battery energy can be saved under the same cabin setpoint for the urban driving cycle. Meanwhile, the robustness of such a scheme against traffic prediction was confirmed. Furthermore, Wang *et al*. [139] exploited MPC and vehicle speed preview by proposing an eco-cooling strategy that can leverage the AC system efficiency sensitivity to the vehicle speed. The experimental results demonstrated a 5.7% of energy saving on average from the vehicle perspective. Park and Kim [140] utilised a supervised learning algorithm to optimise VTMS, with a strategy introduced by artificial neural networks. The total power of the compressor, fans and pumps can be reduced by 48.5% when maintaining battery temperature within an acceptable temperature. However, the cabin temperature was not considered although the energy consumption of the compressor was included in the total energy consumption.

2.4.3 Summary

An integrated thermal management system is the best way to handle EV thermal management compared to considering each part separately. Increasing numbers of researchers are trying to link cabin thermal management with battery and motor thermal management. The best way to combine those three elements is via a heat pump. Recent integrated vehicle thermal management system performance research has all been heat pump driven. The research can be mainly divided into two aspects which are system performance, including secondary coolant loop or pure refrigerant loop, and control optimization. A comparison among the latest integrated thermal management approaches is depicted in Table 2.4. However, most of the studies focus on the second coolant-based integrated thermal

management system, whilst research on the refrigerant-based integrated thermal management system has been very limited, it still needs further investigation. People who studied the performance of secondary coolant loop VTMS always try to achieve a greater energy saving rate and COP by using one of the major advantages of an EV integrated system, waste heat. However, for most of the integrated systems for heating, there is a common obstacle that waste heat may not be sufficient when the vehicle is stopped or running at a low speed, for some high-speed cases, the waste heat may be excess. Hence, we should consider a small energy storage system to store waste heat in high-speed mode and use it in low-speed mode. As for integrated system controllers, most studies achieved results depending on very basic thermal management systems without considering heat pump heating at lower temperatures. These studies introduced more advanced control logic, such as MPC and fuzzy logic, rather than PID controllers to achieve improved battery life and lower energy consumption. The performance of those systems in this area is summarised in **Table 2.5**. It can be seen that research from a system perspective is very limited. For example, most studies are only for cooling mode, and battery and cabin space heating still lack research attention. Meanwhile, when the ambient temperature is between 10 ºC and 20 ºC, cabin heating and battery cooling may occur simultaneously, however, no study has considered this situation in recent years. Furthermore, the performance of refrigerant-based systems and their comparison with secondary coolant loop systems should be further discussed and specific controllers for refrigerant-based systems, for all operating modes, should be further investigated to achieve lower energy consumption.

Table 2.4 Comparison of latest integrated thermal management approaches

	Battery Working medium	loop		Advantages	Disadvantages
Integrated heat pump-based EV thermal management system	Coolant			Low energy consumption	Can only cover normal situations
			Pure coolant	High safety	High weight
			Heat pipe+ coolant	Simple system structure	Reduces battery density
				Easily achieves battery temperature uniformity	Need more heat exchangers
			PCM + coolant	Can easily combine with PTC	
	Refrigerant		Pure refrigerant	High cooling and heating capacity	Need more EEV
				Low space consumption increases potential for heat recovery	Complicated control
			PCM+ refrigerant	Low heat loss	High pressure
				Can cover all operating conditions	Sealing problem
			Heat pipe+refrigerant		Massive refrigerant storage

Table 2.5 Comparison of the performance and operating mode of different integrated systems

Author	Ambient	Working medium	Battery/Motor	Battery charging/discharging rate/ heating and cooling load	Cabin mode	Battery/Motor mode	Performance
Rana et al.[114]	30 °C	Coolant	Dummy	Cooling load 2.5kW	Cooling (27 °C)	Cooling (27 °C)	COP:5.0
Tian et al.[110]	35 °C-43 °C	Coolant	Dummy	Cooling load 0.5kW	Cooling (26 °C)	Cooling	COP:0.86-2.67
Zhang et al. [115]	35 °C	Coolant	Dummy	Cooling load 1.09kW	Cooling (27 °C)	Cooling	COP:2.55
Alkhulaif et al [116]	35 °C	Coolant	Dummy	Cooling load 0.2kW-2.2kW	Cooling	Cooling	COP:2.35-2.88
Cen et al. [120, 121]	40 °C	R134a	18650 2.2Ah	0.5-1.5C	Cooling	Cooling	
Guo et al.[123]	35 °C / 7 °C	R134a	18650 2.75Ah	NEDC	Preheating (20 °C) and cooling (25 °C)	Preheating and cooling	Preheating finishes in 9mins Cooling finishes in 10mins
Shen et al.[122]	35 °C /30 °C	Refrigerant	$LiFeO_4$	UDDS/US06	Cooling (25 °C)	Cooling (25 °C)	COP:2.9-3.9
Vatanparvar et al.[136]	35 °C	-	-	ECE_EUDC	Cooling (25 °C)	SOC	Reduction of 14.4% in energy consumption
Lee et al. [119]	0 °C/-10 °C	Coolant	Numerical	Heating load 5kW	Heating	Cooling	COP:2.3-2.8
Han et al. [141]	-10 °C-5 °C	Coolant	Dummy	Heating load 15-20kW(bus)	Heating	Cooling	COP:2.75-3.25
Yu et al. [2]	-10 °C-10 °C	Coolant	Dummy	Heating load (1kW-2.6kW)	Heating	Cooling	COP:1.54-3.03
Kim et al. [142]	-20 °C-0 °C	Coolant	Dummy	Heating load (2.4kW-3.5kW)	Heating	Cooling	COP:1.8-2.08

2.5 Chapter Summary

In conclusion, the state of art vehicle thermal management is thoroughly reviewed in terms of battery thermal management, heat pump-based cabin thermal management, and integrated thermal management system. Refrigerant-based BTMS or hybrid method (PCM+Refrigerant) has huge potential to cover all working conditions compared to other thermal management systems. Meanwhile, as the refrigerant is the only fluid in the system, it is simple to combine with EV's heat pump system. However, there is limited research on these two aspects, particularly for extreme charging and discharging conditions, and more work is needed in this area.

Cabin thermal comfort is also an important task in electrical vehicle thermal management. The heat pump system was proven, a few years ago, to have a promising future. Recently, scholars tried to find a suitable substitute for R134a, to support the latest CO_2 emission regulations. Most of them paid particular attention to CO_2 which has the largest heating capacity among the candidates but with lower COP. Hence, technologies such as a series gas cooler and intermediate cooling compressor were investigated to increase COP. Meanwhile, vapour injection technology is also a popular research topic to enhance the heating capacity of the heat pump systems using other refrigerants. Different from residential buildings, cabin volume is much smaller, consequently, air humidity is more sensitive. Frost on the front windshield is one of the biggest problems in EVs as the usage of recirculation air causes the relative humidity of the air to be high, therefore, several defogging methods are discussed. Additional dehumidifying heat exchangers or desiccant dehumidifiers are successful methods to pre-process air without sacrificing energy but the layout and performance under low temperatures still need to be explored. However, limited research has considered the frost on OHX when the heat pump operates under low temperatures. Hence, the application of EV's heat pump still faces many obstacles. For instance, the impact on cabin thermal comfort while defrosting, continuously defrosting without stopping or reversing cycle technologies, and the best time to defrost need to be investigated.

Finally, integrated EV thermal management systems were proposed by many researchers to link cabin, heat pump, battery, and even motor and/or other power components altogether which can make the thermal management system more reasonable and effective as waste heat can be utilized. Some studies designed a secondary coolant loop while others introduced refrigerant-based integrated systems. Both methods have been initially proven and can

sufficiently fulfil the tasks with acceptable COP. It should be noted that refrigerant based VTMS has a more promising future as it can cover not only normal conditions but also extreme conditions, even thermal runaway, while a secondary coolant loop system is better for the less severe situations. However, there are still substantial difficulties that need to be overcome in addition to the obstacles mentioned in the battery and heat pump section of this document. For instance, the performance of the whole system under extreme conditions or a situation of heating and cooling taking place at the same time, further dynamic cycle testing or simulation, optimal EEV opening, superheat, refrigerant charging amount etc. Additionally, recent control systems are also reviewed in this paper which is very important to the integrated system energy saving, with a suitable controller like fuzzy logic. Multi-layer MPC can also save a great deal of energy. However, no integrated thermal management optimal control system for extremely fast charging strategy and the fast-discharging situation was discussed.

Therefore, for future zero-emission vehicles, the heat pump is a critical sub-system that can improve the driving range deduction in cold weather and the heat pump integrated thermal management system is vital for developing a state of art energy management system. From the pure heat pump perspective, the trends of heating capacity and COP are always opposite, meanwhile, the higher the heating capacity, the faster the OHX frosts and the faster the performance declines. Hence, the optimization structural design of the OHX to inhibit ice growth is a potential topic, also, the modified Evans-Perkins cycle based heat pump shows great potential for use in vehicles but more investigation should be done especially the material of the heat storage, its performance when using different low GWP refrigerant, and how it would affect the evaporator side. From the heat pump integrated system, future research could first focus on clarifying the practical waste heat that can be obtained under different operating conditions instead of simple assumptions. Furthermore, cascade utilization of the waste heat and waste heat arrangement while defrosting is also a very important topic. Moreover, as more and more battery coolants are cooled by the chiller and some battery thermal management systems even use refrigerant cool down the battery pack directly, hence, it is important to figure out the optimal combination for the battery, heat pump, and cabin, especially for extremely fast charging and discharging scenarios. As future zero-emission emission vehicles are not limited to pure battery vehicle, fuel cell hybrid electric vehicle is also a potential solution. The heat pump system has been initially proven can achieve good performance, but further investigation is still needed. At last, the advanced control logic is a sufficient way to reduce energy consumption, further research could pay

more attention to leveraging vehicle connectivity in terms of weather and traffic forecasts and the application of MPC that could also lower energy consumption. Meanwhile, if machine learning can be adopted, precisely predicting the traffic status and optimal thermal solution in advance could come true. Also, not only battery electric vehicles are zero-emission vehicles, fuel cell vehicles, and fuel cell assisted battery hybrid electric vehicles are also potential solutions. The heat pump applications in such vehicles have not been discussed widely, so they are also potential solutions that can promote decarbonization. Although there are a number of issues to be addressed, a heat pump-based integrated zero-emission thermal management system has huge potential in extending the driving range and providing better cabin comfort.

In this chapter, the disadvantages of VTMS for current EVs are discussed. Although there are some integrated VTMS designed for winter have been investigated, the performance degradation, unstable waste heat source, insufficient heating capacity, and driving range deduction cannot be solved at the same time. Also, the energy consumption caused by the VTMS for cooling, including battery, cabin, and other electronics still needs to be further improved as there is very few innovative VTMS for cooling is investigated. Hereby, the following chapter will design and investigate the integrated VTMS from a heating and cooling perspective in series.

3. Heat Pump and Fuel Cell Integrated Energy System

3.1 Introduction

Conventional internal combustion engine vehicles (ICEVs) significantly changed the way people live and the quality of life. However, the pollution and CO_2 emissions caused by vehicles cannot be ignored [3]. Current research efforts are directed toward phasing out the vehicles that are fuelled by fossil fuels and developing zero-emission vehicles instead [143]. Therefore, zero-emission vehicles such as battery electric vehicles (BEVs) and fuel cell electric vehicles (FCEVs), are attracting increasing attention worldwide. However, the heating demand for BEVs in the cold season, particularly in polar and sub-polar regions, faces a huge challenge due to the lack of waste heat compared to ICEVs. Zhang *et al*. [57] concluded that the heating load varies between 3.3kW to 6.8kW at -20℃ in terms of vehicle speed.

Although the positive temperature coefficient (PTC) heater is the initial solution that can provide enough heat for cabin comfort [144], the reduction in driving range (around 50% [15]), caused during heating, results in a mileage concern for the driver [145]. The mobile air source heat pump (ASHP) which is widely used in residential space heating is seen as a good alternative to the PTC heater. It provides heat for space heating by extracting heat energy from the source with a lower temperature [146]. However, due to the limited space in the vehicle and the COP of the essential heat pump, an ASHP system struggled to provide sufficient heat energy and the COP was marginally less than or greater than 2 in cold climates [59, 147]. In order to improve the performance of the heat pump used in EVs, different approaches have been investigated and reported by scholars. For example, introducing vapour injection (VI) technologies to the system or investigating alternative working refrigerants. Qin *et al*. [148] designed an R134a vapour injection heat pump system for EVs with single and triple portholes on a scroll compressor. The proposed system can offer a heating capacity of 3.6kW but with a low COP of 1.7, at the ambient temperature of -20℃. Nevertheless, when the ambient temperature increased to 0℃, the COP increased to 2 with the same heating capacity and the maximum heating capacity of approximately 4kW was achieved. Similarly, results from other research on the VI R134a heat pump systems also showed a heating capacity between 2.5kW-3.5kW and a COP range from 1.5 to 2.5 from below -20℃ to -10℃ [72, 74, 78, 149, 150]. Therefore, the improvement effect of VI systems is limited, although it can improve the heating capacity to a certain extent, the COP

cannot be improved significantly. Meanwhile, some scholars discussed the application of CO_2 heat pumps for EVs. Wang *et al*. [69] investigated a CO_2 heat pump with a series gas cooler for EVs in order to utilise the heat of mid-temperature refrigerant. At-20℃, the novel CO_2 heat pump system provided at most 6.8kW heat and the COP was 2.2 with a 10Mpa discharging pressure. Compared to the traditional CO_2 system, the suggested system improved the COP and heating capacity by 35% and 33.7% respectively. Dong *et al*. [151] provided an experimental study on CO_2 EVs' heat pumps, and concluded that the proposed system could supply up to 7.5kW heat with a COP of 2.16 and a compressor speed of 7500RPM at a temperature of -20℃. However, different from the R134a heat pump system, the COP of the CO_2 system decreased with the increase of the ambient temperature [69, 151]. Therefore, considering the heat pump in EVs as an isolated component makes it difficult to improve heating capacity and COP simultaneously.

An electrical vehicle is a combination of several subsystems such as a heat pump, battery pack, and motor. Hence, effective integration of such subsystems to recover heat and use it for cabin heating has the potential to increase the performance of a heating system of EV and eventually increase its driving range. However, most of the system-level thermal management systems were from cabin and battery cooling perspectives [152-154], and only a limited number of studies considered utilising the waste heat for heating. Tian *et al*. [155] assessed a heat pump integrated thermal management system that can collect the waste heat generated by the battery, motor and controller. They assumed that those components could provide 2 kW waste heat at -5℃ to 5℃ and with COP ranging between 2.05 and 4.71.Jeff *et al*. [118] carried out an analysis of the whole EV thermal system including motor, transmission, thermal battery, cabin exhaust and battery waste heat and created 32 operating modes. The outcomes indicated that dynamically selecting operating modes could lead to an average energy saving of 14.8%. However, it should be noted that, in the Warmup cycle, none of the combinations met the requirement when the ambient temperature was at -20℃. In the case of the New European Driving Cycle (NEDC) test cycle, those combinations were useless once the temperature was below 0℃. Ding *et al*. [113] developed a distributed multiple-heat source for a large electric vehicle. It used the waste heat from the battery and motor directly to heat the front and back of the vehicle. An air-source heat pump was introduced for the middle section of the vehicle. The results showed the proposed design could save 60% of energy when running 2hours at -22℃ atmospheric temperature. As well as the pure EVs, the fuel cell electrical vehicle is also a solution for the zero-emission vehicle. Although electrical vehicles integrating with fuel cell only accounted for less than 1% of

2018's vehicle market, it is expected to play a critical role in the future of zero-emission vehicles [156]. The fuel cell is a component that can generate heat and electricity at the same time. However, most of the research about fuel cells were from the fuel cell cooling aspect [125] and less attention has been paid to recovering and using waste heat from fuel cell along with the battery for cabin heating. Lee *et al*. [157] experimentally investigated a coolant-source heat pump for fuel cell EVs by using a triple fluid exchanger and waste heat from the fuel cell and electric device. They suggested that using a coolant-source heat pump can improve the driving range up to 10.8% compared to using a PTC heater.

The referred literature indicates that thermal management of an EV based on an isolated heat pump system has been widely investigated only as an isolated heat pump system. However, the results illustrate that it is difficult to improve the heating capacity and COP simultaneously when considering the heat pump as an isolated component. Whilst there has been limited studies conducted into the heating solution from a systematic perspective, it has been shown that compensation from battery waste heat was still not sufficient for extreme cold weather although it could improve the COP in a mild-cold environment.

Therefore, in extremely cold weather, the driving range of an electric vehicle is still significantly reduced due to the need for heating, since a large proportion of the electricity generated by the battery is consumed for the heating effect. Another issue is that most research to date has ignored the frost phenomenon on the outdoor heat exchanger (OHX) that occurs after prolonged operation of the heat pump, which can cause fluctuations in cabin temperature during defrosting. Furthermore, although fuel cells can provide certain waste heat, less attention has been paid to utilising them for cabin heating. Therefore, it is necessary to further investigate how to provide sufficient heat and more importantly, to provide a relatively high COP for EVs' cabin heating at the same time under extremely cold conditions. Additionally, it is crucial to identify a way to avoid the OHX frosting. Meanwhile, management of the waste heat from the fuel cell to reduce the driving range deduction while heating the cabin also needs further investigation.

In this context, in order to provide sufficient and stable heat to the cabin with high COP, this study proposes a heating system integrating a heat pump and battery. Based on the existing heat pump system, a small fuel cell stack is introduced as a backup to the system for effective thermal management of an EV cabin and thus increase the driving range. In this system, the waste heat generated by the fuel cell stack and the battery pack are considered the source of

heat for cabin heating by using a coolant heat pump. A numerical model is developed in MATLAB, which comprised three interconnected sections namely, the heat pump, fuel cell cooling subsystem and refrigerant-based battery thermal management system. The heat transfer coefficient of plate heat exchangers and fin and tube heat exchangers for R134a, battery and fuel cell heat generation model and compressor in the subsystems are investigated and validated. End of the study, the performance of the proposed system is evaluated in detail in terms of the COP, the outlet air temperature, and the heating capacity. A comparison analysis is introduced by comparing the proposed system to a conventional system in order to examine the advantages of the proposed system. The investigation into the proposed integrated system will help tackle the heating problems of current BEVs and extend the driving range in extremely cold weather. This research will be useful for expanding the operating conditions of EVs and promoting the development of EVs to create the net-zero world. This work integrates a heat pump, battery, and fuel cell together to utilise their waste heat which may not only be applied to a zero-emission vehicle but can also be of interest for domestic heat and electricity cogeneration.

3.2 System Description

The schematic diagram of thermal management for proposed FCBEVs is shown in **Figure 3.1**. Unlike existing systems that employ an air source heat pump to extract heat from the low temperature ambient air with a PTC heater as a backup to cover the extreme cold weather, the proposed system in this study introduces a coolant source heat pump and a fuel cell system to replace the PTC heater in order to utilise waste heat and provide high efficiency heat and electricity cogeneration for the vehicle. In the proposed system, waste heat from the fuel cell stack and the battery pack was utilised as a supplement for space heating. The green line, in **Figure 3.1**, represents the R134a refrigerant flow cycle. After the expansion valve, the refrigerant first passes by the battery pack. The battery thermal management system is designed as a refrigerant-based cooling system. The refrigerant flows through the battery pack to absorb the waste heat generated during battery charging and discharging process. The refrigerant then enters a counter-flow plate-type evaporator where heat is absorbed from the coolant (red line) coming from the fuel cell stack and converted into complete vapour. The coolant comes out of the plate heat exchanger and then goes back to the fuel cell stack to cool down the fuel cell continuously. The function of the accumulator is to separate gas and liquid refrigerant to make sure only vapour-phase refrigerant can access the compressor. After the processing of the compressor, pressure and temperature both

increases. The high-pressure and high-temperature refrigerant runs into the fin-tube type crossflow internal condenser. In the condenser, the refrigerant undergoes a heat transfer procedure with the feeding air which will be supplied to the cabin to achieve thermal comfort. The refrigerant from the internal condenser flows past the expansion valve and the cycle continues. The cabin supply air sourced from the environment, first flows across the external fin and tube-type heat exchanger for pre-heating by recovering heat from the hot water produced during the fuel cell reaction represented by the blue line. Operating parameters should be adjusted, such as lowering the fuel cell current output to avoid the freezing point of the water inside the external heat exchanger due to the heat transfer with the cold ambient air. Subsequently, the pre-processed cabin supply air passes over the internal heat exchanger before entering the cabin.

The air intake for the fuel cell comes from the ambient environment and is compressed to high pressure and high temperature by an air compressor (not shown in the diagram) before flowing into the fuel cell stack. H_2 for the fuel cell comes from the onboard hydrogen vessel.

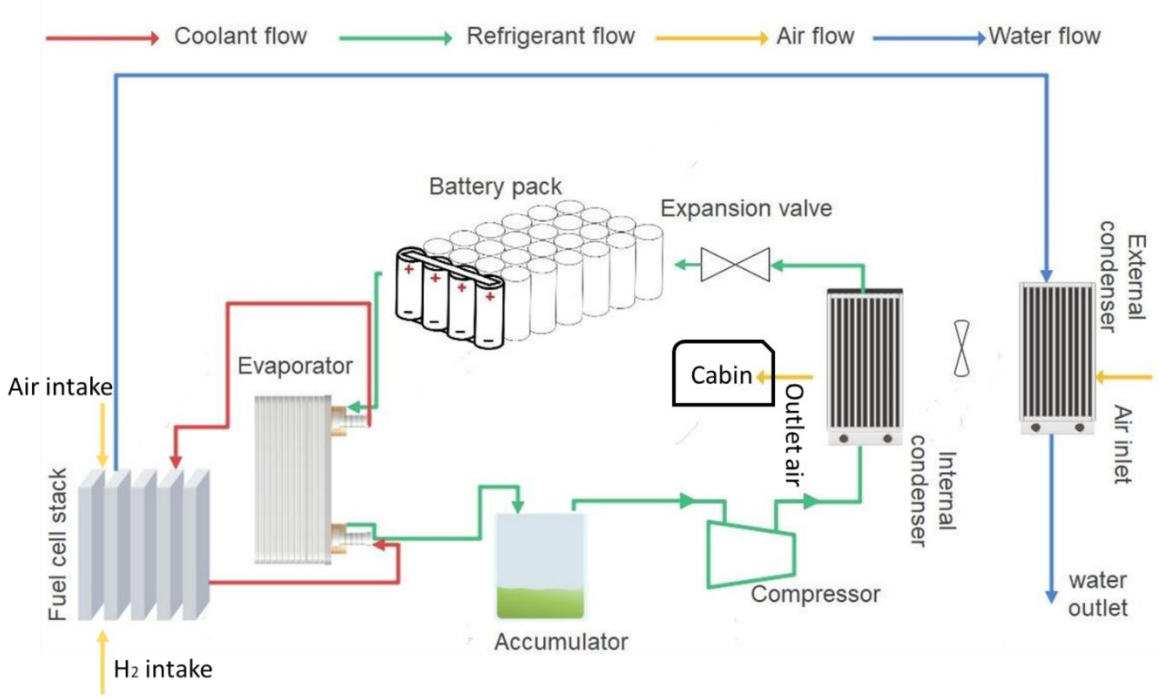

Figure 3.1. Schematic diagram of the heat pump assisted thermal management system for fuel cell backup battery-powered electrical vehicles

The electricity flow operating in the proposed FCBEV with a heat pump is shown in **Figure 3.2**. A fuel cell stack of required capacity is installed in the areas where pure BEV battery packs have been installed, which generates current during the proton exchange procedure

between H_2 and air cross proton-exchange membranes. The fuel cell output current is passed through a DC/DC converter to amplify its voltage to the battery pack level. The Li-ion battery pack still works as the main engine that supplies power to the motor, compressor and other electrical components that are not included in **Figure 3.2**. such as pumps and fans through a DC/AC inverter. However, unlike the common BEVs, the battery pack can be simultaneously recharged on-board by the current generated by the fuel cell in the proposed FCBEV.

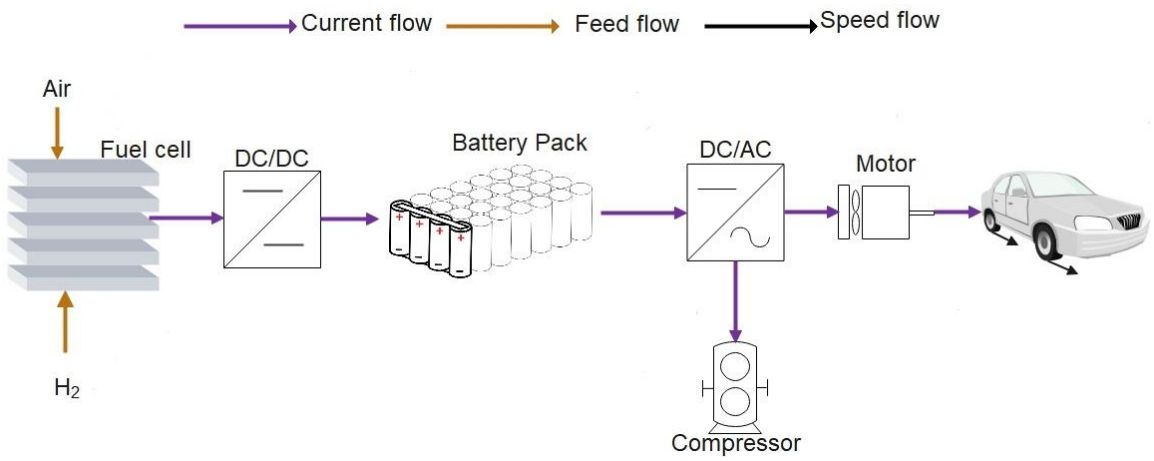

Figure 3.2. Schematic diagram of fuel cell backup battery-powered electrical vehicles

3.3 Model Development

3.3.1 PEMFC heat generation model

The heat generated by the fuel cell is a by-product produced while it is generating power, hence the heat generation model of a Proton-exchange membrane fuel cell (PEMFC) can be introduced by using electro-chemical and thermodynamic theories. The amount of heat generated from a single fuel cell is defined by current and voltage as Eq. (3.1):

$$Q_{FC} = (V_{nernst} - V_{cell}) \times I_{FC} \quad (3.1)$$

where V_{nernst} is the Nernst open-circuit voltage, V_{cell} is the voltage of the single-cell and I_{FC} is the current generated by the single fuel cell. The equation of Nernst open circuit voltage is expressed as Eq. (3.2), where$P_{H_2}$is hydrogen partial pressure, P_{O_2} is oxygen partial pressure and T_{FC} is the temperature of the fuel cell [158].

$$V_{nernst} = 1.228 - [0.85 \times 10^{-3} \times (T_{FC} - 298.15) - 4.3086 \times 10^{-5} \times T_{FC} \times ln(P_{H_2} \times {P_{O_2}}^{0.5})] \quad (3.2)$$

The voltage of a single fuel cell V_{cell} can be presented as shown by Eq. (3.3).

$$V_{cell} = V_{nernst} + V_{act} + V_{ohm} + V_{con} \quad (3.3)$$

where V_{act} , V_{ohm} and V_{con} are activation losses, ohmic losses and concentration, respectively. The term V_{act} is presented as a function of oxygen concentration at the catalyst interface C_{O_2}, I_{FC} and T_{FC} as given by Eq. (3.4), Mann *et al*. [159].

$$V_{act} = \alpha_1 + \alpha_2 \times T_{FC} + \alpha_3 \times T_{FC} \times ln(C_{O_2}) + \alpha_4 \times T_{FC} \times ln(I_{FC}) \quad (3.4)$$

The value of C_{O_2} can be obtained from an expression of Henry's law [160].

Table 3.1 Value of empirical parametric coefficient of activation losses [159]

Parameter	Value	Unit
α_1	-0.944	V
α_2	3.54 X 10^{-3}	V/K
α_3	80 X 10^{-5}	V/K
α_4	-1.96 X 10^{-4}	V/K

The V_{ohm} is defined as shown by Eq. (3.5).

$$V_{ohm} = -I \times (R_{ions} + R_{ele}) \quad (3.5)$$

where R_{ele} is the electronic resistivity which can be ignored [161] while R_{ions} as the ionic resistance is a function of membrane specific resistivity R_m, membrane thickness l_{FC} and membrane surface area A_{FC}, as given by Eq. (3.6) [162].

$$R_{ions} = \frac{R_m \times l_{FC}}{A_{FC}} \quad (3.6)$$

In which:

$$R_m = \frac{181.6 \times [1 + 0.03 \times \left(\frac{I_{FC}}{A_{FC}}\right) + 0.062 \times (\frac{T_{FC}}{303})^2 \times \left(\frac{I_{FC}}{A_{FC}}\right)^{2.5}}{[\gamma - 0.634 - 3 \times \left(\frac{I_{FC}}{A_{FC}}\right)] \times e^{[4.18 \times \left(\frac{T_{FC} - 303}{T_{FC}}\right)]}} \quad (3.7)$$

The value of γ is determined by the wetting level of the membrane, and is 0, 14, and 23 for dry, saturated and oversaturated membranes [162]. The final term on the right-hand side of Eq. (3.3) V_{con} is calculated as given by Eq. (3.8) [163].

$$V_{con} = \frac{3 \times R \times T_{FC}}{4 \times F} \times ln(1 - \frac{i_{FC}}{i_{FC\_max}}) \quad (3.8)$$

where R is the universal gas constant and F is Faraday's constant, i_{FC} is the current density of the fuel cell and i_{FC_max} is the maximum current density which is assumed to be equal to 2.2 A/cm^2 [164].

$$i_{FC} = \frac{I_{FC}}{A_{FC}} \quad (3.9)$$

The consumption of hydrogen and water generation during fuel cell stack reaction are given in Eq. (3.10) and Eq. (3.11) [127].

$$\dot{m}_{H_2} = \frac{I_{FC} \times M_{H_2} \times N_{FC}}{2 \times F} \quad (3.10)$$

$$\dot{m}_{H_2O} = \dot{m}_{H_2} \times \frac{M_{H_2O}}{M_{H_2}} \quad (3.11)$$

where M_{H_2} and M_{H_2O} are the molecular weight of H_2 and H_2O. Air and H_2 utilization in this model are assumed to be 100%. The operational and geometrical details of the fuel cell are provided in **Table 3.2**. The model of the fuel cell heat generation is verified with the experimental results of Liso *et al*. [164] and exhibits a deviation of 5%, as shown in **Figure 3.3**.

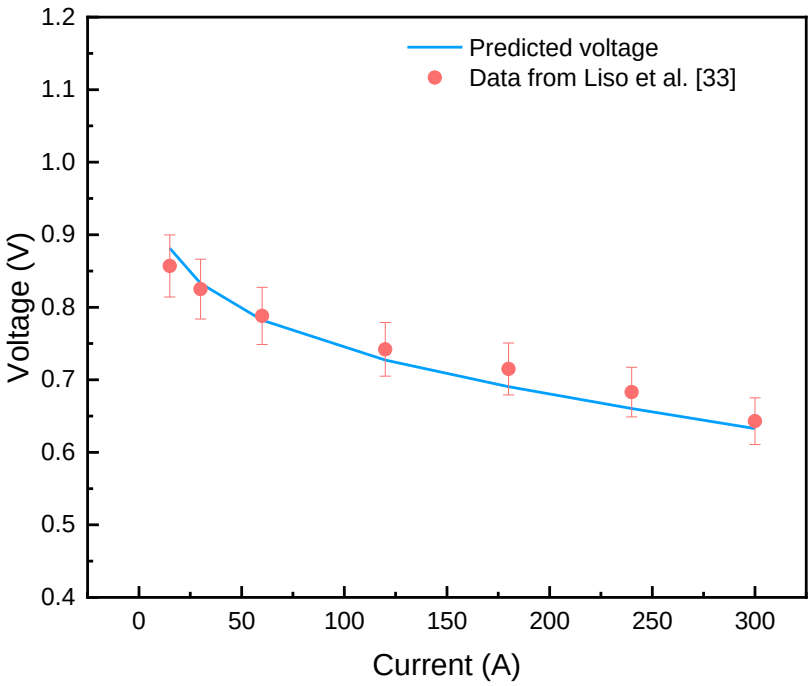

Figure 3.3. Validation of fuel cell heat generation model

3.3.2 Battery thermal model

The heat generation of a battery cell can be divided into two parts, which are irreversible heat Q_{irr} and reversible heat Q_{rev} [165]:

$$Q_{battery} = \underbrace{I_{ch/dch}^2 \times R_{ch/dch}}_{irr} - \underbrace{I_{\frac{ch}{dch}} \times T_{bat} \times \frac{dE_{OC_{bat}}}{dT_{bat}}}_{rev} \quad (3.12)$$

Where $R_{ch/dch}$ is the internal thermal resistance of a single battery while charging or discharging. $\frac{dE_{OC_{bat}}}{dT_{bat}}$, is called the entropy coefficient. The experimental data of both of these two parameters under different State of Charge (SOC), temperature, and the specifications for battery are obtained from ref. [166]. The battery pack was designed based on the Tesla Model S released in 2013 with a 60-kWh pack. The details are presented in **Table 3.2** [167].

Table 3.2 Parameters for fuel cell model and battery [167]

Specification	Value	Unit
Fuel cell		
Fuel cell Operating temperature T_{FC}	65	℃
Inlet O_2 pressure P_{O_2}	2.5	atm
Inlet H_2 pressure P_{H_2}	2.4	atm

Current output I_{FC}	190-230	A
Number of cells N_{FC}	40	/
Area of cell A_{FC}	285.8	cm^2
Thickness of cell l_{FC}	$5.1X10^{-3}$	cm
Battery discharging rate	1.6-2.2	C
Battery		
Battery capacity	8	Ah
Battery voltage	4.2	V
Number of batteries	1764	/
Number of batteries in series for one module	6	/
Number of batteries in parallel for one module	21	/
Number of modules	14	/
SOC	0.5	/
Battery operating temperature	30	℃
Voltage of battery pack	352	V
Battery pack capacity	60	kWh

The thermal model of the battery is validated by examining the heat generation while discharging and the internal resistance is calculated while charging and is compared with Liu *et al*. [166], as shown in **Figure 3.4** (a) and (b) respectively. The predicted heat generation deviates by ±10% (maximum) compared to Liu *et al*. [166] and predicted internal resistance is well within the error band of ±5%.

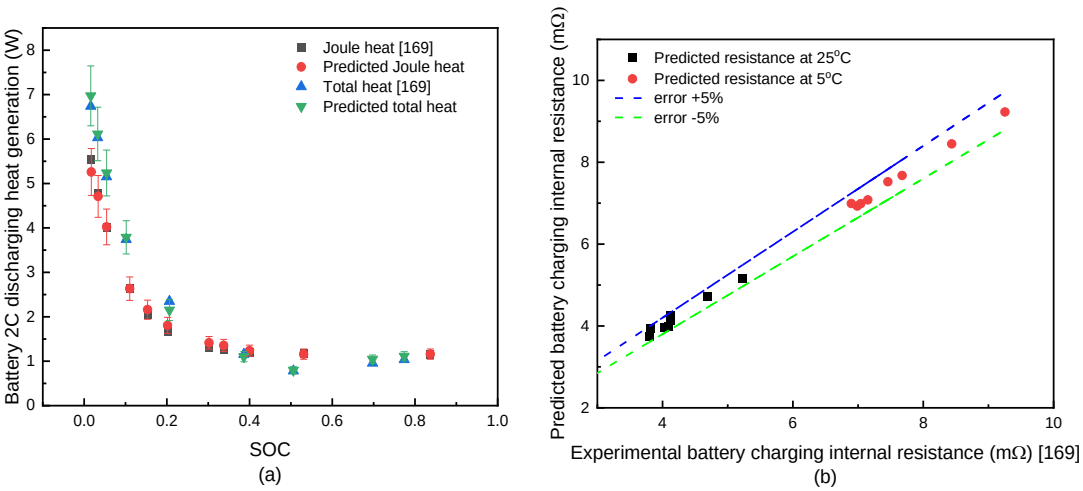

Figure 3.4. Validation results of the battery thermal model under discharging (a) and charging (b) scenarios

3.3.3 Heat transfer model of heat exchanger

The evaporator adopts a counter-flow plate heat exchanger. The refrigerant flows from one side while the coolant flows from the other side. Whereas internal air-cooled fin and tube type of heat exchanger is considered as a condenser and external ones for waste heat recovering from H_2O is seen as the evaporator. The geometrical information of three heat exchangers considered in the proposed FCBEV are presented in **Table 3.3**.

Table 3.3 The specification of heat pump components

components	Specification	Value	Unit
Fuel cell evaporator	type	Plate heat exchanger	/
	Number of plates	110	/
	Plate size	120 X 330	mm^2
	Channel space	2.9	mm
Internal condenser	type	Fin-Tube	/
	inner diameter	7	mm
	Internal area	2.086	m^2
	External area	8.344	m^2
Air preheat condenser	type	Fin-Tube	/
	Inner diameter	8.2	mm
	Internal area	0.2865	m^2
	External area	0.3725	m^2
Inverter Compressor	type	Scroll	/
	Displacement	27	cc/rev
	Compressor speed	3000-5000	rpm

The same amount of heat absorbed or released by the primary refrigerant in the heat exchangers is exchanged with the secondary fluid, as the heat loss between the heat exchanger and the atmosphere is negligible. Hence, the heat balance across heat exchangers is expressed as shown in Eq. (3.13) to (3.15).

$$Q_{eva/cond/OHX} = \dot{m}_{cl/air/H_2O} \times Cp_{cl/air/H_2O} \times \Delta T_{cl/air/H_2O} \quad (3.13)$$

$$Q_{ref} = \dot{m}_{ref} \times (1 - X_{inlet}) \times i_{fg} \quad (3.14)$$

$$Q_{eva/cond/OHX} = U_{eva/cond/OHX} \times A_{eva/cond/OHX} \times LMTD_{eva/cond/OHX} \quad (3.15)$$

where the logarithmic mean temperature difference (LMTD) is described as:

$$LMTD = \frac{\Delta T_1 - \Delta T_2}{ln(\Delta T_1 / \Delta T_2)} \quad (3.16)$$

with

$$\Delta T_1 = T_{h,inlet} - \Delta T_{c,outlet} \quad (3.16a)$$

$$\Delta T_2 = T_{h,outlet} - \Delta T_{c,inlet} \quad (3.16b)$$

It should be noted that for cross-flow a correction factor should be imposed to Eq. (3.16) and the value of the correction factor can be obtained from Ref. [168]. The overall heat transfer coefficient for a plate heat exchanger, i.e., evaporator, can be calculated as below:

$$\frac{1}{U_{eva}} = \frac{1}{h_{cl}} + \frac{1}{h_{eva_{ref}}} + \frac{\delta_{wall}}{\lambda_{wall}} \quad (3.17)$$

where δ_{wall} and λ_{wall} are thickness and thermal conductivity of the plate, respectively. The two-phase heat transfer coefficient correlation for the refrigerant side is expressed as [169]:

$$h_{eva\_ref} = 1.055 \times [1.056 \times Co^{-0.4} + 1.02 \times Bo^{0.9}] \times X_m \times h_{lo} \quad (3.18)$$

where Co is the convective number and Bo is the boiling number, defined as

$$Co = (\frac{\rho_v}{\rho_l})^{0.5} \times ((1 - X_m)/X_m)^{0.8} \quad (3.19)$$

$$Bo = \frac{q''_{wall}}{G_{ref\_eva} \times i_{fg}} \quad (3.20)$$

in which ρ_v and ρ_l are the density of vapour and liquid refrigerant, X_m is the mean vapour quality in the evaporator. q''_{wall} is the heat flux through the wall, G_{ref_eva} is the mass flux of refrigerant in a plate-type evaporator while i_{fg} is the enthalpy of vaporization. Single-phase heat transfer coefficient correlation h_{lo} was modified by [169] based on [170]:

$$h_{lo} = 0.2875 \times Re^{0.78} \times Pr^{1/3} \times \frac{k_l}{D_h} \quad (3.21)$$

where D_h is hydraulic diameter, k_l is the conductivity of liquid refrigerant, Re is the Reynolds number and Pr is the Prandtl number. For the coolant side, the single-phase heat transfer coefficient was conducted as [170]:

$$h_{cl} = 0.2121 \times Re_{cl}^{0.78} \times Pr^{1/3} \times (\frac{\mu_m}{\mu_{wall}})^{0.14} \times \left(\frac{k_{cl}}{D_{h_{eva}}}\right) \quad (3.22)$$

in which μ_m and μ_{wall} are calculated based on the average bulk fluid and wall temperature in the evaporator. For fin and tube heat exchanger i.e., condenser, the overall heat transfer coefficient is shown as:

$$\frac{1}{U_{cond}A_{cond}} = \frac{1}{\eta_0 \times h_{air\_cond} \times A_c} + R_{wall} + \frac{1}{\eta_0 \times h_{ref\_cond} \times A_h} \quad (3.23)$$

where A_c and A_h are the surface areas of the cold side and hot side respectively and η_0 is the overall surface efficiency which equals to:

$$\eta_0 = 1 - \frac{A_f}{A_{tot}} \times (1 - \eta_f) \quad (3.24)$$

in which A_f and A_{tot} stand for total fin area and total area respectively and η_f is the efficiency of a single fin which can be located in [168]. Two different heat transfer principles for the refrigerant side are calculated below [171]. For wavy flow:

$$Nu_{wavy} = \frac{0.23 \times Re_{v\_ref}^{0.12}}{1 + 1.11 \times X_{tt}^{0.58}} \times [\frac{Ga \times Pr_l}{Ja_l}]^{0.25} + cos^{-1}(2 \times \varphi - 1)/\pi \times Nu_{forced} \quad (3.25)$$

$$Nu_{forced} = 0.0195 \times Re_l^{0.8} \times Pr_l^{0.4} \times \sqrt{1.376 + c_1/X_{tt}^{c_2}} \quad (3.26)$$

When $0 < Fr_l \leq 0.7$, Eq. (3.27a) and (3.27b) apply:

$$c_1 = 4.172 + 5.48 \times Fr_l - 1.564 \times Fr_l^2 \quad (3.27a)$$

$$c_2 = 1.773 - 0.169 \times Fr_l \quad (3.27b)$$

When $Fr_l > 0.7$ Eq. (3.28a), (3.28b) apply:

$$c_1 = 7.242 \quad (3.28a)$$

$$c_2 = 1.655 \quad (3.28b)$$

while for annular flow:

$$Nu_{annular} = 0.023 \times Re_l^{0.8} \times Pr_l^{0.4} \times \left[1 + \frac{2.22}{X_{tt}^{0.89}}\right] \quad (3.29)$$

In eq. (3.22) to (3.29), X_{tt} is the turbulent-turbulent Lockhart Martinelli parameter, Ga is the Galileo number, Fr_l is the Froude number, Ja_l is the liquid Jakob number, φ is the void fraction. Expressions of those parameters are shown below:

$$X_{tt} = (\frac{\rho_v}{\rho_l})^{0.5} \times (\frac{\mu_l}{\mu_v})^{0.1} \times (\frac{1 - X_m}{X_m})^{0.9} \quad (3.30)$$

where μ is dynamic viscosity.

$$Ga = g \times \rho_l \times (\rho_l - \rho_v) \times \frac{D_h^3}{\mu_l^2} \quad (3.31)$$

$$Fr_l = \frac{G_{ref\_cond}^2}{\rho_l^2 \times g \times D_h} \quad (3.32)$$

$$Ja_l = C_{p\_ref\_l} \times (T_{cond} - T_{wall})/i_{fg} \quad (3.33)$$

in which $C_{p\_ref\_l}$ is the specific heat at constant pressure for liquid refrigerant, T_{cond} and T_{wall} is the condensing temperature and wall temperature respectively. The void fraction was described as [172]:

$$\varphi = [1 + \frac{1 - X_m}{X_m} \times \left(\frac{\rho_v}{\rho_l}\right)^{\frac{2}{3}}]^{-1} \quad (3.34)$$

Heat transfer coefficients on the refrigerant side of the condenser can be calculated from Nu :

$$Nu_{wavy/annular} = \frac{h_{cond\_ref} \times D_h}{k_{l\_ref}} \quad (3.35)$$

For the air side, a simple heat transfer model was adopted as introduced in Ref [168]:

$$h_{air\_cond} = C \times Re_{air}^m \times Pr^{1/3} \quad (3.36)$$

where the constants C and m are listed in **Table 3.4**.

Table 3.4 Constant of C and m in Eq.(3.36) for cross flow

Re_{air}	C	m
0.4-4	0.989	0.330
4-40	0.911	0.385
40-4000	0.683	0.466
4000-40000	0.193	0.618
40000-400000	0.027	0.805

The verification of the evaporator and condenser are illustrated in **Figure 3.5** (a) and (b) according to the experimental outcomes achieved by Ref. [170] and Ref. [171], respectively. For both heat exchangers, all predicted values fall with an error band of ±10%.

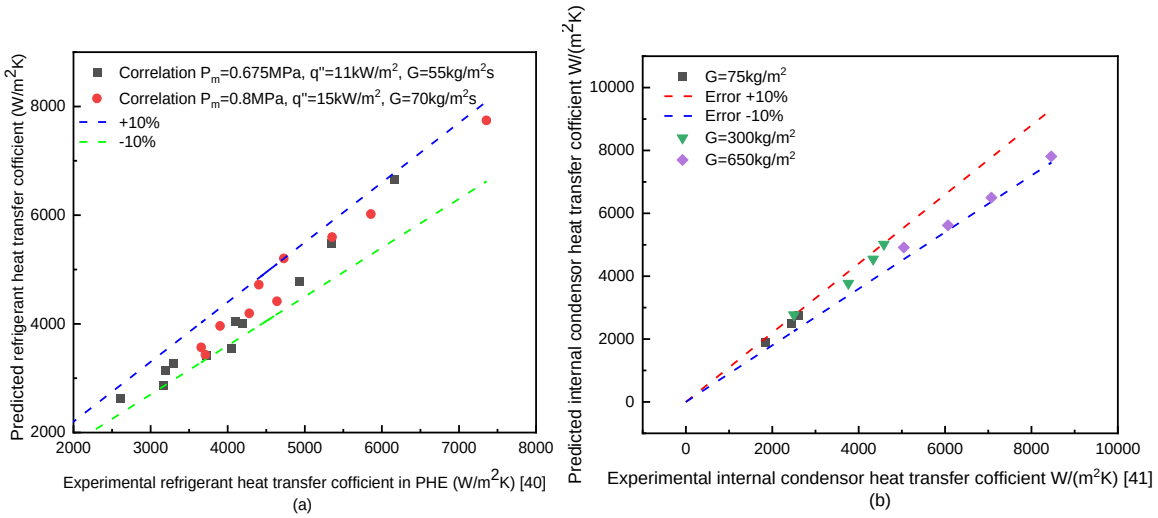

Figure 3.5. Validation results of the heat exchanger heat transfer coefficient model

3.3.4 Compressor model and electronic expansion valve (EEV)

The compressor with variable speed is adopted in the current analysis and the quadratic relation between pressure ratio γ and refrigerant mass flow rate is developed using data from ref. [173]. The correlation is shown in Eq. (3.37). The results were validated by Ref. [109] as shown in Fig. 6. and the specification of the compressor is shown in **Table 3.3**.

$$\gamma = -1566 \times \dot{m}_{ref}^2 + 218.83 \times \dot{m}_{ref} - 3.4801 \quad (3.37)$$

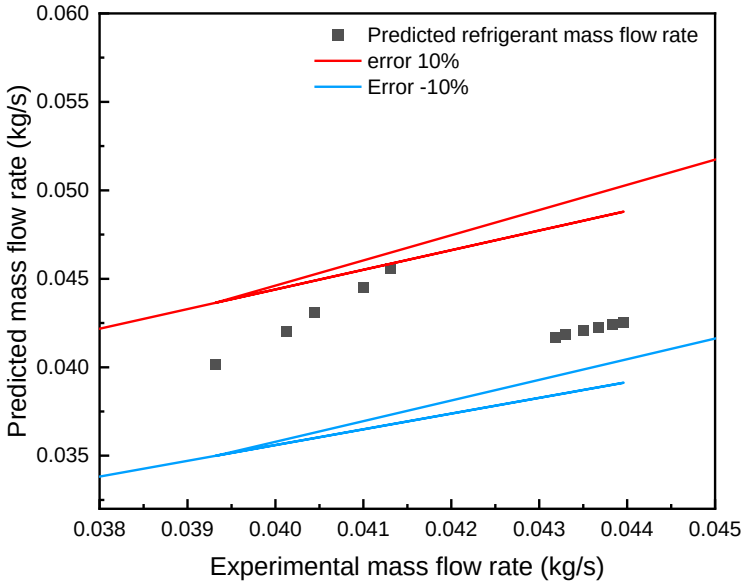

Figure 3.6. Validation results of the simplified compressor model [109]

The mass flow rate through the EEV is calculated from Ref. [155].

$$\dot{m}_{EEV} = C_v A_c \sqrt{2 \times \Delta P_{EEV} \times \rho_{ref\_in}} \quad (3.38)$$

where C_v is the flow coefficient, $C_v = 0.02005 \times \sqrt{\rho_{in}} + 0.634/\rho_{out}$; A_c is the circulation area.

3.3.5 Simulation procedure

Each model described above is coupled to form the proposed thermal management system based on the following assumption.

(1) Coolant temperature at the outlet of the fuel cell stack was fixed i.e. 30℃.

(2) The pressure drops across heat exchangers and inside pipe and heat loss between the heat exchanger and surrounding are neglected.

(3) Fuel cell stack's heat loss was ignored, but the heat loss of the battery pack was calculated under a constant airspeed of 0.5m/s, according to the investigated battery discharging rate.

(4) The power consumption of the fan and pump were omitted, and the inlet air flow rate would not be affected by the vehicle speed.

(5) The difference between the minimum temperature of the coolant in the evaporator and R134a evaporating temperature is assumed as constant i.e., 2 ℃.

(6) The refrigerant at the evaporator outlet is assumed as the saturated vapour and an accumulator was installed before the compressor to make sure only gas can enter the compressor.

The thermal management simulation model of the proposed FCB-EV has been organised as presented in **Figure 3.7**. The model is developed in MATLAB and the thermal properties are obtained by coupling REFPROP with MATLAB code. The simulation started from the PEMFC thermal management side in order to dissipate all the heat generated from PEMFC and to be utilised by the cabin heating system. The cooling capacity of the cold end of the heat pump will be adjusted based on the fuel cell power output and battery discharging C rate. So, with the increasing or decreasing waste heat generation, our system's capacity will also be changed to make sure the thermal equilibrium of the fuel cell stack and battery pack to avoid overcooling or temperature increase in them. Independent variables were selected based on actual application scenarios (including ambient temperature, PEMFC current output, battery discharging rate, subcooling degree and coolant inlet temperature of the evaporator) and their operating range in the simulation are listed in **Table 3.5**. Other parameters, including coolant mass flow rate, refrigerant mass flow rate, evaporating and condensing temperature etc. were intermediate dependent variables after the size of the evaporator, condenser and compressor were set. Those intermediate dependent variables would change to independent variables and the value of those intermediate dependent variables would be finalized by 6 iterative loops nested within each other. Fuel cell cold startup scenarios are not considered in this research. But there are some potential solutions to tackle it. For example, the quick and safe cold startup for fuel cell can be achieved at -15℃ by electrochemical self-heated method [174] or using heat pump and PTC heater [175] powered by battery as supplements when facing more severe conditions.

The proposed model was assumed to be converged when energy balance across heat exchangers as represented by Eq. (3.13) to (3.15) were achieved.

Table 3.5 Operating conditions in the simulation

Parameter	Value	Unit
Ambient temperature (T_{amb})	-25 to 5	℃
Coolant inlet temperature at the entrance of evaporator ($T_{cl\_eva\_inlet}$)	27 to 33	℃
Fuel cell current output (I_{FC})	190 to 230	A
Battery discharging rate ($C_{discharging}$)	0.19 to 0.26	C
Subcooling degree (T_{sub})	0 to 4	℃
Refrigerant	R134a	/
Coolant	Egl-5050	/

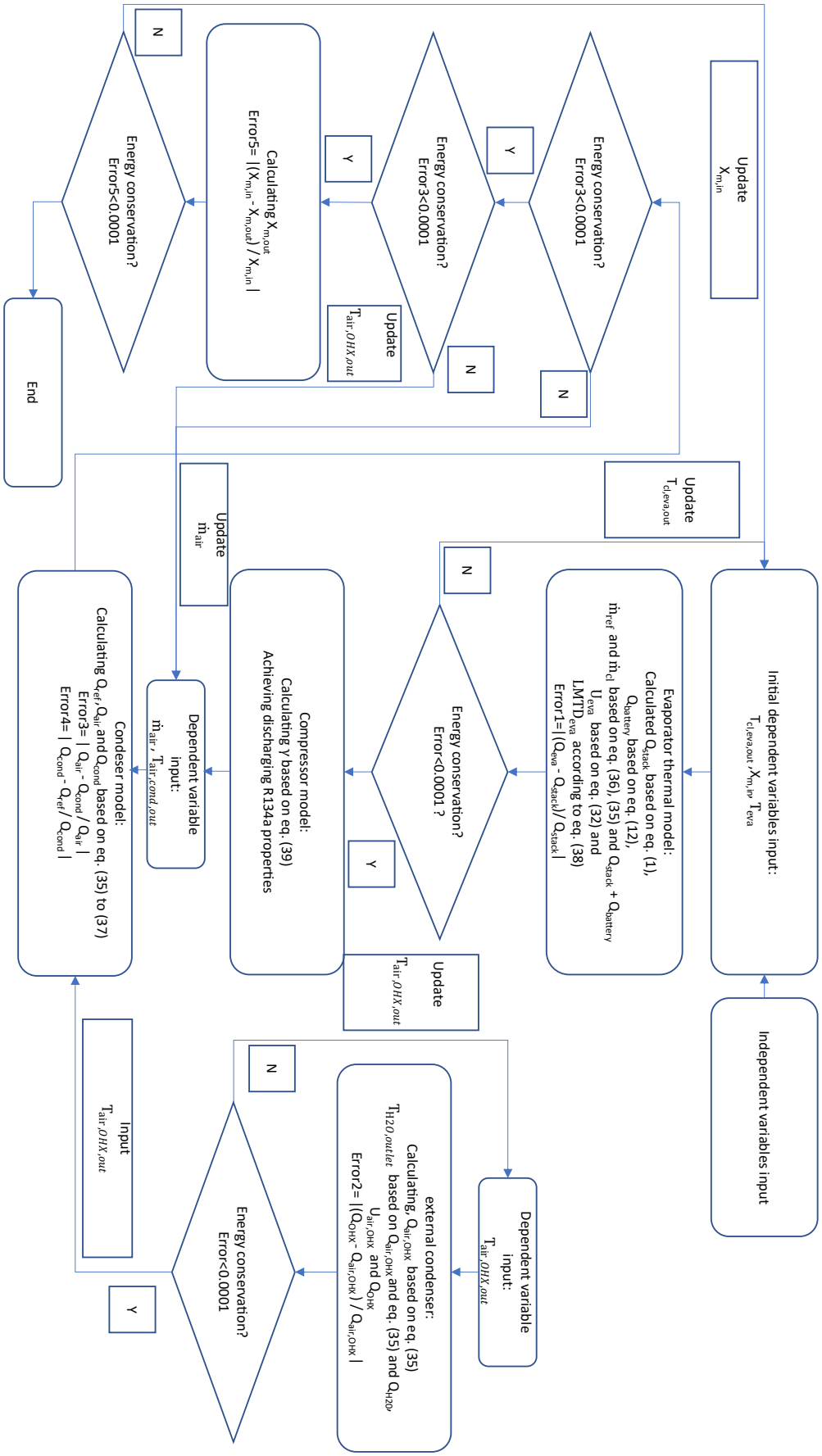

Figure 3.7. Flow chart of proposed system simulation

3.3.6 Performance indicators

COP is a critical performance for heat pump-based heating systems, as it will be affected by any of the parameters inside the system. The COP of a heat pump system is calculated as Eq. (3.39)

$$COP = \frac{Q_{heat}}{W_{tot}} \quad (3.39)$$

in which Q_{heat} is the effective heat that can be input to the target area which equals to Q_{cond} while W_{tot} is the total power consumption that equals the compressor power consumption W_{comp} in this case. The expression of W_{comp} is shown as below:

$$W_{comp} = \frac{(H_{dis} - H_{suc})}{\eta_{isen}} \quad (3.40)$$

where H_{dis} and H_{suc} are the enthalpy of R134a at suction and discharging point respectively, η_{isen} is the isentropic effectiveness of the compressor which is assumed to be 0.67 [173]. Equivalent effective battery capacity (EEBC) is a newly defined performance index which is used to evaluate how much equivalent battery capacity can be used for driving usage in one charging cycle. The expression of EBC is shown in Eq. (3.41).

$$EEBC = BC - W_{hp} + FC_{ch} \quad (3.41)$$

where BC, W_{hp} and FC_{ch} are the initial battery pack capacity, power consumption of the heat pump system, and supplemental battery capacity by fuel cell charging respectively.

3.4 Reults and Discussion

This section presents the influence of several operating variables such as ambient temperature, PEMFC current output, battery discharging rate, subcooling degree and coolant inlet temperature of evaporator and working fluid on the performance of the proposed FCBEV. The input ranges of the variables are presented in **Table 3.5**.

3.4.1 Effect of fuel cell output current

Fuel cell output current is a crucial parameter that decides the onboard battery charging speed. **Figure 3.8**(a) illustrates the impacts of the fuel cell current output on outlet air temperature and COP. It shows that the cabin air inlet temperature inversely correlated with changes in fuel cell output current while the COP increased with the increase of fuel cell output current. The reason for this change can be explained in detail using **Figure 3.8**(b) and (c). When the fuel cell current output increased, the waste heat from the fuel cell stack increased and vice versa as shown in **Figure 3.8**(b). According to assumption (5), LMTD was a single-valued function of evaporator coolant outlet temperature according to Eq. (3.16) to (3.16b). The higher the LMTD the lower the evaporator coolant outlet temperature would be. In order to dissipate all the heat generated inside the fuel cell stack and keep its temperature stable, the evaporator coolant outlet temperature decreased relatively to match the increasing fuel cell current output based on Eq. (3.15). However, because of the difference in growth rate between ΔT_{cl} in Eq. (3.13) and $LMTD_{eva}$ in Eq. (3.15), the coolant mass flow rate descended to compensate it in order to achieve energy conservation as shown in **Figure 3.8**(c). Although the evaporating temperature decreased in terms of the evaporator coolant outlet temperature, **Figure 3.8**(c) demonstrates the refrigerant mass flow rate changed significantly from 0.048kg/s to 0.039kg/s for the given range of fuel cell output current. However, it was not sufficient for the increased cooling demands of FC stack. As a result, the vapour quality before the evaporator decreased by over 50% to increase the latent heat that was needed during evaporation as shown in **Figure 3.8**(b). The average vapour quality in the evaporator dominates over refrigerant flow rate during the evaporating procedure, resulting in a reduction in vapour quality [170]. Since more heat would be released through the internal condenser, increasing the air mass flow rate was the only way to raise the condenser's overall heat transfer coefficient when the inlet air temperature could not be significantly changed. Hence, the air temperature decreased for the sake of increasing

air mass flow rate. Furthermore, with the decrease in the mass flow rate of refrigerant, the compressing ratio should decrease correspondingly and cause an increase in COP. Meanwhile, it should be noted that when the fuel cell output current exceeded a specific value, 217 A in **Figure 3.8**(a), the outlet air temperature would be lower than the coolant temperature out of the fuel cell stack. This means if the fuel cell output current exceeded a specific point, the outlet air temperature of the proposed system may not provide a higher outlet air temperature than using coolant heating the cabin directly. Therefore, fuel cell current has an important impact on heating capacity, outlet air temperature and COP. In order to provide not only enough heating capacity, but also to supply air at a high temperature, the fuel cell current output must be well controlled when other parameters stay constant.

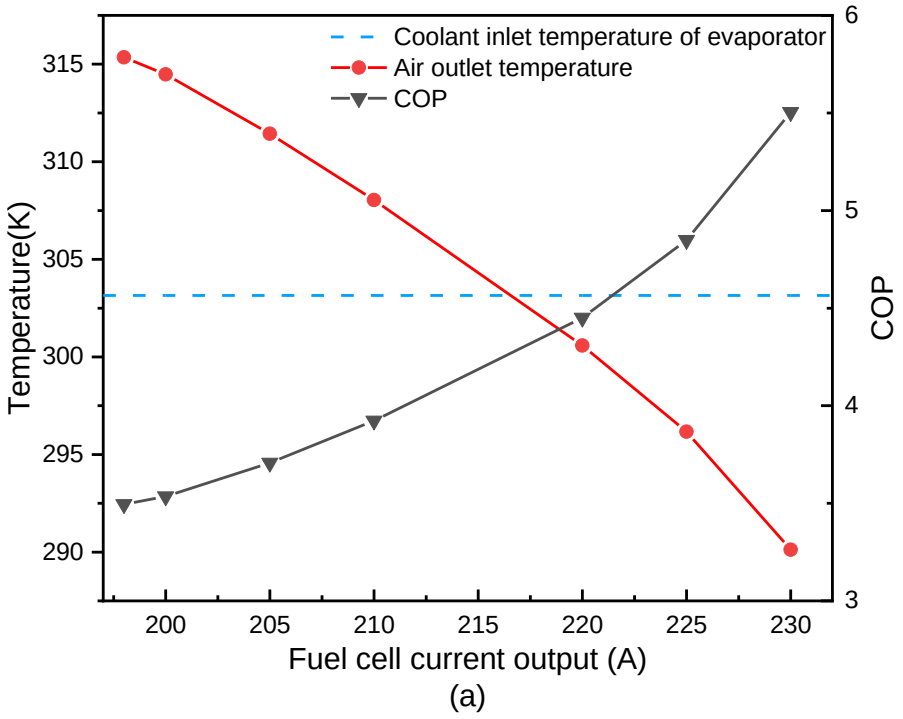

(a)

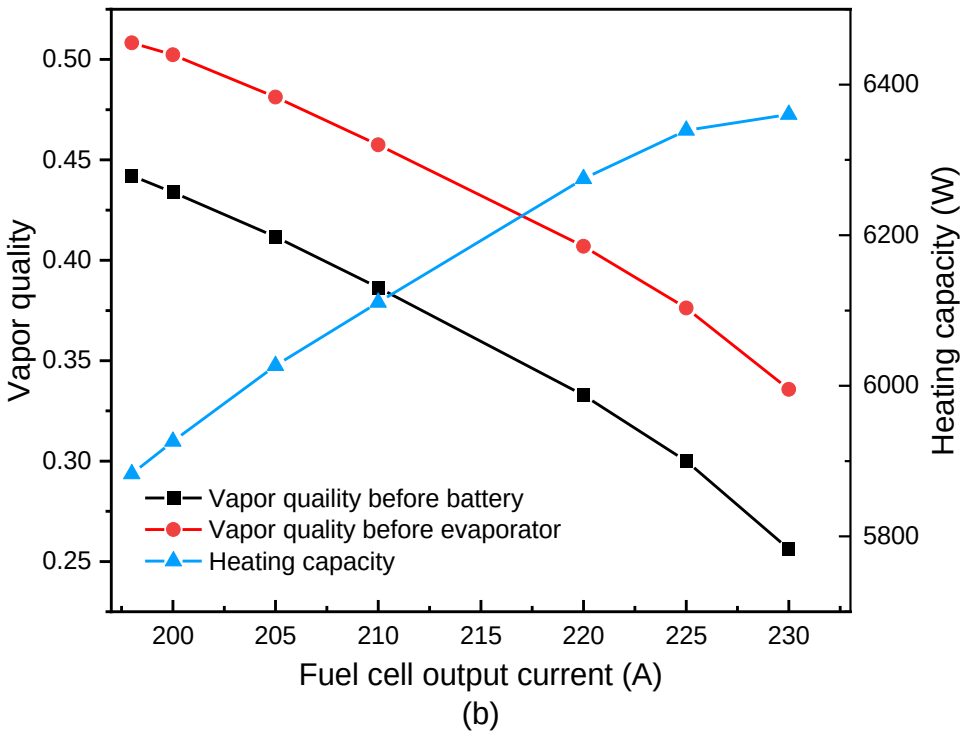

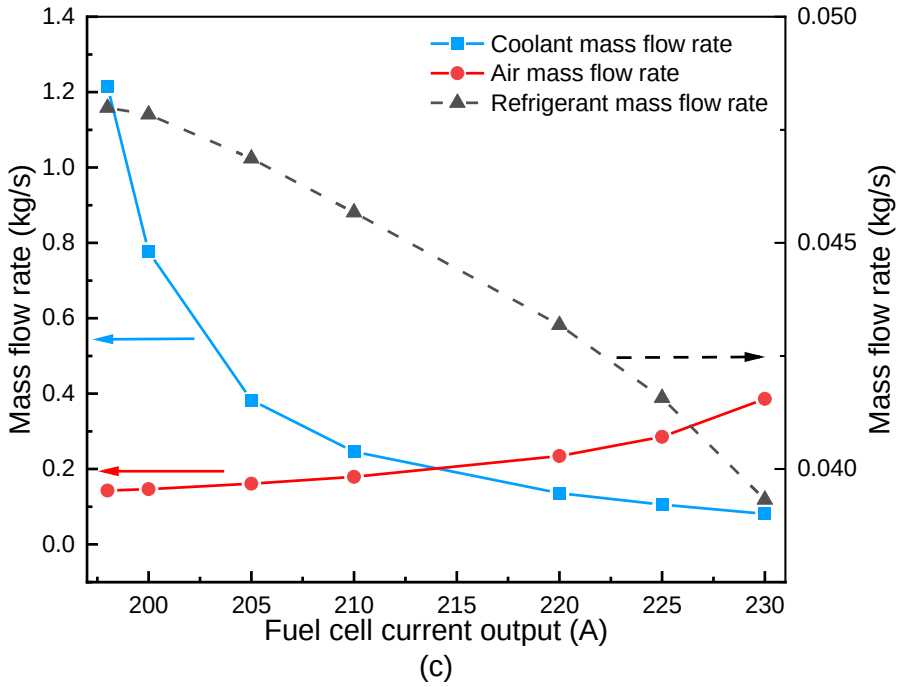

Figure 3.8. (a) Variation of air temperature and COP (b) variation of vapour quality and heating capacity (c) variation of coolant, air, and refrigerant mass flow rate with respect to fuel cell output current (T_{amb}=0°C, $T_{cl\_eva\_inlet}$=30°C, C_{dch}=0.237, T_{sub}=0°C)

3.4.2 The impact of battery discharging rate and subcooling degree

Figure 3.9 presents the impact of battery discharging rate on outlet air temperature, outlet vapour quality and COP while other independent parameters were kept constant. As shown

in **Figure 3.9**(a), the vapour quality for the battery and evaporator both decreased with the increase in battery discharging rate because of the rise of the battery's cooling demand. Notably, the vapour quality difference between battery inlet and evaporator inlet increased. The main reason for this was the proportion of heat generated by the battery increased. With the increasing waste heat from the battery, more liquid refrigerant should transfer into vapour status. Similar to the fuel cell current output, battery discharging C rate also had a negative impact on outlet air temperature due to the increased air flow rate. **Figure 3.9**(b) illustrates an opposite relationship between heating capacity and battery discharging C rate compared to heating capacity and fuel cell current output. With the battery discharging rate varying from 0.195 to 0.26, the system's heating capacity slightly decreased from 6.37kW to 6.14kW. One of the main reasons is a reduction in work undertaken by the compressor. Although the system can absorb more waste heat from the battery pack, the decreasing refrigerant mass flow rate due to the descending inlet vapour quality led to a lower compression work and the decrease is greater than the increase in waste from the battery pack. In contrast, as shown in **Figure 3.9**(b), the COP increased with the increase of the battery discharging rate. The large increase in COP was mainly caused by the limitation of the subcooling degree. From **Figure 3.10**, it can be seen that when there was no limitation of the subcooling degree, the cycle could run as shown in the yellow. With a small decrease in the subcooling degree, the system achieved the target with little change. However, when the subcooling degree was set as unchangeable at 0 ℃, both the compressing ratio and evaporating temperature declined and led to a significant increase in COP. Hence, when the vehicle is accelerating, it would be better to increase the fuel cell output within the allowable operating range in order to compensate for the negative impact on heating capacity caused by the increasing battery discharging rate.

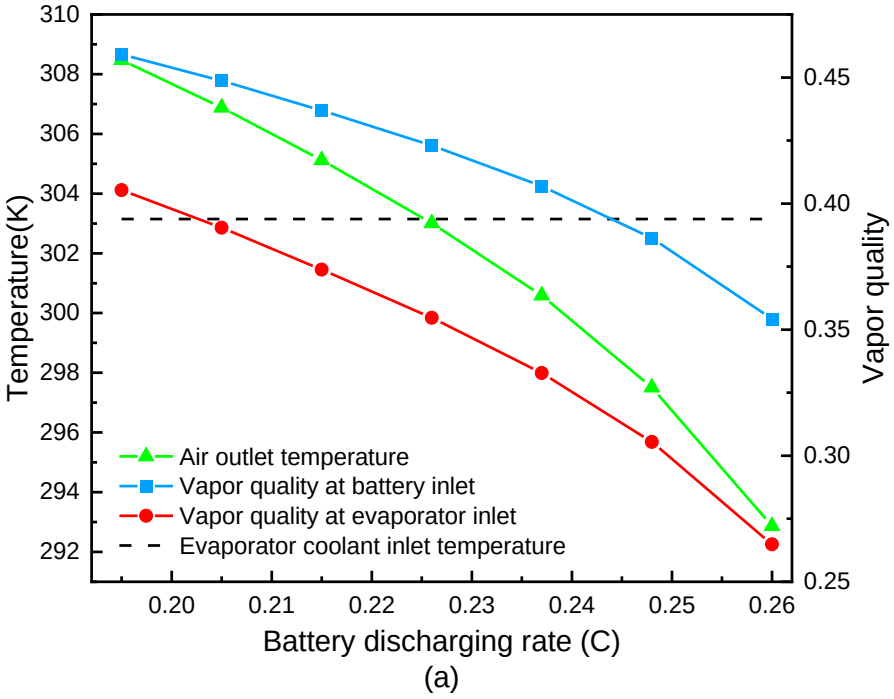

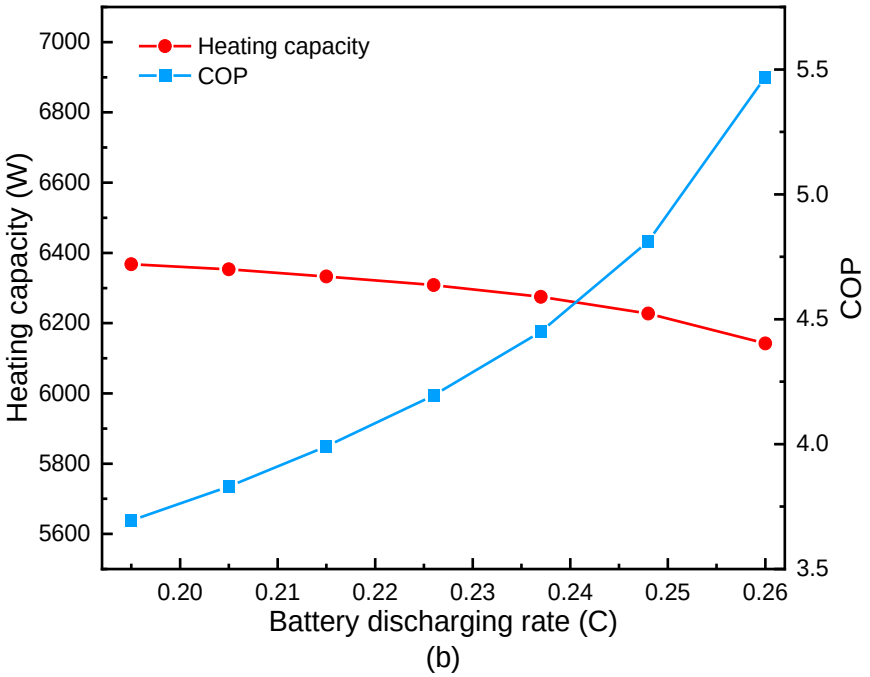

Figure 3.9. The impact of battery discharging rate on (a) air outlet temperature and vapor quality and (b) heating capacity and COP (T_{amb}=0°C, $T_{cl\_eva\_inlet}$=30°C, I_{FC}=220A, T_{sub}=0°C)

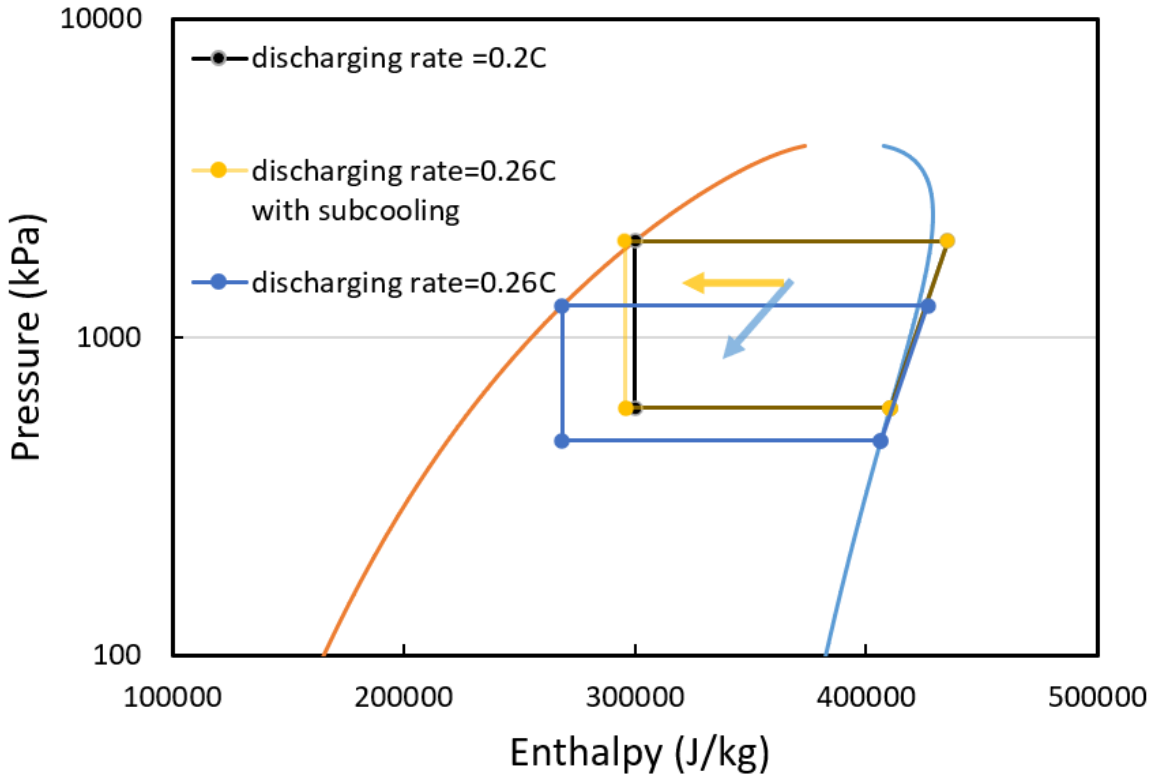

Figure 3.10. Pressure to enthalpy cycle diagram under different battery discharging rate (T_{amb}=0°C, $T_{cl\_eva\_inlet}$=30°C, I_{FC}=220A, T_{sub}=0°C)

Figure 3.11 describes the influence of the condenser subcooling degree when other independent variables are kept constant. It can be seen in **Figure 3.11**(a), the outlet air temperature increased with an increase in the subcooling degree, but the trend of COP was the opposite. When the subcooling degree increased from 0K to 4K the condensing temperature increased by 10.3% correspondingly in order to increase the vapour quality after the adiabatic process of the throttle valve. For the sake of satisfying the cooling demand of the fuel cell and battery pack, the refrigerant mass flow rate increased as well due to the increase in vapour quality. Because of the constant current output from the fuel and ambient temperature, the inlet air temperature of the condenser did not change to some certain value, which meant the last term $LMTD_{cond}$ in Eq. (3.14) on the right-hand side increased as the condensing temperature was the only variable in this equation. In addition, because of the rising refrigerant mass flow rate, the heat transfer coefficient on the refrigerant side also increased. Reducing the air mass flow rate was the only way to control the U_{cond} in Eq. (3.14) to maintain the condenser's conservation of energy. Furthermore, the total amount of heat transferred through the condenser increased as a result of the introduced subcooling. Hence, the air temperature was raised as the degree of subcooling increases according to Eq. (3.13). However, although a certain degree of subcooling could slightly increase the heat release,

the power consumption of the compressor due to the increase of refrigerant mass flow rate was much higher than that part of heat. The increase of compressing power dominated the change in COP and caused a 43% decrease in COP. The application of subcooling could be decided depending on the operating scenario. For example, if the passenger gets into the vehicle, body heating, such as hands and feet is more likely to have the priority. In this case, adjusting the subcooling degree can help passengers feel comfortable quickly. Moreover, **Figure 3.11**(b) displays the operating range when varying the subcooling degree. When the subcooling degree varied from 0 to 2, the operating range raised from 190A-220A to 200A-237A. This is because when the fuel cell current output increases, the evaporation temperature of the proposed system decreases to achieve a larger temperature difference inside the evaporator, but a certain degree of subcooling can reduce the refrigerant temperature at the condenser outlet to reduce an evaporation decrease in temperature. It can be concluded that the higher the fuel cell and battery pack cooling demands, the higher the subcooling degree needed. Additionally, a higher subcooling degree can also offer increased flexibility to the system.

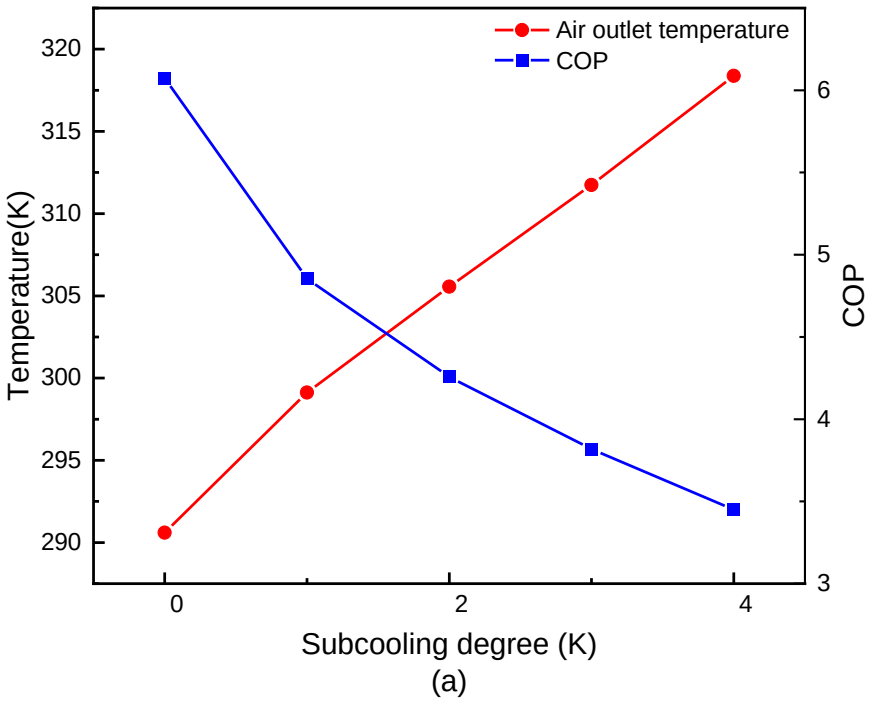

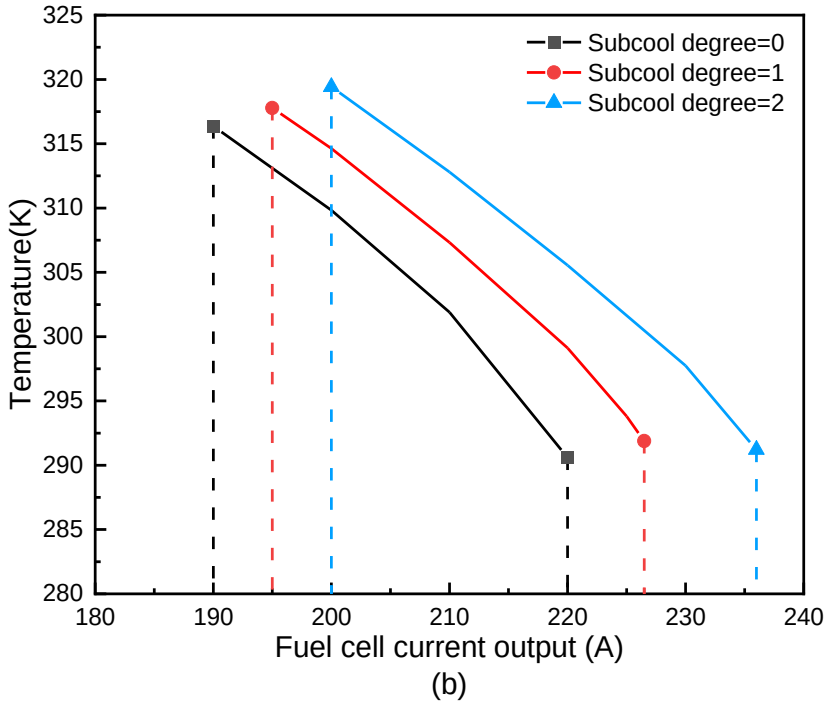

Figure 3.11. The impacts of the subcooling degree on outlet air temperature and COP (a) and operating range (b) (T_{amb}=0℃, $T_{cl\_eva\_inlet}$=32℃, I_{FC}=220A for (a), C_{dch}=0.237)

3.4.3 Effect of ambient temperature and coolant inlet temperature

Ambient air temperature used to be a very crucial parameter for BEV's air-source heat pumps. Qin *et al*. [176] experimentally investigated the performance of an air source R134a heat pump for EV at -20℃. As shown in **Figure 3.12**, the heating capacity and the COP of Qin's vapour injection heat pump system varied by 31% and 52% respectively with respect to the change in ambient temperature. However, the proposed heat pump system in this study showed a stable advantage compared to the traditional air source heat pump in BEV discussed in ref [176]. When the ambient temperature decreased, the heating capacity did not change significantly because the heat source in our study was the waste heat generated from the fuel cell stack and battery pack which was not sensitive to the ambient temperature. Meanwhile, based on assumption (3), that the fuel cell heat dissipated to the external environment was not considered, only the battery pack's heat loss was calculated. Furthermore, although the COP of the proposed system decreased with the drop in ambient temperature, the variation was only between 4.48 and 4.31 when the ambient air temperature changed from 5℃ to -25℃. The reason for the slight difference in COP was that the lower ambient temperature led to a higher $LMTD_{cond}$. So according to Eq. (3.13) and Eq. (3.15), the airflow rate increased, and, correspondingly, the refrigerant mass flow rate reduced a little. Hence, the compressor power consumption also decreased. Due to the unchanged

heating capacity and increased air mass flow rate, when the ambient temperature varied in the range of 5℃ and -25℃, the outlet air temperature decreased, as illustrated in the diagram in the bottom-right corner of **Figure 3.12**. **Figure 3.12** also shows the comparison with the performance of other EV heat pump systems. Wang *et al*. [69] and Dong *et al*. [151] both studied the performance of the CO_2 EV heat pump system. Although Wang's system could provide a higher heating capacity than the proposed system in this article, it had the lowest COP among the four highlighted systems in **Figure 3.12**. Additionally, even though the proposed system used R134a as a working refrigerant, it provided both higher COP and heating capacity than Dong's CO_2 heat pump system under the same ambient temperature.

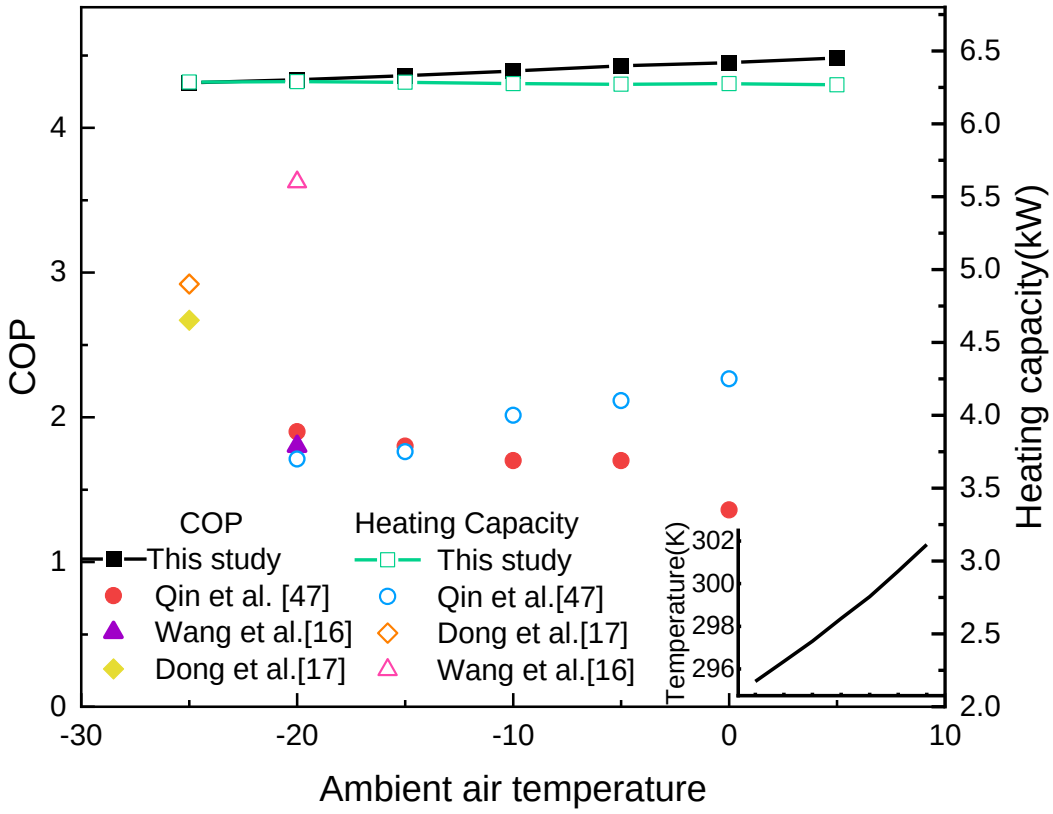

Figure 3.12. Impact of ambient air temperature on COP and outlet air temperature and comparison with previous publications

Figure 3.13 shows the variation of outlet air temperature and system COP in terms of condenser coolant inlet temperature. The results show that the COP increased with the increase of evaporator coolant inlet temperature while the outlet air temperature experienced the opposite trend. The reason could be attributed to the necessity of reducing refrigerant mass flow rate. In order to keep the heat balance between the coolant side and refrigerant side of plate heat exchanger, the model first adjusted the mass flow rate of the coolant as the evaporator coolant inlet temperature increased. The reduction of coolant mass flow rate

needed an increase of ΔT_{cl} in Eq. (3.13) as a compensation. Therefore, the coolant outlet temperature further decreased to guarantee it could abstract all the waste heat from the fuel cell stack. Based on the temperature difference assumption between the coolant outlet temperature and evaporating temperature, the evaporating temperature declined as well. Refrigerant mass flow rate, as a key parameter, directly affected the heat exchanger heat transfer coefficient on the refrigerant side. It was also reduced to ensure the conversation of energy. As a result, the COP is augmented due to the reduction of compressor power consumption under the same heat capacity. Lower refrigerant mass flow rate led to a lower compressing ratio and discharging temperature which also reduced the temperature difference between the condenser and the external environment. Therefore, the air mass flow rate increased and caused a decrease in outlet air temperature. Overall, the evaporator coolant inlet temperature should be carefully controlled because it has a significant influence on COP and outlet air temperature.

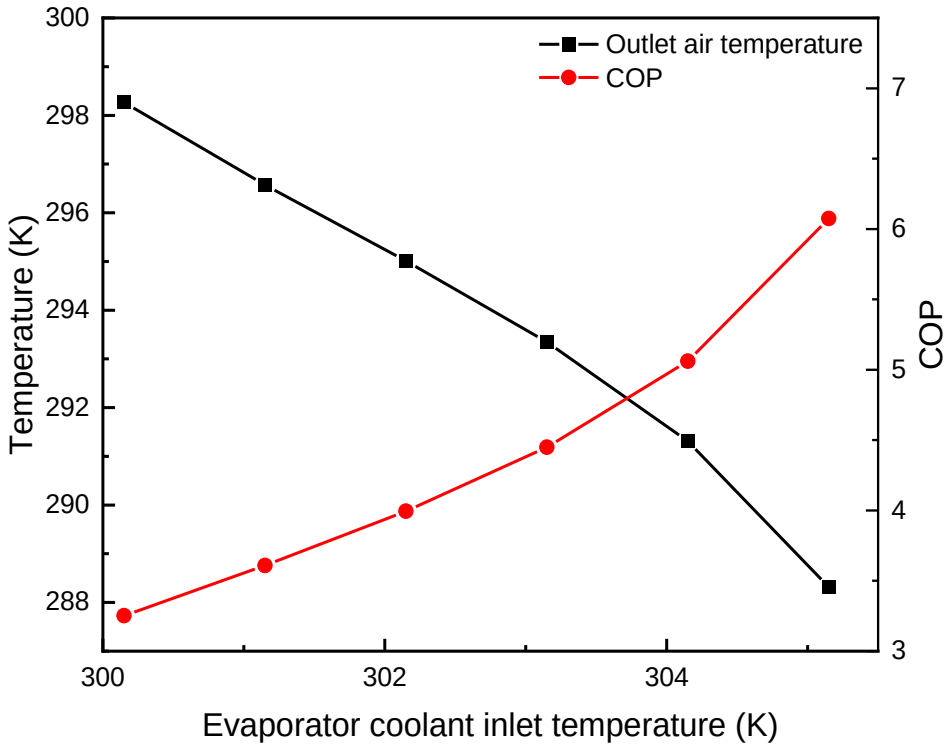

Figure 3.13. Influence of condenser coolant inlet temperature on outlet air temperature and COP

3.4.4 Equivalent effective battery capacity and payback duration

Due to the limited space in the vehicle, a fuel cell backup system would sacrifice some space that was previously used for the battery pack. After the battery pack was scaled down, the

capacity of the battery pack also declined correspondingly. The equivalent battery capacity in the proposed system could be divided into three parts, the fuel cell supplement element, the heat pump consumption part and the initial electrical storage capacity of the remaining battery pack. The remaining portion of the initial battery capacity, after being consumed by the heating system and the replenishment from the fuel cell stack were defined as the EEBC in Eq. (41) which can be used for driving. The variations of those three energy elements over operating hours were displayed in **Figure 3.14**. With the operating time increasing, the heat pump power consumption and fuel cell power supplement were continuously increasing. Meanwhile, the initial part of battery capacity was decreasing but the EEBC was increasing. **Figure 3.15**. shows the EEBC that could be used for driving with respect to the heat pump system running hours. The electric vehicle air source heat pump (EVASHP) was selected from ref. [69], which had proved that the pump can provide around 6kW heat. The working condition in Fig. 15. Was at -20℃ ambient temperature, the heating demand was 5.986kW, In comparison, the proposed system has a COP of 6, while the COP of EVASHP, as described in previous work is only 1.8. [69]. The efficiency of the PTC heater was assumed as 0.9 and the battery initial SOC was assumed as 0.8 to avoid overcharging. It can be concluded that the longer the operating hours the higher the benefit achievable by the proposed FCBEV heat pump-assisted thermal management system. When the operating period was less than 2 hours, the suggested system in this research could only provide the lowest EEBC compared to the EVASHP system and PTC system, as the charging current from the fuel cell stack could not supply equivalent power as sacrificed battery capacity. Hence the electricity that could be used for driving is 17.9% lower than the EVASHP system and 11.4% lower than PTC system. However, the proposed system in this study displayed significant advantages when the operating period was greater than 2h. For example, when the operating period was 5 hours, the available power for driving is increased by 90% compared to EVASHP and 300% compared to the PTC system. It should be mentioned that the EVASHP selected for comparison did not consider the frosting and defrosting phenomenon on its OHX which normally dramatically affects the EVASHP's COP. In contrast, the proposed fuel cell backup heat pump assisted BEV thermal management system recovered the heat from the fuel cell coolant and battery pack and did not suffer from such impact. Therefore, the proposed system has a crucial advantage compared to current existing EVASHP system, but crucial attention should be paid to the amount of H_2 charging within one charging cycle. It is necessary to store on-board H2 that can supply power to the battery pack for at least 2 hours. However, this does not simply mean that more on-board hydrogen

storage results in a better the performance, because issues such as hydrogen storage space and cost also should be considered.

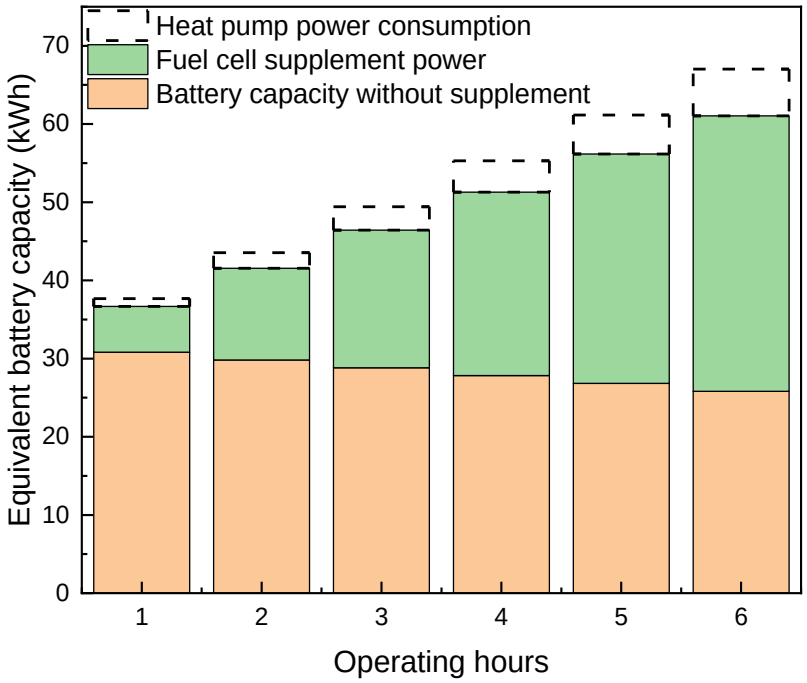

Figure 3.14. Variation of battery capacity of the proposed system over operating time

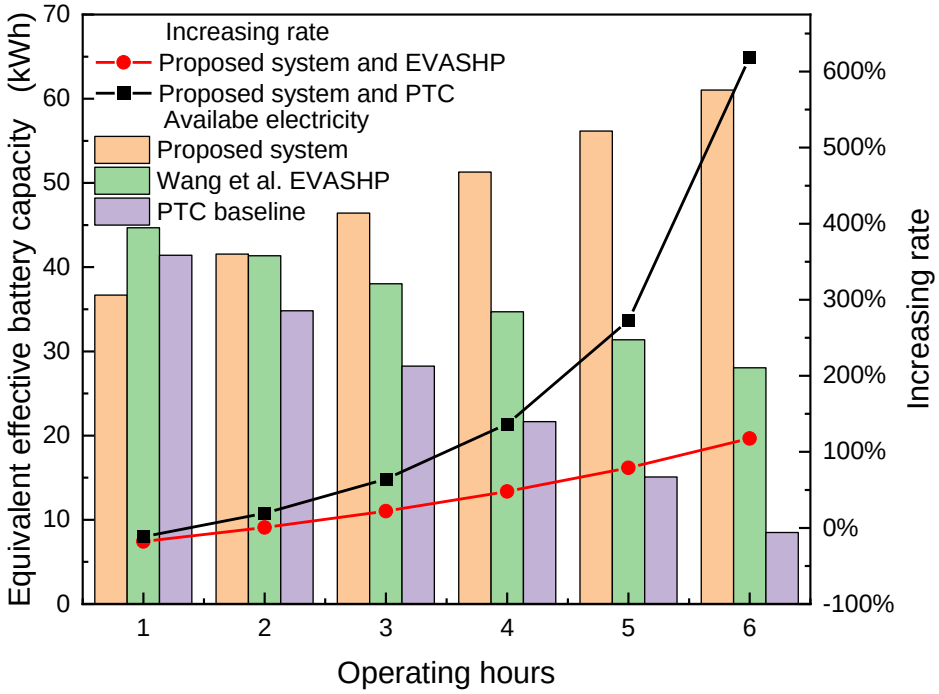

Figure 3.15. Comparison of the amount of electricity that can be used for driving and increasing rate for proposed system, EVASHP system, and PTC system

Assuming the setting heat pump assisted FCBEV system runs for 4 hours with a 51.3kWh equivalent battery capacity within one charging time as the target case. The price of H_2, 5kW fuel cell stack and electricity price are concluded in **Table 3.6**. The price of the 5kW fuel cell stack also includes the cost of sales. Fig. 16 represents an economic analysis of each system with the same battery capacity available for driving. For the proposed system in this study, the cost under the selected case is £10.40 for a single charging cycle while EVASHP system [69] and PTC system is respectively £13.80 and £19.20 which means that the suggested system could save around 16.4% and 39.5% within one charging cycle. Moreover, the payback duration was calculated based on the 5kW fuel cell stack. The result in **Figure 3.16**. shows it will take 10500 charging times to earn back the initial cost of the fuel cell stack. However, the cost of the fuel cell stack and price of hydrogen fuel will be further improved with increasing production requirements and infrastructure development and, consequently, the pay pack duration will reduce sharply in the future.

Table 3.6 Components cost for the proposed system

Components		Prices
H_2[177]		3.26 (£/kg)
Electricity [178]		0.19 (£/kg)
5kW fuel cell stack(10000 units/year)[179]	Manufacturing CHP hardware BOP hardware Sales (50%)	21068.94 (£)

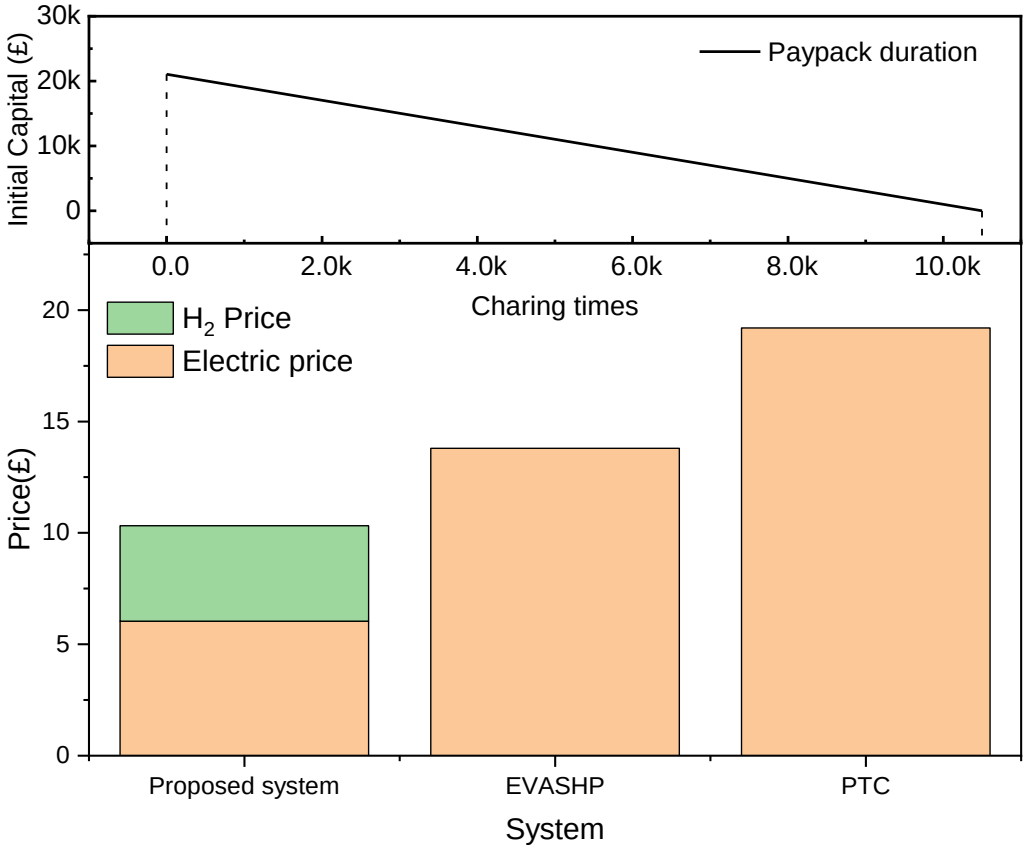

Figure 3.16. Economic analysis for each system and payback cycle for the proposed system under 4 hours of operating period

3.5 Chapter Summary and outlook

A fuel cell backup and heat pump assisted FCBEVs thermal management system was proposed to improve the performance of BEVs under extreme cold weather from both efficiency and economic perspectives. Numerical models for fuel cell, heat exchangers and compressor were developed and validated by using published experimental data. The impacts of different vital operating conditions and the degree of improvement in EEBC were concluded and discussed. Based on the simulation results, the following conclusions were drawn.

- The COP increased with the increase of fuel cell stack output current. Contrarily, the outlet air temperature would reduce as the need for increasing the air mass flow rate occurred. When FC current output is greater than 217A, the outlet air temperature started lower than the FC coolant outlet temperature.

- The battery discharging rate had a similar impact on COP compared to fuel cell current output. However, the inlet vapour quality difference between the FC and battery would be narrowed with a decrease in battery discharging rate.
- The COP showed a decreasing trend while introducing a larger subcooling degree. But the operating range and outlet temperature increased correspondingly. Hence, when the size of components is fixed, regulating the subcooling degree is a useful way to fulfil different ranges or higher air temperature requirements.
- Different from ASHP, the air temperature has no significant effect on the proposed system. When the ambient temperature varied from 5℃ to -25℃, the COP only decreased by 3.7%
- Evaporator coolant inlet temperature had the greatest influence on the COP among the defined independent variables. When the evaporator coolant inlet temperature increased 5℃ from 30℃ to 35℃, the COP could increase by 87%.
- The COP of the proposed system is 2.3 times that of a EVASHP system at -20℃. Heating capacity fluctuated by only 0.3%, while the mentioned counterpart fluctuated by 14.8% when the air temperature dropped from 0℃ to -20℃.
- When the operating period was greater than 2 hours, the increasing rate of effective battery capacity compared to the traditional heat pump thermal management system in BEV increased dramatically, even meeting 79.04% when the operating period was 4 hours.
- The proposed system had the lowest cost for each H_2 and battery charging time. The payback duration was 10500 charging cycles.

The study demonstrated that the proposed fuel cell battery electrical vehicle energy system integrating with a heat pump technology thermal management system could always provide a higher COP than a conventional R134a EVs' air source heat pump and even higher than a CO_2 air source heat pump. Subcooling degrees could extend the operating range to a certain extent. Hence, optimizing the subcooling degree may be a beneficial control strategy to cover a widen operating range without changing the components. Since the performance from a heat pump perspective has a significant improvement and will also increase the equivalent effective battery capacity, it is necessary to further apply the proposed system to a vehicle to examine how much driving range it can increase and how is the impact on the operating cost and CO_2 emission of the vehicle. Therefore, a vehicle motion model and 4E analysis is adopted in next chapter to further evaluate the improvement from a vehicle perspective.

4. 4E Analysis of the Heat Pump and Fuel Cell Integrated System Applying to Electric Vehicles

4.1 Introduction

Climate changes has become the greatest challenge for the human race. COP26 stressed the critical target of maintaining any temperature increase within 1.5 ^{o}C [180]. CO_2 is considered as the largest contributor to global warming, with 20% of direct CO_2 emissions from fuel combustion coming from road vehicles [181]. To comply with the net zero target, many countries and governments have committed to reach 100% Zero Emission Vehicle (ZEV) new sales between 2030 to 2050, including Norway which plans to ban the sale of fossil fuel vehicle by 2025, and Germany by 2030 [182]. Therefore, ZEVs, such as Battery Electric Vehicles (BEVs) and Fuel Cell Electric Vehicles (FCEVs) will see explosive growth in the foreseeable future. However, the reduction in driving range caused by heating systems in extreme cold weather has plagued consumers and hindered the development of decarbonization. It is estimated that the heating load for cabin at -20 ^{o}C is in the range of 3.3kW to 6.8kW [57]. However heating the cabin with a Positive Temperature Coefficient (PTC) heater will cause a reduction of 30% in driving range within one charging cycle, compared to summer condition [183]. Therefore, in recent years, developing high efficiency heating technologies for EVs has gained increasing attention worldwide.

The Air Source Heat Pump (ASHP), that is largely utilised in domestic heating, is considered as a suitable alternative to the PTC heater. It can utilise low grade heat in the low temperature ambient air for cabin thermal comfort [146]. Lee *et al*. [184] studied the performance of an R134a heat pump system for EVs at -10 ^{o}C which can provide 3.1kW heat with a COP of 3.26. They also evaluated the exergy of their designed heat pump system, in which the internal condenser had the greatest exergy destruction. A similar system with a larger compressor and heat exchanger was applied to large passenger EVs which only had a COP of 2.4 at 10 ^{o}C [107]. Qin *et al.* [176] discussed the performance of an R134a EVASHP at -20 ^{o}C, and the results demonstrated that a minimum COP of 2.1 with a maximum heating capacity of 3.3kW can be achieved. Due to the space limitations in EVs, conventional ASHP cannot provide sufficient heat with high COP under extreme cold weather conditions. Some researchers have investigated alternative refrigerants to improve the heating performance in extreme cold conditions and reduce the GWP of the refrigerant, whilst avoiding structural modifications. Direk *et al*. [70] used R1234yf instead of R134a, and the results indicated

that the system can provide up to 2.6kW heat with a COP of 4 at 5℃. Yu *et al.* [185] investigated the performance of three new-developed refrigerants by comparing them to R410a, namely M1 (R32/R1123/R161/R13I1 (22%/35%/8%/35%)), M2 (R32/R1123/R161/R13I1 (22%/30%/13%/35%)) and M3 (R32/R161/R13I1 (22%/48%/30%)). The COP of M3 increased by up to 22% compared to R410a, but only 1.65kW heating capacity can be achieved at -10 ^{o}C. A CO_2 and CO_2 mixture have also been frequently discussed in recent years. Dong *et al*. [151] conducted an experimental study into CO_2 heat pump for EVs. The results proved that CO_2 heat pump could successfully provide over 6kW heat but only had a COP of 2.1 at -20 ^{o}C. Similar heating capacity can also be found in Ref. [69] but the COP is even lower. Additionally, Yu *et al*. [66] evaluated the performance of a CO_2/R41 mixture. They assumed that the higher the R41 mass fraction, the lower the heat capacity would be, but the COP would be marginally improved A number of researchers have attempted to introduce vapor injections technologies to EVASHP in order to improve the performance. Qin *et al.* [148] experimentally investigated a R134a heat pump using a compressor with two different injection portholes. It can be concluded that with the vapour injection, the heating capacity can be improved by 28.6% compared to the traditional system but the COP reduced by a maximum of 25%. Jung *et al*. [77] conducted research on the impacts of an injection port on performance and suggested that the COP could be improved by 7.5% and 9.8% respectively when a single injection port and dual injection port are set to be 440^{o} and 535/335^{o}. Yang *et al*. [186] introduced a vapour injection CO_2 heat pump system to EVs. The authors claimed that the proposed system can work within the range -30 ^{o}C to 50 ^{o}C, but the maximum heating capacity at -30 ^{o}C was only 2.2kW and the COP was 1.45. However, the vapor-injection technology was still able to improve the performance by 75.7% at -30 ^{o}C, compared to basic system. However, a serious problem is regularly ignored when considering the performance of a heat pump, namely frost formation on the Outdoor Heat Exchanger (OHX). Steiner *et al*. [187] highlighted out that, at 0 ^{o}C, the COP declined dramatically after the first 15 min frosting period and reduced by 30% after 25 mins while the compressor power consumption increased by 50%. Zhou *et al*. [105] reversed the heat pump cycle and utilised the heat in the vehicle to defrost the OHX without considering the cabin comfort. Li *et al*. [188] designed a secondary loop to prevent the frost formation. However, the heat source of the secondary loop is from a PTC heater. Additionally, Liu *et al*. [189] also optimized the heat pump system from the heat exchanger perspective to achieve a better temperature uniformity in the OHX which can delay frosting at low temperatures. Similarly, Mahvi *et al*. [190] modified the surface wettability of an aluminium louvered-fin heat exchanger that commonly used in vehicles and the results show

that it can successfully delay the frost formation at -0.7 °C with a 3kW heating capacity and a COP of 2.1. Jung *et al*. [76] investigated the impact of the length of the Internal Heat Exchanger (IHX) and claimed that the optimal COP of 2.7 occurred when IHX's length was 300mm.

Although significant efforts have been undertaken to develop EVASHP, it is likely that the heat pump cannot meet the high COP and high heating capacity simultaneously, and the frosting problem is difficult to address. Hence, many researchers believe integrated energy systems are vital for delivering various energy services [191]. Ahn *et al*. [192] developed a dual source heat pump by using air and waste heat in EVs. They concluded that the heating capacity and the COP increased by 31.5% and 9.3% respectively compared to pure ASHP at 0 °C with 2.5kW waste heat. It was also highlighted that the performance at -10 °C was highly dependent on the amount of waste heat. However, as the waste heat in the paper was simulated by an electric heater, it was unknown whether there was sufficient waste heat in EVs. Han *et al*. [141] investigated the heating performance of a ASHP for an electric bus. According to the results, the improvement could be achieved when the waste heat was over 2kW, and the ambient temperature was below 0 °C. Tian *et al*. [109, 155] did a series of research studies focused on the integrated thermal management system. They considered using the waste from the motor and collectively evaluated the energy, exergy, and economic performance. The highest COP achieved was 2.75 with 1kW waste heat from the motor with a temperature at -7 °C and the system maximum exergy efficiency was 40%. Lee *et al*. [142] experimentally studied a muti-level waste heat recovery vapour injection heat pump system for EVs. Different from the conventional parallel waste heat recovery system, the refrigerant absorbed the waste heat and was injected into the vapor injection compressor at a middle pressure. The results demonstrated that the system proposed by Lee could improve the COP by 6.6% at -20℃ but the COP started lower than conventional systems when the ambient temperature was higher than -5 °C.

In summary, the EVASHP cabin heating system and its performance enhancement technologies, including different refrigerants, vapor injection, and frost formation prevention have been widely discussed. However, considering the heat pump separately from the whole vehicle system cannot provide sufficient heating capacity and high COP simultaneously. Some researchers investigated the heat pump integrated system by using waste from the battery pack or motor. Although the performance can be improved when ambient temperature is in the range of -10 °C to 0 °C and when the waste heat is over 1kW, for most scenarios, the waste heat is provided by the PTC heater and the practical waste heat is at different temperatures under unknown operating conditions. Additionally, devices that

perform well at very low temperatures often perform poorly at high temperatures or may not even function at high temperatures, due to compressor limitations. Compared with ordinary systems, units with full-scale compressors have lower COP and heating capacity over the entire operating range. The most important issue is the severe frosting problem which will mean the heat pump cannot provide stable heating capacity all the time and is sensitive to the ambient temperature. Furthermore, very few studies tried to analysis the integrated system from a whole vehicle perspective, research has been largely undertaken only from heat pump perspective. Therefore, further research on how to provide sufficient and stable heat with high COP, extending the driving range, and avoiding the effects of frost and compressor limitation is still necessary and crucial. Additionally, analysis from the whole vehicle perspective should be adopted to evaluate the performance from a macro perspective. As summarised above, despite the growing interest in EVASHP development technologies and integrated systems, challenges remain to be addressed in terms of efficient cabin heating, CO_2 emissions and driving range reduction. In order to address these challenges, this study proposed a highly integrated energy system by integrating a fuel cell stack, a battery pack, and a heat pump. The cogeneration characteristic of the fuel cell was adopted so that not only the electricity generated by the fuel cell could be used but also the waste heat from the fuel cell stack can be utilized as a stable heat source for cabin heating. A refrigerant-based BTMS was adopted to simplify the system and reduce the exergy deduction. The coolant heat pump was adopted instead of the traditional air source heat pump to recover the waste heat from the fuel cell and battery to maintain their operating temperature and supply stable heating loads to the cabin. The proposed system could operate with high COP, extend the Driving Range (DR) of EVs and reduce CO2 emissions. An acceptable payback period could be achieved due to the lower operating costs. Moreover, the proposed system can be further utilized in other areas such as domestic or city heating systems and provide ideas for future heat and electricity cogeneration energy management systems.

4.2 System Description

The schematic diagram of the proposed system is shown in **Figure 4.1**. Different colours represent different flows, for example, the blue line represents for the refrigerant flow, the green line represents the fuel cell supply air flow, the red line represents the coolant flow, the purple line symbolizes the H_2 flow, brown line symbolizes water flow, and the yellow line represents electricity flow. The arrows on each line demonstrate for the flow direction. The proposed system has three key subsystems: the fuel cell, the battery, and the heat pump.

The fuel cell subsystem includes a fuel supply circuit, a coolant cooling cycle, and a DC/DC power output. In the fuel supply circuit, the supply air passes the air compressor to reach the working pressure but needs to pass through the humidifier and intercooler in order to be further cooled and humidified before entering the fuel cell stack. The pressure of the H_2 stored in the Hydrogen vessel is much greater than the working pressure in the fuel cell stack, hence it is necessary to reduce the pressure of the supplied H_2 before reacting in the fuel cell stack. The operating temperature of the fuel cell stack is controlled by a coolant loop which carries the heat from the fuel cell stack and releases it in the evaporator. The power generated from the reaction is supplied to battery pack via a DC/DC while the by-product of the reaction, water, flows through the external condenser to pre-heat the air supplied to the cabin and cools and humidifies the supplied air to the fuel cell, and finally discharges to the outside. The battery cycle contains a battery pack, a refrigerant based cooling system, a DC/AC, and a motor. From a thermal management perspective, the refrigerant flows into the cold plates inside the battery pack to maintain the operating temperatures of the batteries and finally enters the evaporator as a mixture. Meanwhile, as the main power supplier of the vehicle, the battery also needs to supply electricity via a DC/AC to the motor, but the difference is that it can, simultaneously, also receive power from the fuel cell. The heat pump cycle includes an evaporator, an internal condenser, a refrigerant compressor, and an expansion valve. The refrigerant enters the evaporator to absorb the heat released by the high temperature coolant from the fuel cell stack, to help the coolant complete a full cycle and becomes saturated refrigerant vapour. Whereafter, the vapour refrigerant passes by the compressor and enters the internal condenser to heat the preheated cabin supply air up to the setpoint and finally, the refrigerant passes through the expansion valve to complete a whole cycle. In the proposed integrated thermal management system, the heating capacity of the heat pump is designed to match the heat generated from the battery pack and fuel cell stack in order to always maintain their optimal operating temperature. As the battery pack is still the main power source of the vehicle, the current output of which is decided by different driving scenarios while the fuel cell only works as a power supplement. Therefore, the current output of the fuel cell stack will be actively adjusted to meet different cabin heating demands. With the proposed energy management system, the battery pack and fuel cell stack can always operate under optimal conditions, the heating demands can always be covered and at the same time, the driving range is extended with the power output from the fuel cell stack.

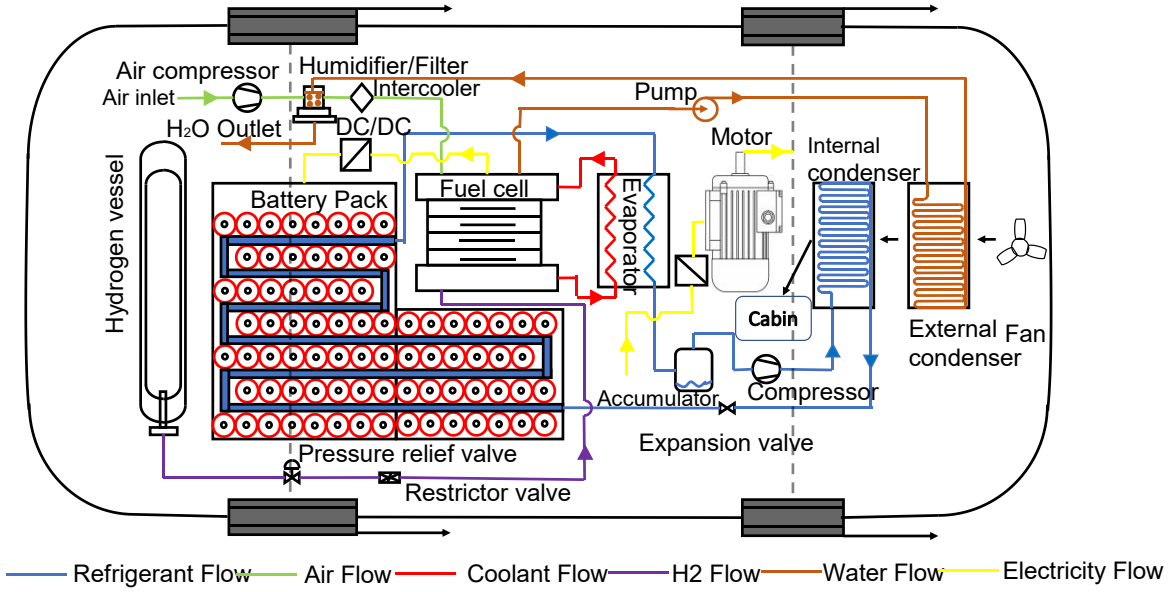

Figure 4.1. Schematic diagram of the heat pump assisted energy management system for FCBEV

4.3 Model Development

4.3.1 PEM fuel cell energy model

The Proton-Exchange Member (PEM) fuel cell is an electrochemical device that converts the chemical energy of fuels such as hydrogen and oxygen into electrical energy and heat. The voltage of a fuel cell can be calculated as:

$$V_{fc} = E_{nerst} - \Delta V_{ohm} - \Delta V_a - \Delta V_c \quad (4.1)$$

in which E_{nerst} is the open-circuit reversible voltage, ΔV_{ohm}, ΔV_a and ΔV_c are the ohmic voltage drop, the activation voltage drops, and the concentration voltage drop respectively. E_{nerst} can be expressed as below [158]:

$$E_{nernst} = 1.228 - [0.85 \times 10^{-3} \times (T_{fc} - 298.15) - 4.3086 \times 10^{-5} \times T_{fc} \times ln(P_{H_2} \times {P_{O_2}}^{0.5}) \quad (4.2)$$

where T_{fc} is the temperature of a fuel cell, P_{H_2} and P_{O_2} are the pressures of hydrogen and the partial pressure oxygen in the air respectively. The ohmic voltage drop can be simply modelled by Eq. (4.3):

$$\Delta V_{ohm} = R_{ohm} \times i_{fc} \quad (4.3)$$

where R_{ohm} is the specific fuel cell resistance (Ωm^2) which can be achieve in Ref. [161, 162] and i_{fc} is the current density of a fuel cell (A/m^2) which is formulated as below:

$$i_{fc} = \frac{I_{FC}}{A_{FC}} \quad (4.4)$$

in which, I_{FC} is the current output of the fuel cell stack and A_{FC} is the surface area of the fuel cell stack. The activation voltage drop ΔV_a is given as following:

$$\Delta V_a = -(\alpha_1 + \alpha_2 \times T_{fc} + \alpha_3 \times T_{fc} \times ln(C_{O_2}) + \alpha_4 \times T_{fc} \times ln\,(i_{fc})) \quad (4.5)$$

α_{1-4} are the coefficient of activation losses which can be obtained from Ref. [159] while the C_{O_2} is the concentration of oxygen which can be determined by Henry's law [160]. The equation of the concentration voltage drop ΔV_c is defined as below:

$$\Delta V_c = \frac{3 \times R \times T_{fc}}{4 \times F} \times ln(1 - \frac{i_{fc}}{i_{fc\_max}}) \quad (4.6)$$

where i_{fc_max} is the maximum current density of a fuel cell which is assumed equal to $2.2X10^{-4}$ (A/m^2) [164], and R is the universal gas constant, while F is the Faraday constant. According to the voltage of a fuel cell and open circuit voltage, the heat generation and the power output of a fuel cell stack can be calculated as below:

$$Q_{FC} = N_{FC} \times I_{FC} \times (E_{nerst} - V_{fc}) \quad (4.7)$$

$$P_{FC} = N_{FC} \times V_{fc} \times I_{FC} \quad (4.8)$$

where N_{FC} is the number of the fuel cell in the fuel cell stack. Additionally, the fuel mass flow of hydrogen and air and the produced H_2O are calculated below [193, 194]:

$$\dot{m}_{H2} = \frac{Q_{FC} + P_{FC}}{\dot{q}_{H2}} \times 10^{-3} \quad (4.9)$$

$$\dot{m}_{air} = 3.57 \times 10^{-7} \times \omega \times \frac{P_{FC}}{V_{fc}} \quad (4.10)$$

$$\dot{m}_{H_2O} = \dot{m}_{H_2} \times \frac{M_{H_2O}}{M_{H_2}} \quad (4.11)$$

where, $\dot{q}_{H2}$ =120MJ/kg is the specific energy of hydrogen and M_{H_2O} and M_{H_2} are the molecular weight of H_2 and H_2O. Therefore, the power consumption of the air compressor in fuel cell supply system is given by:

$$P_{FC,comp} = \dot{m}_{air} \times Cp_{air} \times \frac{\Delta T}{\varepsilon_{FC,comp}} \quad (4.12)$$

where $\varepsilon_{FC,comp}$ is the mechanical efficiency of the air compressor, which is assumed to be 90% in this study. The parameters of the fuel cell selected in this study are shown in **Table 4.1**. and the fuel cell heat generation model validation is shown in **Figure 4.2**.

Table 4.1 Parameters for fuel cell model [164]

Specification	**Value**	**Unit**
Fuel cell operating temperature	65	℃
Inlet O_2 pressure P_{O_2}	2.5	atm
Inlet H_2 pressure P_{H_2}	2.4	atm
Current output I_{FC}	190-230	A
Number of cells N_{FC}	40	/
Area of cell A_{FC}	285.8	cm^2
Thickness of cell l_{FC}	$5.1X10^{-3}$	cm

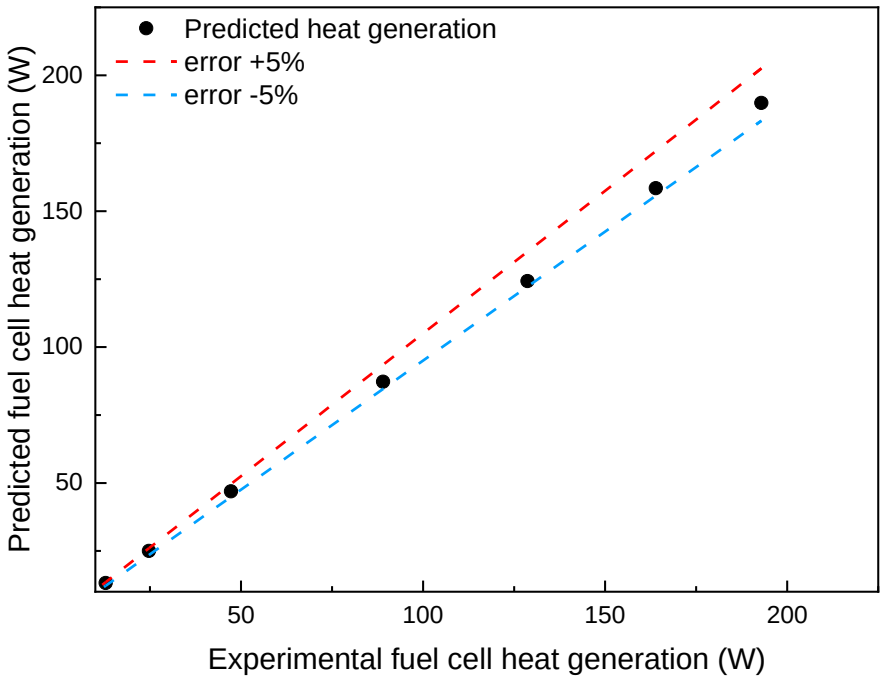

Figure 4.2. Fuel cell heat generation model validation by comparison with experimental data in Ref. [164]

4.3.2 Battery energy model

The simplified heat generation model of a battery cell while the battery is discharging is formulated as below:

$$Q_{bat} = \underbrace{I_{dis}^2 \times R_{dis}}_{irreverssible} - \underbrace{I_{dis} \times T_{bat} \times \frac{dE_{OC_{bat}}}{dT_{bat}}}_{reverssible} \quad (4.13)$$

where I_{dis} and R_{dis} is the current and the battery internal resistance respectively while discharging. $\frac{dE_{OC_{bat}}}{dT_{bat}}$ is the entropy coefficient, and the experimental data can be found in ref. [166]. The heat generated during charging by the fuel cell stack can be determined using the same equation as used for the discharging process. The power input from the fuel cell stack is defined as:

$$P_{chr} = I_{FC} \times \frac{V_{FC}}{N_{ser} \times V_{bat} \times N_{mod}} \quad (4.14)$$

While the discharging power is considered as:

$$P_{dis} = I_{dis} \times N_{par} \times N_{ser} \times V_{bat} \times N_{mod} \quad (4.15)$$

in which V_{bat} is the voltage of a battery, N_{ser}, N_{par} represent the number of cells in parallel and that in series for each string respectively while N_{mod} refers to the number of modules in the battery pack. The 60-kWh battery pack in this study is designed based on a 2013 Tesla model S and the specifications are shown in **Table 4.2**.

Table 4.2. Specifications for battery model

Specification	Value	Unit
Battery capacity	8	Ah
Battery voltage	4.2	V
Number of batteries	2436	/
Number of batteries in series for one module	6	/
Number of batteries in parallel for one module	29	/
Number of modules	14	/
SOC	0.5	/
Battery operating temperature	30	℃
Voltage of battery pack	352	V
Battery pack capacity	60	kWh

The predicted battery model was validated by comparing the heat generation and internal resistance while charging and discharging with Ref. [166] as shown in **Figure 4.3**.

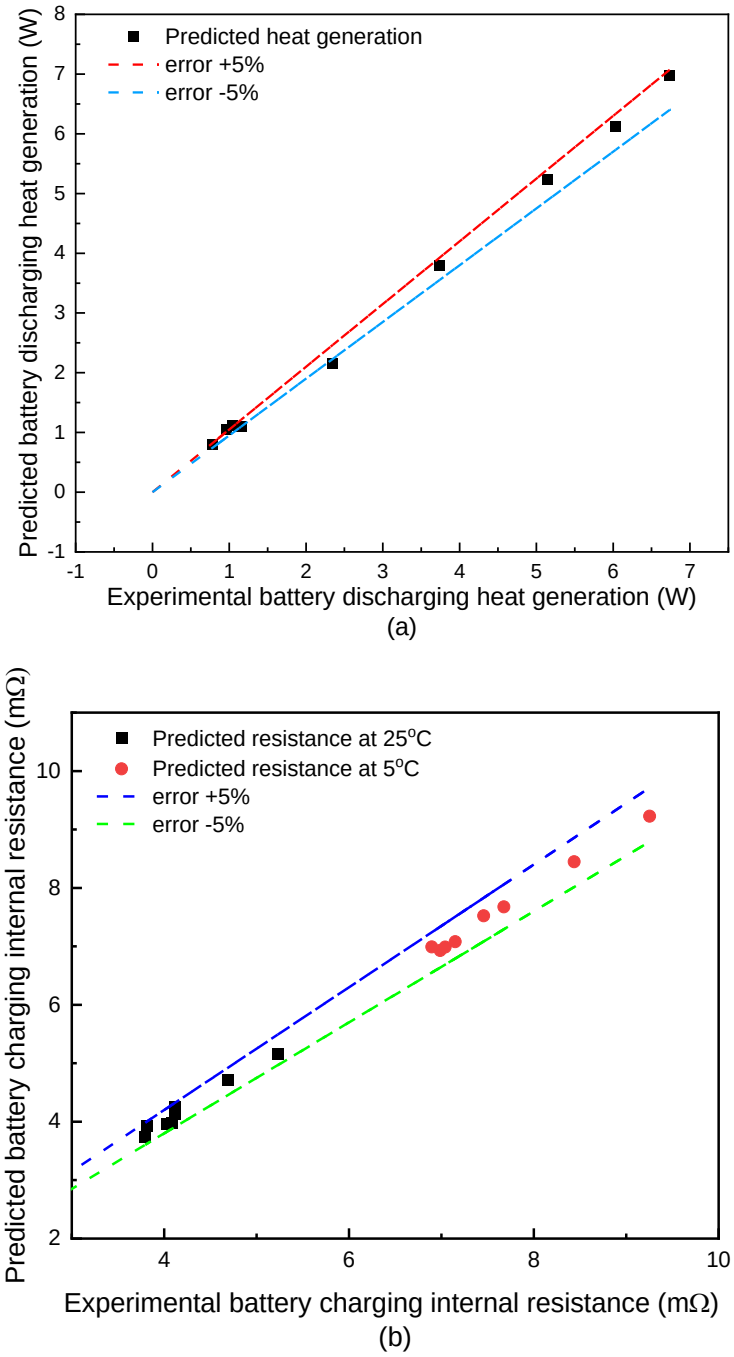

Figure 4.3. Battery energy model validation by comparison with the experimental data in Ref. [166]

4.3.3. Heat exchanger model

In the proposed system, there are three heat exchangers. One of them is the plate heat exchanger which is used as an evaporator while the other two are fin and tube heat exchangers. For the evaporator, the overall heat transfer coefficient U_{eva} can be calculated as:

$$\frac{1}{U_{eva}} = \frac{1}{h_{cl}} + \frac{1}{h_{eva,ref}} + \frac{\delta_w}{\lambda_w} \quad (4.16)$$

where, h_{cl}, $h_{eva,ref}$ is the heat transfer coefficient for coolant side and refrigerant side respectively while λ_w is the plate conductivity and δ_w is the thickness of the plate. The h_{cl} is adopted from Ref. [170]:

$$h_{cl} = 0.2121 \times Re_{cl}^{0.78} \times Pr^{1/3} \times (\frac{\mu_m}{\mu_{wall}})^{0.14} \times \left(\frac{k_{cl}}{D_{h,eva}}\right) \quad (4.17)$$

in which Re_{cl} is the Reynolds number for coolant flow, Pr is the Prandtl number, μ_m and μ_{wall} are the dynamic viscosity calculated based on the coolant bulky temperature and wall temperature. In addition, $D_{h,eva}$ is the hydraulic diameter of the plate heat exchanger and k_{cl} is the conductivity of coolant. For the refrigerant side, the $h_{eva,ref}$ is depicted as [169]:

$$h_{eva\_ref} = 1.055 \times [1.056 \times Co^{-0.4} + 1.02 \times Bo^{0.9}] \times X_m \times h_{lo} \quad (4.18)$$

where Co is the convective number and Bo is the boiling number. X_m is the mean vapour quality in the evaporator and the h_{lo} is the heat transfer coefficient for pure liquid phase refrigerant which can be obtained in Ref. [169]. For the fin and tube internal and external condenser, the overall heat transfer coefficient is formulated as:

$$\frac{1}{U_{cond}A_{cond}} = \frac{1}{\eta_0 \times h_c \times A_c} + R_{wall} + \frac{1}{\eta_0 \times h_h \times A_h} \quad (4.19)$$

in which η_0 is the overall surface efficiency which can be achieved in Ref. [168]. In this study, for the internal condenser, the hot side is the refrigerant side while the cold side is the air side. Similarly, for the external condenser, the fluid on cold side is still air while the fluid on the hot side becomes water. The heat transfer coefficient for the refrigerant side is different depends on the speed of the flow. For the wavy flow, the Nusselt number (Nu_{wavy}) is defined as [171]:

$$Nu_{wavy} = \frac{0.23 \times Re_{vo,ref}^{0.12}}{1 + 1.11 \times X_{tt}^{0.58}} \times [\frac{Ga \times Pr_l}{Ja_l}]^{0.25} + cos^{-1}(2 \times \varphi - 1)/\pi \times 0.0195 \times Re_l^{0.8} \times Pr_l^{0.4} \times \sqrt{1.376 + c_1/X_{tt}^{c_2}} \quad (4.20)$$

in which c_1 and c_2 is determined by the Froude number (Fr), X_{tt} is the turbulent-turbulent Lockhart Martinelli parameter, Ga is the Galileo number, Ja_l is liquid Jakob number, and

φ is the void fraction which is illustrated in Ref. [172]. For the annular flow, the expression of $Nu_{annular}$ is:

$$Nu_{annular} = 0.023 \times Re_l^{0.8} \times Pr_l^{0.4} \times \left[1 + \frac{2.22}{X_{tt}^{0.89}}\right] \quad (4.21)$$

For the external condenser, as there is only one phase water in the tube, Nu_{wo} is defined as:

$$Nu_{wo} = 0.023 \times Re_{wo}^{0.8} \times Pr_{wo}^{0.4} \quad (4.22)$$

For the air side, a simple heat transfer model is adopted as introduced in Ref. [168]:

$$h_{air\_cond} = C \times Re_{air}^{m} \times Pr^{1/3} \quad (4.23)$$

where C and m is determined by the air speed. The heat balance across the evaporator and condensers is formulated as below:

$$Q_{eva/icond/OHX} = \dot{m}_{cl/air/H_2O} \times Cp_{cl/air/H_2O} \times \Delta T_{cl/air/H_2O} \quad (4.24)$$

$$Q_{ref} = \dot{m}_{ref} \times (1 - X_{inlet}) \times i_{fg} \quad (4.25)$$

$$Q_{eva/cond/econd} = U_{eva/icond/econd} \times A_{eva/icond/econd} \times LMTD_{eva/icond/econd} \quad (4.26)$$

where the logarithmic mean temperature difference (LMTD) and i_{fg} is the enthalpy of vaporization of the selected refrigerant R134a. The validations for both heat exchanger models are shown in **Figure 4.4** with errors within 5%.

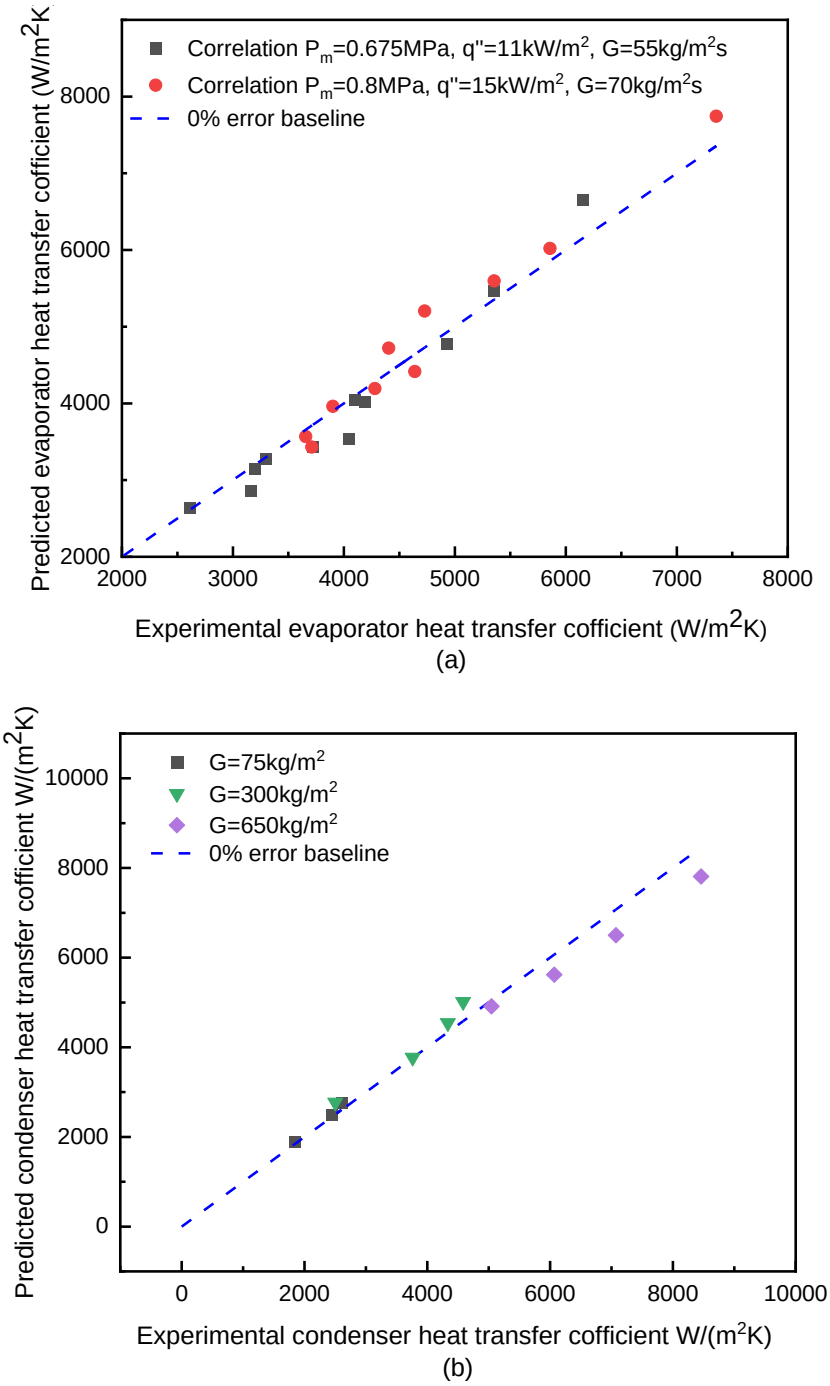

Figure 4.4. Heat exchanger model validation (a) evaporator by comparison with experimental data in Ref. [170] and (b) condenser by comparison with experimental data in Ref. [171]

4.3.4 Compressor and expansion valve model

The compressing ratio (γ) and the compressor power consumption are important. Kinab *et al.* [195] concluded the relationship between refrigerant temperature and mass flow rate for a fixed compressor speed:

$$m_{ref} = b_0 + b_1 t_{eva} + b_2 t_{eva}^2 + b_3 t_{eva}^3 + b_4 t_{cond} + b_5 t_{cond}^2 + b_6 t_{cond}^3 + b_7 t_{eva} t_{cond} + b_8 t_{eva}^2 t_{cond} + b_9 t_{eva} t_{cond}^2 \quad (4.27)$$

in which coefficients b_0 to b_9 can be obtained from Ref. [109]. In this study, the refrigerant evaporating and condensing temperature are related to the pressure via REFPROP and the equation is solved by using MATLAB code. The validation of compressor model is conducted by comparing with the results in Ref. [196], as shown in **Figure 4.5** and the average error is within 5%. The power consumption of the compressor is shown as below:

$$W_{comp} = \frac{\dot{m}_{ref} \times (H_{dis} - H_{suc})}{\eta_{isen}} \quad (4.28)$$

in which H_{dis} and H_{suc} are the enthalpy of R134a at the suction and exit of the compressor respectively, η_{isen} is the isentropic effectiveness of the compressor which is assumed to be 0.67 [173]. The process by which the refrigerant passes by the expansion valve is considered an adiabatic process. During the process, the enthalpy is unchangeable. The mass flow rate through the EEV is calculated as Ref. [155]:

$$\dot{m}_{EEV} = C_v A_c \sqrt{2 \times \Delta P_{EEV} \times \rho_{ref\_in}} \quad (4.29)$$

where A_c is the circulation area while C_v is the flow coefficient, and $C_v = 0.02005 \times \sqrt{\rho_{in}} + 0.634/\rho_{out}$.

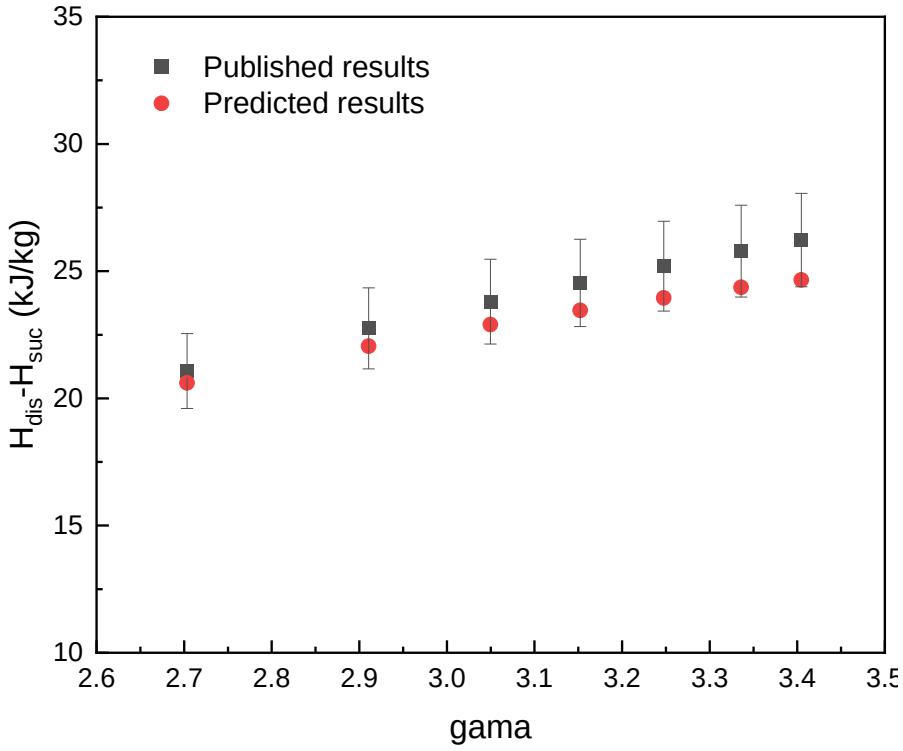

Figure 4.5. Compressor model validation by comparison with experimental data in Ref. [196]

4.3.5 Vehicle motion model

According to Newton's second law, the vehicle longitudinal motion is defined as below:

$$F_{net} = M_{veh} \times a_{veh} \quad (4.30)$$

in which, F_{net} is the net Force on the vehicle, M_{veh} is the mass of the vehicle while a_{veh} refers to the vehicle's acceleration. Additionally, based on the principle of force balance, F_{net} can also be expressed as:

$$F_{net} = F_{tf} - F_{dr} - F_{rr} \pm F_{gr} \quad (4.31)$$

where F_{tf}, F_{dr}, F_{rr}, F_{gr} are the traction force (N), aerodynamic drag resistance (N), rolling resistance (N), and gradient resistance (N). Among them, F_{gr} can be ignored when the vehicle is only driven on a flat road. The expression of the aerodynamic drag resistance is given as following:

$$F_{dr} = 0.5 \times A_{cs} \times \rho_{air} \times C_d \times (v_{veh} \pm v_{wind})^2 \quad (4.32)$$

in which, A_{cs} is the cross-section area of the vehicle (m^2), C_d stands for the drag coefficient for the targeted Tesla model 3 [197]. v_{veh} and v_{wind} refer to the speed of vehicle and wind (m/s) and their relationship depends on their directions. F_{rr} is defined as:

$$F_{rr} = f_{rr} \times M_{veh} \times g \times cos\theta \quad (4.33)$$

where f_{rr} is the coefficient of rolling resistance, which is decided according to the tyres used on a Tesla Model 3.[198] and the results from Ref. [199] and $cos\theta$ is 1 in our scenario. The traction power from the battery is formulated as follows:

$$P_{bat} = \frac{(F_{tf} * v_{veh})}{\varepsilon_p} \quad (4.34)$$

where ε_p is the powertrain efficiency which is assumed to be 0.95 [200]. The total battery power output is considered as:

$$P_{bat,total} = P_{bat} + P_{aux} \quad (4.35)$$

in which P_{aux} refers to the auxiliary power, including the power for the heat pump system, the power for the air pre-processing system, and the pump power consumption. The adopted Tesla Model S specifications and other components are listed in **Table 4.3**.

Table 4.3 Vehicle and components specifications

Parameters	Symbol	Value
Vehicle		
Cross-section area [198]	A_{cs}	1.69*1.43 m^2
Drag coefficient [197]	C_d	0.23
Powertrain efficiency [200]	ε_p	0.95
Rolling coefficient [199]	f_{rr}	0.0084
Weight [198]	M_{veh}	2100 kg
Fuel cell [125, 161]		
Fuel cell Operating temperature T_{FC}		65 ^oC
Inlet O_2 pressure	P_{O_2}	2.5 atm
Inlet H_2 pressure	P_{H_2}	2.4 atm
Number of cells	N_{FC}	40
Area of cell	A_{FC}	285.8 cm^2
Thickness of cell	l_{FC}	5.1X10^{-3} cm
Battery [167]		
Battery capacity		8 Ah
Battery voltage		4.2 V
Number of batteries		1764
Number of batteries in series for one module		6
Number of batteries in parallel for one module		21
Number of modules		14
Battery operating temperature		30 ^oC
Voltage of battery pack		352 V
Battery pack capacity		60 kWh
Other devices		
Fuel cell evaporator		
	Number of plates	110
	Plate size	120 X 330 mm^2
	Channel space	2.9 mm
Internal condenser		
	inner diameter	7 mm
	Internal area	2.086 m^2
	External area	8.344 m^2
Air preheat condenser		
	Inner diameter	8.2 mm
	Internal area	0.2865 m^2
	External area	0.3725 m^2
Inverter Compressor		
	Displacement	27 cc/rev
	Compressor speed	3000-5000 rpm

The model is validated based on the test EPA Coast-Down testing results concluded by Haye and Goodarzai [194]. The numerical results of the traction power under different vehicle speeds, shown in **Figure 4.6**, show an error within 3% compared to the test results.

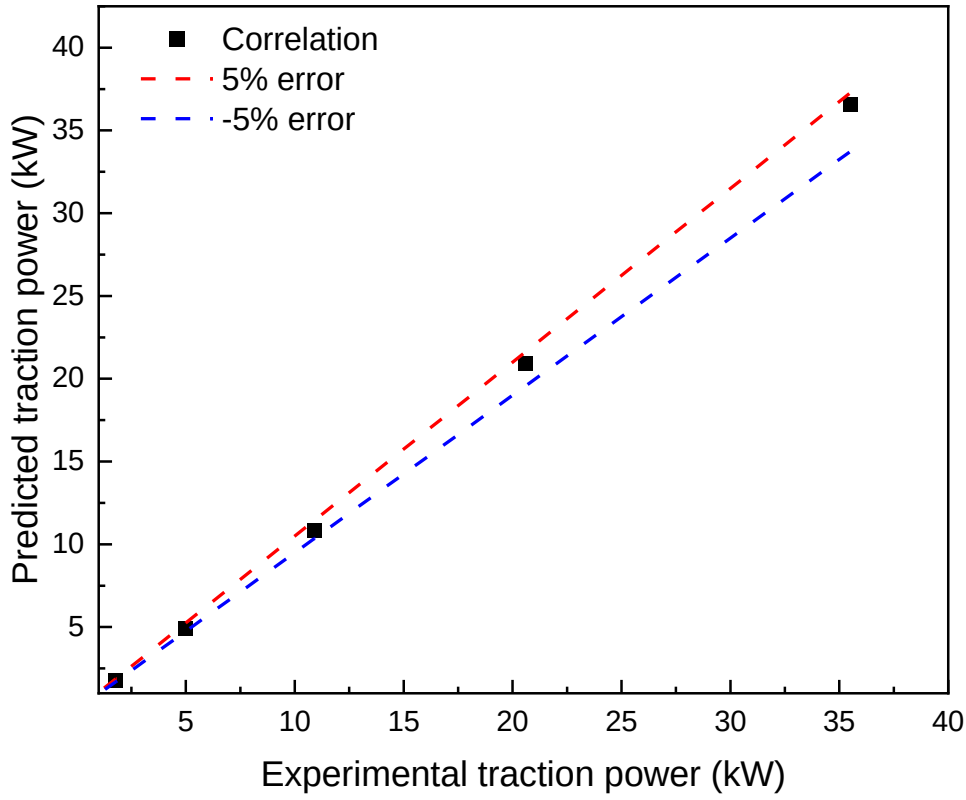

Figure 4.6. Vehicle motion model validation by comparing with experimental data in Ref. [194]

4.3.6 Energy performance indicators

Coefficient of Performance (COP) is an important indicator to evaluate the efficiency of an energy system. According to the definition of COP and the characteristic of proposed integrated system, a COP for System (COPS) is defined as below:

$$COP_{sys} = \frac{Q_{cab,heat} + Q_{bat,cool} + Q_{FC,cool}}{W_{ref,comp} + W_{air,comp} + W_{pump} + W_{fan}} \quad (4.36)$$

where $Q_{cab,heat}$, $Q_{bat,cool}$ and $Q_{FC,cool}$ are the cabin heating capacity, battery cooling capacity, and fuel cell cooling capacity respectively while $W_{ref,comp}$, $W_{air,comp}$, W_{pump} and W_{fan} represent the power consumption of the heat pump compressor and power consumption of the air compressor for the fuel cell air supply, pump power consumption,

and fan power consumption respectively. The power consumption of fan and pump, W_{fan} and W_{pump} are calculated based on Ref. [114] and it is assumed that they are linearly related to the air and coolant velocity.

The Percentage of Waste Heat Recovery (PWHR) is defined as Eq. (4.37) which is used to evaluate the impacts of the waste heat in the vehicle thermal management system:

$$PWHR = \frac{Q_{FC} + Q_{battery}}{Q_{FC} + Q_{battery} + Q_{cab_{heat}}} \quad (4.37)$$

Driving Range Extension Rate (DRER) is a comparative indicator that can intuitively reflect the ratio of Driving Range Extension (DRE) of the selected system compared to Driving Range (DR) of conventional systems. It can be expressed as:

$$DRER = \frac{DRE}{DR} \quad (4.38)$$

4.3.7 Exergy analysis and indicators

Exergy analysis is also important as it helps evaluate an energy management system meaningfully and rationally. It indicates the maximum useful work that can be achieved from the whole system when the system changes reversibly from an arbitrary state to a state in equilibrium with a given environment. The general expression exergy flow is shown below:

$$\dot{E} = \dot{m} \times [(H - H_0) - T_0(S - S_0)] \quad (4.39)$$

in which H_0 and S_0 are the enthalpy and entropy respectively according to the reference temperature T_0 which is 0℃ in this study. The exergy destruction of heat exchangers including FC plate type evaporator, internal fin-tube type condenser, external condenser, and refrigerant battery pack cold plate are calculated by Eq. (4.40) to (4.44) respectively:

$$E_{des\_eva} = m_{ref} \times [(H_5 - H_6) - T_0(S_5 - S_6)] + m_{cl} \times [(H_3 - H_4) - T_0(S_3 - S_4)] \quad (4.40)$$

$$E_{des\_inc} = m_{ref} \times [(H_{11} - H_{12}) - T_0(S_{11} - S_{12})] + m_{air} \times [(H_{18} - H_{19}) - T_0(S_{18} - S_{19})] \quad (4.41)$$

$$E_{des\_exc} = m_{ref} \times [(H_{20} - H_{21}) - T_0(S_{20} - S_{21})] + m_{air} \times [(H_{17} - H_{18}) - T_0(S_{17} - S_{18})] \quad (4.42)$$

$$E_{des\_beva} = Q_{bat} \times \frac{T_0 - \overline{T_{beva}}}{\overline{T_{beva}}} - m_{ref} \times [(H_{16} - H_{15}) - T_0(S_{16} - S_{15})] \quad (4.43)$$

where $\overline{T_{beva}}$ is the average temperature between the battery and the refrigerant. The compressor's exergy destruction, caused by mechanical and electrical losses, is defined as Eq. (4.44):

$$E_{des\_comp} = W_{comp} - \{m_{ref} \times [(H_{10} - H_9) - T_0(S_{10} - S_9]\} \quad (4.44)$$

where W_{comp} is the compressor power consumption, which is expressed in:

$$W_{comp} = \frac{(H_{10} - H_9)}{\eta_{isen}} \quad (4.45)$$

in which η_{isen} is the isentropic effiectiveness of the compressor which is assumed to be 0.67 [173]. The exergy destruction of expension valve (EXV) is desrcibed as Eq. (4.46) due to the constant enthalpy process:

$$E_{des\_exv} = m_{ref} \times T_0 \times (S_{14} - S_{13}) \quad (4.46)$$

For the fuel cell stack, except the general exergy flow metioned in Eq. (4.47), there is also chemical exergy occuring which can be calculated in terms of the following equation:

$$e^{CH} = \sum x_n \times e_n^{CH} + R \times T_0 \times \sum x_n \times ln\, x_n \quad (4.47)$$

where x_n is the mole fraction of the gas fuel. For H_2 the e^{CH} is considered as 119044 (kJ/kg) [201] and the total exergy can be expressed as:

$$\dot{E}_{H2} = m_{H2} \times \left\{ C_{p,H2} \times T_0 \times \left[\frac{T}{T_0} - 1 - ln\frac{T}{T_0} + ln\left(\frac{P}{P_0}\right)^{\frac{k-1}{k}} \right] + e_{H2}^{CH} \right\} \quad (4.48)$$

For air, it consists of 77.48% N_2, 20.59% O_2, 0.03% CO_2 and 1.9% H_2O (g) and the total exergy is shown in Eq. (4.49) [202]:

$$\dot{E}_{air,FC} = m_{air,FC} \times \left\{ C_{p,air,FC} \times T_0 \times \left[\frac{T}{T_0} - 1 - ln\frac{T}{T_0} + ln\left(\frac{P}{P_0}\right)^{\frac{k-1}{k}} \right] + e_{air,FC}^{CH} \right\} \quad (4.49)$$

and the exergy of the water produced during the reaction can be calculated as:

$$\dot{E}_{H2O,FC} = m_{H2O} \times \left\{ C_{p,H2O,FC} \times T_0 \times \left[\frac{T}{T_0} - 1 - \ln \frac{T}{T_0} + \ln \left(\frac{P}{P_0} \right)^{\frac{k-1}{k}} \right] + e_{H2O}^{CH} \right\} \quad (4.50)$$

in which the e_{H2O}^{CH} is assumed as 51.212 kJ/kg [201]. Hence,the fuel cell exergy destruction can be fomulated as:

$$E_{des,FC} = \dot{E}_{H2} + \dot{E}_{air,i,FC} - \dot{E}_{H2O,FC} - \dot{E}_{air,o,FC} - P_{FC} - Q_{FC} \quad (4.51)$$

Hence, the total exergy destrcution of the system can be described as:

$$E_{des,sys} = E_{des,eva} + E_{des,inc} + E_{des,exc} + E_{des,beva} + E_{des,comp} + E_{des,exv} + E_{des,FC} \quad (4.52)$$

In this study, the exergy analysis is carried out with respect to component level and system level, namely, component relative irreversibility rate and system exergy efficiency. The component relative irreversibility is defined as the ratio of exergy destruction of each component to the total exergy destruction of the system, while the exergy efficiency is described as the ratio of the system exergy output to the system exergy. The expressions are shown below:

$$\eta_{ir,name} = \frac{E_{des,name}}{E_{des,sys}} \quad (4.53)$$

in which, the subscripts name represents the name of the component and $\eta_{ir,name}$ is the relative irreversibility of the selected component:

$$\eta_{sys} = \frac{P_{FC} + \overbrace{E_{exc,air,out} - E_{exc,air,in}}^{net\ exergy\ output\ of\ external\ condenser} + \overbrace{E_{inc,air,out} - E_{inc,air,in}}^{net\ exergy\ output\ of\ internal\ condensor}}{\underbrace{\dot{E}_{H2} + \dot{E}_{air,i,FC} - \dot{E}_{H2O,FC} - \dot{E}_{air,o,FC}}_{System\ fuel\ exergy\ consumption} + \underbrace{W_{ref,comp} + W_{air,comp} + W_{pump} + W_{fan}}_{System\ power\ consumption}} \quad (4.54)$$

where, P_{FC} is the power generated by FC, E_{H_2} and E_{O_2}stand for the exergy input of H_2 and O_2 respectively.

4.3.8 Environmental impacts indicators

The environmental impacts of H_2 and refrigerant usage in the backup fuel cell of the proposed system can be evaluated by adopting the concept of the Total Equivalent Warming Impact (TEWI). The TEWI in this study is modified based on Ref. [203], including the

Global Warming Potential (GWP) of the refrigerant (1430 for R134a), mass of refrigerant for waste heat recovery and cabin heating, the annual emission of CO_2 due to the electricity consumption, and refrigerant leakage for chain heating. The expression of the $TEWI_{hp}$ is shown as follows:

$$TEWI_{hp} = GWP \times m_{ref_{chr}} \times \theta_{leak} \times t_{op,year} \times + GWP \times m_{ref_{chr}} \times (1-\alpha) + E_{hp} \times \beta_{elec} \times t_{op,year} \quad (4.55)$$

Furthermore, the Total Equivalent Warming Impact per Km ($TEWI_{DR}$) within one charging cycle is defined as

$$TEWI_{DR} = \left[GWP \times m_{ref_{chr}} \times \theta_{leak} \times t_{op,chr} \times N_{ch,year} + GWP \times m_{ref_{ch}} \times (1-\alpha) + P_{FC} \times \beta_{H_2} \times t_{op,ch} \times N_{ch,year} + E_{bat} \times \beta_{elec} \times N_{ch,year}\right] / DR_{total} \quad (4.56)$$

where $m_{ref_{chr}}$ is the refrigerant charging amount which is assumed to be 1.5 times the required refrigerant mass flow rate. θ_{leak} is the leakage rate of refrigerant from the heat pump and waste heat recovery system which is assumed as 4% according to the leakage rate range mentioned in Ref. [204]. $t_{op,chr}$ is the maximum operating hours of the selected scenario (6kW heating capacity) per full charging cycle while $t_{op,year}$is assumed as 100 hours per year which is 1/4 of the annual driving hours in Ref. [63]. $N_{ch,year}$ stands for the charging times per year. α is the refrigerant recovery rate (%) which is considered as 0.85 according to Ref [205]. P_{FC} is the power generation of the fuel cell stack while E_{bat} is the power consumption of the battery. β_{H_2} is the CO_2 emission factor for H_2 used by the fuel cell which is shown in Table 4.4 while β_{elec} is the average CO_2 for producing electricity which is equal to 0.193kg/kWh based on a report from the UK government [206].

Table 4.4. CO_2 emission factor for H_2 production under different methods [207]

Method of production	type	CO_2 emission factor (gCO_2/gH_2)	CO_2 emission factor for H_2 fuel cell (gCO_2/kWh)
Earth gas	Grey	7.05	375
Electrolysis of water	Mixed (black, brown)	34.68	1716
S-I cycle	Pink	10.34	1025

4.3.9 Economic analysis and indicators

The economic analysis of the system is divided into three sections which are Capital Cost (CC), Additional Capital Costs (ACC), Effective Operating Cost (EOC), and Payback Period (PP). The Additional Capital Costs (ACC) of the proposed FC backup thermal management system is defined according to the additional necessary components compared to basic EV with heat pump. The additional components and their Capital Costs (CC) are listed in **Table 4.5**.

Table 4.5 Components comparison and capital costs

Components	System in this study	Basic BEV system	Extra quantities	ACC
Cabin heating system				
Scroll compressor	●	●	0	
Water Pump	●	●	1	£53 [208]
Plate heat exchanger	●	●	Area difference	
Fin and tube heat exchanger	●	●	Area difference	
Refrigerant	●	●	Mass flow rate difference	
Pipe	●	●	0	
EXV	●	●	0	
Fan	●	●	0	
PTC	○	●	-1	£295 [209]
Liquid tank	●	●	0	
Fuel cell system [210]				
Fuel cell	●	○	1	£1234
Hydrogen tank (Type IV 350 bar)	●	○	1	£2399 [211]
Hydrogen supply system	●	○	1	£1196
Air supply system	●	○	1	£1034
Controls and instrumentation	●	○	1	£906
Electrical	●	○	1	£1956
Assembly components	●	○	1	£593
Battery system				
Battery pack	●	●	-33.7%	-£2710 [212]

The extra labour cost (ACC_{labour}) for assembly is considered 20% of the total ACC, and the cost saving in the battery pack is due to the size scaled down caused by the adopted small fuel cell stack. Hence, the ACC can be defined as:

$$ACC_{total} = \sum ACC_{name} \quad (4.57)$$

There are two aspects when evaluating EOC, and these are EOC for driving ($EOC_{driving}$) and EOC for heating (EOC_{heat}). The EOC is evaluated based on the ratio of the cost of Equivalent Effective Battery Capacity (EEBC) to the Cost Per Fully Charging (CPFC). The EEBC is defined as the available electricity in the battery pack that can be used for driving after considering the thermal management usage and FC charging. The expression of EEBC is shown below:

$$EEBC = BC - W_{hp} - W_{air,comp} - W_{pump} - W_{fan} + FC_{chr} \quad (4.58)$$

where BC, W_{hp} and FC_{chr} are the initial battery pack capacity, power comsuption of heat pump system, namely compressor power consumption, and supplemental battery capacity by fuel cell charging for a certain operating time respectively. The CPFC is calculated by the amount and the price of H_2 and electricity price needed within one fully charging cycle. The O_2 needed by FC comes from air and is considered as free of charge:

$$CPFC = M_{H_2} \times CC_{H_2} + E_{bat} \times CC_{elec} \quad (4.59)$$

where M_{H_2} is the required H_2 quantity (kg) per charging cycle for a specific operating time and E_{bat} is the total battery energy consumption (kWh). CC_{H_2} is the price of H_2 which is assumed as 3.26 (£/kg) [177], CC_{elec} is the average price of electricity which is 0.34(£/kWh) [213]:

$$EOC_{heat} = \frac{Q_{hp}}{CPFC_{heat}} \quad (4.60)$$

$$EOC_{driving} = \frac{EEBC}{CPFC_{driving}} \quad (4.61)$$

The PP calculated based on the driving range is determined by the ratio between operating cost saving and ACC_{total}.

$$PP = \frac{ACC_{total} \times t_{op} \times v_{veh}}{(EEBC_{FCBEV} - EEBC_{BEV}) \times CC_{elec} - (CPFC_{FCBEV} - CPFC_{BEV})} \quad (4.62)$$

4.3.10 Simulation procedure

The numerical simulation was conducted and coded in the MATLAB. The physical characteristics of the refrigerant R134a were obtained from REFPROP with MATLAB codes. The model included four main loops, namely, fuel cell, battery, evaporator, and condenser loop. Five independent inputs were set which were fuel cell current output, battery discharging C rate, evaporator coolant inlet temperature, ambient temperature, and subcooling degree and the associated operating range is shown in **Table 4.6**. The evaporator coolant inlet temperature variation range is set based on the operating range in Ref. [157]. The other parameters were considered as dependent variables which will be adjusted automatically with the changes in the five independent variables mentioned above, including but not limited to coolant, refrigerant and air mass flow rate, compressing ratio, outlet air temperature etc. Fuel cell temperature has the highest priority in the model. The model started with the fuel cell cooling system and evaporator in order to absorb all the heat generation from the fuel cell stack. Eq. (4.24) to (4.26) is used to calculate the conservation of energy for each loop. Only when the error is lower than 0.0001, is the system considered convergent. The assumptions made in the simulation are shown below:

(1) Fuel cell stack coolant outlet temperature was fixed i.e. 30℃.

(2) The pressure drops and heat loss across heat exchangers are neglected.

(3) The difference between the minimum temperature of the coolant in the evaporator and the R134a evaporating temperature is assumed as constant.

(4) Fuel cell stack's heat loss was ignored, but the heat loss of the battery pack was calculated under a constant air speed of 0.5m/s according to the investigated battery discharging rate.

(5) The refrigerant entered the compressor is in saturated vapour and an accumulator was installed before the compressor to make sure only gas can enter the compressor.

Table 4.6 Operating conditions in the simulation

Parameter	Value	Unit
Ambient temperature (T_{amb})	-25 to 5	℃
Coolant inlet temperature at the entrance of evaporator ($T_{cl,eva,inlet}$)	27 to 33	℃
Fuel cell current output (I_{FC})	190 to 230	A
Battery discharging rate (C_{dch})	0.19 to 0.26	C

4.4. Results and Discussion

In this section, the performance of the proposed system under different fuel cell current output, cell discharge C rate, ambient temperature, and evaporator coolant inlet temperature is evaluated from four perspectives: energy, exergy, environment, and economy. The energy performance is assessed by COP_{sys}, COP_{hp}, PWHR, DR, and DRER while exergy is evaluated by exergy destruction, relative irreversibility, and exergy efficiency from the component level. Environment performance is estimated from $TEWI_{hp}$ and $TEWI_{DR}$ aspects and for the economic performance, ACC, EOC and PP are introduced. Furthermore, for more referable results and discussion, the results in this study are compared to some reported data regarding EVASHP and PTC baselines in published literature.

4.4.1 Energy analysis

Figure 4.7 shows the impacts of fuel cell current outputs on the proposed system's energy performance regarding COP_{sys}, COP_{hp}, PWHR, DR, and DRER. In **Figure 4.7**(a), with the increase of the fuel cell current output from 200A to 230A, the PWHR varies in the range of 0.807 to 0.877. This is because of the increasing heat generation in the fuel cell stack when the fuel cell current output increases, according to Eq. (4.7). The COP_{hp} is the traditional indicator for a pure heat pump system that has always been adopted in previous heat pump research. In the proposed system, the COP_{hp} rises from 3.53 to 5.5 as the fuel cell current output increases, however, although COP_{sys} also increases, the gradient of the increase gradually decreases and the COP_{sys} starts decreasing when the fuel cell current output exceeds 225A. The main reason for the difference is that in the COP_{hp} only W_{comp} is considered and the heat output from the internal condenser is the only useful power. However, in the COP_{sys}, the power consumption of the fuel supply for the fuel cell, and the air supply for the cabin should also be considered. Moreover, from a system perspective, the heat supplied to the cabin and also the heat extracted from the fuel cell are both useful, as shown in Eq. (4.36). As a result, the COP_{sys} first increases with the increase of the fuel cell current output. However, due to the higher heating capacity and fuel cell current output, the power of the fan and fuel supply system is increased as there is an increase in air mass flow rate, H2, and air feeding rate, resulting in a decrease in the gradient of the increase and even a decrease in COP_{sys}. In **Figure 4.7**(b), it can be seen that the DR of the proposed system within one charging cycle increases from 623km to 717km when fuel cell current output varies from 200A to 230A. The increase in DR is primarily because of the rise in power

supply from the fuel cell stack to the battery and the COP_{sys} shown in **Figure 4.7**(a). Although the COP_{sys} decreases when the fuel cell current output exceeds 225A, the DR still increases as the increasing current can provide a higher supplement, compared to the increase in system power consumption. A comparison between the proposed FCBEV system and the EVASHP system in Ref. [69] and the PTC baseline is conducted in **Figure 4.7**(b). To provide the same heating capacity as the proposed system in this study, the DR of EVASHP shows a slight decrease caused by the increase in heating capacity. The DRER of the proposed system compared to EVASHP varies in the range of 0.646 to 0.911. The improvement compared to the PTC baseline is even higher and is between 0.83 and 1.16.

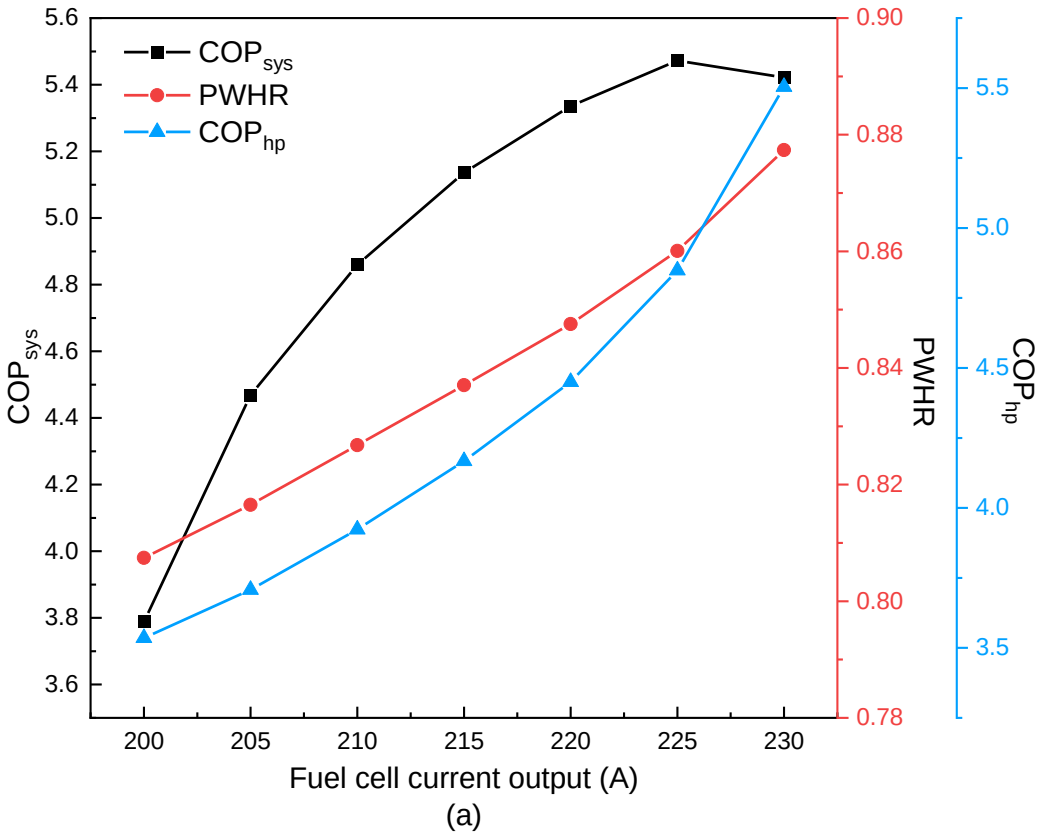

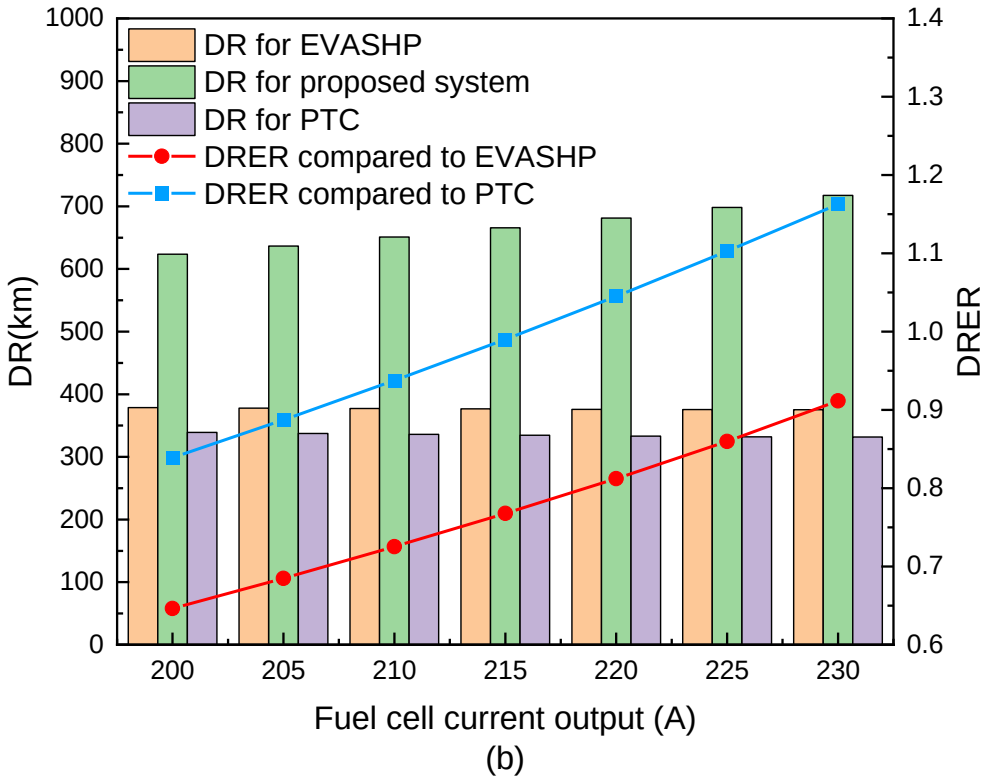

Figure 4.7. The impacts of fuel cell current output on (a) COPsys, COP and PWHR (b) DR and DRER compared with EVASHP [69] and PTC (T_{amb}=-20 ºC, $T_{cl,eva,inlet}$=30 ºC , C_{dch}=0.26)

As shown in **Figure 4.8**(a), when the battery discharging C rate increases, the COP_{sys}, PWHR and COP all increase correspondingly. The reason for the change in PWHR under different battery C rates is similar to that under different fuel cell current outputs. The increasing battery discharging C rate causes higher heat generation in the battery pack which will increase the waste heat ratio in total heating capacity. The COP_{hp} increases by 48% when the battery discharging rate varies from 0.2C to 0.29C. Apart from the extra heat provided by the battery pack, another reason is the increasing cooling demand of the battery leads to the decrease in refrigerant mass flow rate and inlet vapour quality of the refrigerant which reduces the compressor work relatively. The variation in COP_{sys} is different from that when changing fuel cell current outputs as there is no break point on the curve of COP_{sys} in **Figure 4.8**(a). The explanation of the difference is that the increasing discharging C rate will not affect power consumption of fuel cell feeding system and hence has little impact on the total power consumption. Furthermore, although the battery discharging C rate leads to a rise in waste heat, the total heating capacity slightly decreases due to the compressor limits so that the fan power consumption does not experience as greater change as when changing fuel cell current outputs. Contrary to the trend of COP and PWHR, DR negatively correlated

with battery discharging C rate. The DR of the FCBEEV in this study decreases dramatically compared to the DR of the previous EV with the ASHP system in Ref. [69]. To be specific, the DR of the previous EV with the ASHP system drops by only 12% while a 37% decline occurs in the proposed system. The reason is because as the battery discharging C rate increases, there is a corresponding reduction in the operating hours. Furthermore, the running resistance will increase in square according to Eq. (4.32) with the increasing of battery discharging C rate. However, different from traditional EVs, part of the DR of the proposed system comes from the fuel cell power supply and reduced operating hours with a fixed fuel cell power output leads to a decrease in DR. In addition, the advantage of the heat pump system also relies on the operating time which means the longer the operating time, the greater the benefits will be. Therefore, the DRER of the proposed system, compared to the EVASHP system and PTC baseline, declines with an increase of battery discharging C rate.

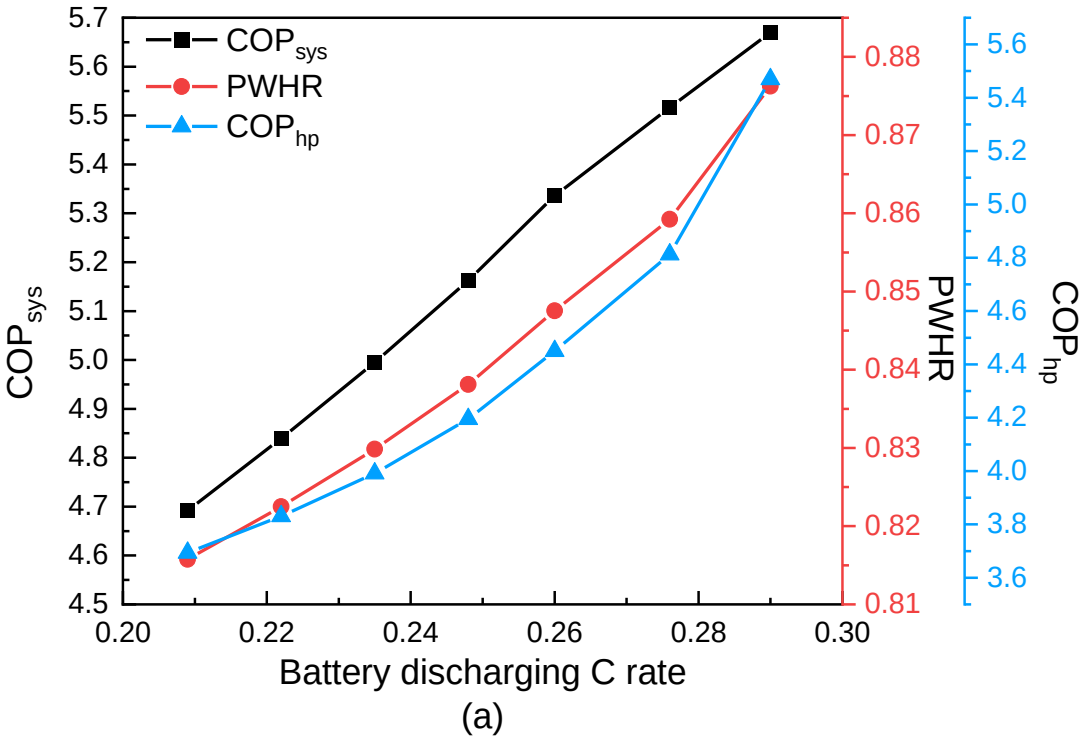

(a)

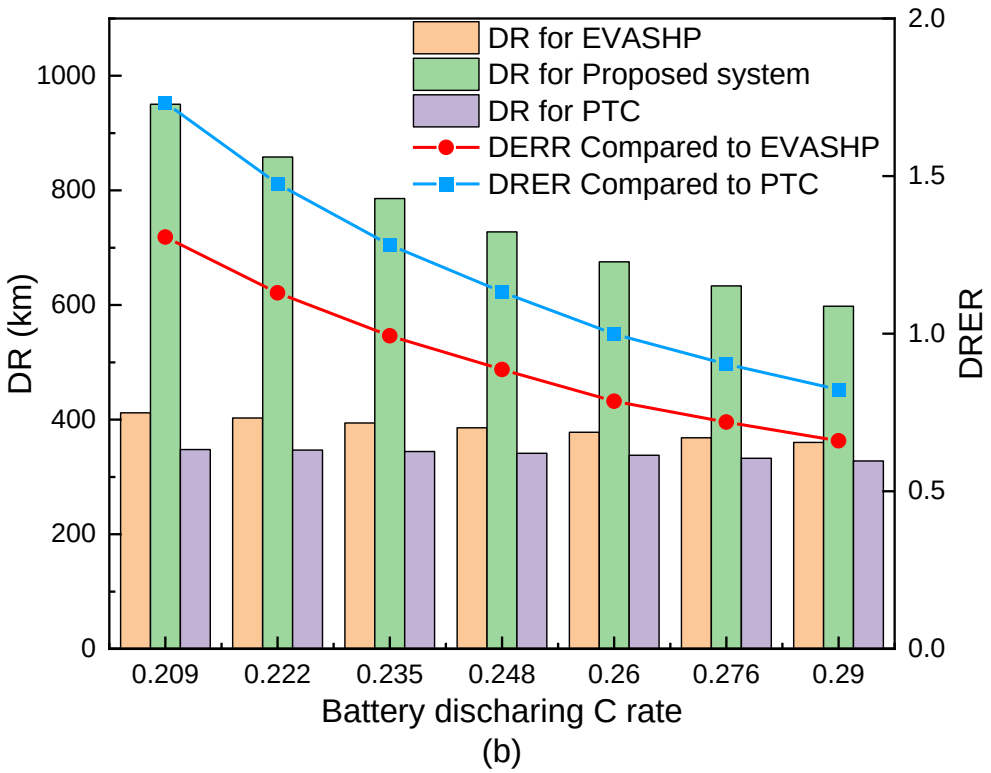

Figure 4.8. The impacts of battery discharging C rate on (a) COPsys, COP, and PWHR (b) DR and DRER compared with EVASHP [69] and PTC (T_{amb}=-20 ^{o}C, $T_{cl,eva,inlet}$=30 ^{o}C, I_{FC}=220A)

Figure 4.9(a) illustrates the relationship between ambient temperature and the performance of the proposed system. It can be concluded that the proposed system is not sensitive to ambient temperature when considering PWHR and COP_{hp} as indicators. For instance, when the ambient temperature increases from -25 ^{o}C to 5 ^{o}C, the PWHR of the system and COP_{hp} only change by 0.5% and 3.9% respectively. This is because a coolant source heat pump is adopted instead of a conventional air source heat pump and consequently the performance of the heat pump largely depends on the temperature of the coolant rather than the ambient air temperature. Additionally, the heat loss of the fuel cell stack to the ambient is ignored. However, because of the lower temperature difference between the cabin inlet air and condensing temperature while increasing the ambient temperature, the air mass flow rate increases dramatically in order to absorb the same amount of heat from the internal condenser. Hence, the COP_{sys} reduced by 7% when the ambient temperature varies from -25 ^{o}C to 5 ^{o}C. In **Figure 4.9**(b), an R134a vapour injection heat pump [176] is selected and compared to the proposed system in this study. Due to the insufficient heating capacity, a PTC heater should be applied to the reference heat pump system as a supplement. It can be seen that the DR of the proposed system is approximately 680km irrespective of how the

ambient temperature changes, and the DRER compared to the reference system is always over 0.88. It should be noted that the DR within one charging cycle of the reference system does not vary as significantly as the high battery discharge C rate and the impact of the temperature on DR will be much greater when the operating time within one charging cycle is longer.

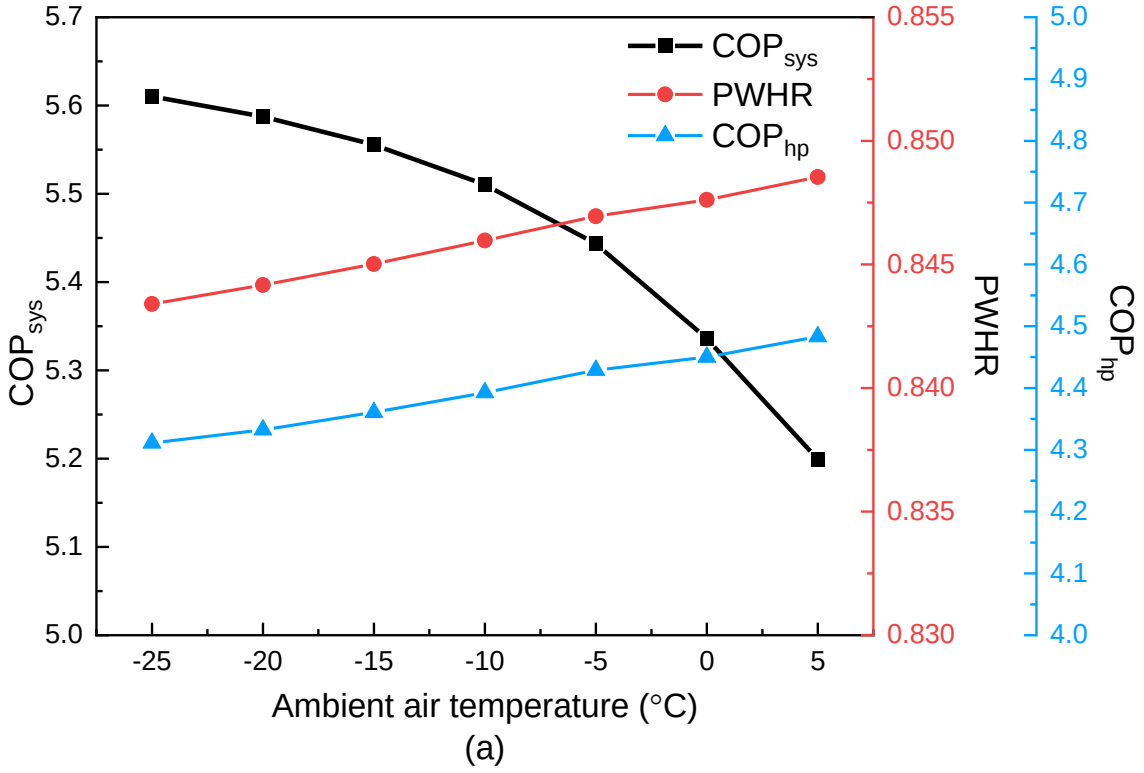

(a)

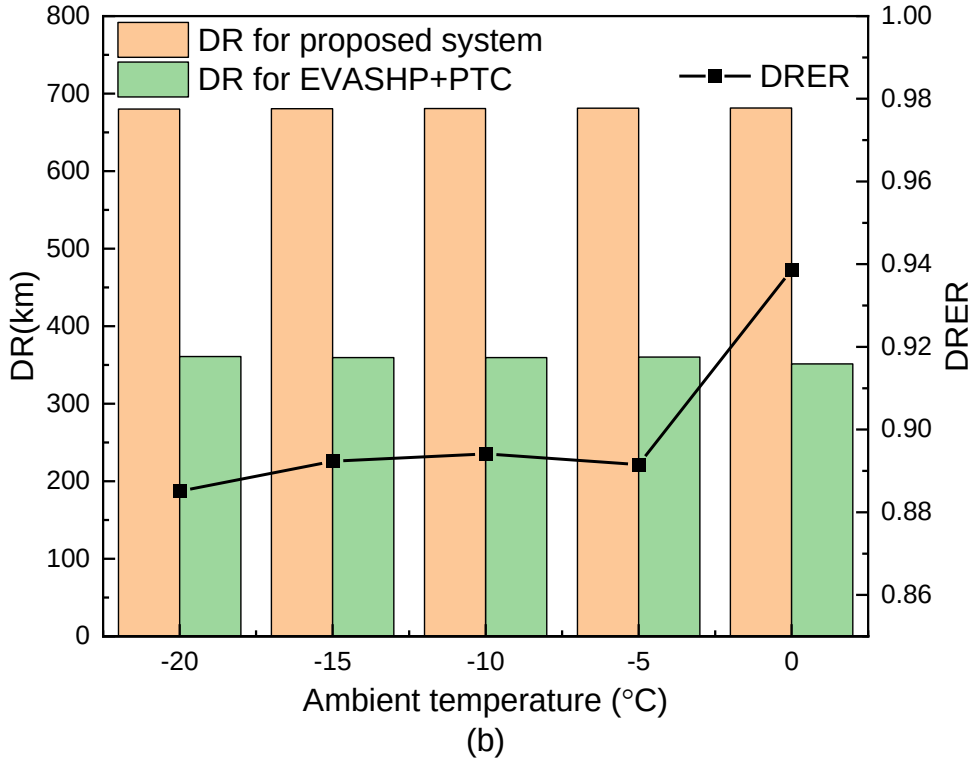

Figure 4.9. The impact of battery discharging C rate on (a) COPsys, COP, and PWHR (b) DR and DRER compared with EVASHP [176] and PTC (C_{dch}=0.26, $T_{cl,eva,inlet}$=30 °C, I_{FC}=220A)

Figure 4.10 describes the influence of the evaporator coolant inlet temperature on the system performance. In **Figure 4.10**(a), COP_{sys}, COP_{hp}, and PWHR are all positively related to the evaporator coolant inlet temperature. When the evaporator coolant inlet temperature increases from 27 °C to 32 °C, the PWHR rises from 0.79 to 0.89 correspondingly. The underlying reason is that, as the evaporator coolant inlet temperature increases, the coolant mass flow decreases and therefore the vapor mass of the post-EXV refrigerant decreases to maintain its cooling capacity. This series of changes will also reduce the refrigerant flow of the system and affect the compression ratio, thereby reducing the overall heating capacity under the condition that the waste heat remains unchanged. Similarly, with a decrease in refrigerant mass flow rate and compressor power consumption, the COP_{hp} increases by 86.8%, and the increasing rate of the change of COP_{hp} increases along with an increase in evaporator coolant inlet temperature due to the evaporator limitation. In contrast, the increasing rate of the change of the COP_{sys} shows a contrary trend compared to COP_{hp}. This is because although the power consumption of the coolant pump and compressor decreases, the cabin supply air speed should be increased to compensate for the deduction of the heat transfer coefficient of the refrigerant side of the internal condenser, according to Eq. (4.19)

and (4.26). In **Figure 4.10**(b), it can be seen that due to the variations in COP, the DR of proposed system increases by 4.5% within one charging cycle while there is no impact on the DR of EV with ASHP system and PTC baseline as they do not have backup fuel cell systems. As a result, the DRER compared to those two traditional systems varies in the ranges of 1.03 to 1.05 and 0.765 to 0.82 respectively.

The results in **Figure 4.7** to **Figure 4.10** demonstrate that the proposed system can always provide a greater DR than the previous EVs with ASHP system and EVs with PTC baseline. In addition, fuel cell current output, battery discharging C rate, and evaporator coolant inlet temperature all have significant impacts on COP_{sys} and COP_{hp}. However, the influence caused by the ambient temperature is lower compared to the other three operating parameters. The difference indicates that proposed system is not sensitive to the ambient temperature so it can provide sufficient and stable heat to the cabin even in extreme cold weather. Furthermore, it can also be concluded that optimization of the fuel cell current output, battery discharging C rate, and evaporator coolant inlet temperature can help the system achieve a better performance. Moreover, only the battery discharging C rate and fuel cell current output have substantial effects on PWHR as they are directly related to the waste heat generation. Additionally, those two parameters also have an impact on DR. The higher the fuel cell current output, the higher the DR and DRER within one charging cycle, which can effectively improve the driving range concern while the battery discharging C rate shows a contrary trend. Therefore, a suitable relationship between fuel cell current output and battery discharging C rate should be built in order to achieve optimal DR.

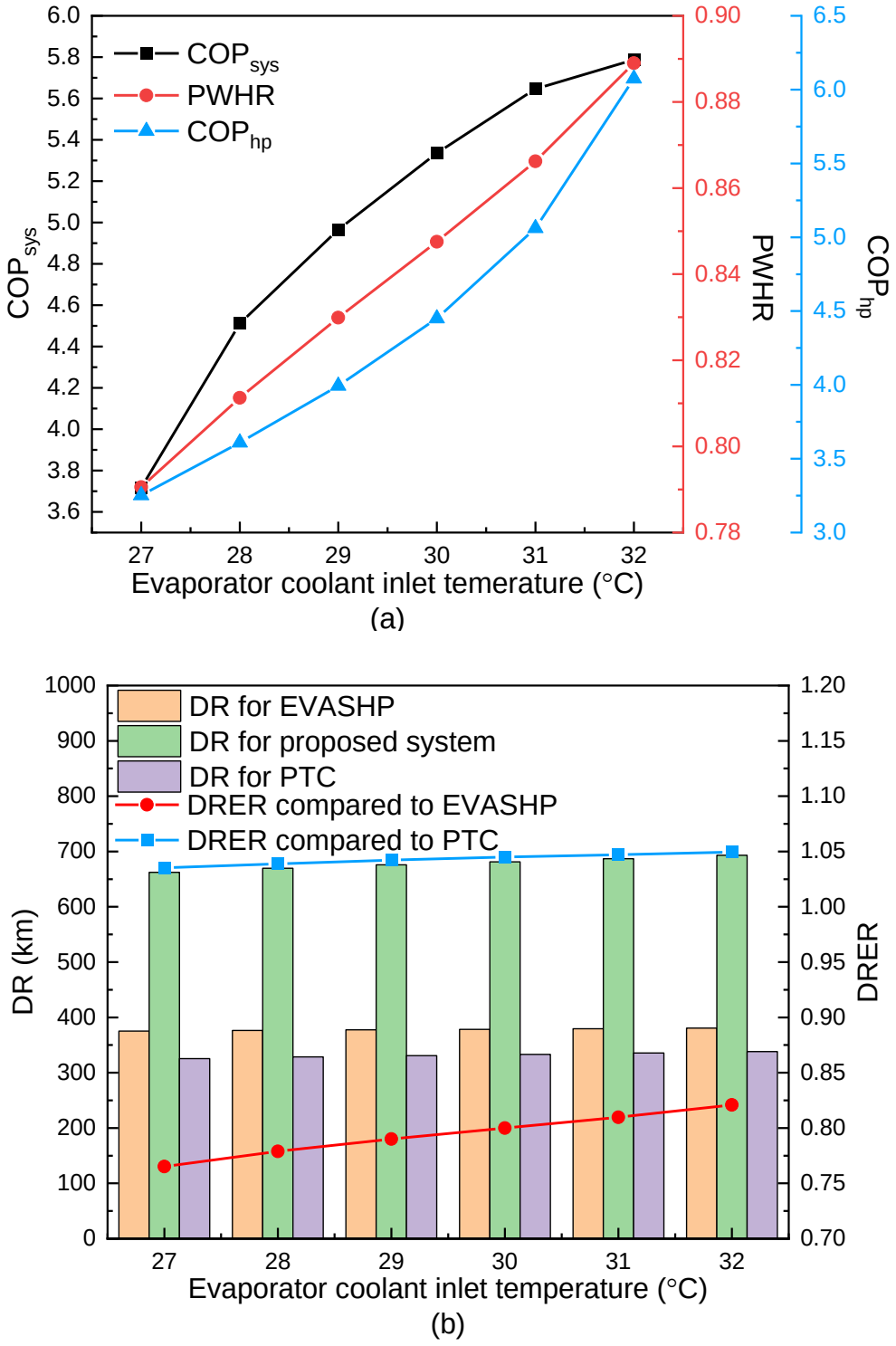

Figure 4.10. The impacts of evaporator coolant inlet temperature on (a) COPsys, COP and PWHR (b) DR and DRER compared with EVASHP [69] and PTC (C_{dch}=0.26, T_{amb}=-20 °C, I_{FC}=220A)

4.4.2 Exergy analysis

Figure 4.11 describes the exergy of the proposed system by considering it from component level and system level. As shown in **Figure 4.11**(a), the system's total exergy destruction

varies within the range 2791W to 3079W when the fuel cell current output rises from 200A to 230A. For the main components in the system, the exergy destruction of the compressor, internal condenser, EXV, and battery evaporator decrease while the exergy destruction of the evaporator, external condenser, and fuel cell increase. The reason for the increase in the evaporator is that the increasing fuel cell current output results in an increase of the $LMTD_{eva}$ due to the increasing coolant mass flow rate. Similarly, the increasing fuel cell current output directly affects the fuel supply and the output of the fuel cell stack. An increased fuel consumption will result in an increased power output, and as a result the fuel cell exergy destruction increases. With regards to the decrease in the internal condenser exergy destruction, the decreasing condensing temperature profits from a reduction in temperature difference between cabin supply air side and refrigerant side. Furthermore, lower compressor power consumption, due to the growing refrigerant mass flow rate, causes a reduction in the exergy destruction of the compressor. Consequently, with the combined effect of all the above results, the exergy destruction of the system falls. Among all the components, the internal condenser and compressor play a decisive role. It is important to highlight that the fuel cell exergy destruction is much lower than a single fuel cell system. As well as the utilization of electrical power in the proposed system, waste heat from the fuel cell stack is also adopted.

Figure 4.11 (b) and (c) illustrates the variation of the relative irreversibility of each component under different fuel cell current outputs and evaporator coolant inlet temperatures. As depicted in **Figure 4.11**(b), when the fuel cell current output increase from 200A to 230A, the irreversibility of the fuel cell suffers the greatest impact, it increases by 8.02% and always has the largest proportion of the total irreversibility. In addition, the relative irreversibility of the internal condenser, compressor, and EXV decrease by 2.8%, 4.57%, 5.8% respectively while the relative irreversibility of the external condenser and evaporator only increase by 2.03% and 4.82%. It can be seen that the relative irreversibility of the EXV is also very sensitive to the fuel cell current output as it has significant impacts on the condensing pressure and the refrigerant outlet vapor quality of the EXV. Furthermore, in **Figure 4.11** (c), the impacts of the evaporator coolant inlet temperature on the components' relative irreversibility can be observed. The relative irreversibility of the fuel cell increases dramatically by 10.6%, when the evaporator coolant inlet temperature increases from 27 ^{o}C to 32 ^{o}C. The principle behind the impacts of evaporator coolant inlet temperature is different from that behind the impacts of fuel cell current output. When the evaporator inlet temperature changes, it does not affect the exergy destruction of fuel cell as there is no

variation in its parameters. However, the total exergy destruction decreases which leads to an increase in the relative irreversibility of the fuel cell. The EXV and compressor are the second and third most sensitive components with regards to the relative irreversibility, and a deduction by 7.56% and 7.01% can be achieved respectively. The main reason for this is the substantial decrease in relative irreversibility of the EXV and the compressor which is caused by the lower discharging temperature and pressure. In **Figure 4.11** (d), the exergy efficiency is presented from a system perspective in terms of the fuel cell current output and the ambient temperature. When the ambient temperature is constant and the fuel cell current output varies from 205A to 225A, the η_{sys} increase by 2.3% due to the lower exergy destruction in the sensitive components. Furthermore, the ambient temperature also has a particular impact on η_{sys} when the fuel cell current output is constant. When the ambient temperature deceases, the η_{sys} also decreases due to the larger temperature difference between the refrigerant side and air side. For example, at 220A fuel cell current output, the η_{sys} reduces by 2.2% when the ambient temperature decreases from 0 ^{o}C to -10 ^{o}C.

From **Figure 4.11**, it can be concluded that fuel cell current output and evaporator make significant impacts on the exergy destruction and relative irreversibility by affecting internal parameters such as refrigerant mass flow rate, compressor pressure ratio, and temperature difference between the hot side and the cold side. Additionally, fuel cell current output and ambient temperature both have particular effects on η_{sys}. Potential improvements can be applied to the fuel cell stack, compressor, and internal condenser to reduce their exergy destruction in order to improve the η_{sys} or the operating parameters can be adjusted to achieve a greater η_{sys}.

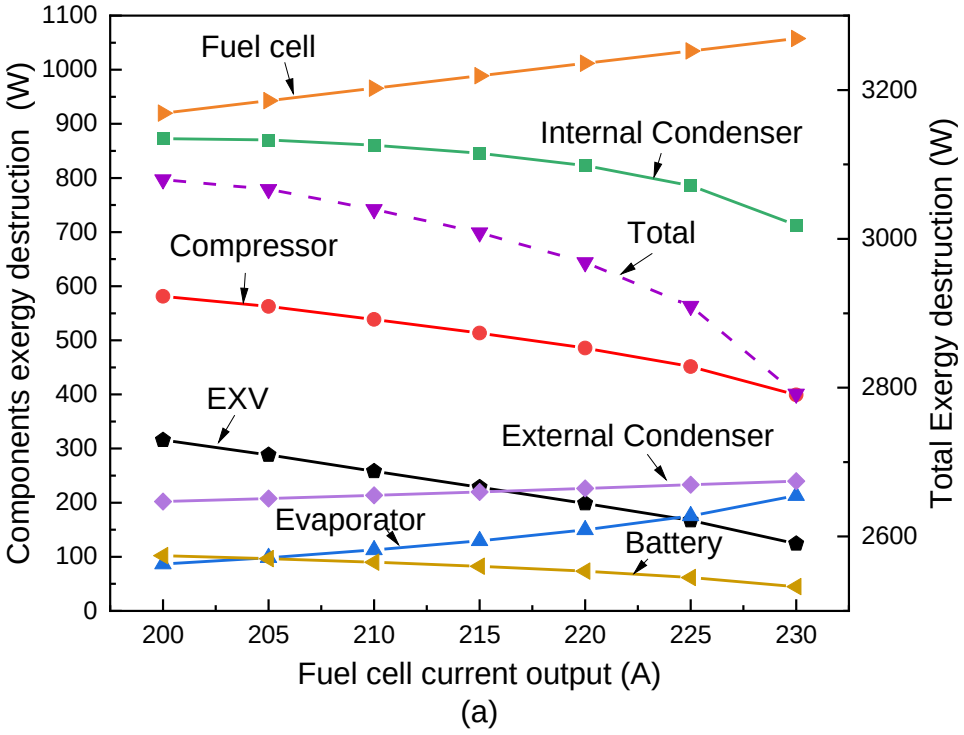
Components exergy destruction (W)
Total Exergy destruction (W)
Fuel cell current output (A)
Fuel cell
Internal Condenser
Total
Compressor
EXV
External Condenser
Evaporator
Battery
1100
1000
900
800
700
600
500
400
300
200
100
0
3200
3000
2800
2600
200
205
210
215
220
225
230

(a)

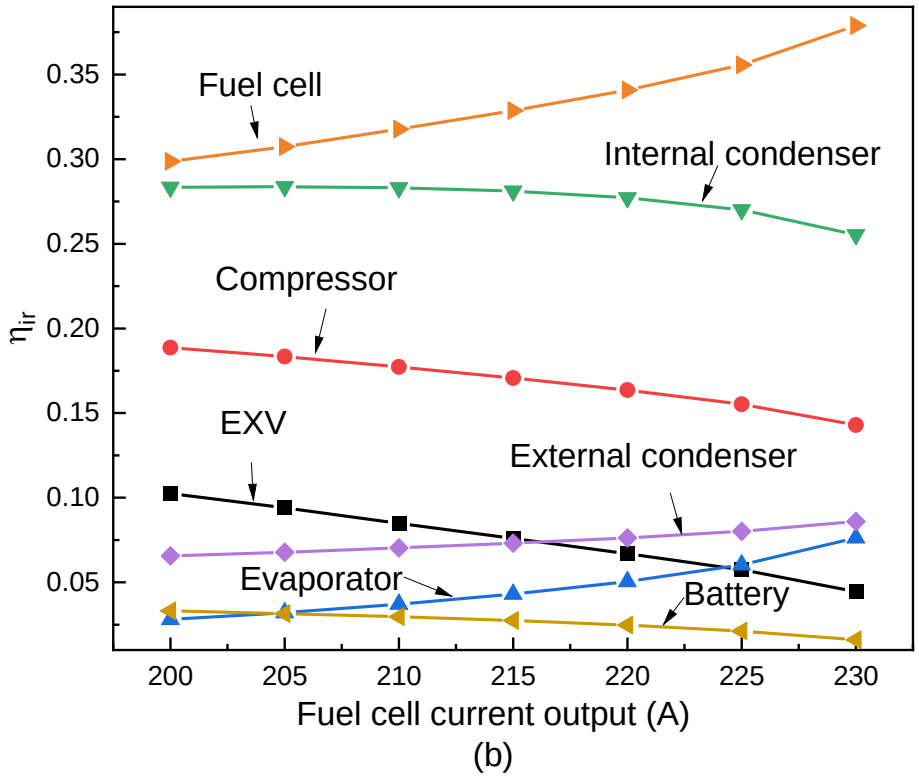
η_{ir}
Fuel cell current output (A)
Fuel cell
Internal condenser
Compressor
EXV
External condenser
Evaporator
Battery
0.35
0.30
0.25
0.20
0.15
0.10
0.05
200
205
210
215
220
225
230

(b)

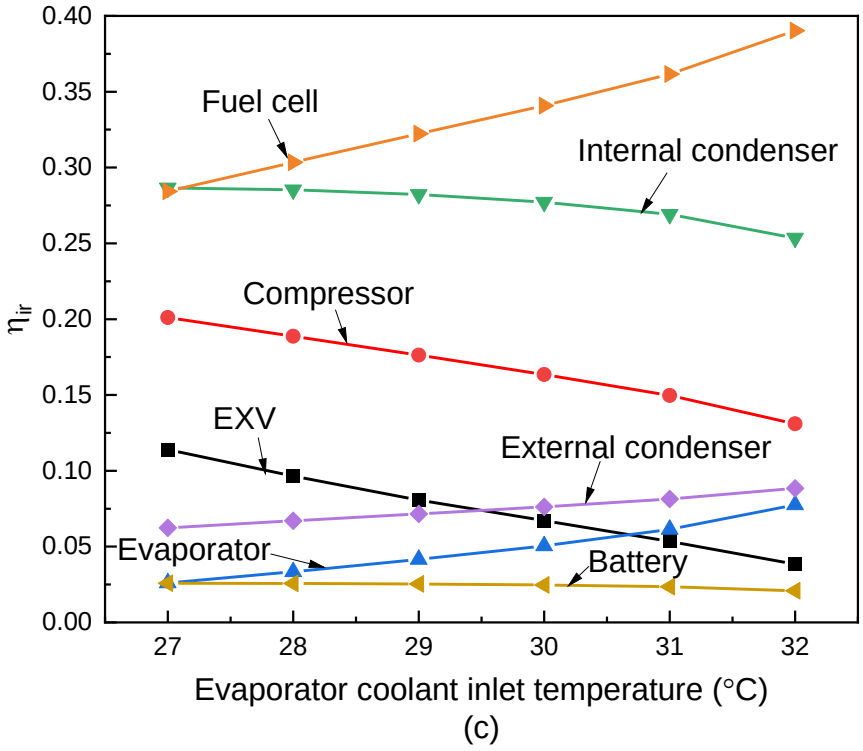

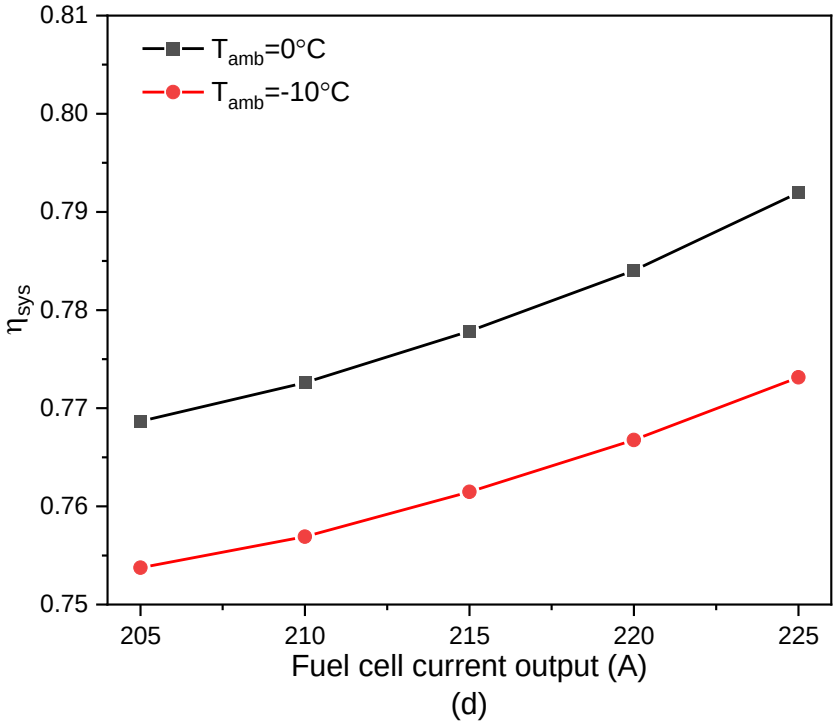

Figure 4.11. The exergy of the proposed system

(a) Exergy destruction (b) Relative irreversibility under different fuel cell current outputs (c) Relative irreversibility under different evaporator coolant inlet temperatures (d) Exergy efficiency

4.4.3 Environmental analysis

Figure 4.12 (a)-(c) describe the environmental impacts of the proposed system by introducing two indicators, namely $TEWI_{hp}$ and $TEWI_{DR}$. These two indicators assess the system from two different perspectives. The $TEWI_{hp}$ evaluates the environmental impacts from a heat pump perspective in terms of the operating hours while the $TEWI_{DR}$ analyses the environmental impacts from a macro perspective which consider the whole vehicle system in terms of the driving range. A comparison with current EV with PTC and ASHP [176] is made to demonstrate the advantages and disadvantages of the proposed system. As shown in **Figure 4.12** (a), the total $TEWI_{hp}$ of the suggested system in this study is 370.5kg while that for an EV with PTC and ASHP system is 383.8kg. Among them, the direct emissions, which represent CO_2 emissions from the leakage and recovery of charged refrigerant, accounts for 88.7% of the total $TEWI_{hp}$, however, only 46% of the $TEWI_{hp}$ of the current EVs with PTC and ASHP system belongs to the direct emissions. This is due to waste heat recovery, all of which is transferred through the refrigerant, resulting in an increase in refrigerant mass flow and refrigerant charge, consequently leading to an increase in direct CO_2 emissions. In contrast, the indirect emission of the proposed system is much lower than the reference counterpart as the COP of proposed system is much higher. However, the difference of total annual $TEWI_{hp}$ among those two systems is not substantial, only 13kg per year. Similarly, the gap in $TEWI_{DR}$ between the suggested system and reference system is also not significant. The proposed system can only achieve an improvement of 4.5% under the specific simulation conditions. Meanwhile, direct emissions of the proposed system are also higher than the reference counterpart while indirect emissions are lower. In order to further investigate the potential of proposed system on environment improvements, the impacts of GWP of the utilised refrigerant and the CO_2 emission factor for H_2 PEMFC on TEWI are discussed in **Figure 4.12** (b) and (c). As displayed in **Figure 4.12** (b), when alternative refrigerants with a lower GWP compared to R134a, which has a GWP of 1430, are adopted, the improvements on $TWEI_{hp}$ and $TEWI_{DR}$ will be greater. For instance, when the GWP of the refrigerant decreases from 1000 to 1, the $TEWI_{hp}$ of proposed system varies from 271.79kg to 42.1kg. Although the $TEWI_{hp}$ of EVs with a heat pump and PTC system can also be improved, descending from 330.33kg to 205.96kg, the gap between the proposed system and EVs with a heat pump and PTC system will be greater. The improvement rate varies in the range of 17.8% to 79.5%. This is because the vast majority of carbon emissions from the proposed coolant heat pump system are from direct emissions rather than indirect emissions, such as traditional EVASHP, as shown in **Figure 4.12 Figure 4.12**(a). Similar

impacts can be found on the $TEWI_{DR}$. The $TEWI_{DR}$ reduces by 34% when the GWP of the refrigerant changes from 1000 to 1. However, $TEWI_{DR}$ of the proposed system does not drop as fast as $TEWI_{hp}$ in conjunction with the decrease in GWP. The reason for this is because, with the exception of the refrigerant, some of the CO_2 emissions of the proposed system also come from the source of the H_2. It should be mentioned that the leakage rate is the main factor that causes the direct emissions, so if it can be well controlled, the proposed system could offer a better performance under the same conditions. **Figure 4.12** (c) depicts how the CO_2 factor of electricity and H_2 affect $TWEI_{DR}$. It can be seen that the CO_2 factor of electricity and H_2 both have substantial impacts on $TEWI_{DR}$. For example, when β_{elec} is 0.3 kg/kWh, β_{H2} is 0.24 kg/kWh, the $TEWI_{DR}$ of the proposed system and EVs with ASHP and PTC system is 0.07115 kg/km and 0.07124 kg/km respectively. However, when β_{elec} and β_{H2} is 0.1 kg/kWh and 0.04 kg/kWh respectively, the $TEWI_{DR}$ of the proposed system will be 0.04494 kg/km while that of EVs with ASHP and PTC system will be 0.0371 kg/km. Therefore, for the refrigerant R134a, only when the β_{H2} and the β_{elec} meet a specific ratio range which should at least lower than 85% in this study, the proposed system can achieve advantages in $TEWI_{DR}$ compared to reference PTC and ASHP system. It should be noted that when using lower GWP refrigerants as alternatives, the acceptable ratio range will be wider.

According to the environmental analysis, the proposed system displays a significant advantage in indirect emissions but a disadvantage in direct emissions. The GWP of the refrigerant is more important to the proposed system than the reference EVASHP and PTC system. Hence, identifying lower GWP alternatives is important to achieve both lower $TEWI_{hp}$ and $TEWI_{DR}$. Another potential method to reduce the $TEWI_{DR}$ is to reduce the CO_2 factor during the production of H_2. It should be noted that the CO_2 factor during the production of H_2 and electricity need to meet certain ratio requirements for the benefits to be gained. For some Nordic countries, the requirements of the CO_2 factor during the production of H_2 are more stringent.

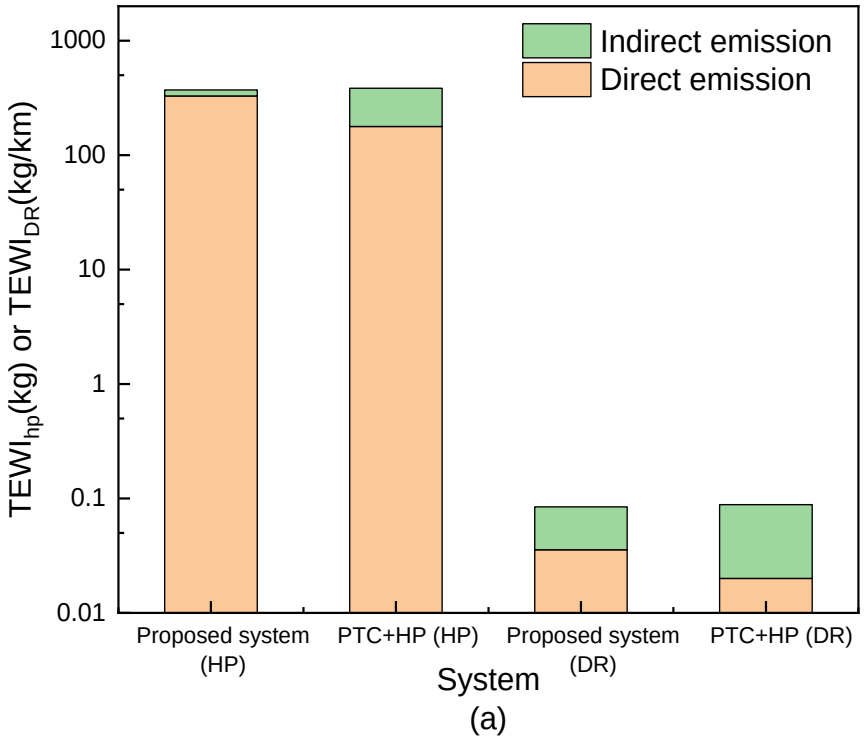
Indirect emission
Direct emission
1000
100
10
1
0.1
0.01
TEWI$_{hp}$(kg) or TEWI$_{DR}$(kg/km)
Proposed system (HP)
PTC+HP (HP)
Proposed system (DR)
PTC+HP (DR)
System

(a)

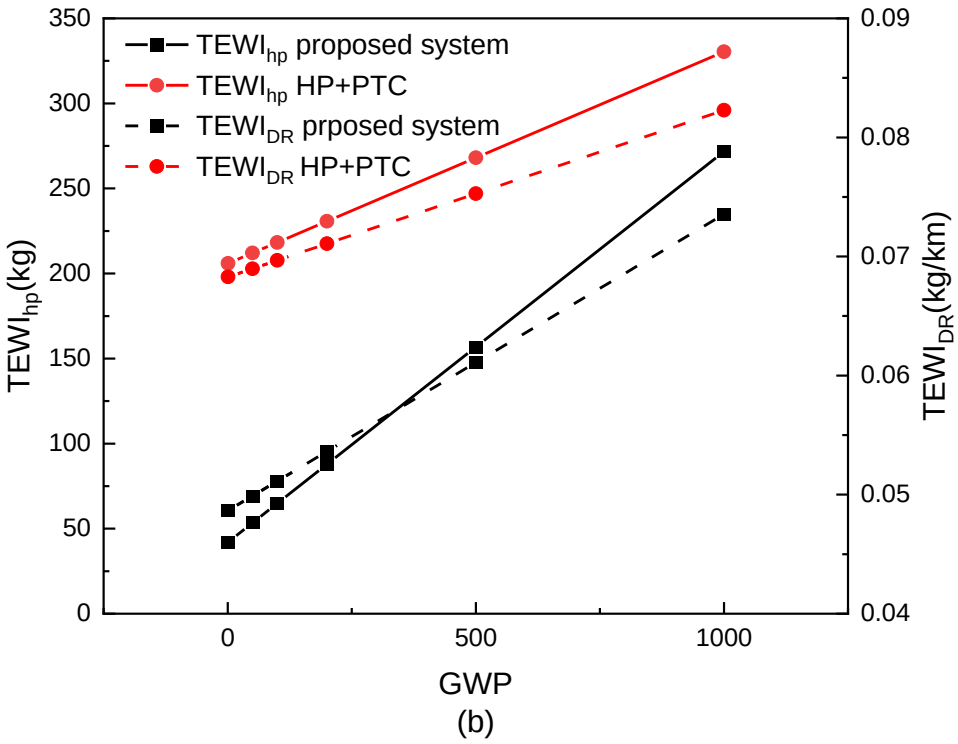
TEWI$_{hp}$ proposed system
TEWI$_{hp}$ HP+PTC
TEWI$_{DR}$ prposed system
TEWI$_{DR}$ HP+PTC
350
300
250
200
150
100
50
0
TEWI$_{hp}$(kg)
0.09
0.08
0.07
0.06
0.05
0.04
TEWI$_{DR}$(kg/km)
0
500
1000
GWP

(b)

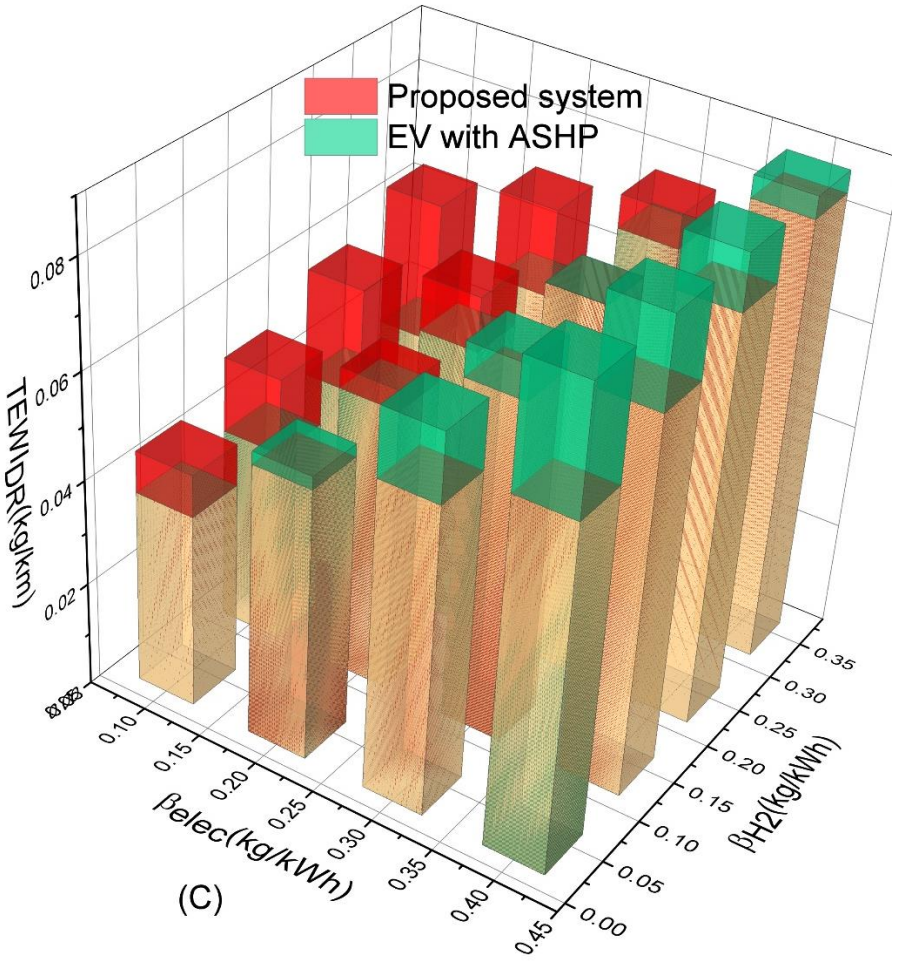

Figure 4.12. Environmental (TWEI and $TEWI_{DR}$) analysis and comparison. (a) different systems (b) different refrigerants (GWPs) (c) different CO_2 factor

4.4.4 Economic analysis

In this section, an economic analysis is carried out by investigating the $EOC_{driving}$, $EOC_{heat,}$ and PP. In **Figure 4.13** (a), a comparison of $EOC_{driving}$ and EOC_{heat} within one charging cycle under specific conditions for the proposed system, EVASHP and PTC combined system [176] and PTC system is described. For the proposed system, the $EOC_{driving}$ is 4.9kWh/£ while the figure is 3.8 kWh/£ and 3.2 kWh/£ for EVASHP and PTC combined system and pure PTC system respectively and the $EOC_{driving}$ of the proposed system is 28.9% higher than the reference EVASHP and PTC system. For the EOC_{heat}, the proposed system is 3.4% lower than the reference system but still much higher than the PTC baseline. This is because when the CPFC for the proposed system is calculated, the consumption of H_2 is also included. Although the COP of the proposed system is higher than the reference system, the reduction in electricity consumption cannot cover the increase in H_2 consumption. However, the H_2 consumption does not only provide enough heat, but also supplies power to the battery

pack to extend the driving range which leads to a higher $EOC_{driving}$ in the proposed system. Additionally, further investigation on the EOC_{heat} is conducted to understand how the H_2 price affects it. The result shows that when the H_2 price decreases from £3.26 to £0.34 the highest EOC_{heat} is 1.69 times the lowest EOC_{heat}. According to the ACC, the PP is shown in **Figure 4.13** (b). When the ACC is £8181 which is the most up to date price, the PP (measured in the driving distance) is 300,000 km based on the most up to date H_2 price. However, when the H_2 price is equal to the current electricity price, the PP reduces to 205,000 km. If the ACC of £4000 can be achieved through a decrease in price of the fuel cell system, the PP at the H_2 price of £3.26 and £0.34 will be 150,000 km and 100,000 km respectively. Considering the typical lifespan of a vehicle which is 250,000–300,000 km or 25 years [214], the proposed system just reaches the upper limit. For commercial vehicles, the annual driving distances can reach 80,000 km to 10,000 km per year [215]. Therefore, a reduction in the cost of the fuel cell system or the H_2 price, would allow the PP to be more competitive and attractive, particularly for commercial vehicles.

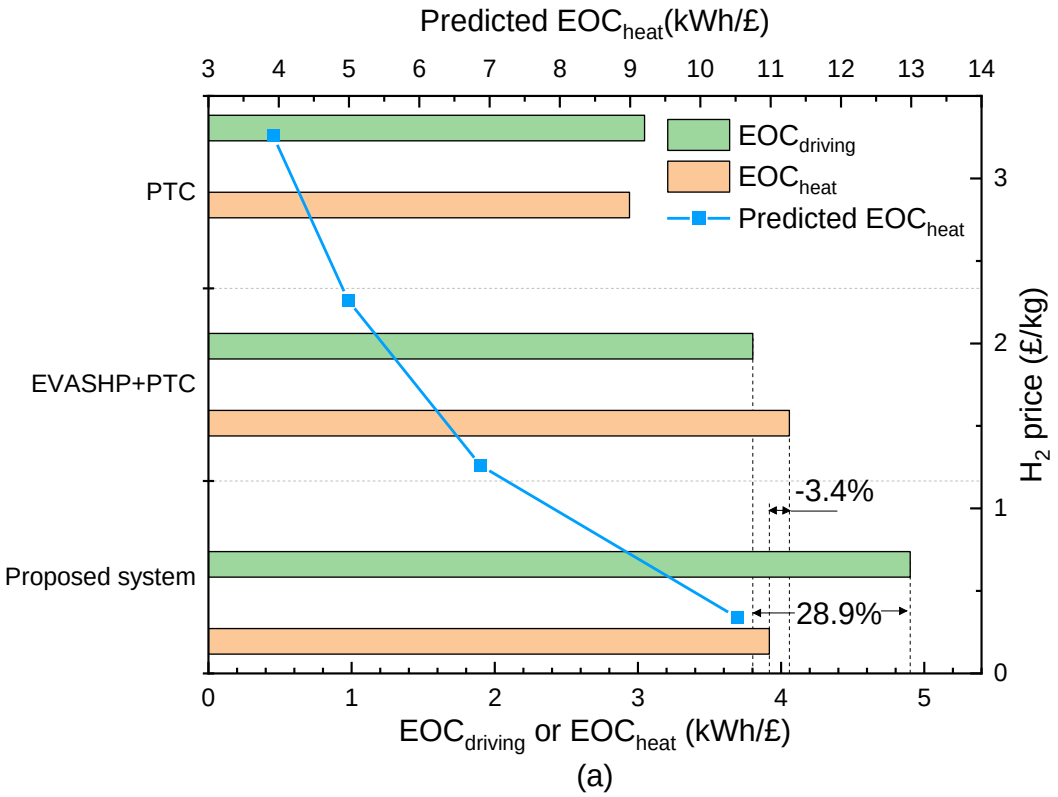

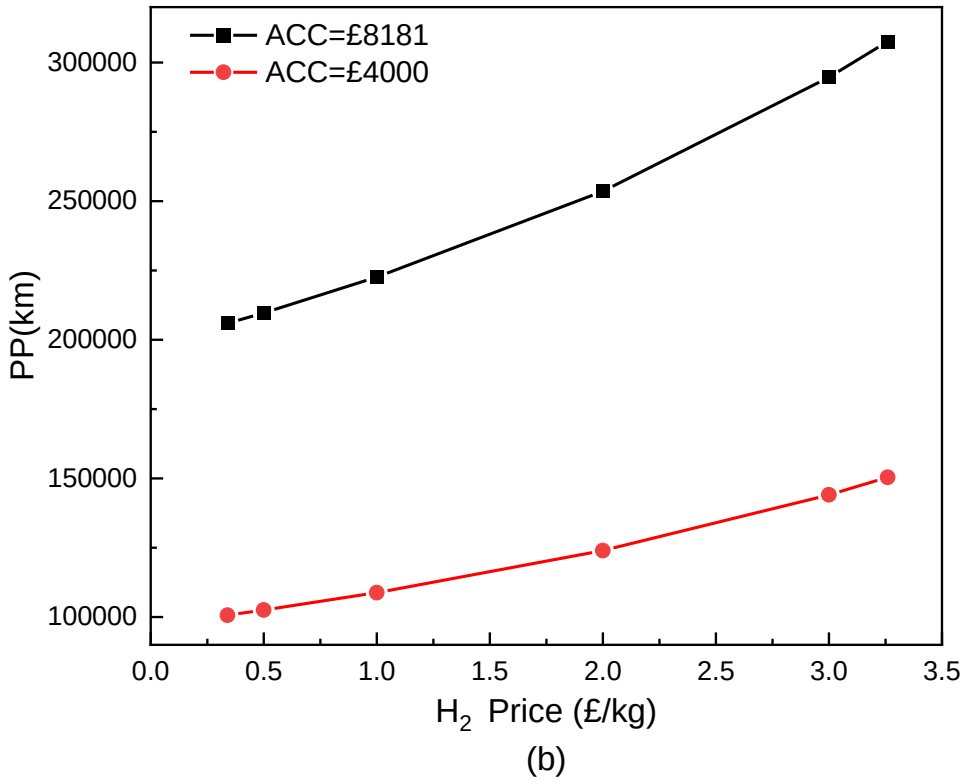

Figure 4.13. Analysis of system economic performance. (a) $EOC_{driving}$ and EOC_{heat}, (b) PP (C_{dch}=0.26, $T_{cl\_eva\_inlet}$=30°C, I_{FC}=220A, T_{amb}=0°C)

4.5 Chapter Summary and Outlook

In this study, a highly integrated heat pump assisted battery electric vehicle with fuel cell backup energy management system was proposed and evaluated to improve the heating performance in extreme cold climates and eliminate anxiety associated withdriving range. A numerical model was developed, and the results were compared to the existing published systems. A detail assessment from energy (COP_{sys}, COP_{hp}, PWHR, DR, DRER), exergy (E_{des}, η_{ir}, η_{sys}), environment ($TEWI_{hp}$, $TEWI_{DR}$) and economic ($EOC_{driving}$, EOC_{heat}, PP) (4E) perspectives was introduced in terms of different operating parameters.

- The proposed system can continuously provide 6kW heating capacity with a PWHR over 0.8, and a COP_{sys} over 3.8 when considering the combined thermal management requirements for FC, battery, and cabin heating.
- The DRER of the designed system is at least 1.64 times the DRER of the reference EVASHP and 1.82 times the PTC baseline when providing the same amount of heat to the cabin. The maximum value of DR and DRER is highly dependent on the I_{FC} and B_{dch}, and it was determined that B_{dch} has a greater impact. The proposed system

can always provide a stable heating load to the cabin with high COPsys by utilizing the waste heat from the battery pack and fuel cell stack. Meanwhile, the driving range is extended compared to vehicles that only have PTC or EVASHP thermal management systems. Great potential for improving the environment and lower operating costs can be achieved compared to vehicles with traditional thermal management systems. Details are concluded below:

- The exergy efficiency of the proposed system varies between 0.7 to 0.8 and it decreases with a decrease in ambient temperature but increases with an increase in fuel cell current output.
- Environmental analysis demonstrates that direct emission accounts for 88.7% and 43% of the total $TWEI_{hp}$ and $TEWI_{DR}$ respectively for the proposed system while direct emissions only account for 46% and 22% respectively for the reference EVASHP and PTC system.
- A lower GWP for the selected refrigerant will result in a greater improvement on the TWEI for the proposed system. Meanwhile, the ratio between β_{H2} and β_{elec} should meet a certain ratio in order to allow the proposed system to achieve a lower $TEWI_{DR}$ compared to the reference system, which in this case is, at most, 85%.
- The $EOC_{driving}$ and the EOC_{heat} of the proposed system is 4.9kWh/£ and 3.91 kWh/£ respectively at the simulation condition. This is 28.9% higher but 3.4% lower than the reference EVASHP system and 62% and 32.8% higher than the PTC baseline.
- The PP of the proposed system calculated based on the most up to date H_2 price when comparing to current EVs with ASHP and PTC is 300,000km. However, it will reduce to 100,000km when the price of H_2 is the same as electricity and the ACC of the proposed system is halved.

Going forward, further performance optimization should be conducted, and other components' heating or cooling demands considered. Different low GWP refrigerants should be applied and analysed in order to achieve lower environmental impacts. The optimal fuel cell size and fuel cell current output should be investigated to lower the capital cost and payback duration and increase the performance. Furthermore, a dynamic model could be built in Matlab Simulink and tested under widely adopted test cycles, such as Worldwide Harmonized Light Vehicles Test Cycle (WLTC). The main aim is to consider fuel cell and battery output and SOC together, in order to better understand the dynamic performance under different operating conditions. A test rig could be built to evaluate the

practical performance and optimize our model. The cooling performance of the proposed system in the summer should be investigated and be compared to current published systems. The previous two chapters have demonstrated that the proposed system can provide stable heating capacity with high efficiency at low ambient temperature, extend the driving range, and also have an acceptable payback period. As mentioned at the end of Chapter 2, it is also necessary to design a new integrated VTMS for summer to reduce the energy consumption caused by the cooling system. Therefore, in the next chapter, a design of VTMS for cooling systems will be provided and evaluated in order to offer a comprehensive solution for future VTMS.

5. Hybrid Integrated Cooling System for Fuel Cell Extender Electric Vehicle

5.1 Introduction

After COP26, there has been a global focus on limiting global warming to +1.5 ^{o}C compared to the pre-industrial era. However, the progress still falls short of the previous goal of controlling warming to under +2 ^{o}C [216]. Hence, all governments now acknowledge the necessity of reducing the use of fossil fuels to reduce Greenhouse Gas (GHG) emissions. In the EU, road transport is heavily dependent on fossil fuels and accounts for 22% GHG emissions [217]. As a result, vehicle decarbonization through electrification has been worldly recognised as the future development tendency for the transport sector in order to reduce GHG emissions by 40% by 2030. However, the shift to electric vehicles has been slower than expected, especially in Europe and the United States, which account for only 20% of global EV sales in total [218]. One of the main reasons for the slow implementation of electric vehicle is driving range anxiety. Additionally, the energy consumption caused by the HVAC system in EVs cannot be neglected. Different from traditional Internal Combustion Engine (ICE) vehicles, the HVAC system in EVs is not only responsible for cooling the cabin in summer but also plays a key role in the vehicle's thermal management system, such as keeping battery and electrical devices within their optimal operating conditions.

The average energy consumption for cabin cooling ranges from 2000W to 4000W when the ambient temperature ranges from 30 ^{o}C to 50 ^{o}C [219]. The peak transient energy consumption for the HVAC system can reach 7800W at mid-day in summer [220]. Recently, research about the performance of EVs' HVAC system has largely focused on the performance of low Global Warming Potential (GWP) refrigerants and advanced control logic as the structure and logic of the HVAC in EVs for cabin comfort as there is no significant difference compared to that in ICE vehicles. Xie *et al*. [221] proposed a two-layered control strategy and compared it to the conventional rule based controllers, for example. The results show that the developed control strategy can improve energy consumptions by 30.2% and 12.4% respectively compared to the on-off controller and proportion-integral-derivative (PID) controller. Meng *et al*. [222] evaluated the performance of the R1234yf/R134a mixture when applied to an automotive air conditioning system. The results indicate that the adopted mixture can provide similar cooling capacity but with a

lower COP compared to using pure R134a refrigerant and the GWP is higher than the pure R1234yf. Fang *et al*. [223] evaluated the cooling performance of a mobile transcritical CO_2 air conditioning system with an internal exchanger. The proposed system could provide cooling capacity up to 4500W and the COP was 1.7, which is lower than the current widely adopted refrigerant R134a air conditioning system. Therefore, with increasingly strict refrigerant GWP regulations and the usage of low GWP refrigerants, the energy consumption for cabin comfort in summer will increase. The inhomogeneity of the temperature field in the cabin when using traditional automobile HVAC system is huge, especially at the air outlet of the air conditioner. This is because of the dehumidification characteristics of the traditional air conditioner, the temperature must reach the dew point temperature, which is far lower than the set temperature of the cabin. This cold air can blow directly on the driver and passengers and cause discomfort. Normally, a pre-heater is installed before the air outlet to compensate for the deep cooling process in traditional air conditioning systems [224]. Alahmer *et al*. [225] introduced an evaporative desiccant cooling and dehumidification system to the vehicle air conditioning system and achieved a COP of 0.7 to 0.9 due to the required heat for regeneration, but the COP would be 3.5 to 4.5 if waste heat can be utilised. However, the proposed system by Alahmer et al. has some drawbacks, including an increase in weight due to the water tank. Membrane based liquid desiccant dehumidification is an alternative to evaporative desiccant cooling and dehumidification system which can provide dehumidification and cooling together but omit the evaporate cooling process. Chen *et al*. [226, 227] investigated the performance of the KCOOH cross flow membrane based liquid desiccant air conditioning system. The results indicated good air moisture removal rate and a certain degree of cooling effect. However, the system's cooling effect is highly dependent on the operating temperature of the solution. And the massive heat requirement for solution regeneration makes it hard to be applied to vehicles. Metal-hydride cooling systems have recently drawn the transport sector's attention and is under consideration as a replacement to the traditional automobile air conditioning system [131]. For fuel cell vehicles, with the traditional air conditioning, only the cabin thermal management would cause a reduction of driving range by 17.3% under New York urban driving cycle when the ambient temperature is 35 ^{o}C [228]. Considering the battery pack and cabin thermal management together, Deng *et al*. [229] designed an integrated system thermal management for plug-in fuel cell electric vehicle with an implementation of the soft actor-critic algorithm. They conducted that 28.12% or even more energy was consumed by the prolonged operation of air conditioning system. Farsi *et al*.[230] proposed an integrated air-based thermal management system for PEMFC-assisted battery electric vehicles in cold weather. The cold air entering the battery pack not

only can keep the battery temperature but also can be supplied to the fuel cell. The fuel cell efficiency could be improved by 3% when the supplied was preheated from 10 ºC to 40 ºC. Similarly, Xu *et al*. [231] also built an integrated system for fuel cells and battery thermal management system for hot weather at 40 ºC degree. The supplied air for the fuel cell was pre-heated by a motor, air compressor, and other electronic components. But the battery pack was still cooled down by the traditional AC system. The results only demonstrated the feasibility of the system but did not mention the efficiency and energy consumption of the system. However, neither Farsi's nor Xu's integrated systems considered the cabin thermal management together. Although Li *et al*. [232] built a vehicle thermal management system for cabin comfort by using waste heat from the fuel cell and battery packs, they only considered using the waste heat for heating mode and no improvement for cooling performance. They concluded that 505.68g H_2 was consumed by the proposed cooling system when the ambient temperature was 34 ºC. To further reduce the cooling energy consumption in summer, metal-hydride cooling systems have recently drawn the transport sector's attention as a replacement for the traditional automobile air conditioning system [131]. However, currently, most of the studies focus on applying the hydrogen storage characteristics to the fuel cell vehicle [233, 234] and integrated with fuel cell to provide required heat for the desorption of the metal hydride. Few studies tried to utilise its thermal characteristics for cooling. Di Giorgio *et al*. [235] introduced a new battery thermal management system by integrating it with metal hydride tank for fuel cell hybrid electric vehicles. The proposed system can successfully reduce the battery temperature by 15 ºC. Meier *et al*. [236] introduced a metal hydride based cooling system for electric vehicle with a fuel cell range extender. They predicted that the proposed system has the potential to reduce the impact of the sensible heat to around 15% resulting in a cooling power of 21% of the generated electricity with specific mass ratio. Weckerle *et al*. [132] developed an open-metal-hydride system with an integrated a fuel cell in order to utilise the energy waste during the pressure drop between the H_2 supply procedure from hydrogen vessel to the fuel cell stack. The experimental results revealed that the system can provide 276 $kW/MH_{(kg)}$ while providing 7kW electric power. However, the performance of the proposed system was affected by the temperature difference between absorption and desorption temperature. Thermal loss occurs when the two metal hydrides work alternately, resulting in a 17% loss of cooling capacity within one cycle, even showing negative effects in the first 20 seconds of the cycle [133].

However, unlike the ICE vehicle, cabin thermal comfort in zero emission vehicles cannot be considered separate from the battery and other electronic devices. Hence, the integrated thermal management system for zero emission vehicles in summer attracts the attention of researchers. Ma et al. [154] experimentally studied the performance of the integrated thermal management system for pure electric vehicles. They emphasized that vehicle level thermal management is necessary from the battery safety perspective even at normal operating conditions. However, that movement would impose more work to HVAC system and require the use of an additional 10.34kWh more energy compared to separate cooling systems. Xu *et al*.[237] studied the range impact of a vehicle level thermal management system which integrated battery coolant and cabin air system together with a refrigerant loop. The proposed model was built based on the parameters of the Tesla model S and model 3. The results demonstrated that the EV range reduced by 38%-45%. Zou *et al*. [108] investigated the performance of an air conditioning system coupling with battery cooling. They demonstrated that with the increasing ambient temperature, more energy will be consumed. Consequently, when the battery output was 0.3C (350W) and 0.8C (850W) the air conditioning system required 42.5% and 18.8% of the total battery capacity. This means, for urban operating conditions, the air conditioning system will consume a significant amount of battery capacity. It should be noted that Zou *et al*. highlighted the potential utilisation of battery waste heat to pre-heat the deep cooling supply air and recommended that it should be further investigated. Gillet *et al*.[238] investigated a multi-evaporator and chiller air conditioning and battery cooling system. A COP of 3.88 and a cooling capacity of 7650W could be achieved when the battery cooling loop was deactivated. However, with the increase in battery cooling demands, the front evaporator tended to be insufficient due to the predominance of the chiller side. This arrangement will sacrifice the cabin's thermal comfort to some extent. Although increasing the total refrigerant mass flow rate could solve the problem, the energy consumption for the thermal comfort will increase correspondingly. Overall, the current HVAC based vehicle thermal management system for zero emission vehicles can require up to 45% battery capacity in hot climates and the value would be much higher with the promotion of low GWP refrigerants and the desire for high-level cabin thermal comfort. Liquid desiccant dehumidification is a good alternative method to avoid deep cooling, increase the thermal comfort level, and supply more fresh air. But the heat required for solution regeneration and how to manage it from a vehicle perspective needs further investigation. Metal hydride cooling systems attract significant attention because of their clean and non-compressing cycle. However, few studies focus on the cooling performance of metal hydride integrated cooling systems for zero-emission vehicles and the

duration of cooling load fluctuations at the beginning of the metal hydrides' transitions from absorption to desorption is long when the cooling load is only provided by the metal hydride system. Moreover, the size of the metal hydrides limited by the cooling power-to-weight ratio is also a main barrier to implementing a metal hydride system. Although some scholars have tried to improve thermal management performance by building an integrated system, the wasted energy has not been fully utilized, and the deduction of driving range is still significant.

In this context, in order to provide stable cooling capacity to cabin, battery, and electronic devices and increase the cabin thermal comfort level but eliminate the driving range deduction, a metal hydride assisted, heat pump supplement liquid desiccant thermal management system for an electric vehicle with a fuel cell backup is proposed in this study. An open-metal-hydride system is designed between the hydrogen vessel and fuel cell stack to provide cooling effects to the liquid desiccant. A liquid desiccant system with low temperature solution is adopted to cool and dehumidify the air to the set point. A heat pump utilises the waste heat for solution regeneration and also works as a supplement for the system. The proposed system has two operating modes in this study which are the non-compressing mode and heat pump supplement mode. Numerical modes for two separating modes are developed in MATLAB and validated based on experimental or published results. At the end of the study, the performance of these two operating modes is evaluated in detail and compared with conventional systems in terms of COP and cooling capacity.

The key innovation of this work is by proposing an integrated system that can provide cooling effects removing the normal dependence on the vapour compression system meeting the cooling requirements of cabin cooling, battery cooling, electronics cooling, and high-level thermal comfort, contributing to the technological development of new cooling energy system for the electric vehicle. In the proposed system, the deep cooling process is not needed, the COP is higher compared to the tradition Air Conditioning System. And the temperature fluctuation can be shortened to improve thermal comfort and efficiency. Furthermore, with the supplement of the heat pump air conditioning system, the proposed system could limit the size of the open metal hydride system. Moreover, the proposed system not only can be used for onboard vehicles supporting the development of Future Zero Emission vehicles but will also be of interest for domestic cooling and electricity cogeneration.

5.2 System Description

In **Figure 5.1**, the working principle of the proposed fuel cell and open metal-hydride based, heat pump assisted liquid desiccant cooling, dehumidification and regeneration system for FCBEV is illustrated. The proposed system contains four subsystems which are open hydride cooling system, fuel cell and battery energy system, heat pump, and liquid desiccant cooling, dehumidification and regeneration system. Among them, the open metal-hydride cooling system and fuel cell and battery energy system are depicted in **Figure 5.2** while the heat pump and liquid desiccant cooling, dehumidification and regeneration system are shown in **Figure 5.1**. The liquid desiccant, after the desiccant cooler (port 12), flows through the open metal-hydride cooling system to acquire cooling loads. If the temperature of the liquid desiccant meets the set point at the exit of the open metal-hydride cooling system, the liquid desiccant can be pumped to a hollow fibre dehumidifier to process the cabin inlet air directly. However, if the cooling loads provided by the open metal-hydride are not enough, the liquid desiccant should pass by the evaporator first before entering the hollow fibre dehumidifier in order to release heat to the refrigerant side of the heat pump system. The outlet liquid desiccant from the hollow fibre dehumidifier is split into two streams, the main one flows through the condenser to extract heat while the other one enters the inter cooler for the fuel cell coolant loop to absorb heat when the waste heat from the battery pack is insufficient for regeneration. The high temperature liquid at port 9 undergoes a heat and mass transfer procedure with ambient air in the hollow fibre regenerator in order to reach the set concentration and then flows through the desiccant cooler, if further cooling is required. In the heat pump subsystem, a traditional cycle containing a chiller, evaporator, accumulator, compressor, condenser, and an electric expansion valve (EEV) is utilized. Refrigerant enters the chiller from port 23 aiming to absorb the waste heat from the battery pack and fuel cell stack (optional). The status of the refrigerant at the outlet of the chiller is controlled by the evaporator. If the evaporator is operating, the refrigerant at the outlet of the chiller is in a mixed state, otherwise it is in a superheated vapor state. After being compressed by the compressor, the hot and high-pressure vapor refrigerant releases the waste heat to the desiccant side and is then throttled by the EEV and the cycle is finished. For the fuel cell and battery coolant side, the fuel cell coolant and battery coolant flow out of the subsystem in parallel. The battery coolant flows along route 14-15-16-17. However, the fuel cell coolant has two streams. The mainstream flows along 18-19-20-21-22-13 while the bypass flows along 18-15-16-13. In the mainstream, the fuel cell coolant first passes the inter-cooler in order to be initially cooled down by the low-temperature desiccant and then flows past the

coolant cooler to further reduce the coolant temperature to the set point by using ambient air. It should be mentioned that the bypass can only be accessed when the desiccant temperature for regeneration is not sufficient. The air flow across the coolant cooler will be utilized in the open metal-hydride cooling system.

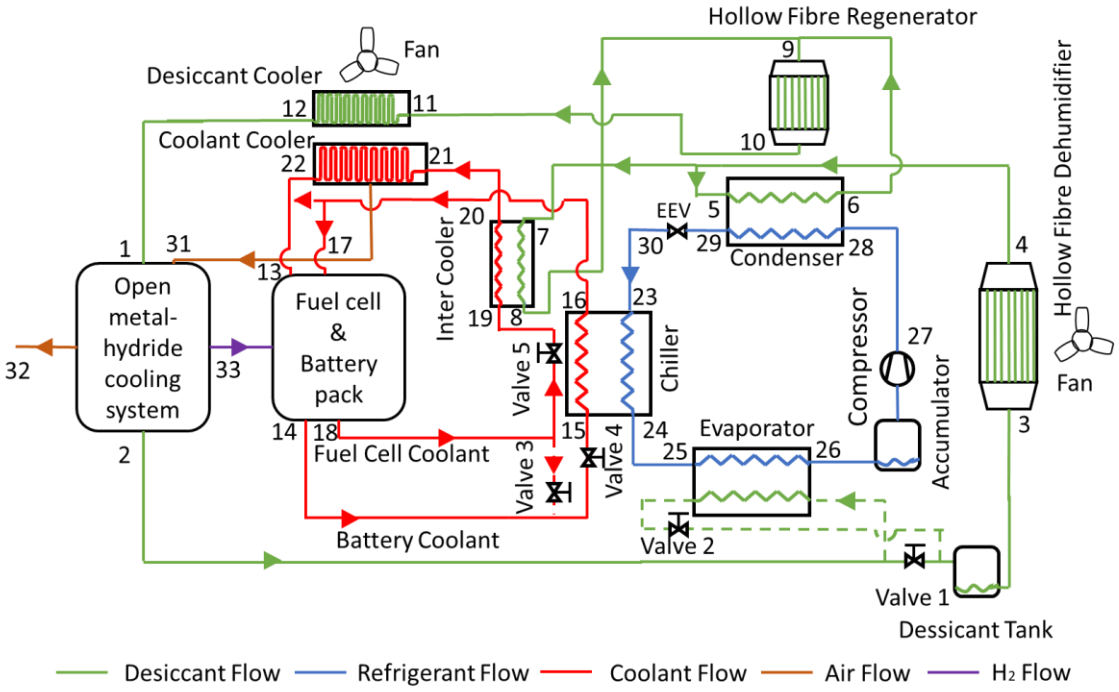

Figure 5.1. Marco schematic diagram of system

The schematic diagram of the open metal-hydride subsystem is shown in **Figure 5.2**. In the middle of the onboard H_2 transportation between the gas-compressed hydrogen vessel and fuel cell stack, two metal hydride reactors are applied in order to utilize the energy waste during the hydrogen de-pressure procedure. The subsystem can be divided into two half cycles, namely a discharging half cycle and a charging half cycle shown as solid and dashed lines respectively. For the charging half cycle, the hydrogen supplied by the hydrogen vessel first relieves its pressure to the required operating status of metal hydrides by passing the pressure relief valve and restrictor valve. The charging hydrogen is absorbed and stocked in the metal hydride reactor 2 and the exothermic heat is released to the air side (air temperature is adjusted by the ratio of air from port 31 and ambient). At the same time, the hydrogen already stocked in reactor 1 is released to the fuel cell with a specific mass flow rate, and the required heat for the endothermic desorption is supplied by the liquid desiccant flow. As a result, the temperature of the liquid desiccant can be cooled down to the set point or at least lower than the ambient temperature. These reactors are alternately charged and discharged when operating for a long time and the air and desiccant flow switch accordingly.

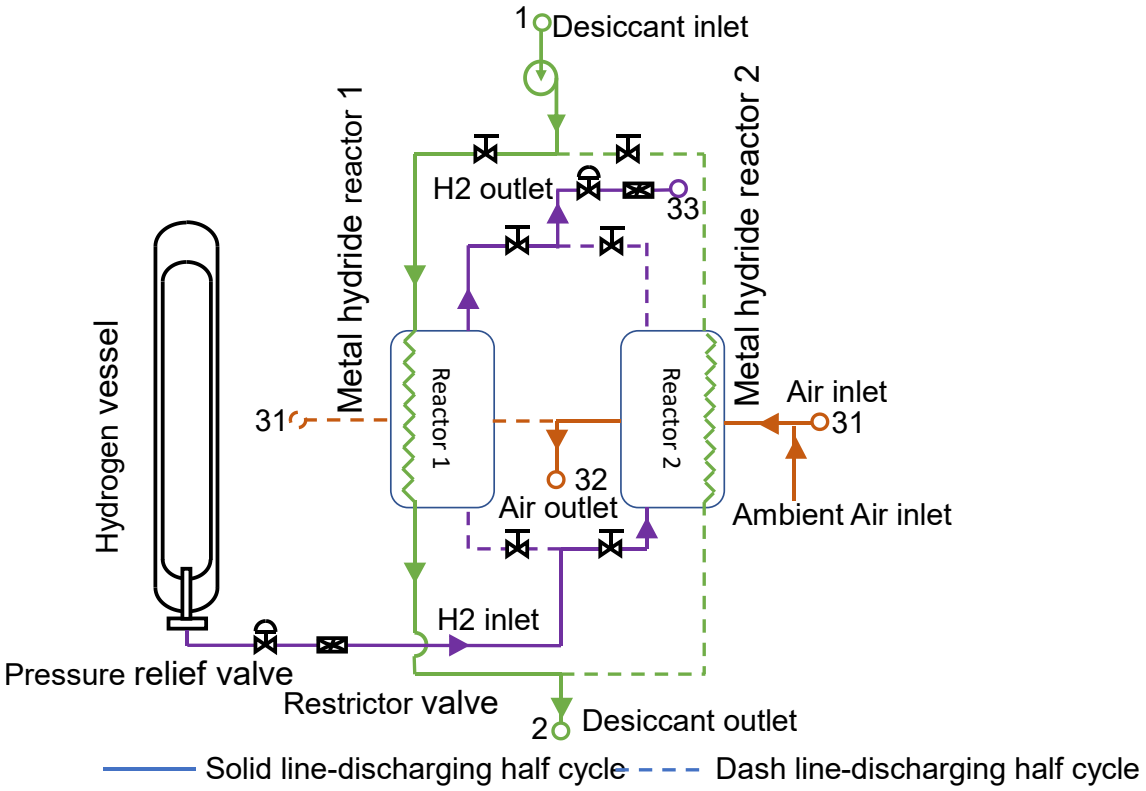

Figure 5.2. Schematic diagram of the open metal-hydride subsystem

5.3 Model Development

5.3.1 PEMFC and battery model

The heat and power cogeneration characteristic of the Proton-exchange membrane fuel cell (PEMFC) enables simultaneous heat and power supply. Electrochemical and thermodynamic theories are widely adopted to describe the heat generation procedure of the PEMFC. The heat generation of the fuel cell stack is expressed in Eq. (5.1)

$$Q_{FC} = (V_{nernst} - V_{cell}) \times I_{FC} \quad (5.1)$$

in which, the V_{nernst} is the Nernst open circuit voltage, V_{cell} is the voltage of a fuel cell, and I_{FC} is the current of the fuel cell. The details of the V_{nernst} can be found in ref. [158].

$$V_{cell} = V_{nernst} + V_{act} + V_{ohm} + V_{con} \quad (5.2)$$

where V_{act}, V_{ohm}, and V_{con} stands for activation losses, ohmic losses, and concentration losses respectively and details can be found in Ref. [128]. The H_2 consumption, while operating the fuel cell stack, can be calculated by Eq. (5.3)[127].

$$\dot{m}_{H_2} = \frac{I_{FC} \times M_{H_2} \times N_{FC}}{2 \times F} \quad (5.3)$$

in which, M_{H_2} is the molecular weight of the H_2, N_{FC} is the number of fuel cells in the stack and F is Faraday's constant. For the battery, the heat generation contains parts, namely irreversible heat and reversible heat. The expression is depicted in Eq. (5.4).

$$Q_{bat} = \underbrace{I_{ch/dch}^2 \times R_{ch/dch}}_{irr} - \underbrace{I_{ch/dch} \times T_{bat} \times \frac{dE_{OC_{bat}}}{dT_{bat}}}_{rev} \quad (5.4)$$

$I_{ch/dch}$ and $R_{ch/dch}$ represents the battery current and the internal thermal resistance while charging or discharging respectively. $\frac{dE_{OC_{bat}}}{dT_{bat}}$ is the entropy coefficient and T_{bat} is the operating temperature of the battery. The correlations concluded from experimental results can be found in ref. [165, 166]. The components parameters and model validation can be found in our previous study [128], in which the predicted results are compared to published results with a deviation of 5%.

5.3.2 Open metal hydride thermal model

Metal hydride (MH) is a material that can store hydrogen. In the open metal hydride system, the absorption and desorption processes are driven by the pressure difference between the inlet and the outlet. The reversible reaction can be described as follows, which is an exothermic reaction.

$$Me(s) + \frac{X}{2} \times H_2(g) \rightleftharpoons MH_X(S) + \Delta H \quad (5.5)$$

and the maximum cooling capacity during desorption is shown in Eq. (5.6),

$$Q_{MH,des,max} = \dot{m}_{H_2}/M_{H_2} \times \Delta H_{des} \quad (5.6)$$

where ΔH_{des} (J/mol) is the heat of formation. The temperature change of the MH can be calculated below:

$$[(1-\epsilon) \times \rho_{MH} \times Cp_{MH} + \varepsilon_{MH} \times \rho_{H2} \times Cp_{H2}] \times \frac{\partial T_{MH}}{\partial t} + \nabla(-\lambda_{eff} \times \nabla T) = Q_{MH} \quad (5.7)$$

in which ϵ_{MH} is the porosity of the MH which is 0.67 [239], ρ_{MH} and Cp_{MH} are the density and specific heat capacity of the solid MH and ρ_{H2} and Cp_{H2} are the density and specific heat capacity of the hydrogen. λ_{eff} is the effective heat conductivity of the MH bed. In order to utilise the cooling capacity, a separating steel plate and the heat transfer fluid, which is the liquid desiccant solution in the proposed system, is needed. Based on [133], the energy balance for the designed separating plate is considered as Eq. (5.8)

$$\rho_{SP} Cp_{SP} b d_{SP} l \frac{\partial T_{SP}}{\partial t} + \nabla(-\lambda_{SP} b d_{SP} l \nabla T_{SP}) = bl([h_{MH}(T_{MH} - T_{SP}) - h_{sol}(T_{SP} - T_{sol})] \quad (5.8)$$

where b and l are the width and length of the reactor, d_{SP} is the thickness of the separating plate. h_{MH} and h_{sol} are the convective heat transfer coefficient of the MH and liquid desiccant solution. The h_{sol} is given by:

$$\frac{h_{sol} \times \lambda_{sol}}{d_{h,sol}} = 0.205 \times Pr_{sol}^{\frac{1}{3}} \times \left[f_{ges} \times Re_{sol}^2 \times sin\,(2\beta)\right]^{0.374} \times \frac{\mu_{sol}}{\mu_{sol,wall}} \quad (5.9)$$

where μ_{sol} and $\mu_{sol,wall}$ are the dynamic viscosity of the solution in the middle of the channel and at the wall. β is the inclination angle of a chevron pattern plate heat exchanger. $\mathrm{f_{ges}}$ is called the fanning friction factor which can be expressed as:

$$f_{ges} = \left\{ \frac{cos\,(\beta)}{\left[0.045 \times tan(\beta) + 0.09 \times sin(\beta) + \frac{16}{Re_{sol}} \times cos\,(\beta)^{-1}\right]^{0.5}} + \frac{1 - cos\,(\beta)}{(\frac{37.05}{Re_{sol}^{0.0289}})^{0.5}} \right\}^{0.5} \quad (5.10)$$

The Prandtl number and Reynolds number are defined by

$$Pr_{sol} = \frac{\mu_{sol} \times \rho_{sol} \times Cp_{sol}}{\lambda_{sol}} \quad (5.11)$$

$$Re_{sol} = \frac{v_{sol} \times d_{h,sol}}{\mu_{sol}} \quad (5.12)$$

where v_{sol} is the velocity of the solution inside the channel and $d_{h,sol}$ is the hydraulic diameter of the solution flow channel. For the solution temperature, the energy balance equation along the solution flow direction x is defined as:

$$\rho_{sol} \times Cp_{sol} \times b \times l \times d_{sol} \times \frac{\partial T_{sol}}{\partial t} + \dot{m} \times Cp_{sol} \times l \times \frac{\partial T_{sol}}{\partial x} = h_{sol} \times b \times l \times (T_{SP} - T_{sol}) \quad (5.13)$$

The specifications of the metal hydride are displayed in **Table 7**.

Table 7. Specifications of the metal hydride

Parameters	Value	Units
MH Specifications [133]		
Material	Hydralloy C2	/
Mass per metal hydride (m_{MH})	1.55	kg
Density (ρ_{SP})	6375.3	Kg/m^3
Heat conductivity (λ_{eff})	1	W/(m·K)
Heat transfer coefficient	$1X10^4$	$W/(m^2 \cdot K)$
Maximum hydrogen capacity (W_{max})	1.7	%
Lowest hydrogen capacity (W_{min})	0.47	%
Porosity (ε)	0.67	
Specific heat capacity (Cp_{MH})	500	J/(kg·K)
Operating Conditions		
Regeneration temperature ($T_{MH,reg}$)	35	^oC
Discharging temperature ($T_{MH,dch}$)	30	^oC
Maximum pressure	30	bar
Lowest pressure	9	bar
Maximum hydrogen capacity (W_{max})	1.7	%
Lowest hydrogen capacity (W_{min})	1.3	%

The thermal model of the proposed metal hydride reactor during the desorption process is validated depending on the outlet temperature of the heat transfer fluid in the Ref. [133]. The desorption process of the open metal system is similar to the solid green line shown in **Figure 5.2**. In order to examine the model, the property of the heat transfer fluid, initial metal hydride temperature, and the dimensions of the rector are defined as variable parameters in this work. The outlet temperature of the heat transfer fluid is used to validate the proposed thermal model of the metal hydride reactor in this study. The results are shown in **Figure 5.3** and the deviation is always within 5%. Also, the characteristic of the metal hydride's pressure variation along with its hydrogen capacity is validated by comparing it to the results in Ref. [133] and the changes in metal hydride's pressure, when the fuel cell current output is 5kW, are shown in **Figure 5.4** and **Figure 5.5**. During the process, the metal hydride 1 desorbs for 150s till the pressure reached 9 bar and then metal hydride 2 started desorbing for another 150s.

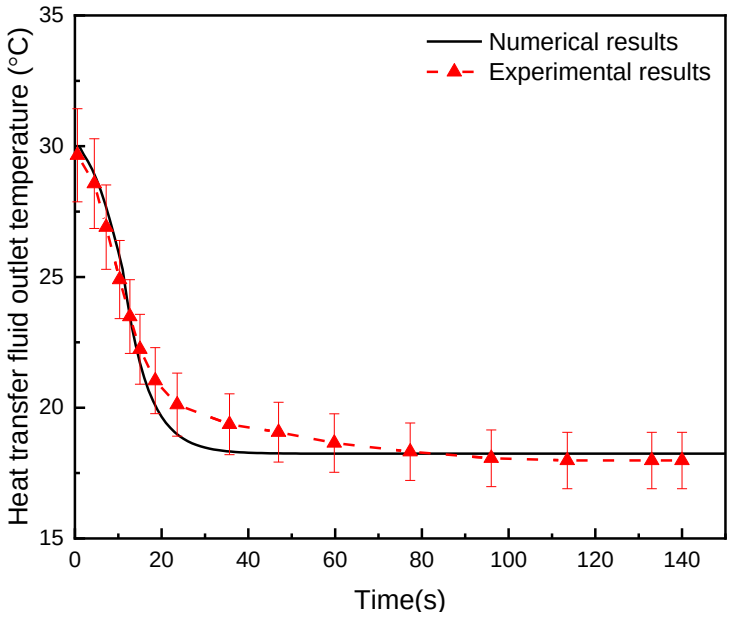

Figure 5.3. Open metal hydride thermal model validation compared to Ref. [133]

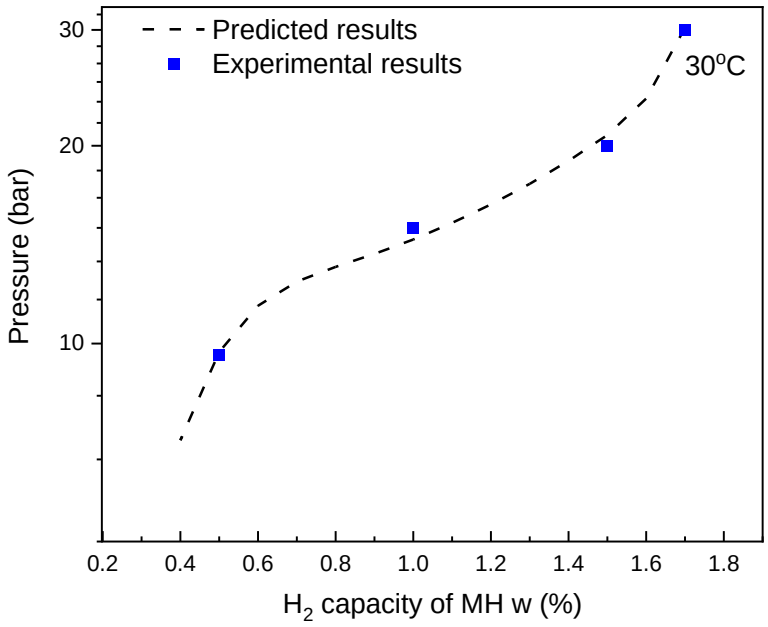

Figure 5.4. Metal hydride's pressure variation along with its hydrogen capacity

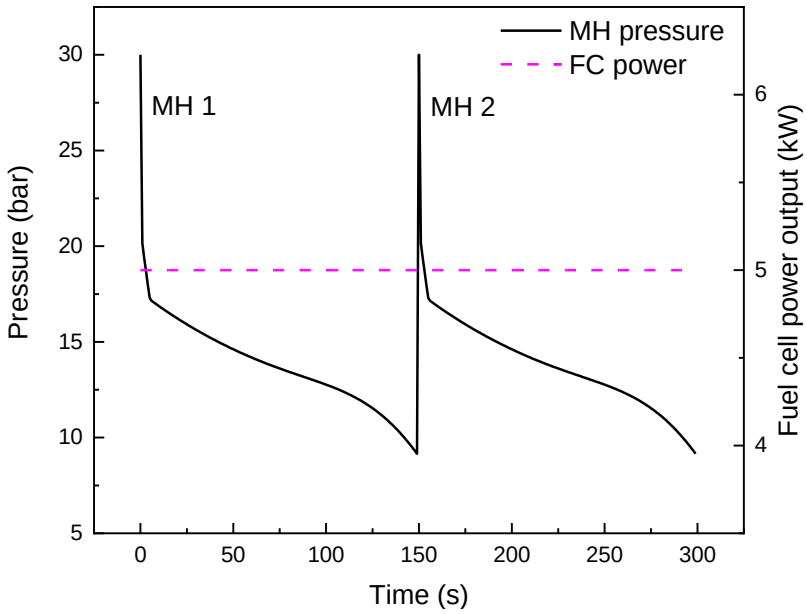

Figure 5.5. Characteristic curve of the pressure of the metal hydride

5.3.3 Hollow fibre liquid desiccant dehumidifier heat and mass transfer model

A one dimensional model for air and liquid desiccant solution flow was developed in this study due to the homogenous transverse variables [224].

$$\frac{\dot{m}_{sol}}{n_{eq}d_{inn}} \times \frac{\partial T_{sol}}{\partial y} \times Cp_{sol} = U_{de,h} \times (T_{air} - T_{sol}) + i_{fg} \times K_{de,m} \times \rho_{air} \times (\omega_{air} - \omega_{sol}) \quad (5.14)$$

$$\frac{\dot{m}_{sol}}{n_{eq}d_{inn}} \times \frac{\partial X_{sol}}{\partial y} = K_{de,m} \times \rho_{air} \times (\omega_{air} - \omega_{sol}) \quad (5.15)$$

$$\frac{\dot{m}_{air}}{n_{ach}d_{h}} \times Cp_{sol} \times \frac{\partial T_{air}}{\partial x} = U_{de,h} \times (T_{sol} - T_{air}) \quad (5.16)$$

$$\frac{\dot{m}_{air}}{n_{ach}d_{h}} \times \frac{\partial \omega_{air}}{\partial x} = K \times (\omega_{sol} - \omega_{air}) \quad (5.17)$$

In Eqs. (5.14)to (5.17), x is the direction of the solution flow along the hollow fibres while y is the direction of the cross-air flow. n_{eq} and n_{ach} are the equivalent number of fibres and airflow channel numbers respectively. d_{inn} and d_h represent the inner diameter of hollow fibres and the hydraulic diameter of the airflow channel respectively. $U_{de,h}$ (W/m^{2}K) is the overall heat transfer coefficient while $K_{de,m}$ (m/s) is the overall mass transfer coefficient. X_{sol} is the concentration of the solution and ω (kg/kg) is the specific humidity. The expressions of the specific humidity and concentration of the solution are shown below [240].

$$\omega_{sol} = 0.622 \times \frac{P_{sol}(X_{sol}, T_{sol})}{P_{atm} - P_{sol}(X_{sol}, T_{sol})} \quad (5.18)$$

in which, P_{sol} is the vapor pressure of the solution at a particular concentration and temperature. The concentration of the solution is also a function of temperature which can be obtained in Ref. [241]. The expressions of the $U_{de,h}$ and $U_{de,m}$ is defined as the following equations.

$$\frac{1}{U_{de,h}} = \left[\frac{1}{h_{de,sol}} \times \left(\frac{d_{out}}{d_{inn}}\right) + \frac{\delta}{\lambda_m} \times \left(\frac{d_{out}}{\bar{d}}\right) + \frac{1}{h_{de,air}}\right] \quad (5.19)$$

$$\frac{1}{K_{de,m}} = \left[\frac{1}{k_{de,sol}} \times \left(\frac{d_{out}}{d_{inn}}\right) + \frac{\delta}{D_m} \times \left(\frac{d_{out}}{\bar{d}}\right) + \frac{1}{k_{de,air}}\right] \quad (5.20)$$

where, δ is the thickness of the membrane, D_m (m/s) is the mass diffusivity of the hollow fibre, and λ_m (W/mK) is the thermal conductivity of the hollow fibre. The heat transfer coefficients for solution and air are calculated based on the following equations [242, 243]:

$$\frac{h_{de,sol} \times d_h}{\lambda_{sol}} = 3.658 + \frac{0.085 \times \left(\frac{Re_{sol} \times Pr_{sol} \times d_h}{L}\right)}{1 + 0.047 \times \left(\frac{Re_{sol} \times Pr_{sol} \times d_h}{L}\right)^{0.67}} \times \left(\frac{\mu_{sol}}{\mu_w}\right)^{0.14} \quad (5.21)$$

$$\frac{h_{de,air} \times d_h}{\lambda_{air}} = 1.33 \times 0.648 \times Re_{air}^{0.198} \times Pr_{air}^{\frac{1}{3}} \quad (5.22)$$

And the mass transfer coefficient for the solution side and air side can be calculated based on Eqs. (5.23) to (5.24) respectively [244].

$$\frac{k_{de,sol} \times d_h}{D_{w,sol}} = 1.62 \times \left(\frac{d_{inn}^2 \times u_{sol}^2}{L \times D_{w,sol}}\right)^{\frac{1}{3}} \quad (5.23)$$

$$\frac{k_{de,air} \times d_h}{D_{w,air}} = (14.06\phi^4 - 29.21\phi^3 + 22.59\phi^2 - 7.71\phi + 1.03) Re_{air}^{0.33} \left(\frac{\mu_{air}}{\rho_{air} D_{w,air}}\right)^{0.33} (0.882 D_f - 0.535) \quad (5.24)$$

Where ϕ is the packing fraction of the dehumidifier, $D_{w,air}$ and $D_{w,sol}$ stand for water diffusivity in air and solution respectively. D_f is the fractal dimension of the fibre packing, the value of that can be found in Ref. [245]. The hollow fibre liquid desiccant dehumidifier model is validated in our previously published study [224].

5.3.4 Heat pump model

There are five main components in this study's proposed heat pump cycle. Two evaporators (called chiller and evaporator), a compressor, a plate condenser, and an expansion valve. The heat transfer model for the plate-type evaporator, compressor and expansion valve has been developed and validated from a component perspective in our previously published work [128]. The heat transfer model for the adopted plate-type condenser is developed in this sub-chapter. The heat transfer process in the condenser includes three regions: vapor de-superheating region, two-phase region, and liquid subcooling region. In this study, the vapor de-superheating region and the two-phase region are considered together as the heat transfer rate only accounts for a small fraction (1.4% to 1.6%) [246]. For the two-phase region, the heat transfer coefficient for the refrigerant side is considered as [247]:

$$h_{cond,ref} = \frac{4.118 \times Re_{eq}^{0.4} \times Pr_{cond,ref}^{\frac{1}{3}} \times \lambda_{cond,ref}}{D_h} \quad (5.25)$$

in which, the $\mathrm{Re_{eq}}$ is the equivalent Reynolds number which is defined as:

$$Re_{eq} = \frac{\dot{m}_{ref} \times \left[1 - X_m + X_m \times \left(\frac{\rho_{ref,lq}}{\rho_{ref,v}}\right)^{0.5}\right] \times D_h}{A_{cross} \times \mu_{ref,lq}} \quad (5.26)$$

where $\dot{m}_{ref}$ is the refrigerant mass flow rate, A_{cross} is the flow channel cross-section area. X_m is the average vapor quality between the inlet and outlet of the two-phase region and $\rho_{ref,lq}$ and $\rho_{ref,vp}$ are the density of the liquid and vapor refrigerant respectively. For the single-phase liquid desiccant solution, the single-phase correlation for water was adopted [246].

$$\frac{h_{cond} d_h}{\lambda_{cond}} = 0.4225 Re_{cond}^{0.733} Pr_{cond}^{1/3} \left(\frac{\mu_{cond}}{\mu_{wall}}\right)^{0.14} \quad (5.27)$$

For the liquid subcooling region, Eq. (5.27) is utilized for both the refrigerant side and the solution side. Therefore, the overall heat transfer coefficients for these two regions are depicted as below:

$$\frac{1}{U_{cond}} = \frac{1}{h_{cond,ref}} + \frac{\sigma_{wall}}{\lambda_{wall}} + \frac{1}{h_{cond}} \quad (5.28)$$

The conservation of energy of the condenser can be described as:

$$\dot{Q}_{cond} = U_{cond} \times A_{cond} \times LMTD_{cond} \quad (5.29)$$

$$\dot{Q}_{cond,ref} = \dot{m}_{ref} \times Cp_{ref} \times \Delta T_{cond,ref} \quad (5.30)$$

$$\dot{Q}_{cond,des} = \dot{m}_{cond,des} \times Cp_{des} \times \Delta T_{cond,des} \quad (5.31)$$

The condenser model was validated with the published results in Ref. [247] as shown in **Figure 5.6**.

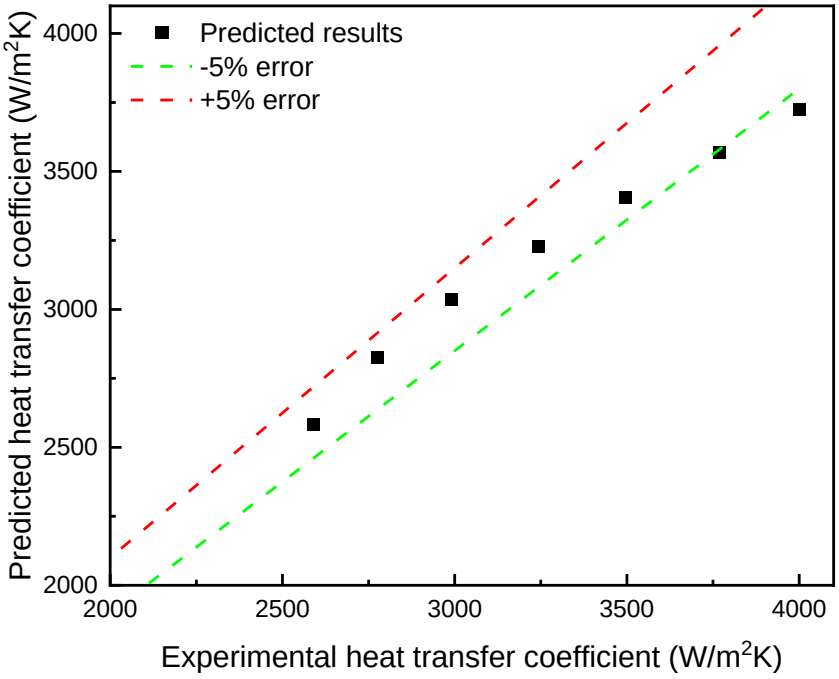

Figure 5.6. Condenser validation model by comparison with the experimental data in Ref. [247]

For the compressor model, the correlation introduced by Ref. [109] was adopted. The compressing ratio (γ) and the compressor power consumption are important. Kinab *et al.* [195] concluded the relationship between refrigerant temperature and mass flow rate for a fixed compressor speed:

$$\dot{m}_{ref} = b_0 + b_1 t_{eva} + b_2 t_{eva}^2 + b_3 t_{eva}^3 + b_4 t_{cond} + b_5 t_{cond}^2 + b_6 t_{cond}^3 + b_7 t_{eva} t_{cond} + b_8 t_{eva}^2 t_{cond} + b_9 t_{eva} t_{cond}^2 \quad (5.32)$$

in which coefficients b_0 to b_9 can be obtained from Ref. [109]. The power consumption of the compressor is shown below:

$$W_{comp} = \frac{\dot{m}_{ref} \times (H_{dis} - H_{suc})}{\eta_{isen}} \quad (5.33)$$

in which H_{dis} and H_{suc} are the enthalpy of R134a at the suction and exit of the compressor respectively, η_{isen} is the isentropic effectiveness of the compressor which is assumed to be 0.67 [173]. The EEV throttle process is considered an isenthalpic process and the mass flow rate flow through the EEV can be calculated as below:

$$\dot{m}_{EEV} = C_v \times A_c \sqrt{2 \times \Delta P_{EEV} \times \rho_{ref\_in}} \quad (5.34)$$

where A_c is the circulation area while C_v is the flow coefficient, and $C_v = 0.02005 \times \sqrt{\rho_{in}} + 0.634/\rho_{out}$ [155].

5.3.5 Performance indicator

In order to evaluate the efficiency of the system, the Coefficient of Performance (COP) is introduced in this study. The COP in this study is defined as below:

$$COP = \frac{Q_{cool}}{W_{hp}} \quad (5.35)$$

in which Q_{cool} is the cooling capacity provided by the liquid desiccant dehumidifier, the expression of which is defined in Eq. (5.36) W_{hp} is the heat pump energy consumption when it is required.

$$Q_{cool} = m_{air} \times (H_{air,in} - H_{air,out}) \quad (5.36)$$

where, $H_{air,in}$ and $H_{air,out}$ are the enthalpy of the inlet air and outlet air of the dehumidifier respectively. The specifications of the components in the proposed system are shown in **Table 5.8**.

Table 5.8 Specifications of the components

Components	Type	Specifications
Compressor	Scroll	Displacement: 27 cm^3/s Nominal power: 2.5kW Speed: 2000 RPM
Chiller	Plate type	Number of plates: 30

Evaporator	Plate type	Plate size: 60 X 160 mm^2 Channel space: 2.0 mm Number of plates: 30
Condenser	Plate type	Plate size: 60 X 160 mm^2 Channel space: 2.0 mm Number of plates: 30
Dehumidifier	Hollow fibre type	Plate size: 60 X 160 mm^2 Channel space: 2.0 mm Module cross section: 0.2 m Module height: 0.7 m Number of fibres: 6500 Fibre outer diameter: 1.6 mm Fibre inner diameter: 1.4mm Porosity: 0.6 Packing fraction: 0.32
Metal hydride reactor	Plate type	Number of separating plates: 36 Plate size: 0.279 X 0.08509 m^2 Channel space: 8.8 X 10^{-4} m Porosity: 0.67 Thickness of separating plates: 4 X 10^{-4} m
Fuel cell	PEMFC	Number of cells: 40 Area of cell: 5.1 X 10^{-3} cm Area of cell: 285.8 cm^2
Battery pack	Modified based on Tesla Model S [167]	Pack capacity: 60kWh Number of batteries: 1764 Number of batteries in series for one module: 6 Number of batteries in parallel for one module: 21 Number of modules: 14 Battery capacity: 8Ah Battery voltage: 4.2V

5.3.6 Simulation procedure

The numerical model for the proposed system is programmed in MATLAB. The physical characteristics of the refrigerant R134a were sourced from the embedded REFPROP in MATLAB. The model includes a fuel cell and battery model, a heat pump model, an open metal hydride system model, and a liquid desiccant solution (KCOOH) dehumidification and regeneration model. Those models were integrated with the following assumptions and the flow chart of the simulation process is shown in **Figure 5.7**. The simulation started from the chiller side in order to make sure that all the waste heat generated by the battery pack could be released to keep the battery pack can always operating under an optimal temperature. Several input assumptions were made, and these assumptions were required to be adjusted based on the energy conservation (error<0.0001) in the chiller, evaporator, dehumidifier, and condenser respectively. In the end, outputs such as air temperature, relative humidity, and COP could be achieved. The operating conditions and working flow constant physical properties are shown in **Table 5.9**.

(1) The temperature of the outlet coolant was set at 25 ^{o}C and the temperature difference of the battery coolant at the inlet and outlet of the chiller was controlled at 4 ^{o}C in order to maintain the temperature consistency of the battery pack [248].
(2) The thermophysical properties of the liquid desiccant KCOOH and metal hydride bed, such as density, heat conductivity, etc., are assumed to be constant.
(3) In the dehumidifier, the water molecules' diffusion and heat conduction along the solution flow direction was ignored [249].
(4) The pressure drop in the heat exchanger was neglected and the de-superheating region was combined into the two-phase region [246].
(5) The temperature variation along the direction perpendicular to the flow of solution and the heat losses in the metal hydride reactor were ignored [133].
(6) The inlet solution temperature of the open metal hydride system was assumed to be very close to the ambient temperature after being cooled by the ambient air.

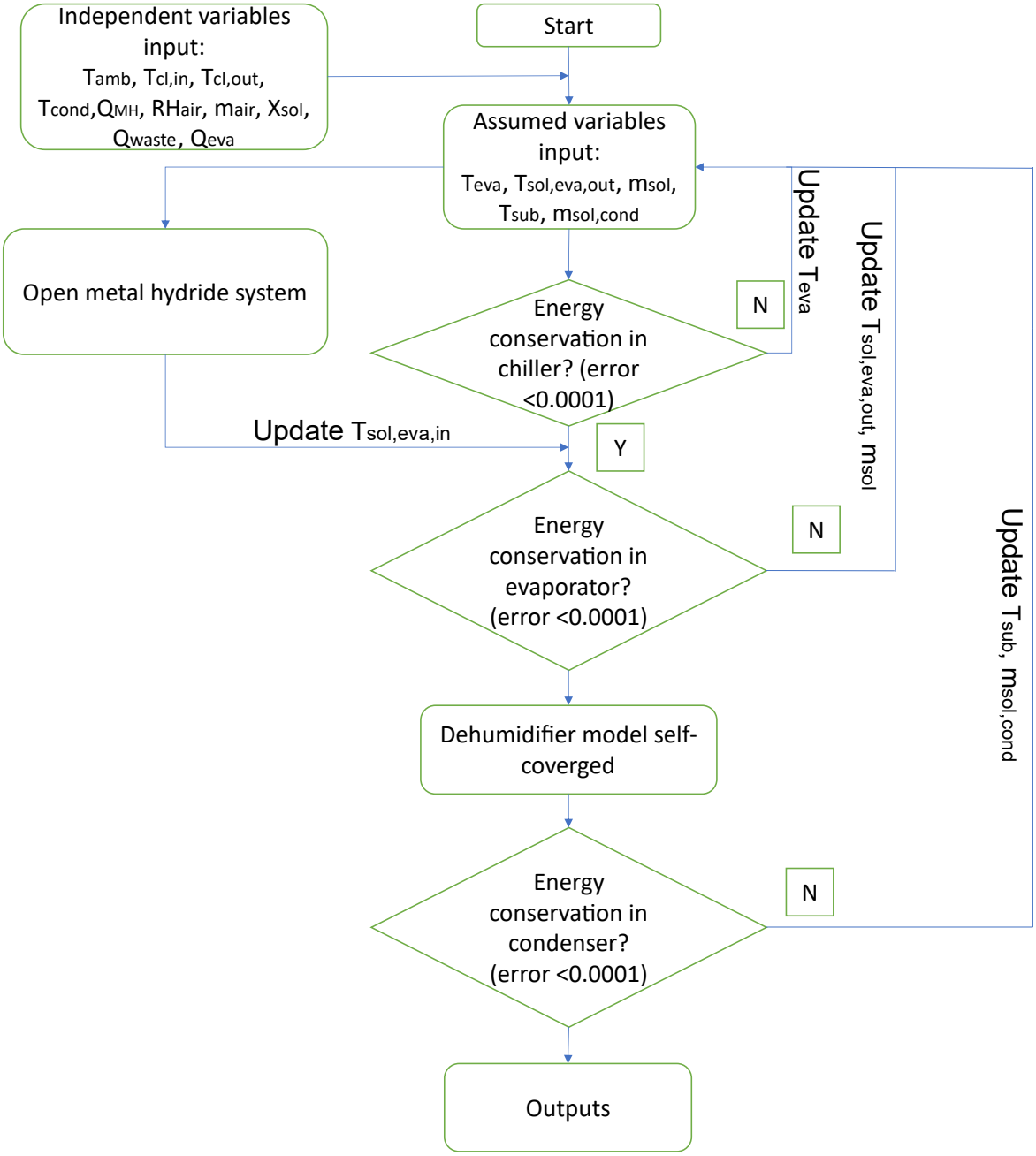

Figure 5.7. Proposed system numerical model simulation flow chart

Table 5.9 Operating conditions and physical properties in the simulation

Parameters	Value	Unit
Fuel cell temeprature	65	^{o}C
Battery temperature	25	^{o}C
Ambient temperature (T_{amb})	26-30 (std:30)	^{o}C
Ambient relative humidity (RH_{air})	80	%
MH max pressure	30	bar
MH lowest pressure	9	bar
MH absorbtion temperature ($T_{MH,abs}$)	35	^{o}C
MH desorption temperature ($T_{MH,des}$)	30	^{o}C
Battery discharging C rate (B_{dch})	0.45-0.66 (std:0.5755)	C
Battery charging C rate (B_{ch})	0.05-0.18 (std: 0.1364)	C
Solution working temperature ($T_{sol,eva,o}$)	15-23	^{o}C
Solution working concentration ($X_{sol,eva,o}$)	62	%
Air mass flow rate	0.07	kg/s
Cooling demands	2-4	kW
Cabin temperature set point	25	^{o}C
Cabin relative humidity set point	50	%

5.4 Results and Discussion

5.4.1 Performance of the non-compressive cooling and dehumidification cycle

5.4.1.1 Impacts of the ambient temperature

In the non-compressive cooling cycle, the compressor is not utilised in the cooling system and the cooling capacity is provided by the open metal hydride system. **Figure 5.8** shows the influence of the ambient temperature on the performance of the non-compressive cooling system. With the increasing ambient air temperature, the air outlet temperature, specific humidity, and the proposed system's cooling capacity increases. As shown in **Figure 5.8** (a) and (b) when the ambient temperature increases from 26 ^{o}C to 34 ^{o}C with an unchangeable air mass flow rate of 0.03kg/s and 1kW of Q_{MH}, the air outlet temperature increases from 23.25 ^{o}C to 25.69 ^{o}C, and the specific humidity also increased by 38%. This is because raising the ambient temperature also leads to a raising of the air-specific humidity when the RH is constant. Both of them cause more heat and mass transfer between the solution and air in the dehumidifier. However, the sensible heat and latent heat during mass dehumidification will increase the temperature of the solution dramatically and as a result, increase the water vapor partial pressure of the solution which reduces the ability to transfer mass and possibly transfer heat back to the air according to Eq. (5.14) to (5.17). This is perhaps the reason why the temperature-increasing gradient increases significantly with the increase in the ambient air temperature. Although the decrease in both air temperature and air specific humidity, compared to the inlet conditions, because of the increase of the ambient air temperature, the cooling capacity still increases. This is because the increasing rate in air outlet temperature and air specific humidity is always lower than that in ambient temperatures. For example, when the ambient air temperature and specific humidity increase by 30.5% and 60%, the outlet air temperature and specific humidity only increase by 28% and 52.6% respectively in the worst-case scenario (m_{air}=0.07kg/s). Furthermore, when the air mass flow rate increases from 0.03kg/s to 0.05kg/s to0.07kg/s, the air outlet temperature, specific humidity, and cooling capacity also increase. This is due to the increasing heat and mass transfer rate in terms of Eq. (5.21) to (5.24) and less time consumed by a unit volume of solution flowing through a dehumidifier. But the impacts of the air mass flow rate on air temperature, specific humidity, and cooling capacity decrease with the increase of the mass flow rate because of the capacity limit of the polymer hollow fibre heat and mass exchanger.

So, when the ambient temperature increases, the air mass flow rate should be adjusted in order to provide sufficient inlet air if other parameters are not changed.

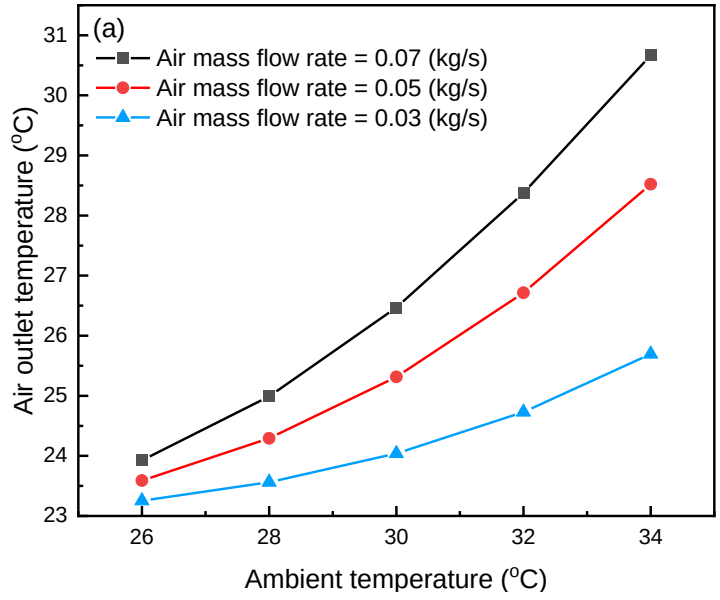

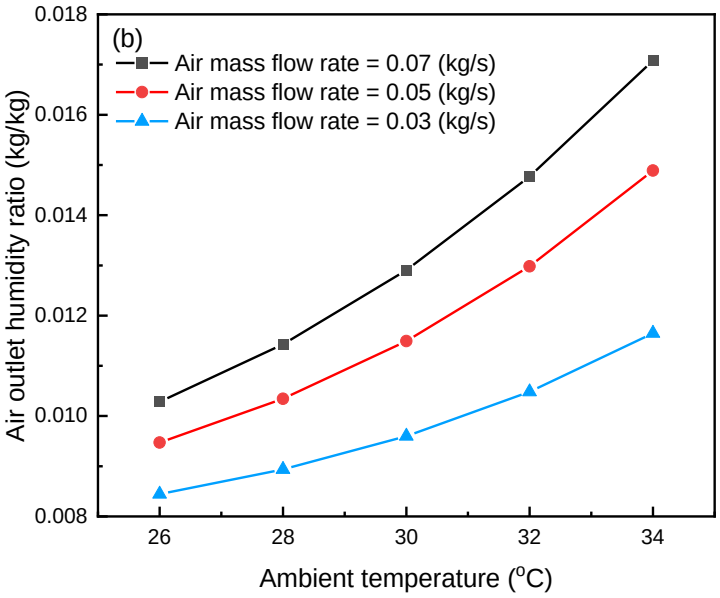

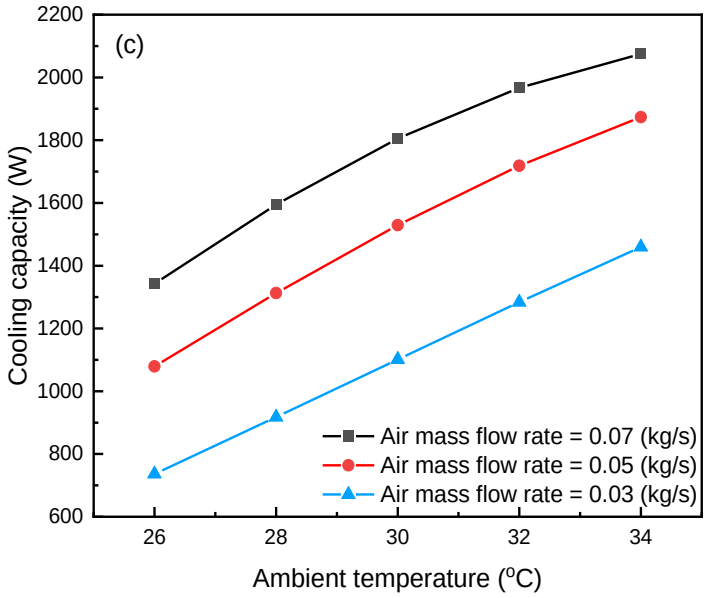

Figure 5.8. The impacts of the ambient temperature and air mass flow rate on air outlet temperature (a), specific humidity (b), cooling capacity (c) (RH_{air}=80%, X_{sol}=62%, B_{ch}=0.1, $T_{sol,MH,out}$=23 °C)

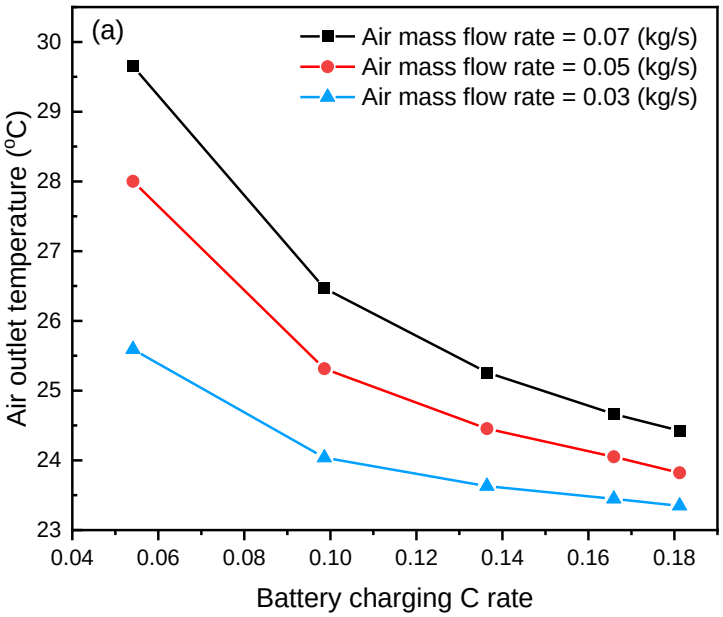

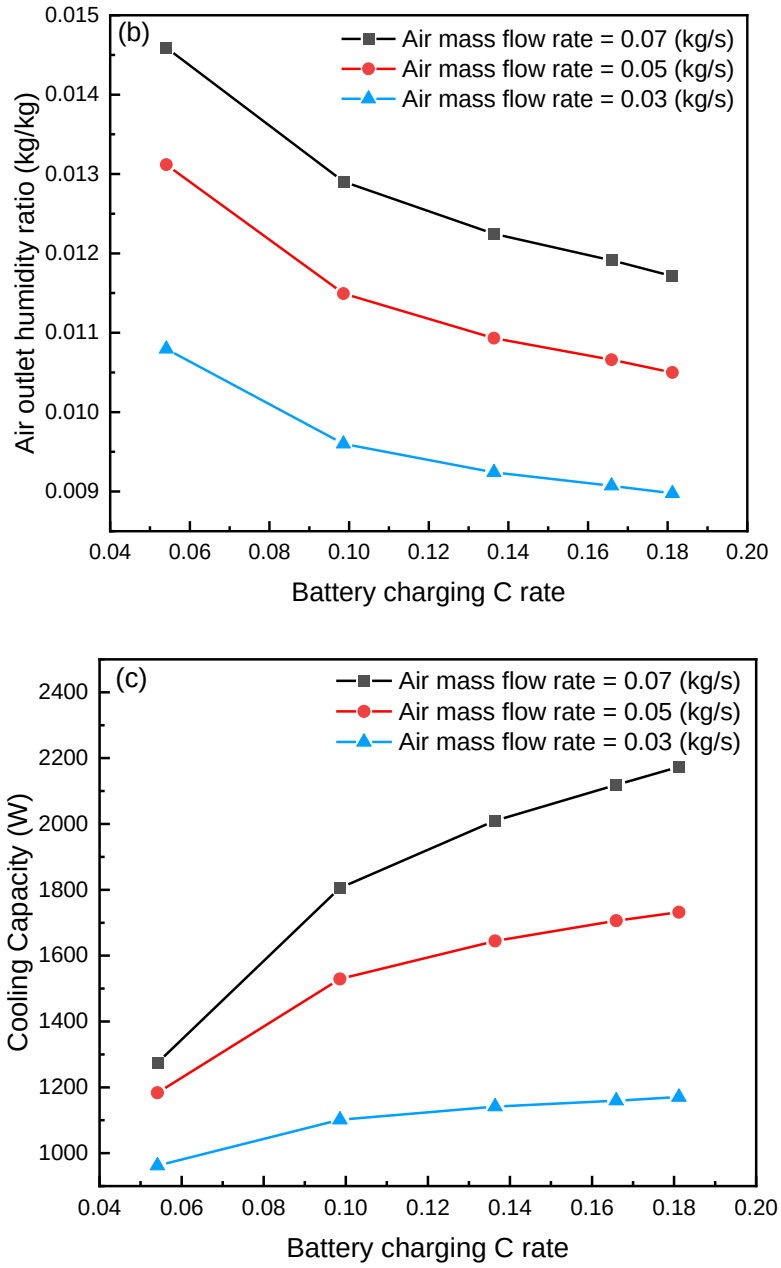

Figure 5.9. The impacts of the battery charging C rate and air mass flow rate on air outlet temperature (a), specific humidity (b), cooling capacity (c) (RH_{air}=80%, X_{sol}=62%, T_{amb}=30 ^{o}C, $T_{sol,MH,out}$=23 ^{o}C)

5.4.1.2 Impacts of battery charging C rate

The impact of the battery charging C rate on ambient air temperature and air specific humidity is opposite to that of the ambient temperature. The battery charging current is supplied by the fuel cell stack and the H_2 required by the fuel cell stack is provided by the vessel via an open metal-hydride cooling system. Therefore, the increasing battery discharging C rate also represents an increase in the mass flow rate flow through the MH and the cooling capacity of the adopted open-metal hydride system. As a result, due to the

stable inlet and outlet solution temperature of the open-metal hydride system, the solution mass flow rate across the MH and evaporator increases correspondingly. Based on the variation in solution mass flow rate, the average temperature, and water vapor partial pressure of the solution in the dehumidifier decline. Hence, the temperature and equivalent specific humidity differences between the air and solution in Eq. (5.14) to (5.17) increase and cause greater variations in air temperature and specific humidity and lead to a decrease in air outlet temperature and outlet air specific humidity. The results in **Figure 5.9** (a) and (b) reflect the analysis above. For instance, when air mass flow is 0.05kg/s, the battery charging C rate increases from 0.05 to 0.18, the air outlet temperature decreases from 28 ^{o}C to 23.8 ^{o}C and the air outlet specific humidity drops from 0.013kg/kg to 0.0105kg/kg. Furthermore, the decrease in air mass flow rate will weaken the impacts of the battery discharging C rate. For example, when the battery discharging C rate increases from 0.05 to 0.1, the outlet air temperature decreases by 4%, 9.6%, and 10.8% for air mass flow rate of 0.03kg/s, 0.05kg/s, and 0.07kg/s respectively. This is due to the lower heat and mass transfer coefficient and lower driving force caused by the deeper cooled and dehumidified air inside the dehumidifier. The battery charging C rate has a similar impact on cooling capacity compared to ambient temperature. As shown in **Figure 5.9**, the cooling capacity increases by 46% when the air mass flow rate equals 0.05kg/s and the battery charging C rate increases by 2.34 times. However, the principle behind the influence is different. For the battery charging C rate, it increases the heat and mass transfer by increasing the solution mass flow rate which allows more heat and moisture to be absorbed by the solution.

5.4.1.3 Impacts of liquid desiccant solution working temperature

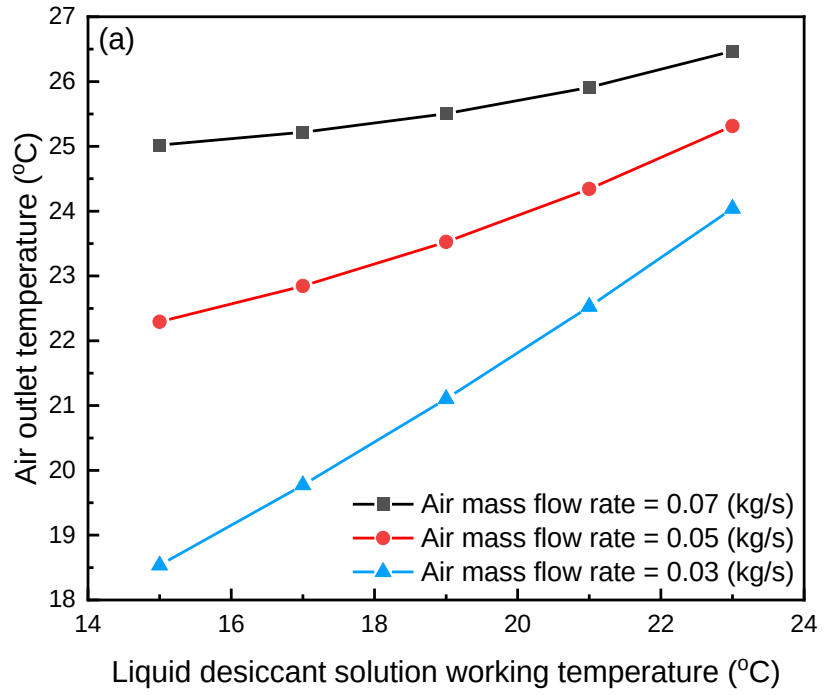

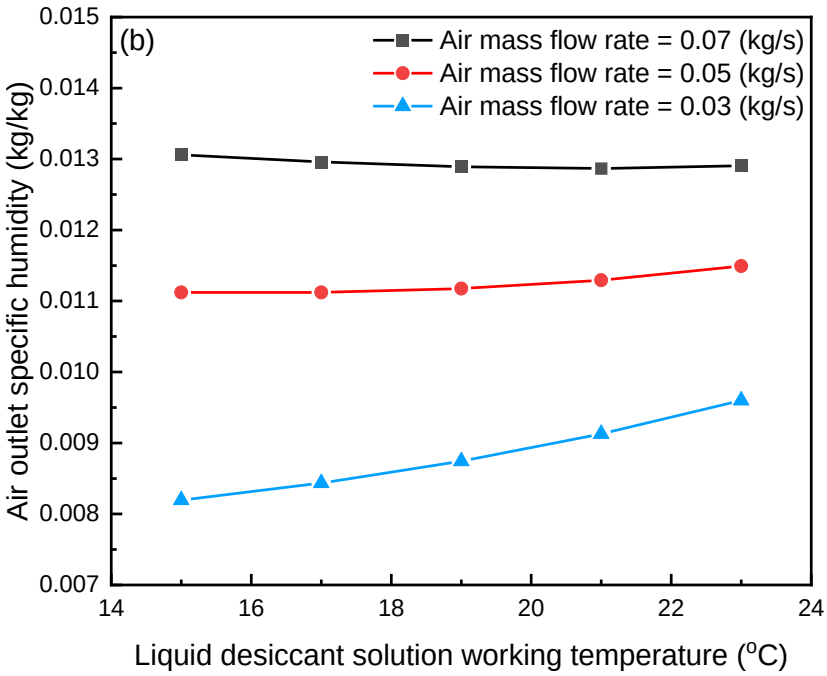

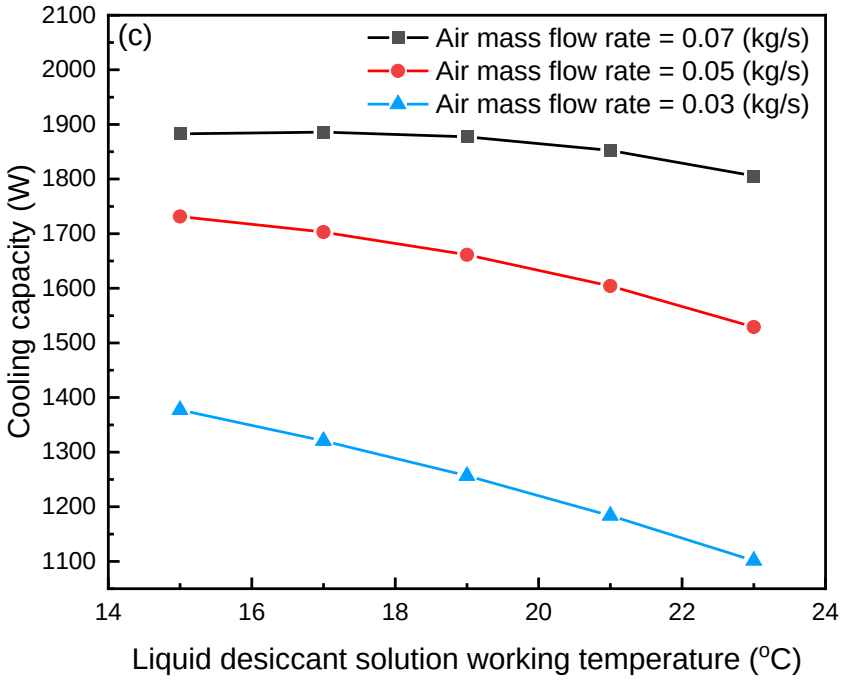

Figure 5.10. The impacts of the solution temperature and air mass flow rate on air outlet temperature (a), specific humidity (b), cooling capacity (c) (RH_{air}=80%, X_{sol}=62%, T_{amb}=30°C, B_{ch}=0.1)

The solution working temperature is also an important parameter for the performance. As shown in **Figure 5.10** (a), with the decreasing solution working temperature, from 23°C to 15°C, the air outlet temperature also decreases from 23°C to 18.5°C when the air mass flow rate is 0.03kg/s. This is because of the increasing temperature difference between the solution side and the air side, according to Eq. (5.16). But when the air mass flow rate increases to 0.05kg/s and 0.07kg/s, the decreasing speed drops, and a similar trend can be observed when the solution temperature is lower. For example, the reductions in the air outlet temperature are only 9.5% and 5.4% for the air mass flow rate of 0.05kg/s and 0.07kg/s respectively. Also, when the air mass flow rate is 0.05kg/s, with the solution working temperature decreasing from 23 °C to 21 °C, the outlet air temperature decreases by 4%. However, when the solution working temperature decreases from 19 °C to 17 °C, the outlet air temperature only decreases by 3%. The main reason is the increasing latent heat caused by the increasing absorbed water vapor makes the solution temperature higher than the air and starts transferring heat to the air side. The increasing absorbed water vapor can be found in **Figure 5.10** (b). When the air mass flow rate is 0.03kg/s, the outlet air specific humidity decreased by 14.5% when the solution working temperature descends from 23 °C to 15 °C. However, it should be noted that when the air mass flow rate increased to 0.07kg/s, the change in air outlet specific humidity can be ignored. This is because the decreasing solution

working temperature also reduces the solution mass flow rate. Although at lower solution working temperature, the initial greater temperature difference between the inlet air and inlet solution will increase the heat transfer rate, the temperature increase in the solution is also substantial due to the lower solution mass flow rate, causing the water vapor partial pressure in a solution to easily achieve the same level as that in the air. The impacts of the solution working temperature on cooling capacity show a reverse trend compared to that on outlet air temperature and specific humidity. As depicted in **Figure 5.10** (c), the cooling capacity increases with the decreasing solution working temperature. For example, the cooling capacity increased by 276W when the solution working temperature was reduced from 23 ^{o}C to 15 ^{o}C. This is the outcome of the decreasing outlet air specific humidity and temperature However, the impact is also not obvious when the air mass flow rate is 0.07kg/s.

5.4.1.4 Real time performance

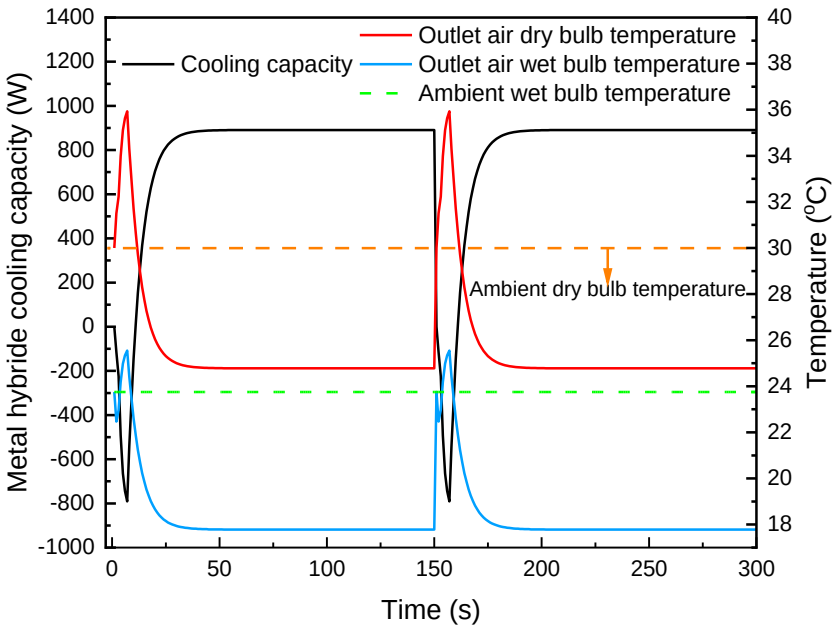

Figure 5.11. Real-time performance of the non-compressive cooling cycle (T_{abs}=35 ^{o}C, T_{des}=30 ^{o}C, RH_{air}=80%, X_{sol}=62%, T_{amb}=30 ^{o}C, m_{air}=0.03kg/s)

In order to provide continuous cooling capacity to the cabin, two MHs should be used alternately. However, since the absorption temperature is higher than the desorption temperature, the system cannot always provide maximum and stable heat to the solution due to the heat loss that occurs when switching operation modes between the two MHs. Once the transition occurs, the effects of fluid exchange losses and heat losses can be observed. As shown in **Figure 5.11**, there is an 800W loss at the beginning of the transition and it will take approximately 46s to reach the stable stage. In the recovery stage, due to the heat loss,

the solution temperature will increase which leads to an increase in outlet air dry bulb temperature. The outlet air dry bulb temperature peaked at 7s and dropped to the ambient level at 12s. However, the proposed system not only cools the air temperature but also dehumidifies the supply of air. The duration of time that the outlet air wet-bulb temperature is higher than the inlet air wet-bulb temperature is shorter than the time that the outlet air dry-bulb temperature is higher than the temperature of the inlet air. The duration is only 5s, which occurs between 4s and 9s, greatly reducing the duration of discomfort when the heat pump is not involved. In the stable stage, the proposed non-compressive cooling and dehumidification system can always provide the supply air with a wet bulb temperature of 17.8 ^{o}C which equals the wet bulb temperature under 25 ^{o}C and 50% RH.

In order to provide continuous cooling capacity to the cabin, two MHs should be used alternately. Therefore, the proposed open-metal hydride-assisted non-compressive cooling and dehumidification system can successfully cool down the supply air to the set point, which is 25 ^{o}C with 50%RH. However, the cooling performance of the proposed system is affected by several factors such as the ambient temperature, air mass flow rate, battery charging C rate, and solution working temperature. For a certain battery charging C rate that corresponds to the fuel cell output, there is a limit to the outlet air mass flow rate. Exceeding the limit, the system cannot provide sufficient supply air, although the cooling capacity may meet the requirements. Meanwhile, higher ambient air temperature and RH also bring negative effects on performance. Increasing the fuel cell power output may be a solution, but it strongly depends on the State of Charge (SOC) of the battery and the fuel cell's maximum current density limitation. When conditions permit, the proposed system can provide enough cooling capacity with sufficient air temperature and RH to the cabin without extra power consumption. However, since the absorption temperature is higher than the desorption temperature, the system cannot provide stable cooling loads during the transitions. Moreover, in practice, the battery charging C rate cannot be infinitely high to provide for high cooling demands scenario such as start-up stage or high ventilation requirement and the fluctuations during MHs' transition needed to be avoided. As a result, a heat pump system could be adopted as a supplement to the proposed cooling and dehumidification system in order to overcome severe operating situations and utilize more waste heat for solution regeneration.

5.4.2 Performance of the metal hydride assisted cooling and dehumidification cycle with supplement of heat pump

5.4.2.1 Impacts of the ambient temperature

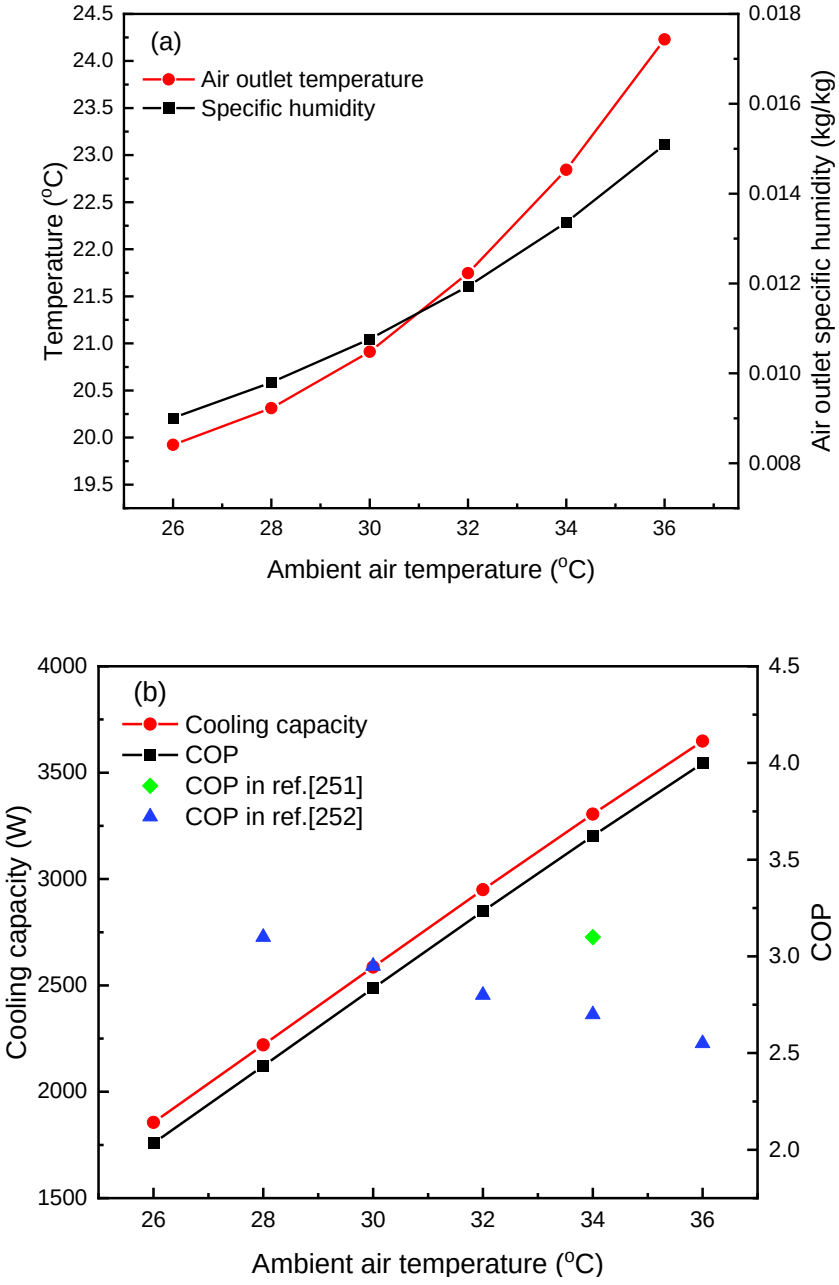

Figure 5.12. The impacts of the ambient temperature on performance and comparison with published results (RH_{air}=80%, X_{sol}=62%, B_{ch}=0.1C, m_{air}=0.07kg/s B_{dch}=0.57C, $Q_{eva+chi}$=3kW)

Figure 5.12, demonstrates that when the ambient temperature increases from 26 °C to 36 °C, the outlet air temperature and specific humidity both increases. The impacts of the ambient

temperature on those two parameters are similar to that in sub-section 5.4.1.1. However, the difference is the heat pump supplement system provides cooling loads to the solution via the evaporator which can further reduce the working temperature of the solution. The outlet air temperature and specific heat of the heat pump supplement system are only 20.9 ^{o}C and 0.0107kg/kg which are lower by 25% and 26.7% respectively, compared to those in the above non-compressive system mentioned in section 5.4.1.1 when the operating conditions are the same. The cooling capacity of the system also increases from 1855W to 3648W due to the higher temperature and water vapor partial pressure between the solution and air in the humidifier. As the heat pump system does not interact with ambient air, the compressor power consumption does not change during the variation of the ambient temperature. Hence, the COP of the proposed system increases with the increased cooling capacity. By comparing to the previously published results in Ref [251], the COP of the proposed system improved by 16.9% when the ambient air temperature is 34 ^{o}C. Meanwhile, similar improvement can be observed when compared to the results in Ref. [252] when the ambient air is over 32 ^{o}C and the set cabin temperature is 21.25^{o}C. However, it should be noted that the COP of the proposed system starts lower than the COP in Ref. [252] when the ambient temperature is lower than 30 ^{o}C. This can be explained from two aspects. First, on the condenser side of the reference air conditioning system, the refrigerant in the condenser transfers heat to the ambient air, and the condensing pressure decreases as the ambient air temperature decreases, resulting in a reduction in compressor power consumption. Second, the intake air in the reference is only 30% of the air mass flow, which is lower than the fresh air mass flow in the proposed system. However, the performance disadvantage of the proposed system at non-high temperature conditions can be compensated by the non-compressive cooling system mentioned above.

5.4.2.2 Impacts of the battery discharging C rate

As shown in **Figure 5.13**, the battery discharging C rate also has a significant influence on the performance of the proposed system. In **Figure 5.13** (a), when the battery discharging C rate increases from 0.45C to 0.66C, the outlet air temperature and the specific humidity decrease by 9.1% and 3% respectively. This is because, when the battery discharging C rate increases, the waste heat through the chiller also increases. As the battery coolant inlet and outlet temperature of the chiller are set as constant, the evaporating temperature is reduced in order to increase the LMTD in the chiller. Meanwhile, as the heat transfer rate in the chiller and evaporator is constant, the mass flow rate of the solution also decreases in order

to compensate for the increasing LMTD and reduce the heat transfer rate in the evaporator to maintain the energy conversion. Due to the decrease in the solution mass flow rate, the solution working temperature decreases correspondingly, although the total cooling capacity provided by the evaporator and MH is reduced. The solution with a lower temperature in the dehumidifier enhances the temperature difference between the air side and solution side resulting in a higher heat and mass transfer coefficient according to Eq. (5.14) and (5.17). **Figure 5.13** (b) reflects the relationship between the cooling capacity, COP, and battery discharging C rate. The cooling capacity and COP increase by 7.9% and 4.3% respectively when the battery discharging C rate varies from 0.45C to 0.66C. Due to the unchangeable air mass flow rate which leads to the lower outlet air temperature and specific humidity, the cooling capacity increases with the increasing battery discharging C rate. Although the increasing battery discharging C rate leads to a decrease in evaporating temperature, resulting in a higher compressing ratio and compressor higher power consumption based on Eq. (5.33), the increased ratio in cooling capacity is much higher. Therefore, according to Eq. (5.35), the COP increases with the increasing battery discharging C rate. However, the increased speed of the COP gradually decreases in this process which is because the decreases in outlet air specific humidity gradually slow down and tend to be constant at a high battery discharging C rate. Furthermore, the faster-reducing speed of evaporating temperature due to the lower refrigerant mass flow rate caused by increasing heat of evaporation maybe also be a contributing reason.

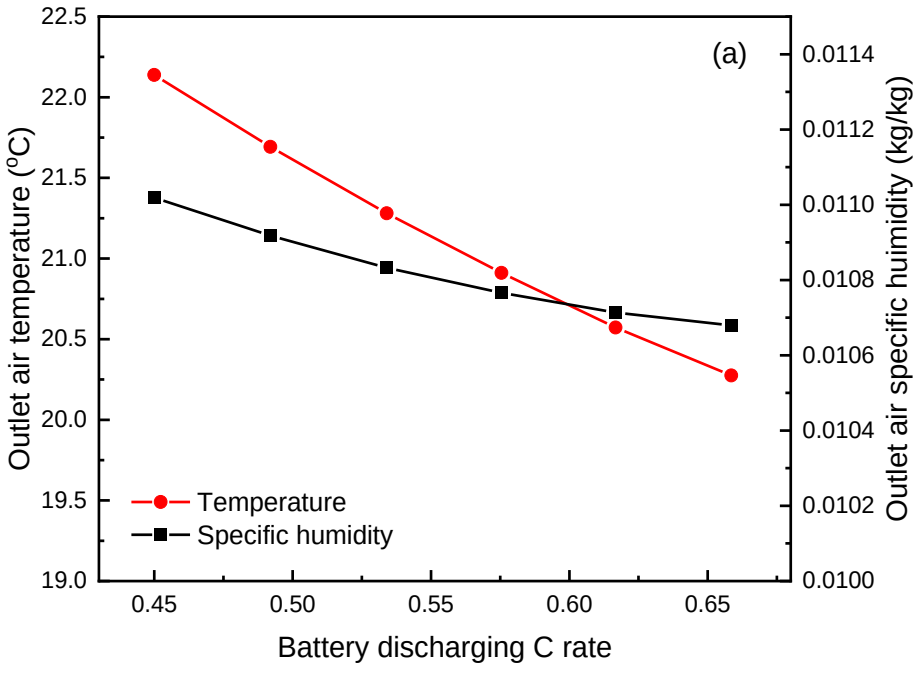

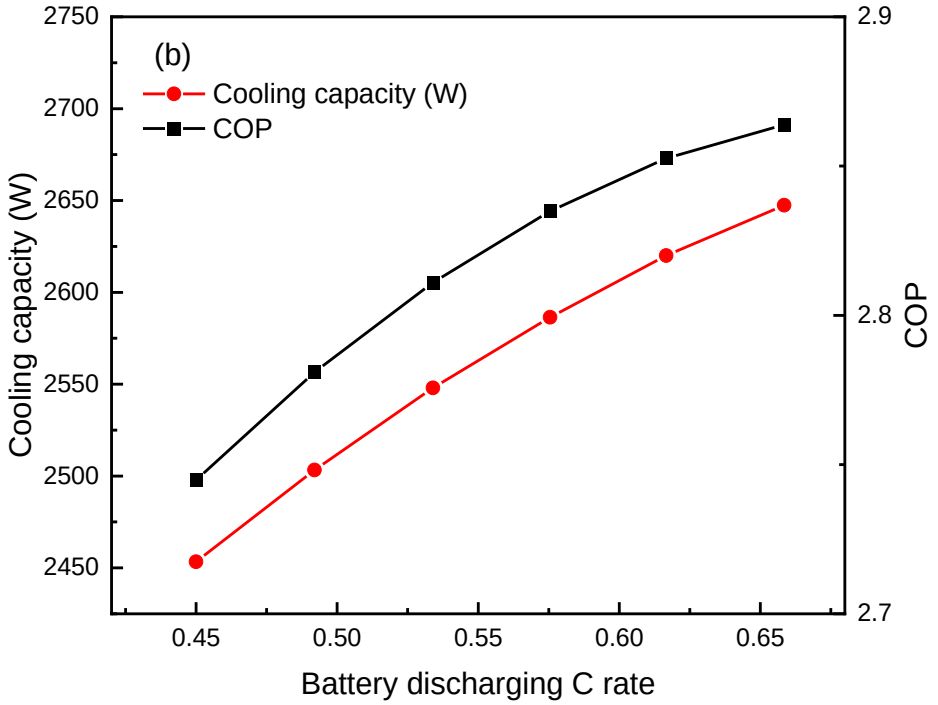

Figure 5.13. Impact of the battery discharging C rate on performance (RH_{air}=80%, X_{sol}=62%, B_{ch}=0.1, m_{air}=0.07kg/s, Tamb=30 ^{o}C, $Q_{eva+chi}$=3kW, B_{ch}=0.1)

5.4.2.3 Impacts of the battery charging C rate

Figure 5.14 describes the influence of battery charging C rate on the performance of the proposed heat pump supplement, open-metal hydride system assisted cooling, and dehumidification system. In the proposed cases, the impacts of the battery charging C rate are lower due to the introduced heat pump complement compared to the non-compressive system mentioned in section 5.4.1.2. With the battery charging C rate increasing from 0.054 to 0.0182, the outlet air temperature only declines by 0.7 ^{o}C, from 21.3 ^{o}C to 20.6 ^{o}C. Additionally, the dehumidification ability also increases marginally, which leads to the outlet air specific humidity decreasing by 3.8%. The reason for this is that when the battery charging C rate increases, the required hydrogen mass flow rate discharged by MH increases correspondingly and increases the cooling capacity supplied by the open metal hydride system. As a result, the solution temperature out of the open metal-hydride system decreases. However, due to the pinch point limits of the evaporator, the mass flow rate of the solution increases and leads to a stable solution working temperature according to Eq. (5.29) to (5.31). Hence, the increasing solution mass flow rate increases the average vapor partial pressure and temperature of the solution inside the humidifier and enhances the heat and mass transfer inside the dehumidifier and leading to an increased cooling capacity. The COP also increases by 5% when the battery charging C rate changes from 0.054C to 0.182C. This is because the

battery waste heat does not increase, so the compressor power consumption can be seen as constant which leads to an increase in the COP with the help of the increased cooling capacity.

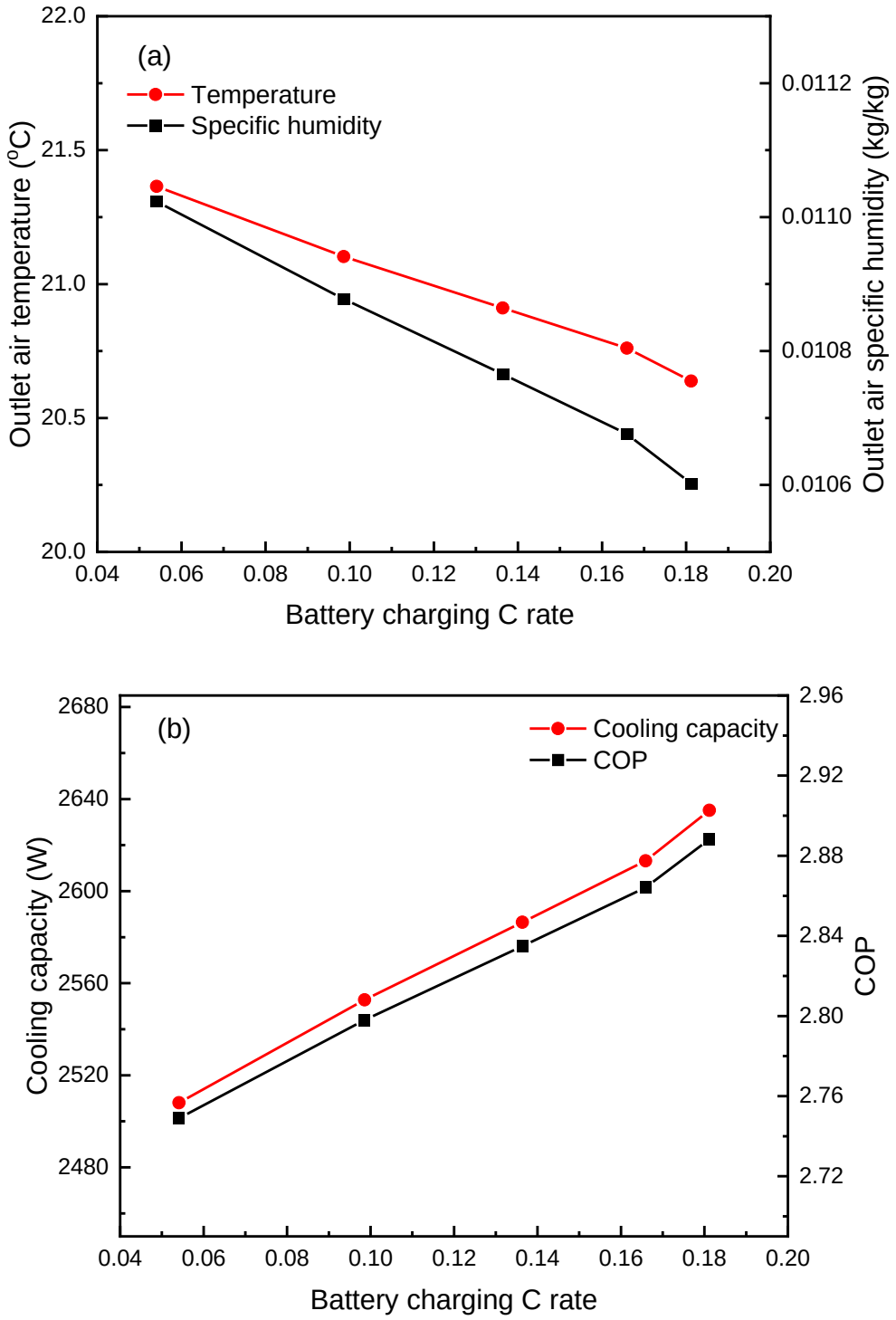

Figure 5.14. Impacts of the battery charging C rate on performance (RH_{air}=80%, X_{sol}=62%, B_{ch}=0.1, m_{air}=0.07kg/s, Tamb=30 °C, Q_{eva} =1.7kW, B_{dch}=0.57, Q_{chi}=1.3kW)

5.4.2.4 Real time performance

Figure 5.15 shows the real-time performance of the proposed open-metal hydride-assisted, heat pump-supplemented cooling and dehumidification system. The results show that the proposed system can substantially improve performance, especially during the metal hydride transition stage. The maximum outlet air temperature is lower than the supply air temperature in a non-compressive system and far lower than the ambient temperature even with an air mass flow rate of 0.07kg/s which is the maximum air mass flow rate mentioned in Ref. [250]. Although the outlet air temperature was slightly above the cabin set point for a period of 2 and 12 seconds above the wet bulb temperature set point, this could be improved by increasing the cooling capacity of the evaporator or reducing the mass air flow if the cooling demand is flexible.

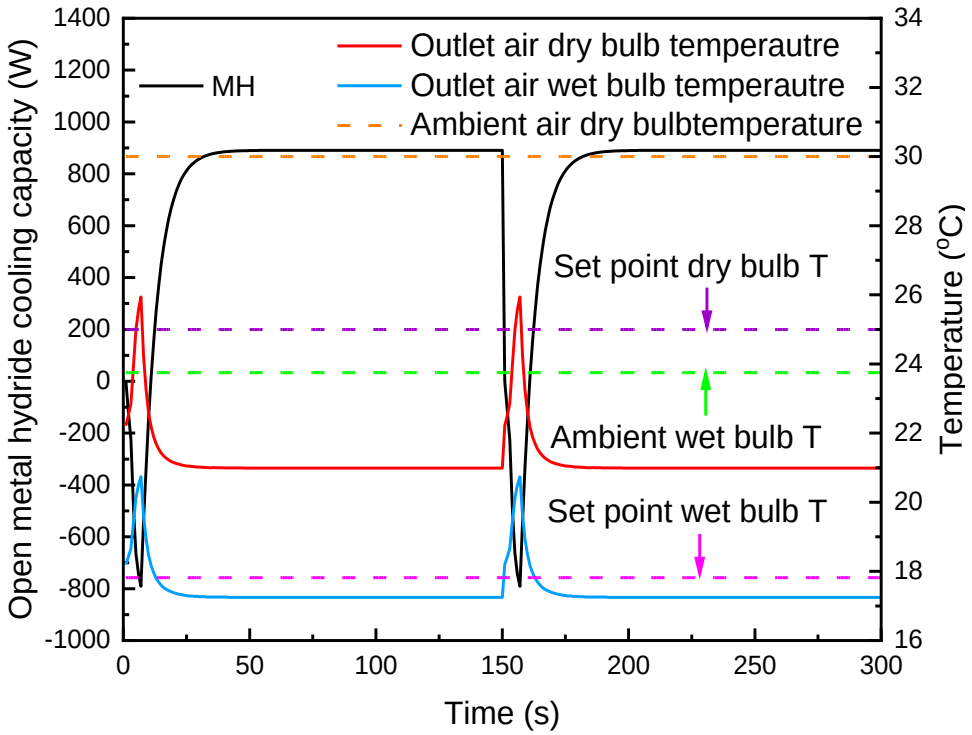

Figure 5.15. Real-time performance of the non-compressive cooling cycle (T_{abs}=35 °C, T_{des}=30 °C, RH_{air}=80%, X_{sol}=62%, T_{amb}=30 °C, m_{air}=0.07kg/s)

In summary, the proposed heat pump supplemented, open metal hydride-assisted, cooling and dehumidification system has better performance under high temperature and high humidity conditions compared to the previously published results in Ref.[251, 252]. In particular, the COP can be improved by 64% at an ambient temperature of 36 °C, however, it starts operating detrimentally when the ambient temperature is lower than 30 °C. This

could be solved by switching the heat pump supplemental mode and non-compressive model alternatively as the non-compressive cooling mode can provide sufficient cooling capacity without the compressor power consumption and increase the overall system COP. The proposed system is also affected by the battery discharging C rate which performs better under high battery power output conditions. The performance under low power output conditions could be improved by adjusting the battery coolant inlet and outlet temperature. This may have specific effects on the battery temperature uniformity, but the Model Predictive Control (MPC) strategy may minimize the impacts. The performance could be improved with the help of the increasing battery charging C rate, but the improvement is limited by the maximum fuel cell current density.

5.5 Chapter Summary

A highly integrated hybrid cooling system for an electric vehicle with a fuel cell extender, open-metal-hydride system, liquid desiccant dehumidification system, and heat pump waste system was proposed. The newly designed system can operate with or without the compressed refrigerant cycle which can improve the COP of the vehicle thermal management system and the cabin comfort in a hot climate. A numerical model was developed and validated by experimental results and published results. According to the results, the following conclusions were drawn:

- Under no-compressive operating mode, the cooling capacity of the proposed system improved by 25% to 70% when the battery charging C rate ranged from 0.05 to 0.18, and the improvement slowed down when the charging C rate exceeded 0.1.
- The fluctuations due to the thermal losses during the transition between two MHs caused 12s of the invalid cooling process, during which the proposed system ran under the non-compressive mode.
- The proposed system can achieve better performance with the increase of the ambient temperature while operating in heat pump supplemental mode. The COP increased by 40.9% when the ambient temperature varied from 30 ^{o}C to 36 ^{o}C.
- The COP of the proposed system under heat pump supplemental mode was 16.7% higher than that of the cited traditional vehicle air conditioning system when the ambient temperature was 34 ^{o}C with the same cabin temperature set point of 25 ^{o}C
- With the assistance of the heat pump, the proposed system could always provide supply air with a temperature under the setpoint of 24.5 ^{o}C, but a 12s insufficient

dehumidification period could be observed if the relative humidity of the setpoint was 50%.

Potential Future direction of the research

Further research could focus on how to further eliminate the fluctuation during the transition between the two MHs. Additionally, analysis of the performance under each operating mode from an operating vehicle perspective would be beneficial to help understand how much energy could be saved when the vehicle is running under the practical testing cycle. Moreover, the timing for the transition between the two operating modes should be further optimized in order to find the most efficient solution.

6. Conclusions and Future Plan

6.1 Conclusions

The worldwide usage of fossil fuels by ICE vehicles is having a direct impact on the rising global temperature as a result of CO_2 emissions. The UK government along with other countries has set ambitious targets to reach net zero carbon emissions. To achieve these goals, transport authorities in many countries have announced the phasing out of fossil fuel vehicles, as they account for more than 25% of total CO_2 emissions. However, the speed of promoting vehicle electrification is slow, and one of the main reasons is driving range anxieties. Around 30% to 50% electricity of a fully charged battery pack is consumed by the vehicle's thermal management including cabin, battery, and other electronics. Therefore, addressing the driving range anxieties via a vehicle thermal management perspective attracts great attention recently. The heat pump is widely discussed but the improvement of a separate heat pump system is limited as it cannot enhance the outlet air temperature and COP simultaneously. Considering integrating the heat pump with other component shows great potential but the unstable waste heat in EVs limits the effect of the integrated thermal management system and very little attention are paid to reducing energy consumption while cooling. This work set out to design and investigate a highly integrated vehicle thermal management system in order to provide high-level thermal comfort, high efficiency, and electricity at the time to eliminate the driving range deduction due to the vehicle thermal management, extend the driving range, and promoting the development of the vehicle electrification.

Initially, a heat pump-assisted, fuel cell backup integrated thermal management system was developed. The system utilized the cogeneration characteristic of the fuel cell to provide electricity and waste heat at the same time. A coolant heat pump was adopted to recover the waste heat from the fuel cell and battery for cabin heating. The numerical model was set up and validated by published results. An initial evaluation of the performance of the system regarding air outlet temperature, COP, heating capacity, and EEBC was discussed. A comparative analysis was introduced by comparing it to a traditional heat pump integrated system. The heat pump in the proposed system could operate with a COP of ranged from 4 to 5.5. The ambient temperature had no significant effect on the proposed system and as a result, it showed significant advantages at extremely cold temperatures compared to a normal system. The COP of the heat pump in the proposed system is 2.3 times that of an EVASHP system at -20 ℃. The trend of the EEBC of the proposed system is different from that of the

traditional heat pump thermal management system in BEVs. The EEBC increased along with the operating hours and was greater than the traditional EVASHP when operating over 2 hours.

Afterward, 4E analysis method was adopted to analyse the performance from a vehicle perspective by introducing an electric vehicle model to the model of the proposed system. The proposed system performs well in four aspects. For the energy performance, the system COP declined compared to the heat pump COP, but it could still operate with a system COP of over 3.8 under extremely cold weather. The driving range could be extended by 1.82 times compared to the widely adopted PTC heating system when providing the same amount of heat to the cabin. For the exergy performance, the exergy efficiency of the proposed system varies between 0.7 and 0.8 under the simulating operating parameters. For the environmental analysis, it demonstrated that from a driving vehicle level, the $TEWI_{DR}$ of the suggested system was only lower than that of traditional heat pump and PTC system when the GWP of the working refrigerant was lower than 470 or the ratio between emission factor of H_2 and electricity was lower than 85%. The effective operating cost for driving and heating is 4.9kWh/£ and 3.91 kWh/£ respectively under the simulation condition. The payback duration of installing the proposed system to EVs was 300,000km, but it will be largely reduced when the H_2 price and fuel cell price reduce in the future.

To provide a comprehensive solution not only for winter but also for summer, an integrated hybrid cooling system is proposed for the heat pump assisted fuel cell backup system designed above. The proposed system utilised metal hydride to recover the waste energy between the hydrogen vessel and fuel cell stack. A liquid desiccant dehumidification system was adopted to improve thermal comfort by supplying milder outlet air. The waste heat from fuel cell, battery and motor was transported by heat pump for solution regeneration. The proposed cooling system could operate in two different modes, namely non-compressive mode and heat pump supplement mode. Under the non-compressive mode, the cabin cooling system was not driven by VC system but the open metal hydride system. The cooling performance was limited by the size of the metal hydride and the battery charging C rate. The cooling capacity improved by 25% to 70% when the battery charging C rate ranged from 0.05 to 0.18. There was a 12s insufficient cooling period caused by the transition during two metal hydrides. To shorten the fluctuations and cover the insufficient cooling loads when cooling demands were higher, the heat pump supplemental operating mode was suggested. Compared to the traditional AC system, the proposed system under heat pump supplemental

mode improved the COP by 16.7% under 34 ºC ambient temperature. The insufficient cooling duration was reduced to 2s with the help of the heat pump.

The designed highly integrated vehicle energy management based on fuel cell and heat pump was demonstrated can provide better performance for cabin heating and cooling and can also fulfil the cooling demands of the fuel cell stack and the battery pack. The cogeneration characteristic of the fuel cell stack was well utilised to extend the vehicle driving range which can largely reduce the driving range anxiety. The proposed integrated system could provide a potential solution for developing energy management system for future zero emission vehicles and can also be adopt for domestic energy system to promote net zero.

6.2 Future plan

Although the performance and feasibility of the fuel cell and heat pump based energy management system has been discussed in this thesis, there are still a number of shortcomings and challenges in this research. From the practical application perspective, the price of the hydrogen, the way of producing the hydrogen will largely affect the impacts of the proposed systems on economic and environment. The safety of the hydrogen tank due to the high pressure and the stability of the metal hydride adopted in the integrated cooling system required additional examinations. From the research method perspective, in this thesis, only verified numerical model was carried out. Only partial dynamic model was built in this research and the optimal control logic was not considered. Therefore, in the future, firstly, the results in chapter 3 indicate that the variation in fuel cell current output and battery discharging C rate may lead to a lower supply air temperature, therefore, a good match between the fuel cell output C rate and battery discharging C rate should be further discussed. Secondly, a dynamic model could be built in Matlab Simulink and tested under widely adopted test cycles, such as Worldwide Harmonized Light Vehicles Test Cycle (WLTC). The main aim is to consider fuel cell and battery output and SOC together, in order to better understand the dynamic performance under different operating conditions. Thirdly, the optimization in the ratio of the fuel cell stack's and the battery pack's size, the size of the heat exchange, and the size of the metal hydride could be conducted in the future in order to achieve better performance and greater economic advantages. Last but not least, it would be better if a test rig could be built to evaluate the practical performance and optimize our model.

References

[1] Statistics N. 2021 UK greenhouse gas emissions, provisional figures. In: Department for Business EIS, editor.2022.
[2] Yu X, Jiang R, Lu G, Liu H, Tong Y, Qian G, et al. A novel energy-economic-environmental evaluation model for heat pump air conditioners integrated with waste heat recovery in electric vehicles. Case Studies in Thermal Engineering. 2023;41:102605.
[3] Canals Casals L, Martinez-Laserna E, Amante García B, Nieto N. Sustainability analysis of the electric vehicle use in Europe for CO2 emissions reduction. Journal of cleaner production. 2016;127:425-37.
[4] Shahbaz M, Nasir MA, Hille E, Mahalik MK. UK's net-zero carbon emissions target: Investigating the potential role of economic growth, financial development, and R&D expenditures based on historical data (1870-2017). Technological forecasting and social change. 2020;161:120255.
[5] Liu H, Wei Z, He W, Zhao J. Thermal issues about Li-ion batteries and recent progress in battery thermal management systems: A review. Energy Conversion and Management. 2017;150:304-30.
[6] Kandlikar SG, Lu Z. Thermal management issues in a PEMFC stack – A brief review of current status. Applied Thermal Engineering. 2009;29:1276-80.
[7] Qi Z. Advances on air conditioning and heat pump system in electric vehicles – A review. Renewable and Sustainable Energy Reviews. 2014;38:754-64.
[8] Wu W, Wang S, Wu W, Chen K, Hong S, Lai Y. A critical review of battery thermal performance and liquid based battery thermal management. Energy Conversion and Management. 2019;182:262-81.
[9] Zhao C, Zhang B, Zheng Y, Huang S, Yan T, Liu X. Hybrid Battery Thermal Management System in Electrical Vehicles: A Review. Energies. 2020;13:6257.
[10] Qin P, Sun J, Yang X, Wang Q. Battery thermal management system based on the forced-air convection: A review. eTransportation. 2021;7:100097.
[11] Kim J, Oh J, Lee H. Review on battery thermal management system for electric vehicles. Applied Thermal Engineering. 2019;149:192-212.
[12] Tomaszewska A, Chu Z, Feng X, O'Kane S, Liu X, Chen J, et al. Lithium-ion battery fast charging: A review. eTransportation. 2019;1:100011.
[13] Peng Q, Du Q. Progress in Heat Pump Air Conditioning Systems for Electric Vehicles—A Review. Energies. 2016;9:240.
[14] Zhang Z, Wang J, Feng X, Chang L, Chen Y, Wang X. The solutions to electric vehicle air conditioning systems: A review. Renewable and Sustainable Energy Reviews. 2018;91:443-63.
[15] Zhang Z, Wang D, Zhang C, Chen J. Electric vehicle range extension strategies based on improved AC system in cold climate – A review. International Journal of Refrigeration. 2018;88:141-50.
[16] Antti Lajunen S, Yinye Yang and AliEmadi. Review of Cabin Thermal Management for Electrified Passenger Vehicles. IEEE TRANSACTIONS ON VEHICULAR TECHNOLOGY. 2020;69.
[17] Chen K, Wu W, Yuan F, Chen L, Wang S. Cooling efficiency improvement of air-cooled battery thermal management system through designing the flow pattern. Energy. 2019;167:781-90.
[18] Chen K, Chen Y, She Y, Song M, Wang S, Chen L. Construction of effective symmetrical air-cooled system for battery thermal management. Applied Thermal Engineering. 2020;166:114679.
[19] Zhang F, Lin A, Wang P, Liu P. Optimization design of a parallel air-cooled battery thermal management system with spoilers. Applied Thermal Engineering. 2021;182:116062.
[20] Chen J, Zhao X, Wang B, Zhang C, Xuan D. Multiobjective optimization of air-cooled battery thermal management system based on heat dissipation model. Ionics. 2021;27:1307-22.
[21] Yang Y, Li W, Xu X, Tong G. Heat dissipation analysis of different flow path for parallel liquid cooling battery thermal management system. International Journal of Energy Research. 2020;44:5165-76.
[22] Wang H, Tao T, Xu J, Mei X, Liu X, Gou P. Cooling capacity of a novel modular liquid-cooled battery thermal management system for cylindrical lithium ion batteries. Applied Thermal Engineering. 2020;178:115591.

[23] Tan X, Lyu P, Fan Y, Rao J, Ouyang K. Numerical investigation of the direct liquid cooling of a fast-charging lithium-ion battery pack in hydrofluoroether. Applied Thermal Engineering. 2021;196:117279.
[24] Chang G, Cui X, Li Y, Ji Y. Effects of reciprocating liquid flow battery thermal management system on thermal characteristics and uniformity of large lithium-ion battery pack. International Journal of Energy Research. 2020;44:6383-95.
[25] Chung Y, Kim MS. Thermal analysis and pack level design of battery thermal management system with liquid cooling for electric vehicles. Energy Conversion and Management. 2019;196:105-16.
[26] Huang Y, Wang S, Lu Y, Huang R, Yu X. Study on a liquid cooled battery thermal management system pertaining to the transient regime. Applied Thermal Engineering. 2020;180:115793.
[27] Zhu Y, Fang Y, Su L, Fei Y. Experimental study on thermal performance of a pumped two-phase battery thermal management system. International Journal of Energy Research. 2020;44:4664-76.
[28] Wang Y-F, Wu J-T. Thermal performance predictions for an HFE-7000 direct flow boiling cooled battery thermal management system for electric vehicles. Energy Conversion and Management. 2020;207:112569.
[29] Park S, Jang DS, Lee D, Hong SH, Kim Y. Simulation on cooling performance characteristics of a refrigerant-cooled active thermal management system for lithium ion batteries. International Journal of Heat and Mass Transfer. 2019;135:131-41.
[30] Hong SH, Jang DS, Park S, Yun S, Kim Y. Thermal performance of direct two-phase refrigerant cooling for lithium-ion batteries in electric vehicles. Applied Thermal Engineering. 2020;173:115213.
[31] Shen M, Gao Q. Structure design and effect analysis on refrigerant cooling enhancement of battery thermal management system for electric vehicles. Journal of Energy Storage. 2020;32:101940.
[32] Wang Y, Gao Q, Wang H. Structural design and its thermal management performance for battery modules based on refrigerant cooling method. International Journal of Energy Research. 2020;45:3821-37.
[33] Yue QL, He CX, Jiang HR, Wu MC, Zhao TS. A hybrid battery thermal management system for electric vehicles under dynamic working conditions. International Journal of Heat and Mass Transfer. 2021;164:120528.
[34] Chen F, Huang R, Wang C, Yu X, Liu H, Wu Q, et al. Air and PCM cooling for battery thermal management considering battery cycle life. Applied Thermal Engineering. 2020;173:115154.
[35] Akbarzadeh M, Jaguemont J, Kalogiannis T, Karimi D, He J, Jin L, et al. A novel liquid cooling plate concept for thermal management of lithium-ion batteries in electric vehicles. Energy Conversion and Management. 2021;231:113862.
[36] Lv Y, Liu G, Zhang G, Yang X. A novel thermal management structure using serpentine phase change material coupled with forced air convection for cylindrical battery modules. Journal of Power Sources. 2020;468:228398.
[37] Yao M, Gan Y, Liang J, Dong D, Ma L, Liu J, et al. Performance simulation of a heat pipe and refrigerant-based lithium-ion battery thermal management system coupled with electric vehicle air-conditioning. Applied Thermal Engineering. 2021;191:116878.
[38] Jindal P, Bhattacharya J. Criticality of incorporating explicit in-situ measurement of temperature-dependent heat generation for accurate design of thermal management system for Li-ion battery pack. International Journal of Energy Research. 2020;44:6023-34.
[39] Xu M, Wang R, Reichman B, Wang X. Modeling the effect of two-stage fast charging protocol on thermal behavior and charging energy efficiency of lithium-ion batteries. Journal of Energy Storage. 2018;20:298-309.
[40] Ye Y, Saw LH, Shi Y, Somasundaram K, Tay AAO. Effect of thermal contact resistances on fast charging of large format lithium ion batteries. Electrochimica Acta. 2014;134:327-37.
[41] Ye Y, Saw LH, Shi Y, Tay AAO. Numerical analyses on optimizing a heat pipe thermal management system for lithium-ion batteries during fast charging. Applied Thermal Engineering. 2015;86:281-91.

[42] Ren D, Liu X, Feng X, Lu L, Ouyang M, Li J, et al. Model-based thermal runaway prediction of lithium-ion batteries from kinetics analysis of cell components. Applied Energy. 2018;228:633-44.
[43] Bao Y, Fan Y, Chu Y, Ling C, Tan X, Yang S. Experimental and Numerical Study on Thermal and Energy Management of a Fast-Charging Lithium-Ion Battery Pack with Air Cooling. Journal of Energy Engineering. 2019;145:04019030.
[44] Zheng Y, Shi Y, Huang Y. Optimisation with adiabatic interlayers for liquid-dominated cooling system on fast charging battery packs. Applied Thermal Engineering. 2019;147:636-46.
[45] Wang J, Zhang Y. Research on Cooling Characteristics of Power Battery Fast-charging of Refrigerant-based Direct Cooling System. IOP Conference Series: Earth and Environmental Science. 2021;696:012007.
[46] Al-Zareer M, Dincer I, Rosen MA. A thermal performance management system for lithium-ion battery packs. Applied Thermal Engineering. 2020;165:114378.
[47] Qian L. A comprehensive thermal analysis for the fast discharging process of a Li‐ion battery module with liquid cooling. International Journal of Energy Research. 2019;44:12245-58.
[48] Zhang W, Liang Z, Yin X, Ling G. Avoiding thermal runaway propagation of lithium-ion battery modules by using hybrid phase change material and liquid cooling. Applied Thermal Engineering. 2021;184:116380.
[49] Yang W, Zhou F, Zhou H, Wang Q, Kong J. Thermal performance of cylindrical lithium-ion battery thermal management system integrated with mini-channel liquid cooling and air cooling. Applied Thermal Engineering. 2020;175:115331.
[50] Xu J, Lan C, Qiao Y, Ma Y. Prevent thermal runaway of lithium-ion batteries with minichannel cooling. Applied Thermal Engineering. 2017;110:883-90.
[51] Mohammed AH, Esmaeeli R, Aliniagerdroudbari H, Alhadri M, Hashemi SR, Nadkarni G, et al. Dual-purpose cooling plate for thermal management of prismatic lithium-ion batteries during normal operation and thermal runaway. Applied Thermal Engineering. 2019;160:114106.
[52] Kshetrimayum KS, Yoon Y-G, Gye H-R, Lee C-J. Preventing heat propagation and thermal runaway in electric vehicle battery modules using integrated PCM and micro-channel plate cooling system. Applied Thermal Engineering. 2019;159:113797.
[53] Liu T, Tao C, Wang X. Cooling control effect of water mist on thermal runaway propagation in lithium ion battery modules. Applied Energy. 2020;267:115087.
[54] Liu T, Hu J, Tao C, Zhu X, Wang X. Effect of parallel connection on 18650-type lithium ion battery thermal runaway propagation and active cooling prevention with water mist. Applied Thermal Engineering. 2021;184:116291.
[55] Huang Y, Wu Y, Liu B. Experimental investigation into the use of emergency spray on suppression of battery thermal runaway. Journal of Energy Storage. 2021;38:102546.
[56] Liu Y, Gao Q, Wang G, Zhang T, Zhang Y. Experimental study on active control of refrigerant emergency spray cooling of thermal abnormal power battery. Applied Thermal Engineering. 2021;182:116172.
[57] Zhang Z, Li W, Zhang C, Chen J. Climate control loads prediction of electric vehicles. Applied Thermal Engineering. 2017;110:1183-8.
[58] Lajunen A. Energy Efficiency and Performance of Cabin Thermal Management in Electric Vehicles. SAE Technical Paper. 2017:2017-01-0192.
[59] Qin F, Shao S, Tian C, Yang H. Experimental Investigation on Heating Performance of Heat Pump for Electric Vehicles in Low Ambient Temperature. Energy Procedia. 2014;61:726-9.
[60] Wang Z, Wei M, Guo C, Zhao M. Enhance the Heating Performance of an Electric Vehicle AC/HP System under Low Temperature. Energy Procedia. 2017;105:2384-9.
[61] Zhang N, Lu Y, Ouderji ZH, Yu Z. Review of heat pump integrated energy systems for future zero-emission vehicles. Energy. 2023:127101.
[62] PARLIAMENT TE. Relating to emissions from air-conditioning systems in motor vehicles and amending Council

Directive 70/156/EEC. Official Journal of the European Union. 2006;161:8.
[63] Wu J, Zhou G, Wang M. A comprehensive assessment of refrigerants for cabin heating and cooling on electric vehicles. Applied Thermal Engineering. 2020;174:115258.

[64] Wang Y, Wang D, Yu B, Shi J, Chen J. Experimental and numerical investigation of a CO2 heat pump system for electrical vehicle with series gas cooler configuration. International Journal of Refrigeration. 2019;100:156-66.
[65] Song X, Lu D, Lei Q, Cai Y, Wang D, Shi J, et al. Experimental study on heating performance of a CO2 heat pump system for an electric bus. Applied Thermal Engineering. 2021;190:116789.
[66] Yu B, Yang J, Wang D, Shi J, Guo Z, Chen J. Experimental energetic analysis of CO2/R41 blends in automobile air-conditioning and heat pump systems. Applied Energy. 2019;239:1142-53.
[67] Junqi D, Yibiao W, Shiwei J, Xianhui Z, Linjie H. Experimental study of R744 heat pump system for electric vehicle application. Applied Thermal Engineering. 2021;183:116191.
[68] Liu C, Zhang Y, Gao T, Shi J, Chen J, Wang T, et al. Performance evaluation of propane heat pump system for electric vehicle in cold climate. International Journal of Refrigeration. 2018;95:51-60.
[69] Wang D, Yu B, Li W, Shi J, Chen J. Heating performance evaluation of a CO2 heat pump system for an electrical vehicle at cold ambient temperatures. Applied Thermal Engineering. 2018;142:656-64.
[70] Direk M, Yüksel F. Experimental Evaluation of an Automotive Heat Pump System with R1234yf as an Alternative to R134a. Arabian Journal for Science and Engineering. 2019;45:719-28.
[71] Feng L, Hrnjak P. Performance Characteristics of a Mobile Heat Pump System at Low Ambient Temperature. 2018;1.
[72] Choi YU, Kim MS, Kim GT, Kim M, Kim MS. Performance analysis of vapor injection heat pump system for electric vehicle in cold startup condition. International Journal of Refrigeration. 2017;80:24-36.
[73] Zhai K, Chen X. R410A Based Automotive Heat Pump System That Hits Cabin Heating Goal Successfully in -30 °C Extreme Ambient. 2019;1.
[74] Kwon C, Kim MS, Choi Y, Kim MS. Performance evaluation of a vapor injection heat pump system for electric vehicles. International Journal of Refrigeration. 2017;74:138-50.
[75] Khandaker M, Uddin A, Sanikal V, Fuad K, Lindquist C, Baker G, et al. Utilization of Bench Testing in Vehicle Thermal System Development for Extreme Cold Ambient Condition. SAE Technical Paper Series2020.
[76] Jung J, Jeon Y, Cho W, Kim Y. Effects of injection-port angle and internal heat exchanger length in vapor injection heat pumps for electric vehicles. Energy. 2020;193:116751.
[77] Jung J, Jeon Y, Lee H, Kim Y. Numerical study of the effects of injection-port design on the heating performance of an R134a heat pump with vapor injection used in electric vehicles. Applied Thermal Engineering. 2017;127:800-11.
[78] Qin F, Liu H, Zou H, Chen D, Tian C. Experiment Investigation and Control Strategies on Two-Phase Refrigerant Injection Heat Pump System for Electric Vehicle in Start-up Stage. Journal of Thermal Science. 2021;30:828-39.
[79] Mei Z, Hwang Y, Kim J. Thermodynamic analysis and LCCP evaluation of kangaroo heat pump cycle for electric vehicles. Energy. 2022;259:124995.
[80] Wang Y, Li W, Zhang Z, Shi J, Chen J. Performance evaluation and prediction for electric vehicle heat pump using machine learning method. Applied Thermal Engineering. 2019;159:113901.
[81] Cuevas C, Declaye S, Lemort V. Experimental characterization of a reversible heat pump for hybrid and electric vehicles. Advances in Mechanical Engineering. 2019;11:168781401984580.
[82] Wang Y, Li W, Zhang Z, Shi J, Chen J. Performance evaluation and prediction for electric vehicle heat pump using machine learning method. Applied Thermal Engineering. 2019;159.
[83] Li H-J, Zhou G-H, Li A-G, Li X-G, Li Y-N, Chen J. Heat pump air conditioning system for pure electric vehicle at ultra-low temperature. Thermal Science. 2014;18:1667-72.
[84] Chen Y, Zou H, Dong J, Wu J, Xu H, Tian C. Experimental investigation on the heating performance of a CO2 heat pump system with intermediate cooling for electric vehicles. Applied Thermal Engineering. 2021;182:116039.
[85] Wang A, Cao F, Jia F, Liu Y, Yin X, Song Y, et al. Development of the effective defrosting criterion for electric vehicles transcritical CO2 heat pumps under constant heating capacity operation. International Journal of Refrigeration. 2023;145:388-96.

[86] Li K, Lan J, Zhou G, Tang Q, Cheng Q, Fang Y, et al. Investigation on the Influence of Refrigerant Charge Amount on the Cooling Performance of Air Conditioning Heat Pump System for Electric Vehicles. Journal of Thermal Science. 2019;28:294-305.
[87] Li K, Xu D, Lan J, Su L, Fang Y. An experimental and theoretical investigation of refrigerant charge on a secondary loop air‐conditioning heat pump system in electric vehicles. International Journal of Energy Research. 2019;43:3381-98.
[88] Li K, Luo S, Wang Z, Zhang H, Su L, Fang Y, et al. An experimental investigation of oil circulation ratio influence on heating performance in an air condition heat pump system for electrical vehicles. International Journal of Refrigeration. 2021;122:220-31.
[89] Tang X, Guo Q, Li M, Jiang M. Heating Performance Characteristics of an Electric Vehicle Heat Pump Air Conditioning System Based on Exergy Analysis. Energies. 2020;13:2868.
[90] Li W, Liu Y, Liu R, Wang D, Shi J, Yu Z, et al. Performance evaluation of secondary loop low-temperature heat pump system for frost prevention in electric vehicles. Applied Thermal Engineering. 2021;182:115615.
[91] Li K, Yu J, Yu R, Su L, Fang Y, Yang Z. Experimental Investigation on Heating Performance of Newly Designed Air Source Heat Pump System for Electric Vehicles. Journal of Thermal Science and Engineering Applications. 2021;13.
[92] Yu Z, McKeown A, Hajabdollahi Ouderji Z, Essadik M. A flexible heat pump cycle for heat recovery. Communications Engineering. 2022;1:17.
[93] Pan L, Liu C, Zhang Z, Wang T, Shi J, Chen J. Energy-saving effect of utilizing recirculated air in electric vehicle air conditioning system. International Journal of Refrigeration. 2019;102:122-9.
[94] Zhang G, Zou H, Qin F, Xue Q, Tian C. Investigation on an improved heat pump AC system with the view of return air utilization and anti-fogging for electric vehicles. Applied Thermal Engineering. 2017;115:726-35.
[95] Chang T-B, Sheu J-J, Huang J-W. High-Efficiency HVAC System with Defog/Dehumidification Function for Electric Vehicles. Energies. 2020;14:46.
[96] Zhang L, Hashimoto K, Hasegawa H, Saikawa M. Performance analysis of a heat pump system with integrated desiccant for electric vehicles. International Journal of Refrigeration. 2018;86:154-62.
[97] Bellocchi S, Leo Guizzi G, Manno M, Salvatori M, Zaccagnini A. Reversible heat pump HVAC system with regenerative heat exchanger for electric vehicles: Analysis of its impact on driving range. Applied Thermal Engineering. 2018;129:290-305.
[98] Dvorak D, Basciotti D, Gellai I. Demand-Based Control Design for Efficient Heat Pump Operation of Electric Vehicles. Energies. 2020;13:5440.
[99] He H, Jia H, Huo W, Yan M. Stochastic Dynamic Programming of Air Conditioning System for Electric Vehicles. Energy Procedia. 2017;105:2518-24.
[100] He H, Jia H, Sun C, Sun F. Stochastic Model Predictive Control of Air Conditioning System for Electric Vehicles: Sensitivity Study, Comparison, and Improvement. IEEE Transactions on Industrial Informatics. 2018;14:4179-89.
[101] Cvok I, Škugor B, Deur J. Control trajectory optimisation and optimal control of an electric vehicle HVAC system for favourable efficiency and thermal comfort. Optimization and Engineering. 2020;22:83-102.
[102] Cvok I, Ratković I, Deur J. Optimisation of Control Input Allocation Maps for Electric Vehicle Heat Pump-based Cabin Heating Systems. Energies. 2020;13:5131.
[103] Zhu J, Elbel S. Implementation of Reinforcement Learning on Air Source Heat Pump Defrost Control for Full Electric Vehicles. 2018;1.
[104] Li K, Luo S, Yu J, Tang Q, Su L, Fang Y. An experimental investigation on frosting characteristics of a microchannel outdoor heat exchanger in an air conditioning heat pump system for electric vehicles. International Journal of Energy Research. 2020;44:7807-19.
[105] Zhou G, Li H, Liu E, Li B, Yan Y, Chen T, et al. Experimental study on combined defrosting performance of heat pump air conditioning system for pure electric vehicle in low temperature. Applied Thermal Engineering. 2017;116:677-84.

[106] Ahn JH, Lee JS, Baek C, Kim Y. Performance improvement of a dehumidifying heat pump using an additional waste heat source in electric vehicles with low occupancy. Energy. 2016;115:67-75.
[107] Lee D-Y, Cho C-W, Won J-P, Park YC, Lee M-Y. Performance characteristics of mobile heat pump for a large passenger electric vehicle. Applied Thermal Engineering. 2013;50:660-9.
[108] Zou H, Jiang B, Wang Q, Tian C, Yan Y. Performance Analysis of a Heat Pump Air Conditioning System Coupling with Battery Cooling for Electric Vehicles. Energy Procedia. 2014;61:891-4.
[109] Tian Z, Gan W, Zhang X, Gu B, Yang L. Investigation on an integrated thermal management system with battery cooling and motor waste heat recovery for electric vehicle. Applied Thermal Engineering. 2018;136:16-27.
[110] Tian Z, Gu B. Analyses of an integrated thermal management system for electric vehicles. International Journal of Energy Research. 2019;43:5788-802.
[111] Tian Z, Gu B, Gao W, Zhang Y. Performance evaluation of an electric vehicle thermal management system with waste heat recovery. Applied Thermal Engineering. 2020;169:114976.
[112] Varma M, Jaybhay S, Kadam K, Venu S, Kulkarni S, Kapoor S. Cabin and Battery Cooling Performance Trade-off in an Electric Vehicle. 2020;1.
[113] Ding P, Wang Z, Wang Y, Li K. A distributed multiple-heat source staged heating method in an electric vehicle. Renewable Energy. 2020;150:1010-8.
[114] Rana T, Yamamoto Y. Universal Electric Vehicle Thermal Management System. SAE International Journal of Advances and Current Practices in Mobility. 2020;3:604-13.
[115] Zhang G, Qin F, Zou H, Tian C. Experimental Study on a Dual- parallel-evaporator Heat Pump System for Thermal Management of Electric Vehicles. Energy Procedia. 2017;105:2390-5.
[116] Alkhulaifi YM, Qasem NAA, Zubair SM. Improving the performance of thermal management system for electric and hybrid electric vehicles by adding an ejector. Energy Conversion and Management. 2019;201:112133.
[117] Zhang K, Li M, Yang C, Shao Z, Wang L. Exergy Analysis of Electric Vehicle Heat Pump Air Conditioning System with Battery Thermal Management System. Journal of Thermal Science. 2019;29:408-22.
[118] Jeffs J, McGordon A, Picarelli A, Robinson S, Tripathy Y, Widanage WD. Complex Heat Pump Operational Mode Identification and Comparison for Use in Electric Vehicles. Energies. 2018;11:2000.
[119] Lee S, Chung Y, Kim S, Jeong Y, Kim MS. Predictive optimization method for the waste heat recovery strategy in an electric vehicle heat pump system. Applied Energy. 2023;333:120572.
[120] Cen J, Li Z, Jiang F. Experimental investigation on using the electric vehicle air conditioning system for lithium-ion battery thermal management. Energy for Sustainable Development. 2018;45:88-95.
[121] Cen J, Jiang F. Li-ion power battery temperature control by a battery thermal management and vehicle cabin air conditioning integrated system. Energy for Sustainable Development. 2020;57:141-8.
[122] Shen M, Gao Q. System simulation on refrigerant-based battery thermal management technology for electric vehicles. Energy Conversion and Management. 2020;203:112176.
[123] Guo J, Jiang F. A novel electric vehicle thermal management system based on cooling and heating of batteries by refrigerant. Energy Conversion and Management. 2021;237:114145.
[124] Behling NH. Chapter 2 - Fuel Cells and the Challenges Ahead. In: Behling NH, editor. Fuel Cells: Elsevier; 2013. p. 7-36.
[125] Xu J, Zhang C, Fan R, Bao H, Wang Y, Huang S, et al. Modelling and control of vehicle integrated thermal management system of PEM fuel cell vehicle. Energy. 2020;199.
[126] Kim S, Jeong H, Lee H. Cold-start performance investigation of fuel cell electric vehicles with heat pump-assisted thermal management systems. Energy. 2021;232.
[127] Şefkat G, Özel MA. Experimental and numerical study of energy and thermal management system for a hydrogen fuel cell-battery hybrid electric vehicle. Energy. 2022;238.
[128] Zhang N, Lu Y, Kadam S, Yu Z. Investigation of the integrated fuel cell, battery, and heat pump energy systems. Energy Conversion and Management. 2023;276:116503.

[129] Young K. Metal Hydrides☆. Reference Module in Chemistry, Molecular Sciences and Chemical Engineering: Elsevier; 2018.
[130] Kölbig M, Weckerle C, Linder M, Bürger I. Review on thermal applications for metal hydrides in fuel cell vehicles: Operation modes, recent developments and crucial design aspects. Renewable and Sustainable Energy Reviews. 2022;162:112385.
[131] Vashisht S, Rakshit D. Recent advances and sustainable solutions in automobile air conditioning systems. Journal of Cleaner Production. 2021;329:129754.
[132] Weckerle C, Nasri M, Hegner R, Linder M, Bürger I. A metal hydride air-conditioning system for fuel cell vehicles – Performance investigations. Applied Energy. 2019;256:113957.
[133] Weckerle C, Bürger I, Linder M. Numerical optimization of a plate reactor for a metal hydride open cooling system. International Journal of Hydrogen Energy. 2019;44:16862-76.
[134] Min H, Zhang Z, Sun W, Min Z, Yu Y, Wang B. A thermal management system control strategy for electric vehicles under low-temperature driving conditions considering battery lifetime. Applied Thermal Engineering. 2020;181:115944.
[135] Pan C, Tao Y, Wang L, Li H, Yang J. Fuzzy energy management strategy for electric vehicle combining driving cycle construction and air-conditioning load identification. Advances in Mechanical Engineering. 2021;13:168781402199438.
[136] Vatanparvar K, Faruque MAA. Design and Analysis of Battery-Aware Automotive Climate Control for Electric Vehicles. ACM Transactions on Embedded Computing Systems. 2018;17:1-22.
[137] Vahidi A, Sciarretta A. Energy saving potentials of connected and automated vehicles. Transportation Research Part C: Emerging Technologies. 2018;95:822-43.
[138] Amini MR, Wang H, Gong X, Liao-McPherson D, Kolmanovsky I, Sun J. Cabin and Battery Thermal Management of Connected and Automated HEVs for Improved Energy Efficiency Using Hierarchical Model Predictive Control. IEEE Transactions on Control Systems Technology. 2020;28:1711-26.
[139] Wang H, Amini MR, Hu Q, Kolmanovsky I, Sun J. Eco-Cooling Control Strategy for Automotive Air-Conditioning System: Design and Experimental Validation. IEEE Transactions on Control Systems Technology. 2021;29:2339-50.
[140] Park J, Kim Y. Supervised-Learning-Based Optimal Thermal Management in an Electric Vehicle. IEEE Access. 2020;8:1290-302.
[141] Han X, Zou H, Wu J, Tian C, Tang M, Huang G. Investigation on the heating performance of the heat pump with waste heat recovery for the electric bus. Renewable Energy. 2020;152:835-48.
[142] Lee S, Chung Y, Jeong Y, Kim MS. Experimental study on an electric vehicle heat pump system with multi-level waste heat recovery using a vapor injection technique at low ambient temperatures. Energy Conversion and Management. 2022;267:115935.
[143] Smith P, Beaumont L, Bernacchi CJ, Byrne M, Cheung W, Conant RT, et al. Essential outcomes for COP26. Global change biology. 2022;28:1-3.
[144] Shin YH, Sim S, Kim SC. Performance Characteristics of a Modularized and Integrated PTC Heating System for an Electric Vehicle. Energies. 2016;9:18.
[145] Higuchi Y, Kobayashi H, Shan Z, Kuwahara M, Endo Y, Nakajima Y. Efficient heat pump system for PHEV/BEV. SAE Technical Paper; 2017.
[146] Marcotte M, Grabowski S. 16 - Minimising energy consumption associated with drying, baking and evaporation. In: Klemeš J, Smith R, Kim J-K, editors. Handbook of Water and Energy Management in Food Processing: Woodhead Publishing; 2008. p. 481-522.
[147] Zhang Z, Li W, Shi J, Chen J. A Study on Electric Vehicle Heat Pump Systems in Cold Climates. Energies. 2016;9:881.
[148] Qin F, Zhang G, Xue Q, Zou H, Tian C. Experimental investigation and theoretical analysis of heat pump systems with two different injection portholes compressors for electric vehicles. Applied Energy. 2017;185:2085-93.
[149] Jung J, Jeon Y, Cho W, Kim Y. Effects of injection-port angle and internal heat exchanger length in vapor injection heat pumps for electric vehicles. Energy. 2020;193.
[150] Li W, Liu R, Liu Q, Liu Y, Wang D, Xia S, et al. Upstream and downstream injection effects on R134a economized vapor injection heat pump system at low temperatures for electric vehicles. International Journal of Refrigeration. 2020;120:1-11.

[151] Junqi D, Yibiao W, Shiwei J, Xianhui Z, Linjie H. Experimental study of R744 heat pump system for electric vehicle application. Applied Thermal Engineering. 2021;183.
[152] Shen M, Gao Q. System simulation on refrigerant-based battery thermal management technology for electric vehicles. Energy Conversion and Management. 2020;203.
[153] Varma M, Jaybhay S, Kadam K, Venu S, Kulkarni S, Kapoor S. Cabin and Battery Cooling Performance Trade-off in an Electric Vehicle. SAE Technical Paper Series2020.
[154] Ma J, Sun Y, Zhang S, Li J, Li S. Experimental study on the performance of vehicle integrated thermal management system for pure electric vehicles. Energy Conversion and Management. 2022;253:115183.
[155] Tian Z, Gu B, Gao W, Zhang Y. Performance evaluation of an electric vehicle thermal management system with waste heat recovery. Applied Thermal Engineering. 2020;169.
[156] Ehrenstein M, Galán-Martín Á, Tulus V, Guillén-Gosálbez G. Optimising fuel supply chains within planetary boundaries: A case study of hydrogen for road transport in the UK. Applied Energy. 2020;276:115486.
[157] Lee H, Lee D, Kim Y. Heating performance of a coolant-source heat pump using waste heat from stack and electric devices in fuel cell electric vehicles under cold conditions. Energy Conversion and Management. 2022;252:115092.
[158] Albayati I, Ali R, Calay R. Modelling and Examining Open Circuit Voltage for PEM Fuel Cells. Journal of Electrical Engineering. 2013;13:140-6.
[159] Mann RF, Amphlett JC, Hooper MA, Jensen HM, Peppley BA, Roberge PR. Development and application of a generalised steady-state electrochemical model for a PEM fuel cell. Journal of power sources. 2000;86:173-80.
[160] Khan M, Iqbal M. Dynamic modeling and simulation of a small wind–fuel cell hybrid energy system. Renewable energy. 2005;30:421-39.
[161] Saleh IMM, Ali R, Zhang H. Simplified mathematical model of proton exchange membrane fuel cell based on horizon fuel cell stack. Journal of Modern Power Systems and Clean Energy. 2016;4:668-79.
[162] Wang Y, Wang C-Y. Modeling polymer electrolyte fuel cells with large density and velocity changes. Journal of the Electrochemical Society. 2005;152:A445.
[163] Dicks A, Rand D. Fuel Cell Systems Explained2018.
[164] Liso V, Nielsen MP, Kær SK, Mortensen HH. Thermal modeling and temperature control of a PEM fuel cell system for forklift applications. International Journal of Hydrogen Energy. 2014;39:8410-20.
[165] Mahamud R, Park C. Reciprocating air flow for Li-ion battery thermal management to improve temperature uniformity. Journal of Power Sources. 2011;196:5685-96.
[166] Liu G, Ouyang M, Lu L, Li J, Han X. Analysis of the heat generation of lithium-ion battery during charging and discharging considering different influencing factors. Journal of Thermal Analysis and Calorimetry. 2014;116:1001-10.
[167] TRANSPORTATION USDO. New car assessment program (NCAP) FMVSS NO. 305 incidant test. 2013.
[168] Incropera FP, DeWitt DP. Fundamentals of Heat and Mass Transfer: Wiley; 2002.
[169] Donowski V. Theoretical investigation of the evaporation heat transfer coffifficient of refrigerant R-134a in a plate heat exchanger: Rochester Institute of Technology; 1999.
[170] Yan YY, Lin TF. Evaporation Heat Transfer and Pressure Drop of Refrigerant R-134a in a Plate Heat Exchanger. Journal of Heat Transfer. 1999;121:118-27.
[171] Dobson MK, Chato JC. Condensation in Smooth Horizontal Tubes. Journal of Heat Transfer. 1998;120:193-213.
[172] Wallis GB. Discussion: “Estimation of Steady-State Steam Void-Fraction by Means of the Principle of Minimum Entropy Production” (Zivi, S. M., 1964, ASME J. Heat Transfer, 86, pp. 247–251). Journal of Heat Transfer. 1964;86:252-.
[173] Cuevas C, Fonseca N, Lemort V. Automotive electric scroll compressor: Testing and modeling. International Journal of Refrigeration. 2012;35:841-9.
[174] Ríos GM, Schirmer J, Gentner C, Kallo J. Efficient thermal management strategies for cold starts of a proton exchange membrane fuel cell system. Applied Energy. 2020;279:115813.

[175] Luo M, Zhang J, Zhang C, Chin CS, Ran H, Fan M, et al. Cold start investigation of fuel cell vehicles with coolant preheating strategy. Applied Thermal Engineering. 2022;201:117816.
[176] Qin F, Xue Q, Albarracin Velez GM, Zhang G, Zou H, Tian C. Experimental investigation on heating performance of heat pump for electric vehicles at −20 °C ambient temperature. Energy Conversion and Management. 2015;102:39-49.
[177] Ajanovic A, Glatt A, Haas R. Prospects and impediments for hydrogen fuel cell buses. Energy. 2021;235:121340.
[178] Labor DoLLUSDo. Average energy prices for the United States, regions, census divisions, and selected metropolitan areas. United States government; 2022.
[179] Institute BM. Manufacturing Cost Analysis of 1, 5, 10 and 25 kW Fuel Cell Systems for Primary Power and Combined Heat and Power Applications. In: energy USDo, editor.2017.
[180] Grant N. The Paris Agreement's ratcheting mechanism needs strengthening 4-fold to keep 1.5°C alive. Joule. 2022;6:703-8.
[181] Axsen J, Bhardwaj C, Crawford C. Comparing policy pathways to achieve 100% zero-emissions vehicle sales by 2035. Transportation Research Part D: Transport and Environment. 2022;112:103488.
[182] Lauvergne R, Perez Y, Françon M, Tejeda De La Cruz A. Integration of electric vehicles into transmission grids: A case study on generation adequacy in Europe in 2040. Applied Energy. 2022;326:120030.
[183] Fetene GM, Kaplan S, Mabit SL, Jensen AF, Prato CG. Harnessing big data for estimating the energy consumption and driving range of electric vehicles. Transportation Research Part D: Transport and Environment. 2017;54:1-11.
[184] Lee H-S, Lee M-Y. Steady state and start-up performance characteristics of air source heat pump for cabin heating in an electric passenger vehicle. International Journal of Refrigeration. 2016;69:232-42.
[185] Yu B, Ouyang H, Shi J, Guo Z, Chen J. Experimental evaluation of cycle performance for new-developed refrigerants in the electric vehicle heat pump systems. International Journal of Refrigeration. 2021;129:118-27.
[186] Yang T, Zou H, Tang M, Tian C, Yan Y. Experimental performance of a vapor-injection CO2 heat pump system for electric vehicles in −30 °C to 50 °C range. Applied Thermal Engineering. 2022;217:119149.
[187] Steiner A, Rieberer R. Simulation based identification of the ideal defrost start time for a heat pump system for electric vehicles. International Journal of Refrigeration. 2015;57:87-93.
[188] Li W, Liu Y, Liu R, Wang D, Shi J, Yu Z, et al. Performance evaluation of secondary loop low-temperature heat pump system for frost prevention in electric vehicles. Applied Thermal Engineering. 2021;182.
[189] Liu N, Cui Q, Li H, Li K, Fang Y, Su L, et al. Investigating the performance optimization of an outdoor condenser–evaporator for an electric vehicle heat pump system. Energy Reports. 2021;7:5130-40.
[190] Mahvi AJ, Boyina K, Musser A, Elbel S, Miljkovic N, National Renewable Energy Lab GCO. Superhydrophobic heat exchangers delay frost formation and enhance efficency of electric vehicle heat pumps. International journal of heat and mass transfer. 2021;172:121162.
[191] Lu Y, Chen H, Wang L, Yu Z, Huang Y, Yu X, et al. Energy Storage driving towards a clean energy future. Energy Reports. 2021;7:8128-30.
[192] Ahn JH, Kang H, Lee HS, Jung HW, Baek C, Kim Y. Heating performance characteristics of a dual source heat pump using air and waste heat in electric vehicles. Applied Energy. 2014;119:1-9.
[193] Larminie J, Dicks A. Fuel cell systems explained. 2nd ed. Chichester, West Sussex: J. Wiley; 2003.
[194] Hayes JG, Goodarzi GA. Electric powertrain: energy systems, power electronics and drives for hybrid, electric and fuel cell vehicles. Hoboken, New Jersey: Wiley; 2018.
[195] Kinab E, Marchio D, Rivière P, Zoughaib A. Reversible heat pump model for seasonal performance optimization. Energy and Buildings. 2010;42:2269-80.
[196] Guo JJ, Wu JY, Wang RZ, Li S. Experimental research and operation optimization of an air-source heat pump water heater. Applied Energy. 2011;88:4128-38.

[197] Zaareer M, Mourad A-H. Effect of Vehicle Side Mirror Base Position on Aerodynamic Forces and Acoustics. Alexandria Engineering Journal. 2022;61:1437-48.
[198] Tesla. MODEL S OWNER'S MANUAL. www.tesla.com: Tesla; 2022.
[199] Szirtes T. Applied dimensional analysis and modeling: Butterworth-Heinemann; 2007.
[200] Habermehl C, Jacobs G, Neumann S. A modeling method for gear transmission efficiency in transient operating conditions. Mechanism and Machine Theory. 2020;153:103996.
[201] Leo TJ, Durango JA, Navarro E. Exergy analysis of PEM fuel cells for marine applications. Energy. 2010;35:1164-71.
[202] Amidpour M, Khoshgoftar Manesh MH. Chapter 5 - Exergy and thermoeconomic evaluation of cogeneration and polygeneration systems. In: Amidpour M, Khoshgoftar Manesh MH, editors. Cogeneration and Polygeneration Systems: Academic Press; 2021. p. 55-74.
[203] Kadam ST, Kyriakides A-S, Khan MS, Shehabi M, Papadopoulos AI, Hassan I, et al. Thermo-economic and environmental assessment of hybrid vapor compression-absorption refrigeration systems for district cooling. Energy. 2022;243:122991.
[204] Koronaki IP, Cowan D, Maidment G, Beerman K, Schreurs M, Kaar K, et al. Refrigerant emissions and leakage prevention across Europe – Results from the RealSkillsEurope project. Energy. 2012;45:71-80.
[205] O'Neill NF, Ma JM, Walther DC, Brockway LR, Ding C, Lin J. A modified total equivalent warming impact analysis: Addressing direct and indirect emissions due to corrosion. Science of The Total Environment. 2020;741:140312.
[206] Ember. Carbon intensity of the power sector in the European Union in 2021, by country (in grams of CO_2 per kilowatt-hour). www.statista.com: Statista; 2022.
[207] Rievaj V, Gaňa J, Synák F. Is hydrogen the fuel of the future? Transportation Research Procedia. 2019;40:469-74.
[208] Washers KP. Mini 12v (DC) Submersible Water Pump To Run 10/122 From Tank. https://kranzle-pressure-washers.co.uk/products/mini-12v-submersible-water-pump2022.
[209] Beijing Golden Nanfeng International Manufacturer TC. High Voltage Electric Vehicle PTC heater similar to Webasto high-voltage heater (HVH) for electric and hybrid vehicles. https://www.alibaba.com/product-detail/High-Voltage-Electric-Vehicle-PTC-heater_1600504411156.html2022.
[210] Institute BM. Manufacturing Cost Analysis of PEM Fuel Cell Systems for 5- and 10-kW Backup Power Applications. U.S. Department of Energy; 2016.
[211] Hua T, Ahluwalia R, Peng J-K, Kromer M, Lasher S, McKenney K, et al. Technical Assessment of Compressed Hydrogen Storage Tank Systems for Automotive Applications United States: Argonne National Laboratory; 2010.
[212] Duffner F, Wentker M, Greenwood M, Leker J. Battery cost modeling: A review and directions for future research. Renewable and Sustainable Energy Reviews. 2020;127:109872.
[213] GOV.UK. Energy bills support factsheet. In: Department for Business EIS, editor. GOV.UK: GOV.UK; 2022.
[214] Candelaresi D, Valente A, Bargiacchi E, Spazzafumo G. 16 - Life cycle assessment of hybrid passenger electric vehicle. In: Lo Faro M, Barbera O, Giacoppo G, editors. Hybrid Technologies for Power Generation: Academic Press; 2022. p. 475-95.
[215] Hao X, Wang H, Lin Z, Ouyang M. Seasonal effects on electric vehicle energy consumption and driving range: A case study on personal, taxi, and ridesharing vehicles. Journal of Cleaner Production. 2020;249:119403.
[216] COP 26 in Glasgow. International Journal of Refrigeration. 2021;132:v-vi.
[217] Robaina M, Neves A. Complete decomposition analysis of CO2 emissions intensity in the transport sector in Europe. Research in Transportation Economics. 2021;90:101074.
[218] Crabtree G. The coming electric vehicle transformation. Science. 2019;366:422-4.
[219] Bridge D, Dutta N, Porteous S, Rouaud C, Beloe N. Use of palliative technologies in minimising HVAC loads and their impact on EV range. Vehicle Thermal Management Systems Conference Proceedings (VTMS11): Woodhead Publishing; 2013. p. 251-65.
[220] Kambly KR, Bradley TH. Estimating the HVAC energy consumption of plug-in electric vehicles. Journal of Power Sources. 2014;259:117-24.

[221] Xie Y, Yang P, Qian Y, Zhang Y, Li K, Zhou Y. A two-layered eco-cooling control strategy for electric car air conditioning systems with integration of dynamic programming and fuzzy PID. Applied Thermal Engineering. 2022;211:118488.
[222] Meng Z, Zhang H, Lei M, Qin Y, Qiu J. Performance of low GWP R1234yf/R134a mixture asa replacement for R134a in automotive air conditioning systems. International Journal of Heat and Mass Transfer. 2018;116:362-70.
[223] Fang J, Yin X, Wang A, Sun X, Liu Y, Cao F. Cooling performance enhancement for the automobile transcritical CO2 air conditioning system with various internal heat exchanger effectiveness. Applied Thermal Engineering. 2021;196:117274.
[224] Zhang N, Chen X, Su Y, Zheng H, Ramadan O, Zhang X, et al. Numerical investigations and performance comparisons of a novel cross-flow hollow fiber integrated liquid desiccant dehumidification system. Energy. 2019;182:1115-31.
[225] Alahmer A. Thermal analysis of a direct evaporative cooling system enhancement with desiccant dehumidification for vehicular air conditioning. Applied Thermal Engineering. 2016;98:1273-85.
[226] Chen X, Su Y, Aydin D, Bai H, Jarimi H, Zhang X, et al. Experimental investigation of a polymer hollow fibre integrated liquid desiccant dehumidification system with aqueous potassium formate solution. Applied Thermal Engineering. 2018;142:632-43.
[227] Chen X, Zhang N, Su Y, Aydin D, Zheng H, Bai H, et al. Performance analysis and design implementation of a novel polymer hollow fiber liquid desiccant dehumidifier with aqueous potassium formate. Thermal Science and Engineering Progress. 2019;13:100366.
[228] Wu S, Feng L, Changizian S, Raeesi M, Aiedi H. Analysis of air conditioning system impact on a fuel cell vehicle performance based on a realistic model under actual urban conditions. International Journal of Hydrogen Energy. 2022;47:25899-912.
[229] Deng L, Li S, Tang X, Yang K, Lin X. Battery thermal- and cabin comfort-aware collaborative energy management for plug-in fuel cell electric vehicles based on the soft actor-critic algorithm. Energy Conversion and Management. 2023;283:116889.
[230] Farsi A, Rosen MA. PEM fuel cell-assisted lithium ion battery electric vehicle integrated with an air-based thermal management system. International Journal of Hydrogen Energy. 2022;47:35810-24.
[231] Xu J, Zhang C, Fan R, Bao H, Wang Y, Huang S, et al. Modelling and control of vehicle integrated thermal management system of PEM fuel cell vehicle. Energy. 2020;199:117495.
[232] Li L, Gao S, Wang B, Li C, Wang Y, Sun B, et al. Analysis of cooling and heating characteristics of thermal management system for fuel cell bus. International Journal of Hydrogen Energy. 2023;48:11442-54.
[233] Lototskyy M, Tolj I, Klochko Y, Davids MW, Swanepoel D, Linkov V. Metal hydride hydrogen storage tank for fuel cell utility vehicles. International Journal of Hydrogen Energy. 2020;45:7958-67.
[234] Davids MW, Lototskyy M, Malinowski M, van Schalkwyk D, Parsons A, Pasupathi S, et al. Metal hydride hydrogen storage tank for light fuel cell vehicle. International Journal of Hydrogen Energy. 2019;44:29263-72.
[235] Di Giorgio P, Di Ilio G, Jannelli E, Conte FV. Innovative battery thermal management system based on hydrogen storage in metal hydrides for fuel cell hybrid electric vehicles. Applied Energy. 2022;315:118935.
[236] Meier K, Kurtz C, Weckerle C, Hubner M, Bürger I. Air-conditioning system for vehicles with on-board hydrogen. Applied Thermal Engineering. 2018;129:1150-9.
[237] Xu B, Arjmandzadeh Z. Parametric study on thermal management system for the range of full (Tesla Model S)/ compact-size (Tesla Model 3) electric vehicles. Energy Conversion and Management. 2023;278:116753.
[238] Gillet T, Andres E, El-Bakkali A, Lemort V, Rulliere R, Haberschill P. Sleeping evaporator and refrigerant maldistribution: An experimental investigation in an automotive multi-evaporator air-conditioning and battery cooling system. International Journal of Refrigeration. 2018;90:119-31.
[239] Weckerle C, Bürger I, Linder M. Novel reactor design for metal hydride cooling systems. International Journal of Hydrogen Energy. 2017;42:8063-74.

[240] Fumo N, Goswami DY. Study of an aqueous lithium chloride desiccant system: air dehumidification and desiccant regeneration. Solar Energy. 2002;72:351-61.
[241] Melinder Å. Thermophysical Properties of Aqueous Solutions Used as Secondary Working Fluids [Doctoral thesis, comprehensive summary]. Stockholm: KTH; 2007.
[242] Pakowski Z. Chemical Engineering Research and Design. 2007;85:1683-4.
[243] Zhang LZ, Jiang Y, Zhang YP. Membrane-based humidity pump: performance and limitations. Journal of Membrane Science. 2000;171:207-16.
[244] Zhang L-Z. Heat and mass transfer in a randomly packed hollow fiber membrane module: A fractal model approach. International Journal of Heat and Mass Transfer. 2011;54:2921-31.
[245] Zhang L-Z. Fabrication of a lithium chloride solution based composite supported liquid membrane and its moisture permeation analysis. Journal of Membrane Science. 2006;276:91-100.
[246] Zhang J, Kærn MR, Ommen T, Elmegaard B, Haglind F. Condensation heat transfer and pressure drop characteristics of R134a, R1234ze(E), R245fa and R1233zd(E) in a plate heat exchanger. International Journal of Heat and Mass Transfer. 2019;128:136-49.
[247] Yan Y-Y, Lio H-C, Lin T-F. Condensation heat transfer and pressure drop of refrigerant R-134a in a plate heat exchanger. International Journal of Heat and Mass Transfer. 1999;42:993-1006.
[248] Akbarzadeh M, Jaguemont J, Kalogiannis T, Karimi D, He J, Jin L, et al. A novel liquid cooling plate concept for thermal management of lithium-ion batteries in electric vehicles. Energy Conversion and Management. 2021;231.
[249] Seyed-Ahmadi M, Erb B, Simonson CJ, Besant RW. Transient behavior of run-around heat and moisture exchanger system. Part I: Model formulation and verification. International Journal of Heat and Mass Transfer. 2009;52:6000-11.
[250] Fojtlin M, Planka M, Fišer J, Pokorny J, Jicha M. Airflow Measurement of the Car HVAC Unit Using Hot-wire Anemometry. EPJ Web of Conferences. 2016;114:02023.
[251] Subiantoro A, Ooi KT, Stimming U. Energy Saving Measures for Automotive Air Conditioning (AC) System in the Tropics. 2014.
[252] Pino FJ, Marcos D, Bordons C, Rosa F. Car air-conditioning considerations on hydrogen consumption in fuel cell and driving limitations. International Journal of Hydrogen Energy. 2015;40:11696-703.

Appendix 1

The requirements for an alternative format thesis containing published works or submitted works are that the text of the publications must be un-altered. As such, changes have only been made to allow the thesis to be understood as a coherent whole (e.g. figure and table numbers, chapter numbering etc.). The work presented in this thesis has been published in peer reviewed journals or submitted to a journal but not yet approved for publication. Where other authors are listed, this is in a supervisory capacity. My contribution to each section was greater than 50%.

Chapter 2: Nan Zhang, Yiji Lu, Zahra Hajabdollahi Ouderji, Zhibin Yu, Review of heat pump integrated energy systems for future zero-emission vehicles, Energy, Volume 273, 2023, 127101

Chapter 3: Nan Zhang, Yiji Lu, Sambhaji Kadam, Zhibin Yu, Investigation of the integrated fuel cell, battery, and heat pump energy systems, Energy Conversion and Management, Volume 276, 2023, 116503

Chapter 4: Nan Zhang, Yiji Lu, Sambhaji Kadam, Zhibin Yu, A fuel cell range extender integrating with heat pump for cabin heat and power generation. Applied Energy, Volume 348, 121600

Chapter 5: Nan Zhang, Yiji Lu, Zhibin Yu, A cleaner and efficient energy system achieving a sustainable future for road transport. Journal of Cleaner Production, Volume 418, 2023,137982